Dynamical Modeling and Control of Multiphase Heat Transport Systems Based on Loop Heat Pipes

Zur Erlangung des akademischen Grades eines
DOKTOR-INGENIEURS
von der KIT-Fakultät für
Elektrotechnik und Informationstechnik
des Karlsruher Instituts für Technologie (KIT)
genehmigte

DISSERTATION

von
Thomas Christoph Gellrich, M.Sc.
geb. in Heilbronn

Tag der mündlichen Prüfung:	23. Juni 2022
Hauptreferent:	Prof. Dr.-Ing. Sören Hohmann
Korreferent:	Prof. Dr.-Ing. Thomas Wetzel

Preface

This thesis is the result of my work as a research scientist in the department Control in Information Technology (CIT) at the FZI Research Center for Information Technology and at the Institute of Control Systems (Institut für Regelungs- und Steuerungssysteme; IRS) at the Karlsruhe Institute of Technology (KIT).

First of all, I would like to thank Prof. Dr.-Ing. Sören Hohmann sincerely for his continuous support. In the years under your supervision, I have always felt your support in this project and your confidence in my work.

I would also like to thank Prof. Dr.-Ing. Thomas Wetzel for his genuine interest in this topic and his agreement to review this thesis. Already at our first meeting during my work on the Bachelor's thesis, I have appreciated your helpful assistance and the pleasant conversations.

The work was partly carried out on behalf of the Space Administration of the German Aerospace Center (Deutsches Zentrum für Luft- und Raumfahrt; DLR) with funds from the German Federal Ministry for Economic Affairs and Energy (Bundesministerium für Wirtschaft und Energie; BMWi) with the reference number 50YH1612. The continuous support by the Space Administration for the joint project is gratefully acknowledged. The author would also like to thank the project partners Tesat-Spacecom GmbH & Co. KG and the Institute of Thermal Process Engineering (Institut für Thermische Verfahrenstechnik; TVT) at the KIT for their support, the fruitful discussions, and the preparation and provision of the measurement data.

Also, I would like to thank my colleagues both at the FZI and the KIT. I will always remember the friendly atmosphere in both facilities and the interesting exchanges about science and life. My sincere thanks go especially to Stefan, Mathias, Balint, Tobias, and Thomas for their valuable feedback on this thesis. I am also grateful to all the students who have supported me over the years with their work and joy of discussion on the subject. Special thanks go to my real and virtual roommate Balint, with whom I could discuss my findings before and during the coronavirus pandemic and who kept on pushing me to the final goal.

Last but not least, my deepest gratitude goes to my family, who has always believed in me, who has experienced with me the ups and downs that such a work entails, and who has encouraged me to continue to the end.

Tübingen, March 2022

Meiner Frau und meinen Eltern

Zusammenfassung

Zur effektiven Thermalkontrolle in der Luft- und Raumfahrt sowie in terrestrischen Anwendungen werden Loop Heat Pipes (LHPs) eingesetzt. Um die Betriebstemperatur dieser mehrphasigen Wärmetransportsysteme zu regeln, werden elektrische Heizelemente genutzt. Aktuelle Regler der Heizelemente mit aufwändigem, heuristischem Entwurfsprozess erreichen jedoch mäßige Regelungsergebnisse und können nichtlineare Phänomene, wie Temperaturschwingungen, nicht kompensieren. Des Weiteren stoßen diese Regler bei hochentwickelten Wärmetransportsystemen mit mehreren LHPs oder Komponenten an ihre Grenzen. Um diese Defizite zu eliminieren, konzentriert sich diese Arbeit auf die dynamische Modellierung und den modellbasierten Reglerentwurf.

Zur Modellierung des dynamischen Verhaltens der geregelten Temperaturen gegenüber Eingangs- und Störgrößenänderungen wird ein nichtlineares Zustandsraummodell der LHP entwickelt. Auf Basis dieses Modells werden nichtlineare Zustandsregler entworfen, um die Betriebstemperatur konstant zu halten. Anhand eines vereinfachten Modells können alternative Regler modellbasiert entworfen werden, die durch einen geringeren Implementierungs- und Rechenaufwand sowie niedrige Sensoranforderungen charakterisiert sind. Durch modulare Erweiterungen werden das nichtlineare Modell und entsprechend die Regler an die hochentwickelten Wärmetransportsysteme angepasst.

Die umfangreiche Validierung der Modelle erfolgt durch Messungen verschiedener LHP-Systeme. Außerdem wird das Verhalten interner, schwer zugänglicher Variablen und die Performance der vorgeschlagenen Regler in einer numerischen LHP-Simulation verifiziert und verglichen. Darüber hinaus können die ungewollten Temperaturschwingungen während des Betriebs der LHP reproduziert und durch die entwickelten Regler kompensiert werden. Die Ergebnisse dieser Arbeit legen den Grundstein für die Optimierung von Reglerparametern und -strukturen sowie den effizienten Reglerentwurf für zukünftige LHP-Anwendungen.

Contents

List of Figures

List of Tables

Abbreviations and Symbols

Abbreviations

Abbreviation	Description
ArHP	arterial heat pipe
AW	anti-windup
BMWi	Bundesministerium für Wirtschaft und Energie (Federal Ministry for Economic Affairs and Energy)
CC	compensation chamber
CIT	Control in Information Technology
CO	condenser
CPU	central processing unit
DF	disturbance feedforward control
DLR	Deutsches Zentrum für Luft- und Raumfahrt (German Aerospace Center)
EDRS	European Data Relay System
EKF	extended Kalman filter
ESA	European Space Agency
EV	evaporator
FZI	FZI Forschungszentrum Informatik (FZI Research Center for Information Technology)
HFLA	high frequency low amplitude
HTS	heat transport system
ID	parameter identification
IRS	Institut für Regelungs- und Steuerungssysteme (Institute of Control Systems)
ISS	International Space Station
KIT	Karlsruhe Institute of Technology
LCT	laser communication terminal
LEO	low-Earth orbit
LFHA	low frequency high amplitude
LHP	loop heat pipe
LHS	left-hand side
LL	liquid line
LTI	linear time-invariant
LY	nonlinear Lyapunov-based controller
MAD	maximal absolute deviation

Abbreviation	Description
MIMO	multiple-input-multiple-output
Model 4D	four-dimensional complex state-space model of a conventional LHP
Model C	complex state-space model of a conventional LHP
Model M	advanced state-space model of a single LHP with attached thermal mass
Model P	advanced state-space model of parallel LHPs with ArHPs
Model S	simplified state-space model of a conventional LHP
nMIAC	nonlinear model identification adaptive control
nMIACc/S	cascade control based on nMIAC/S
nMIAC/S	nonlinear model identification adaptive control based on Model S
NPV	nonlinear parameter-varying
nSF/C	nonlinear PI state feedback controller based on Model C
nSFc/C	cascade control based on nSF/C
nSF/M	nonlinear PI state feedback controller based on Model M
nSFc/M	cascade control based on nSF/M
nSF/P	nonlinear PI state feedback controller based on Model P
OF	output feedback control
OP	operating point
OT	operating temperature
P	proportional
PE	parameter estimation
PI	proportional-integral
piAW/M	PI controller with AW structure based on Model M
piAW/P	PI controller with AW structure based on Model P
piAW/S	PI controller with AW structure based on Model S
piAWc/S	cascade control based on piAW/S
PID	proportional-integral-derivative
piDF/S	PI controller with disturbance feedforward control based on Model S
piDFc/S	cascade control based on piDF/S
piDF/M	PI controller with disturbance feedforward control based on Model M
piOF/S	PI output feedback control based on Model S
piOFc/S	cascade control based on piOF/S
PR	state prediction
RAM	random access memory
RHS	right-hand side
RMSE	root mean square error
SE	state estimation
SF	state feedback control
SIM	numerical LHP simulation of [MKHW19]
SIMO	single-input-multiple-output
SISO	single-input-single-output
SRUKF	square-root unscented Kalman filter
SSOT	steady-state operating temperature
TEC	thermoelectric cooler

Abbreviation	Description
TS	temperature sensor
TVT	Institut für Thermische Verfahrenstechnik (Institute of Thermal Process Engineering)
UKF	unscented Kalman filter
UT	unscented transformation
VCHP	variable conductance heat pipe
VL	vapor line

Symbols

Symbol	Description
A	cross-sectional area
A_p	pipe cross-sectional area of the condenser / transport lines
A_s	heat transfer surface area
$A_{s,ll}$	effective heat transfer surface area of the LL
$A_{s,vl}$	effective heat transfer surface area of the VL
A_{wf}	Antoine constant A of the working fluid
$\boldsymbol{A}_{ex}$	extended system matrix
$\boldsymbol{A}_{lin}$	system matrix
$\boldsymbol{A}_{npv}$	system matrix of the NPV system
$\boldsymbol{A}_{tn}$	system matrix of a thermal network
$\boldsymbol{a}$	unforced vector function of the state equation of an input-affine system
$\mathcal{A}$	parameter
α	convective heat transfer coefficient
α_{rad}	effective radiation heat transfer coefficient
α_{ukf}	SRUKF parameter
B	momentum
B_{wf}	Antoine constant B of the working fluid
$\boldsymbol{B}$	momentum vector
$\boldsymbol{B}_{lin}$	input matrix
$\boldsymbol{B}_{tn}$	input matrix of a thermal network
$\boldsymbol{b}$	forced vector function of the state equation of an input-affine system
$\boldsymbol{b}_{ex}$	extended input vector
$\boldsymbol{b}_{lin}$	input vector
$\boldsymbol{b}_{npv}$	input vector of the NPV system
$\mathcal{B}$	parameter
β	volume fraction ratio of the CC subsystem

Symbol	Description
β_{co}^{op}	volume fraction ratio of the condenser subsystem in the OP
β_{ukf}	SRUKF parameter
C	controller transfer function
C_{cc}	thermal capacity of the CC subsystem
C_{cc}^{op}	thermal capacitance of the CC subsystem in the OP
C_{co}^{op}	thermal capacitance of the condenser subsystem in the OP
C_{ev}^{op}	thermal capacitance of the evaporator subsystem in the OP
$C_{ev,sf}$	thermal capacitance of the evaporator body
C_{th}	thermal capacitance
C_{tm}	thermal capacitance of the LCT structure
C_{wf}	Antoine constant C of the working fluid
$\boldsymbol{C}_{lin}$	output matrix
$\boldsymbol{C}_{tn}$	output matrix of a thermal network
c	velocity
$\bar{c}$	mean isobaric specific heat capacity
c_p	isobaric specific heat capacity
c_p^l	isobaric specific heat capacity of liquid
c_p^v	isobaric specific heat capacity of vapor
$\boldsymbol{c}$	velocity vector / output vector function of an input-affine system
$\boldsymbol{c}_{lin}^{\top}$	output vector
$\mathcal{C}$	parameter
D	thickness
D_i	inner diameter of a pipe
D_p	pipe diameter of the condenser / transport lines
$\boldsymbol{D}_{lin}$	direct transition matrix
$\boldsymbol{d}$	disturbance vector
$\boldsymbol{d}^{op}$	disturbance vector in the OP
$\boldsymbol{d}_{tn}$	disturbance vector of a thermal network
$\mathcal{D}$	parameter
Δh^v	(latent) heat of evaporation
Δh_{cc}^v	(latent) heat of evaporation at T_{cc}
Δh_{co}^v	(latent) heat of evaporation at $T_{co,s}$ / T_{co}
Δh_{ev}^v	(latent) heat of evaporation at $T_{ev,s}$ / T_{ev}
ΔL	length difference
$\Delta \dot{m}$	mass flow rate difference
Δp_{ca}	capillary pressure
$\Delta \dot{Q}_{cc}$	CC power difference
ΔT	temperature difference
Δt	time difference
ΔT_{cc}	CC temperature difference
ΔT_{coo}	condenser outlet temperature difference
ΔT_m	logarithmic mean temperature difference
δ	relative degree

Symbol	Description
δ_{npv}	relative degree of the NPV system
E_{kin}	kinetic energy
E_{pot}	potential energy
E_{sys}	total energy of a system
$\boldsymbol{E}_{lin}$	state disturbance matrix
$\boldsymbol{E}_{tn}$	state disturbance matrix of a thermal network
e	CC control error
e_{ev}	evaporator control error
$\boldsymbol{e}_{id}$	identification error vector
$\boldsymbol{e}_{ukf}$	residual output error vector
$\mathbb{E}$	expectation
E	set of edges
$\mathcal{E}$	parameter
ϵ	surface emissivity
η	coefficient
η_{ukf}	scaling parameter
F	force / Laplace transform of f
F_{fr}	friction pressure force
F_w	weight against z-direction
$\boldsymbol{F}$	force vector / vector function of the discrete state equation
$\boldsymbol{F}_{tn}$	output disturbance matrix of a thermal network
f	function
$\boldsymbol{f}$	vector function of the state equation
$\boldsymbol{f}_{npv}$	vector function of the NPV system
$\mathcal{F}$	parameter
φ	phase margin
G	system transfer function
$\boldsymbol{G}$	vector function of the discrete output equation
g	gravitational constant / function
$\boldsymbol{g}$	vector function of the output equation
G	graph
$\mathcal{G}$	parameter
γ	coefficient
$\bar{\gamma}$	mean void fraction in the two-phase region of the condenser
γ_{ukf}	scalar weighting factor
H	enthalpy
H_{cc}	enthalpy of the CC subsystem
H_{cc}^{l}	liquid enthalpy of the two-phase fluid in the CC subsystem
H_{cc}^{v}	vapor enthalpy of the two-phase fluid in the CC subsystem
$\boldsymbol{H}$	vector function of the discrete parameter-dependent output equation
$\dot{H}$	enthalpy flow rate
$\dot{H}_{cc,i}^{l}$	liquid enthalpy flow rate into the CC subsystem
$\dot{H}_{cc}^{l}$	liquid enthalpy flow rate out of the CC subsystem

Symbol	Description
h	specific enthalpy
h^l	specific enthalpy of liquid
h^v	specific enthalpy of vapor
$\mathcal{H}$	parameter
$\boldsymbol{I}$	identity matrix
i	index
i_{pi}	integral part of the PI controller
$\mathcal{I}$	parameter
$\boldsymbol{J}$	Jacobian matrix
j	index
$\mathcal{J}$	parameter
K_{aw}	feedback gain of the AW structure
K_i	integral gain
K_{i2}	integral gain of the outer control loop
K_p	proportional gain
K_{p1}	proportional gain of the inner control loop
K_{p2}	proportional gain of the outer control loop
K_q	gain of the disturbance feedforward control
K_r	maximum setpoint rate
$\boldsymbol{K}_{ex}$	state feedback gain matrix of the extended control system
$\boldsymbol{K}_s$	first part of $\boldsymbol{K}_{ex}$
$\boldsymbol{K}_{ukf}$	Kalman gain matrix
$\boldsymbol{K}_x$	state feedback gain matrix of the linear control model
k	discrete time
$k_{2\phi}$	heat transfer coefficient of the two-phase region in the condenser
k_{ll}	heat transfer coefficient of the LL
k_{sc}	heat transfer coefficient of the subcooled region in the condenser
k_{sh}	heat transfer coefficient of the superheated region in the condenser
k_{th}	overall heat transfer coefficient
k_{vl}	heat transfer coefficient of the VL
$\mathcal{K}$	parameter
L	length / Lie derivative
$L_{2\phi}$	length of the two-phase region in the condenser subsystem
$L_{2\phi}^{op}$	length of the two-phase region in the OP
L_{co}	total length of the condenser subsystem
L_{lc}	total length of the liquid column in the LHP
L_{ll}	length of the LL
L_{sc}	length of the subcooled region in the condenser subsystem
L_{sh}	length of the superheated region in the condenser subsystem
L_{vl}	length of the VL
l	index
$\mathcal{L}$	parameter
λ	eigenvalue

Symbol	Description
λ_{ly}	rate of decrease of the control Lyapunov function V_{ly}
λ_{th}	thermal conductivity
λ_{ukf}	scaling parameter
$\boldsymbol{M}$	leading principal minor
m	mass
$m_{cc}^{2\phi}$	total mass of the two-phase fluid in the CC subsystem
m_{cc}^{l}	liquid mass of the two-phase fluid in the CC subsystem
m_{cc}^{v}	vapor mass of the two-phase fluid in the CC subsystem
m^{l}	liquid mass
$\dot{m}^{l,op}$	liquid mass flow rate in the OP
m^{v}	vapor mass
$\dot{m}$	mass flow rate
$\dot{m}_{o}^{2\phi}$	mass flow rate across the boundary between the two-phase and the subcooled region in the condenser
$\dot{m}_{i}^{2\phi}$	mass flow rate across the boundary between the superheated and the two-phase region in the condenser
$\dot{m}^{l}$	liquid mass flow rate
$\dot{m}^{v}$	vapor mass flow rate
$\mathcal{M}$	parameter
μ	dynamic viscosity
$\mu_{co,o}^{l}$	dynamic viscosity of the liquid at the outlet of the condenser subsystem
μ^{l}	dynamic viscosity of the liquid
$\boldsymbol{N}$	identification matrix
n	number of state variables / temperature nodes in a thermal network
$\mathcal{N}$	parameter
∇T	temperature gradient
$\boldsymbol{\nu}_{mn}$	measurement noise
$\boldsymbol{\nu}_{pn}$	process noise
$\boldsymbol{\nu}_{ppn}$	parameter process noise
$\mathcal{O}$	parameter
P	power
$\boldsymbol{P}_{xy}$	cross-covariance matrix
p	pressure / number of input variables
p_{cc}	saturation pressure in the CC subsystem
p_{co}	saturation pressure in the two-phase region of the condenser subsystem
p_{ev}	saturation pressure in the evaporator subsystem
p_{s}	saturation pressure
$\boldsymbol{p}$	parameter vector
$\boldsymbol{p}^{*}$	optimal parameter vector
$\hat{p}$	estimated parameter
$\hat{\boldsymbol{p}}$	estimated parameter vector
$\hat{\boldsymbol{p}}^{-}$	updated parameter vector
$\mathcal{P}$	parameter

Symbol	Description
$\mathbf{p}$	sigma point vector of the parameters
Q	heat
$\boldsymbol{Q}_{ctr}$	controllability matrix
$\boldsymbol{Q}_{ctr,ex}^{-1}$	inverse controllability matrix of the extended control system
$\boldsymbol{Q}_{obs}$	observability matrix
$\dot{Q}$	heat flow rate
$\dot{Q}_{2\phi}$	heat flow rate from the two-phase condenser region to the heat sink
$\dot{Q}_{cc}$	rate of heat input to the CC by the control heater
$\dot{Q}_{cc}^{op}$	rate of heat input to the CC by the control heater in the OP
$\dot{Q}_{co}$	overall heat flow rate at the condenser subsystem to the heat sink
$\dot{Q}_{ev}$	heat load at the evaporator
$\dot{Q}_{ev}^{op}$	heat load at the evaporator in the OP
$\dot{Q}_{ev}^{SIM}$	heat load at the evaporator of SIM
$\dot{Q}_{hs}$	dissipated heat of the heat source
$\dot{Q}_{lk}$	heat leak
$\dot{Q}_{ll}$	heat flow rate to the LL subsystem from the surroundings
$\dot{Q}_{sc}$	heat flow rate from the subcooled condenser region to the heat sink
$\dot{Q}_{sf}$	heat load at the surface of a thermal mass
$\dot{Q}_{sh}$	heat flow rate from the superheated condenser region to the heat sink
$\dot{Q}_{ssot,h}$	highest heat load, for which the SSOT can be controlled at the setpoint temperature by CC heating
$\dot{Q}_{ssot,l}$	lowest heat load, for which the SSOT can be controlled at the setpoint temperature by CC heating
$\dot{Q}_{ssot,m}$	heat load at the minimal SSOT
$\dot{Q}_{ssot,t}$	heat load at the transition of the LHP operation mode from fixed to variable conductance mode
$\dot{Q}_{vl}$	heat flow rate from the VL subsystem to the surroundings
q	number of output variables / external heat flows into a thermal network
$\boldsymbol{q}_{ctr,ex}^{\top}$	last row of the inverse controllability matrix $\boldsymbol{Q}_{ctr,ex}^{-1}$
$\dot{q}$	heat flux
R	specific gas constant
R_{co}	thermal resistance of the heat flow at the condenser to the heat sink
$R_{hp1,tm}$	thermal resistance between ArHP 1 and the LCT structure
$R_{hp2,tm}$	thermal resistance between ArHP 2 and the LCT structure
R_{lk}	thermal resistance of the heat leak
R_p	pore radius of the primary wick
R_{sf}	thermal resistance between the surface and the fluid of the evaporator
$R_{sf,tm}$	thermal resistance between the evaporator surface and the LCT structure
R_{sh}	thermal resistance of the superheated vapor in the evaporator subsystem
R_{th}	thermal resistance
$\boldsymbol{R}_{mn}$	measurement noise covariance matrix

Symbol	Description
$\boldsymbol{R}_{pn}$	process noise covariance matrix
r	number of LHPs in a coupled heat transport system
$\mathbb{R}$	set of real numbers
$\mathcal{R}$	parameter
ρ	density
$\rho^{2\phi}$	homogeneous density in the two-phase region of the condenser
ρ_{cc}^{l}	liquid density in the CC subsystem
ρ_{cc}^{v}	vapor density in the CC subsystem
ρ_{co}^{l}	liquid density in the two-phase region of the condenser subsystem
$\rho_{co,o}^{l}$	liquid density at the outlet of the condenser subsystem
$\rho_{cc,i}^{l}$	liquid density at the inlet of the CC subsystem
ρ_{co}^{v}	vapor density in the two-phase region of the condenser subsystem
S	entropy
$\boldsymbol{S}_y$	Cholesky factor of the output covariance matrix
$\boldsymbol{S}$	Cholesky factor of the state covariance matrix
$\boldsymbol{S}_p$	Cholesky factor of the state covariance matrix of the parameter process
$\boldsymbol{S}^{-}$	updated $\boldsymbol{S}$
$\boldsymbol{S}_p^{-}$	updated $\boldsymbol{S}_p$
$\dot{S}_g$	entropy generation rate
s	complex variable in the Laplace domain
σ	surface tension
T	temperature
T_{amb}	ambient temperature
T_{cc}	mean temperature in the CC subsystem
$T_{cc,i}$	temperature at the CC inlet
$T_{cc,m}$	measured CC temperature
T_{cc}^{off}	temperature offset of the CC subsystem
T_{cc}^{op}	CC temperature in the OP
T_{co}	mean temperature in the condenser subsystem
$T_{co,i}$	temperature at the condenser inlet
$T_{co,o}$	temperature at the condenser outlet
$T_{co,s}$	saturation temperature in the condenser subsystem
T_d	delay time constant
T_{ev}	mean temperature in the evaporator subsystem
$T_{ev,m}$	measured evaporator temperature
$T_{ev,s}$	saturation temperature in the evaporator subsystem
$T_{ev,sf}$	evaporator surface temperature
T_{hp1}	temperature of ArHP 1
T_{hp2}	temperature of ArHP 2
T_i	inlet temperature
T_o	outlet temperature
T_{ref}	reference temperature
T_s	saturation temperature

Symbol	Description
T_{set}	setpoint temperature for the CC temperature
$T_{set,act}$	actual setpoint temperature for the CC temperature
$T_{set,ev}$	setpoint temperature for the evaporator temperature
T_{sk}	sink temperature
T_{sk}^{op}	sink temperature in the OP
$T_{ssot,m}$	minimal SSOT
T_{st}	sampling time constant
T_{tm}	temperature of the LCT structure
t	time
T	set of vertices
θ_c	contact angle in the primary wick
θ_e	elevation angle of the system
U	internal energy / Laplace transform of u
U_{cc}	internal energy of the CC subsystem
U_{co}	thermal conductance of the heat flow at the condenser to the heat sink
U_{ev}	internal energy of the evaporator subsystem
U_{lk}	thermal conductance of the heat leak
U_{ll}	thermal conductance of the LL
U_{sys}	internal energy of a system
U_{th}	thermal conductance
U_{vl}	thermal conductance of the VL
u	specific internal energy / input variable
u^{op}	input variable in the OP
u_{tn}	input variable of a thermal network
$\boldsymbol{u}$	input vector
$\boldsymbol{u}_{tn}$	input vector of a thermal network
V	volume
V_{cc}	total fluid volume of the CC subsystem
V_{ly}	control Lyapunov function
v	specific volume / input variable
v^l	specific liquid volume
v^v	specific vapor volume
$\boldsymbol{v}$	input vector
W	work
w	height
x_{aw}	output of the AW structure
x_{ex}	external state variable
x_{tn}	state variable of a thermal network
$\boldsymbol{x}$	state vector
$\boldsymbol{x}_0$	initial state vector
$\boldsymbol{x}_{in}$	internal state vector
$\boldsymbol{x}^{op}$	state vector in the OP
$\boldsymbol{x}_{tn}$	state vector of a thermal network

Symbol	Description
$\hat{\boldsymbol{x}}$	estimated state vector
$\hat{\boldsymbol{x}}^-$	updated state vector
x	sigma point vector of the states
Y	Laplace transform of y
y	output variable
y_{cl}	output of the total control
y_{df}	output of the feedforward control
y_p	output of the P controller
y_{pi}	output of the PI controller
$\boldsymbol{y}$	output vector
$\boldsymbol{y}_d$	desired output vector
$\boldsymbol{y}_{tn}$	output vector of a thermal network
$\hat{\boldsymbol{y}}^-$	updated output vector
$\hat{\boldsymbol{y}}_d^-$	updated desired output vector
y	sigma point vector of the outputs
Z^a	weight of a sigma point
Z^b	weight of a sigma point transition error
$\boldsymbol{Z}$	decoupling matrix
z	Cartesian coordinate
$\mathcal{Z}$	parameter

1 Introduction

The reliability, durability, and performance of an electronic device depend significantly on its thermal management. During the operation, electrical energy is partially transformed into waste heat that raises the operating temperature (OT) of the device. Thus, the excess heat must be transferred to a suitable cooling system at a lower temperature in order to keep the OT at a required setpoint for optimal operating conditions.

The thermal control of electronic components in space applications is a particular challenge although space is just above absolute zero [KW15]. Since space is a vacuum, matter can only release its heat in the form of electromagnetic waves. Thus, thermal radiation is the fundamental heat transfer mechanism that enables the dissipation of heat into space. In order to transfer the waste heat of an electronic component to the radiant heat sink of the spacecraft, heat transport systems are necessary. Through the removal of the excess heat, the OT of the electronic component is controlled. To satisfy the growing power demands of electronic components in space applications and to push these components toward optimal performance and long service lifetimes for successful missions near the earth or in outer space, accurate and reliable heat transport systems are needed to achieve the best possible operating conditions.

An example of space applications with integrated heat transport systems can be found in the European Data Relay System (EDRS), the ongoing project of the public-private partnership between the European Space Agency (ESA) and Airbus Defence and Space [Eur15a].

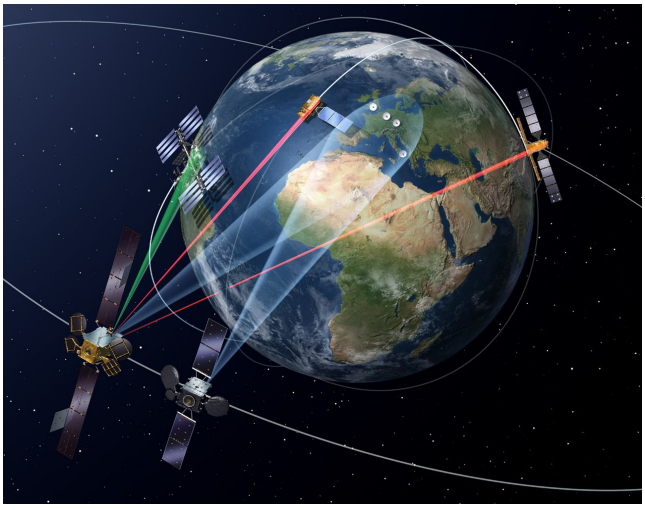

Figure 1.1: The European Data Relay System (EDRS) with two geostationary satellites connecting the ground stations in Europe with two satellites and the International Space Station (ISS) on low-Earth orbits (LEOs) [Eur14]

As depicted in Fig. 1.1, two geostationary nodes of the EDRS network are currently orbiting around Earth on host satellites to relay data between low-Earth orbit (LEO) satellites and the fixed ground stations in Europe. Due to the higher position of the relay satellites on the geostationary orbit at approximately $36{,}000\,\mathrm{km}$, these satellites always have a direct line of sight with the ground stations for a continuous data transmission. In contrast, LEO satellites have only a limited transmission window with the ground stations on their trajectory around Earth. Based on the indirect communication with the ground stations through the relay satellites, the transmission window of LEO satellites is considerably increased. Furthermore, the data transmission in the EDRS network is based on laser communications technology, which reduces the transfer delays and increases the data transfer rate compared to the commonly used radio technology [Eur15a].

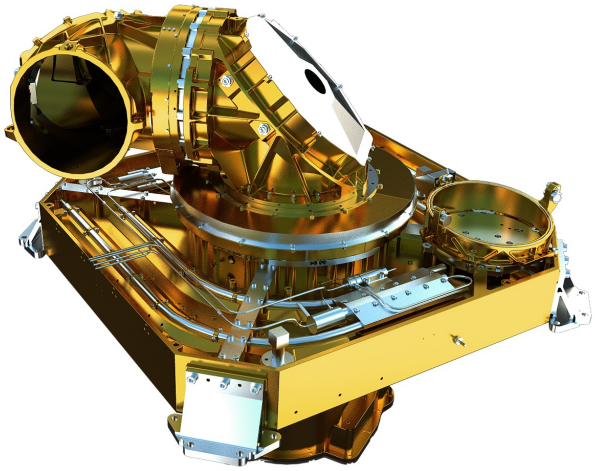

Figure 1.2: Laser communication terminal (LCT) with loop heat pipes (LHPs) for thermal control [Eur15b]

The geostationary host satellites are equipped with laser communication terminals (LCTs) (see Fig. 1.2), which have been developed by Tesat-Spacecom GmbH & Co. KG. The optical direct link between two LCTs reaches data transfer rates with up to $1800\,\mathrm{Mbit\,s^{-1}}$ over more than $40{,}000\,\mathrm{km}$ to transfer data from space to ground in near real-time [Eur15a]. These numbers are only possible if the laser is controlled in a narrow temperature corridor. Thus, the excess heat of the LCT must be transferred to the remote radiator with adequate heat transport systems.

For the thermal control of LCTs, Tesat-Spacecom works with so-called loop heat pipes (LHPs) (see silver structure on the LCT platform in Fig. 1.2). LHPs are widely used in thermal control of aerospace systems due to their passive, two-phase working principle [Ku99]. As multiphase thermodynamic systems, LHPs use the latent heat of the phase transition to reach a higher heat transport capacity, i.e. a higher overall thermal conductance, than conventional single-phase heat transport systems. Thus, the size and the weight of the heat transport system based on two-phase LHPs can be reduced to meet the strict mass requirements in aerospace applications [vEvG13]. Another advantage of LHPs is connected with the passive driving force of the mass flow in the pipes. Without the use of power-consuming, error-prone mechanical pumps, the

mass flow of the working fluid in the flexible transport lines is established self-sufficiently by capillary forces in a fine-pored wick during evaporation [May05]. This wick is located in the evaporator (EV), one of the five components of an LHP (see Fig. 1.3). The evaporator near the heat source is named after the phase transition process evaporation. It is connected to the corresponding condenser (CO) near the heat sink via the transport lines: one line for the vapor phase (vapor line, VL) and one line for the liquid phase (liquid line, LL). A reservoir or compensation chamber (CC) is attached to the evaporator to balance the two-phase mass distribution in transient states. Compared to conventional multiphase heat pipes without the local separation of evaporation and condensation via transport lines, LHPs provide a reliable and effective solution to the heat transport problem against gravity and over increased distances [Shu15].

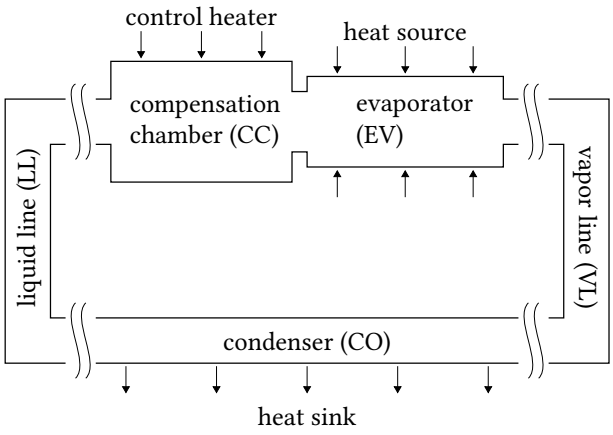

Figure 1.3: Schematic of a conventional LHP with its five components and three main external influences

Although the specific benefits of LHPs in terms of their power and mass effectiveness are especially relevant for aerospace systems [vEvG13], their application has spread to various other domains in recent years, such as server and automotive systems (see [ZSC+08], [MVPF10] and [PAP16], [BCG+18]). These terrestrial applications make additional use of the LHP's high thermal conductance, flexibility, and quiet, reliable operation. For all applications, an LHP has to be characterized and designed specifically by a thermodynamic engineer to meet the various requirements of the cooled object and its environment. However, the use of LHPs as heat transport systems also poses a significant challenge to control engineers. In order to keep the OT of the cooled object in a desired temperature corridor, the OT of the LHP itself must be controlled. Different control devices exist to regulate the OT of the LHP of which electrical control heaters (see Fig. 1.3) are most common for their simple implementation [Ku08] and reliable operation without any mechanical parts. Such control heaters are installed on the LHPs used in the LCT. While the OT is fixed at a desired setpoint temperature by a comparably small amount of applied heat, the natural behavior of the LHP, which is the transport of large amounts of excess heat, is maintained.

So far, heuristic controllers for the control heaters are applied to characterize and design temperature-controlled LHPs. The repeated manual adaptions of these controllers to their specific applications requires a high number of experiments. These experiments are performed on test benches in vacuum chambers for a near-space simulation of the slow thermodynamic processes and therefore consume a lot of expensive test bench time. Moreover, the current controllers with a trial-and-error parameterization show moderate control results and reach their limits in advanced LHP systems, i.e. systems with more than one LHP, multiple LHP components or further attachments. Thus, the performance of control heaters in LHP-based heat transport systems must be improved.

A model-based control design does not share the disadvantages of the current heuristic approach. Instead, it lays the foundation for an improved control performance of LHP-based heat transport systems by adjusting the control architecture and control parameters to the modeled system's dynamics. This requires the profound understanding of the fundamental dynamics of the basic LHP up to the advanced LHP system. Accurate physical modeling of an LHP like any other multiphase system, however, is challenging because of the individual complexity of the combined heat and mass transfer processes [Ku99]. Furthermore, the model-based control design has to be aligned with the situation of the LHP application. The collaboration between the manufacturer and the end user of the LHP may complicate the modeling and control design process. Considering the example of the LCT, the LHP manufacturer is not willing to share detailed information about the interior of the LHP with the LCT manufacturer as LHP end user and control designer who also maintains business relationships with competitive LHP manufacturers. Since the internal structures of LHP components are subject to the trade secret of the LHP manufacturer, internal geometries and parameters are rarely included when acquiring an LHP. In addition, constructional changes of the LHP as hermetically sealed heat transfer device to influence and measure its OT need to be avoided since toxic ammonia is used as working fluid inside the LHP to meet the thermal requirements in space. That is why the LHP end user prefers noninvasive actuators and sensors to provide information about the system, which are usually easy to install. However, the possibility and the accuracy to determine internal variables and parameters externally with surface measurements is naturally limited. Consequently, there is a particular need for a model-based control design for LHP-based systems which focuses on a limited number of internal parameters and variables and still achieves the desired model accuracy and control performance.

Sustainable improvement must be obtain by an alternative control design in order to mitigate the shortcomings of current LHP controllers regarding their control performance and their application to advanced LHP-based heat transport systems. To meet the demands for accurate and reliable LHP-based systems with a cost-effective adaption to future applications and missions, this thesis focuses on the following two goals:

- Modeling and simulation of the fundamental dynamics of LHP-based heat transport systems for model-based control design
- Corresponding development of control strategies and model-based design of adequate control algorithms based on the introduced models for the OT control of LHP-based heat transport systems

The necessity to reach these goals is further underlined by the current state of science in Chapter 2. It elucidates why the previous control approaches are not sufficient for the LHP-based heat transport systems under investigation in terms of their disturbance behavior and which undesired phenomena, such as temperature oscillations, are to be eliminated by a model-based control design. For this reason, different modeling approaches of LHP systems are discussed considering their applicability in model-based control design under consideration of the available parameters and variables. The modeling in this thesis is introduced by thermodynamic preliminaries regarding the heat and mass transfer in multiphase systems and the fundamental LHP characteristics under operating temperature control in Chapter 3. A complex dynamical model of a basic LHP is derived in Chapter 4 which adapts, combines, and extends the existing approaches in the literature to the needs of a model-based control design. Subsequently, the chosen control design approach, which is consistent with the structure of the derived dynamical model, is presented. In order to take advantage of a model-based control design in LHP applications with limited energy and mass, which is especially relevant in the aerospace sector, the complex dynamical model is further simplified in Chapter 5. It becomes clear which influences and dynamics are explicitly considered by the proposed simple controllers like the state-of-the-art controller with lower hardware requirements in comparison to the computationally complex controllers introduced before. Furthermore, the control parameters and architectures of already delivered LHP-based heat transport systems can be improved and updated on the short run according to the model-based control design and in consideration of the existing hardware. The extension of the complex modeling and control approach in Chapter 4 to advanced LHP systems with further attachments or multiple LHPs is shown in Chapter 6. In this chapter, the advantages of the modular modeling approach and the extensibility of the previously introduced control algorithm become apparent. A comprehensive comparison and validation of the proposed models and controllers is performed in Chapter 7. This chapter shows that the proposed controllers are able to achieve the aforementioned requirements including an improved control performance and the elimination of undesired behaviors. At the end, a short summary and conclusion completes this thesis in Chapter 8.

2 State of Science

In this chapter, the state of science concerning the modeling and control of LHP-based heat transport systems is outlined in order to identify the research gap to be closed in this thesis. At first, different control devices are discussed to introduce the corresponding state-of-the-art control algorithms for the operating temperature control of LHPs. Subsequently, the modeling approaches of LHPs in the literature are detailed and classified to clarify their usability for a model-based control design. In the third section, the focus is set on the extensions in advanced LHP systems and their impact on the LHP behavior, which presents another challenge to the modeling and the control design. An undesired behavior to be eliminated by an adequate controller is temperature oscillation, which is differentiated in terms of its occurrence and cause in the different advanced LHP-based systems. A discussion on the addressed aspects concerning the modeling as well as the control of LHP systems is given, before the research gap and related research questions of this thesis are finally stated.

2.1 Operating Temperature Control of Loop Heat Pipes

The fundamental task of an LHP is the transfer of heat between a heat source and a heat sink. Due to its passive, self-sufficient working principle induced by the heat transfer itself, the LHP adapts its OT to changes in the temperature of the heat sink and the amount of heat dissipated by the cooled object. This OT variation in order to maintain the thermal equilibrium affects the temperature of the cooled object in return. Temperature-sensitive electronic devices, however, require a narrow temperature corridor to reach their maximum performance. As for the mentioned LCT, the pointing mechanism of the laser requires a stable, homogeneous OT to achieve the desired precision [RMT16]. Therefore, the OT of the heat transport system must be controlled to adjust a stable temperature level at the cooled object under varying operating conditions. Furthermore, the startup of an LHP can be supported by adequate control devices. The LHP startup is characterized by the initialization of the circulation of the mass flow through evaporation and condensation. An additional heat input to the evaporator promotes a fast liquid evaporation and thus a successful startup. Thus, this thesis concentrates on the OT control during the continuous operation of a running LHP.

Overviews of several OT control devices of LHPs are given in [NKS99] and [Ku08]. Basically, the devices are classified concerning both the power consumption and the heat resource. Passive control devices without the need of external energy redistribute heat autonomously between hot and cold areas of the LHP, whereby the thermal equilibrium is altered internally to a desired OT level. Examples are the organized heat exchange with coupling blocks [NKS99], [NW07], [Ku08] and the pressure regulators like valves in a bypass line [NKS99] or with a bypass line [BSR+05], [TMK14]. Since passive devices achieve a rough temperature control

for a fixed setpoint while adding more mass and complexity to the system, they are often combined with or transferred into active devices. Thus, the precision of the control result is increased, and the required amount of external energy is reduced. In addition, the setpoints of active devices can be changed during operation according to the task or due to aging [Ku08]. By attaching an electrical heater on the bypass valve, an active saturation pressure regulation is established. This enables a heat transfer stop in the LHP to avoid situations where the cooled electronic components are too cold to start or operate. Due to the internal redistribution of the hot vapor mass flow, active valves consume less power than other active control devices. However, electrical heaters are often attached directly on LHP components, such as the compensation chamber or the liquid line, which carry the cold liquid from the condenser [NKS99]. By heating one of these LHP components externally, a control heater is able to alter the saturation temperature and therefore the OT of the LHP reliably. In contrast, valves are not as reliable, as they entail an increased risk of failure due to moving parts. Typically, the CC is cold-biased so that heating is sufficient to keep the desired setpoint temperature over the considered operating range [Ku08]. Nevertheless, active cooling and heating is possible with thermoelectric coolers (TECs). TECs are able to supply and withdraw heat based on the Peltier effect [HMS16, p. 758]. This thermoelectric effect describes the occurrence of a temperature difference by applying an electric potential difference to a solid. Depending on the flow direction of the electric current, the temperature gradient between both sides of the TEC can be inverted. The effectiveness of the TEC is mainly defined by the thermal conductivity of the interfaces to the evaporator and the CC [Ku08]. Furthermore, the heat exchange between the two LHP components is intensified by the TEC since both heat resources are combined: internal heat is redirected through the interface as external heat is provided [NKS99]. A TEC contributes to the reduction of the required external energy and a successful LHP startup [NKS99], i.e. the evolution of a mass flow in the LHP cycle for a continuous heat transport. However, the thermal interfaces are prone to shear stress [Ku08]. In addition, the lifetime of the TEC is rather short for a successful application in aerospace systems without any maintenance option [NW07]. Further approaches combining the internal and external heat exchange for the reduction of the power consumption are based on the organized heat exchange with a secondary evaporator, a variable conductance heat pipe (VCHP), or a separate subcooler, which add additional mass to the system and complicate the routing of the transport lines [Ku08].

In recent years, two innovative LHP control device concepts have been published. In [JGKY15], the saturation pressure of the LHP is controlled by injecting and withdrawing immiscible gas into and out of the CC, respectively. Due to the hydraulic action, the pressure-controlled LHP achieves a stable and precise OT control. The second concept, introduced in [KAS18], integrates a steel ball into the evaporator in order to manipulate the heat and mass flow mechanically. By moving the steel ball inside the evaporator with two external magnets, the flow resistance is altered. Consequently, the OT of the LHP adapts itself to the new conditions demonstrating a new active control possibility. Both concepts are still under development, but may extend the variety of active control devices for different LHP applications in the future.

A different active control concept for special LHP-based cooling systems is presented in [LWL10] and [DLWW12]. Due to the combination of an LHP with a variable emittance radiator as heat sink, one of the influences on the operating conditions of the LHP is controlled. By manipulating the heat dissipation of the radiator through a microelectromechanical louver,

the cooling ability of the heat sink at the condenser is adjusted. This LHP-related control concept does not correspond to the investigated LHP systems and the focus on a direct OT control in this thesis. Furthermore, the mechanical structure is susceptible to shear stresses and thus more prone to failure.

Most of the literature about actively controlled LHPs concentrates on the experimental and numerical investigation of the feasibility and control performance of the proposed control devices. Only a few mention the designs of the underlying control algorithms for their active devices, e.g. [BSR+05], [SN17], [UK17]. Among these control algorithms, a feedback control structure with a temperature measurement is commonly used to determine the electrical power of the active control device. Depending on the characteristics of the power supply, the active control device is either turned on and off or is able to provide a variable heat output. A two-point controller is used in [GKB06] to turn the heater of a bypass valve on and off according to the measured temperature moving above or below the setpoint temperature. The same simple controller type is applied in [BBD98], [KB01], and [KSK+14] to regulate control heaters on the CC. A hysteresis is added in [UK17] to reduce the switching of the control heater and therefore stabilize the temperature near the setpoint temperature. In [BSR+05], the control law for the heater of a bypass valve is adapted linearly to the temperature of the cooled object to reduce its stationary deviation from the setpoint temperature. Classical feedback controllers with proportional-integral-derivative (PID) action are utilized for control heaters and TECs in several works, e.g. [KN07], [KPM11a], [KPM11b], [SN17]. Compared to the results with a two-point controller, a smoother temperature curve near the setpoint temperature is observed with PID controllers. Furthermore, the feedback controllers with an integral term show a converging behavior of the temperature toward its setpoint temperature minimizing the residual control error. The authors of [KPM11a] and [KPM11b] describe the impact of different temperature sensor locations on the controller performance. Depending on the LHP component, temperature oscillations occur, which suggests the adaption of the control parameter to different LHP settings. However, the design process of the control parameters is not reported in any literature, indicating a heuristic control parameter tuning on the test bench.

To the best of the author's knowledge, there is no physically motivated, model-based design process of the proposed controllers. In general, the control technology of LHPs is little researched which may be related to the fact that LHPs are often regarded as passive thermal control devices [DLWW12]. The increased development time of a model-based design approach may be another reason why this approach has not been applied in the control technology of LHPs so far. However, a model-based design approach for the active OT control of LHPs contributes to the minimization of expensive test-bench time, facilitates the adaption to new systems, and lays the foundation for more elaborate control algorithms with a higher accuracy and robustness. The development of model-based LHP controllers requires the existence of an adequate dynamical model of the LHP. Therefore, the current thermal modeling approaches of LHP systems in the literature are presented in the next section.

2.2 Modeling Approaches for Loop Heat Pipes

The variety of LHP models in the literature can be divided into two main groups: stationary models and transient models. Stationary models are commonly developed for thermodynamic systems since the variation of the temperature in time is not necessary for the characterization and design of these systems. While numerical stationary models are rather used to simulate the steady-state characteristics of the LHP, analytical stationary models are preferred for the specification of the design and sizing of LHP components [Fur06]. Transient models, however, are essential to evaluate the coupled time-variant heat and mass transfer processes, characterize the impact of external influences, and understand the overall dynamics and transient phenomena of an LHP. Hence, transient models are required for a model-based control design. Many publications establish their model equations mainly on a physical basis by considering the mass, energy, and momentum conservation laws. These numerical transient models focus on the local one-dimensional discretization of the LHP into many segments or nodes to handle the coupled thermodynamic and hydraulic behavior of the different LHP components. For the mathematical description of the resulting nodal networks, the conservation equations are derived for each node. For the simulation of the overall transient LHP behavior, the balancing solutions of the large-scale equation systems are obtained numerically achieving satisfactory agreements between the models and the experiments. Some publications rely on commercial software products like EcosimPro [GTPK05], [KPGT08] or Sinda/Fluint [KR10] to solve the large-scale equation systems, where not all specific model equations are accessible or given. In most of the available publications, the numerical models are stated completely.374.8651pt

In order to classify the variety of numerical transient LHP models of the past decades according to the modeling aspects in this thesis, an extensive literature review is carried out. The results of the review are presented in Table 2.1. The available LHP models differ in their modeling purpose. Due to their specific purpose, differently detailed discretizations in axial and radial direction are chosen to consider the geometric structures of the LHP components and spatial distribution of the two-phase fluid. The possibility to track the liquid-vapor interfaces in the CC and the condenser is mainly based on the determination of the two-phase volume and the vapor quality in each node for a precise identification of the local temperatures in the complex, two-phase regions of the LHP. The evaluation of the model reactions to external heat changes, either by uncontrolled components like the heat source and the heat sink or by the control heater, is especially relevant to characterize the model performance in terms of designing and testing adequate controllers.

In [SN17], the active temperature control with a TEC is compared between experiments and the established numerical model. As in [BCG$^+$18], [NNK13], [AFN19], [BLW10], and [VR08], the discretization of the LHP components focuses on an axial one-dimensional discretization of the pipe system including the condenser and the transport lines. Radially, only the wall mass of the evaporator is considered with one layer of nodes in [SN17] and [BCG$^+$18]. The liquid-vapor interface of the condenser in [SN17] is not tracked in contrast to the rest of the numerical models, since the condenser temperatures are not evaluated. Instead, the uncontrolled and controlled temperatures at the CC-evaporator assembly are presented showing stationary and dynamic deviations in both the uncontrolled and the controlled case for variable heat loads.

Publication	LHP components		Modeling purpose	Liquid-vapor interface tracking	Operating conditions
	Axial 1D discretization	Radial discretization			
[SN17]	condenser, transport lines	evaporator (single layer)	active TEC control	no tracking	variable source and CC control, constant sink
[BCG+18]	condenser, transport lines	evaporator (single layer)	waste heat usage in electric vehicles	condenser	variable source, constant sink
[NNK13]	condenser, transport lines	evaporator (multilayer)	heat load distribution	condenser	variable source, constant sink
[AFN19]	condenser, transport lines	evaporator (multilayer)	internal flow and temperature oscillations	condenser	constant source and sink
[BLW10]	condenser, transport lines	all LHP components (single layer)	startup scenarios	condenser	constant source, sink, and CC control
[VR08]	condenser, transport lines	all LHP components (single layer), evaporator (multilayer)	space conditions at radiator and condenser	condenser, CC	variable source and sink, constant CC control
[MKHW19]	condenser	no walls considered	overall LHP dynamics for LHP end users	condenser	variable source, constant sink
[HK03]	Lagrangian fluid flow method	all LHP components (single layer)	LHP fluid dynamics for design refinements	condenser, CC	variable source, constant sink
[LPDJ07]	global hydraulic balance	CC, evaporator (single layer)	temperature oscillations	condenser, CC	variable source and sink

Table 2.1: Classification of numerical transient LHP models

Even an opposite behavior of the CC temperature due to the roughly determined heat leak and the stationary flow model is observed without control. The model is more sensible to the controller action than the measured system due to inaccurate thermal capacities and heat transfer coefficients.

By tracking the liquid-vapor interface in [BCG+18], the effects of different working fluids on the LHP performance are detailed. A focus is set on a numerical model with low computational effort to perform a feasibility study and parametric analysis of LHP designs for the waste heat usage in electric vehicles. The model reproduces the overshoots of the evaporator wall temperature to heat load changes correctly, but stationary and dynamic differences persist. In [NNK13], the steady-state error between the calculated and measured variables under heat load variations is smaller, but the deviation in the dynamic behavior remains as well due to inaccuracies in the thermal capacities and heat transfer coefficients. As a result of the analysis of the heat flow distribution, the heat flows between the CC and the surroundings and between the CC and the bayonet may be neglected compared to the heat leak from the evaporator to the CC as part of the heat load as well as the subcooling of the liquid flow from the condenser. Both the models in [NNK13] and [AFN19] use a detailed radial model of the evaporator and its wick with multiple layers of nodes to specify the heat flows and the internal mass flows, respectively. According to [AFN19], the impact of the internal flow on the simulated temperature oscillations of LHPs without active control is traced back to the two-phase fluid penetration into the LL. In addition, a temperature oscillation is connected with an oscillation of the condensation length in the condenser.

The simulation of the LHP startup regarding the change in the temperatures at different constant operating conditions is modeled in [BLW10] considering the walls of all components to include the effects of the thermal capacities. It is concluded that a successful startup is promoted by a high initial heat load at the evaporator, a low heat leak to the CC, and active CC cooling. The walls of all components are also modeled in [VR08] but with a different modeling purpose. The validated model is used to simulate changing space conditions at the heat sink, namely the condenser and the radiator, to predict the expected LHP performance in space. By considering the variations of the liquid-vapor interfaces in both the condenser and the CC, the responses of the wall temperatures in the CC-evaporator assembly to heat load changes show a good agreement between the simulated and measured results. The aforementioned two-phase fluid penetration is observed in the simulation results as well due to changing conditions at the radiator and condenser or active CC control. Moreover, a high sensitivity of the CC to control heater actions is also reported as before. A mutual advantage of the models in both publications, [BLW10] and [VR08], over the previous models is the consideration of the momentum of the fluid flow to model the dynamics of the distributed mass flow rates in the condenser adequately. In contrast, only a stationary functional determination of a single mass flow rate in the entire loop is established in [SN17], [BCG+18], [NNK13], and [AFN19].

An overall simulation of the LHP dynamics for LHP end user is the objective of the "pragmatic modeling approach" [MKHW19, p. 898] of Meinicke et al. In combination with an inexpensive experimental characterization with only noninvasive surface measurements, the model is able to capture the most significant dynamic behaviors of different measured and unmeasured variables. By dividing the condenser into fine segments, the internal mass flow rates and

phase distributions are calculated separately in each time step. The accumulation of the locally distributed two-phase mass changes in the condenser nodes defines the difference of the mass flow rates in the LL and the VL making a balancing solution method necessary. Furthermore, the mass and energy conservation equations to derive the thermal submodel are established for the remaining LHP components without local division. To model the impact of the operating conditions on the temperatures in close agreement with the measurements, the heat leak is finally fitted from the derived experimental data as a function of the operating conditions.

A different modeling approach is chosen in [HK03] to model the LHP fluid dynamics for LHP design refinements. The transient liquid flow is established with the Lagrangian fluid flow method, where the position and velocity of the liquid flow particles are regarded instead of locally discretizing the pipes containing the liquid. The heat flows of the thermal submodel are derived from the thermal energy balance of the LHP. Combined with the momentum equation of the liquid flow and the change of the vapor volume in the condenser, the overall model forms a mass-spring-damper system introducing one possible explanation for temperature oscillations in LHPs. The presented numerical model is used for the transient simulation of the LHP and shows the qualitative LHP behavior to heat load changes without experimental validation. At low heat loads, however, the predicted heat leak is much lower than the presented test data reveal.

In contrast to the previous models, a more global numerical approach is chosen in [LPDJ07] to model the temperature oscillations of LHPs without active control at the limits of the operating range. By establishing the global thermal and hydraulic balance of each LHP component, the dynamics of the temperatures and the mass flow rates are described in a more explicit way. To consider the transient mass flow rate in the LL, the mass and momentum balance equations of the liquid are established. The hydraulic balance in the condenser is based on the condenser modeling in [WBB78], which neglects a superheated region at the beginning of the condenser. This superheat, however, is modeled in [AFN19], [BLW10], and [MKHW19] to consider the temperature gradient in the VL for a more accurate determination of the vapor temperatures. In order to track the liquid-vapor interfaces in the condenser and in the CC under variations of the heat source and the heat sink, the dynamics of the liquid CC volume are derived from the two-phase mass balance in the CC. In addition to the interface tracking, the frequency and amplitude of the reported temperature oscillations can be determined from the simulations. Nevertheless, a numerical solution is necessary due to implicit equations and a case-by-case analysis.

None of these numerical models are intended or designed for a model-based control design. Classically, dynamical models for the model-based design of controllers are given by a set of ordinary differential equations in the explicit state-space form according to Def. 2.1.

Definition 2.1 (State-space model of a dynamic system (cf. [Kha15, p. 14]))
The state-space model of a dynamic system is given by the following nonlinear vector equations:

$$\dot{\boldsymbol{x}}(t) = \boldsymbol{f}(\boldsymbol{x}(t), \boldsymbol{u}(t), t), \tag{2.1a}$$
$$\boldsymbol{y}(t) = \boldsymbol{g}(\boldsymbol{x}(t), \boldsymbol{u}(t), t) \tag{2.1b}$$

with the state vector $\boldsymbol{x}(t)$ containing the n state variables $x_i(t)$ $(i = 1, ..., n)$, its derivative $\dot{\boldsymbol{x}}(t)$ w.r.t. the time variable t, the input vector $\boldsymbol{u}(t)$ containing the p input variables $u_j(t)$ $(j = 1, ..., p)$, and the output vector $\boldsymbol{y}(t)$ containing the q output variables $y_l(t)$ $(l = 1, ..., q)$. The initial condition of (2.1) *is given by the initial state $\boldsymbol{x}_0$:*

$$\boldsymbol{x}(0) = \boldsymbol{x}_0. \tag{2.2}$$

In terms of control technology, the state variables $x_i(t)$ in the state vector $\boldsymbol{x}(t)$ stand for the independent storage of a dynamic system. The influence of external variables on the system is represented by the input variables $u_j(t)$ in the input vector $\boldsymbol{u}(t)$. The output variables $y_l(t)$ in the output vector $\boldsymbol{y}(t)$ resemble physically measurable variables or variables with a desired behavior. [Kha15, p. 13]

The nonlinear vector function $\boldsymbol{f}$ in the state equation (2.1a) is formed from the n coupled first-order ordinary differential equations:

$$\dot{x}_1(t) = f_1(x_1(t), ..., x_n(t), u_1(t), ..., u_p(t), t), \tag{2.3}$$
$$\dot{x}_2(t) = f_2(x_1(t), ..., x_n(t), u_1(t), ..., u_p(t), t), \tag{2.4}$$
$$\vdots \quad \vdots$$
$$\dot{x}_n(t) = f_n(x_1(t), ..., x_n(t), u_1(t), ..., u_p(t), t). \tag{2.5}$$

Correspondingly, the nonlinear vector function $\boldsymbol{g}$ in the output equation (2.1b) is derived from the q equations that define the output variables $y_l(t)$:

$$y_1(t) = g_1(x_1(t), ..., x_n(t), u_1(t), ..., u_p(t), t), \tag{2.6}$$
$$y_2(t) = g_2(x_1(t), ..., x_n(t), u_1(t), ..., u_p(t), t), \tag{2.7}$$
$$\vdots \quad \vdots$$
$$y_q(t) = g_q(x_1(t), ..., x_n(t), u_1(t), ..., u_p(t), t). \tag{2.8}$$

For linear time-invariant (LTI) systems, where the vector functions $\boldsymbol{f}$ and $\boldsymbol{g}$ do not depend explicitly on the time t, the general state-space form in Def. 2.1 can be rewritten into the following matrix representation:

Definition 2.2 (Linear state-space model)
The state-space model of an LTI system is given by the following equations:

$$\dot{\boldsymbol{x}}(t) = \boldsymbol{A}_{lin} \cdot \boldsymbol{x}(t) + \boldsymbol{B}_{lin} \cdot \boldsymbol{u}(t), \tag{2.9a}$$
$$\boldsymbol{y}(t) = \boldsymbol{C}_{lin} \cdot \boldsymbol{x}(t) + \boldsymbol{D}_{lin} \cdot \boldsymbol{u}(t) \tag{2.9b}$$

with the state matrix $\boldsymbol{A}_{lin} \in \mathbb{R}^{n \times n}$, the input matrix $\boldsymbol{B}_{lin} \in \mathbb{R}^{n \times p}$, the output matrix $\boldsymbol{C}_{lin} \in \mathbb{R}^{q \times n}$, and the direct transition matrix $\boldsymbol{D}_{lin} \in \mathbb{R}^{q \times p}$. The initial condition of (2.9) *is given by the initial state $\boldsymbol{x}_0$:*

$$\boldsymbol{x}(0) = \boldsymbol{x}_0. \tag{2.10}$$

Besides the state-space representation of LTI systems in the time domain, the frequency domain is often used in the context of control technology to describe the input-output behavior of linear dynamic systems. The representation in the frequency domain is also utilized in this thesis and in the following literature and shall therefore be briefly explained here. Due to the decomposition of the signals at the system's input and output into periodic signals, the transformation of the system from the time domain into the frequency domain is achieved by the *Laplace transform* [Lun20a, p. 257]:

$$F(s) = \int_{-0}^{\infty} f(t) \cdot \exp(-s \cdot t)\, \mathrm{d}t \tag{2.11}$$

with the Laplace transform $F(s)$ of the signal $f(t)$. By introducing the complex Laplace variable or complex frequency s, the transfer characteristics of a linear dynamic system is described by the so-called transfer function $G(s)$:

$$g(t) \circ\!\!-\!\!\bullet\, G(s) = \frac{Y(s)}{U(s)} \tag{2.12}$$

with the Laplace transforms $U(s)$ and $Y(s)$ of the input signal $u(t)$ and the output signal $y(t)$, respectively. The order of a transfer function corresponds to the highest order of the linear differential equation that describes the LTI system.

Considering the dynamical modeling of an LHP, few efforts are made in the literature to accomplish this goal since the thermohydraulic coupling complicates the design of dynamical models.

In [HHL09], the proportional time-delaying behavior of the CC temperature has motivated the identification of multiple second-order transfer functions in different operating points to study the dynamic behavior of the LHP temperatures. The different identified transfer functions are combined in a variable structure system that depends on the operating conditions. Accordingly, four startup modes in dependence on the heat load are defined: failure, oscillation, overshoot, and normal. However, the averaged dynamical black-box model without physical background is only accurate when the condenser is fully utilized and higher heat loads result in higher temperatures.

The thermo-fluid dynamics of an LHP are investigated in [Shu08]. The ordinary differential equation of the vapor temperature is established based on the mass and the energy conservation equations in the condenser assuming the vapor to be a compressible ideal gas. The vapor temperature at the LHP startup is simulated for two different heat loads showing only a small deviation between both cases. Furthermore, the radial heat leak in the wick from the evaporator to the CC is determined according to Fourier's law (see Sec. 3.1.2). The average wick temperature is presented as a function of the dimensionless Fourier number under a varying heat load. Unfortunately, all simulation results in [Shu08] are given without any numerical or experimental validation so that a final evaluation of the proposed modeling approaches for the two LHP components, i.e. the condenser and the CC-evaporator assembly, is not possible.

For the analysis of the transient performance of the aforementioned microelectromechanical thermal management system based on a variable emittance radiator and an LHP in Sec. 2.1, three dynamical models of the overall system are presented in [LWL10]. The models are compared in simulations to obtain the necessary level of detail for the desired performance analysis. Based on the detailed numerical model of an LHP with a radiator in [VR08], both a three-nodal and a four-nodal thermal network of the overall system are derived. In these networks, the LHP subsystem is represented by only one and two temperature nodes, respectively. The four-nodal network extends the purely thermal modeling of the three-nodal network to include the transient behavior of the liquid and the vapor phases in the LHP. However, the corresponding enthalpies of both phases and the saturation pressure of the working fluid inside the LHP are calculated by fitted polynomials as functions of the nodal temperatures without a physical background for a deeper understanding. For the extension of the system modeling, the models of both networks are combined to form a hybrid model with one intermediate mass flow in the entire LHP cycle. Such a kind of modeling is also chosen for the numerical models in [SN17], [BCG+18], [NNK13], and [AFN19] since the assumption of a single mass flow rate simplifies the complex, two-phase flow dynamics of an LHP vastly. The single mass flow rate in the hybrid model is expressed as a function of only the thermal parameters. Thus, the dependency of the resulting hybrid model on hydraulic parameters is eliminated to be more independent of design and material specifications. For the validation of the transient performances of the presented dynamical models with different levels of detail, a variable heat load profile is applied to the four-nodal model, the hybrid model, and the detailed numerical model. As a result, the temperatures of the cooled object in all three models agree for sufficiently small heat load changes. The simplifications of the LHP subsystem with two temperature nodes and a single mass flow are sufficient for the analysis of the coarse transient performance of the overall thermal management system with the presented hybrid model, but the model is only accurate for the local behavior around an equilibrium point. However, for an adequate dynamical modeling of the temperatures of all LHP components, especially the governing CC, over the entire operating range of the LHP, the hybrid model lacks further temperature nodes and a convenient tracking of the liquid-vapor interface movement in the condenser.

So far, the focus has been set on modeling approaches for heat transport systems comprising a single conventional LHP. In the next section, different extensions and combinations of LHPs in advanced heat transport systems are shortly highlighted.

2.3 Advanced Loop Heat Pipe Systems

A conventional LHP includes a single evaporator and a single condenser and is utilized as a two-phase heat transport system in many applications. To reach the most effective and reliable heat exchange between a heat source and a heat sink, a conventional LHP is often extended to enlarge its range of application. Reasons for these extensions are the cooling of electronic components with distributed heat sources or the requirement of a higher overall thermal conductance. Thus, the gained flexibility in the design and operation of such heat transport systems comes along with an increase in complexity [Ku99]. Furthermore, any extension has a significant impact on the dynamic behavior of the LHP due to the thermodynamic interdependence.

Two kinds of extensions are presented in the literature: changes with effects on the flow cycle of the working fluid and changes to the proximity of the LHP body. The former include the integration of multiple components in one LHP flow cycle: dual evaporator LHP [BWN+97], LHP with two evaporators and two condensers [Ku99], [KB01], [KOB04], LHP with multiple evaporators and multiple condensers [GGK00]. Thus, the dissipated heat of several distributed heat sources can be transported in one system. The main focus in the literature is set on the fabrication and test of such advanced LHP systems since new guidelines for the sizing of the LHP components and the charging with a working fluid are required [BWN+97]. A successful OT control is reported in [KB01] when either one or both CC temperatures are controlled in an LHP with two evaporators and two condensers. For this type of advanced LHP system, a steady-state model is presented in [HK04], while the transient performance of an LHP with multiple evaporators is simulated in Sinda/Fluint [KR10].

Several other publications focus on the second kind of extension around the body of an LHP. The obvious modification to the LHP body is the attached electronic component or heat source itself since it adds mass to the evaporator's own mass. In many LHP tests on ground, the heat load at the evaporator is simulated by directly attached heaters without considering any additional mass [Ku99]. However, the overall mass of the evaporator that stores thermal energy has a significant impact on the dynamic behavior of the LHP. Although an increased thermal mass helps to damp out fast transients due to heat load changes [Ku99], several disadvantages are reported in the literature. In general, a high heat load at the evaporator contributes to a successful LHP startup due to a fast initialization of the liquid evaporation. A large mass at the evaporator, however, may complicate the LHP startup since most of the heat is used to raise the temperature of the thermal mass, and the initial heat load at the evaporator is low. Therefore, the startup can take some time since less heat is presented for the boiling process [Ku16]. Furthermore, the transient behavior of the heat load at the evaporator as the driving force of the mass flow is not only influenced by the heat source but also by the OT and therefore by the CC temperature. Due to the bilateral influence, the net heat load at the evaporator can be higher or lower than the dissipated heat of the heat source for a short time according to the rise and fall of the CC temperature [KOB04]. The intensity of the modulation of the net heat load depends on the size of the total thermal mass of the evaporator including its own mass and the attached mass. In combination with the interaction between the thermal interface and the fluid, the LHP temperatures tend to oscillate at low heat loads depending on the ratio between the total evaporator mass and the total CC mass [Hoa19].

Furthermore, the interaction has an impact on the OT control with control heaters on the CC. The OT control is impaired by the thermal mass that increases the time delay between the control action and the system's response [GGK+13]. As mentioned before in Sec. 2.1, different locations of the temperature sensor for the OT control of the LHP with two-point and PID controllers are tested experimentally in [KPM11a] and [KPM11b]. Especially with a sensor on the thermal mass, the controlled temperature tends to oscillate, while the direct control of the CC temperature shows a smoother progression over time. Previous transient models that consider such an additional thermal mass at the evaporator in form of a cooled object [LWL10], an evaporator saddle as an interface to a cooled object [VR08], or a heating block [NNK13], include the extra component as thermal capacity in their thermal networks. However, the models showed no oscillatory behavior under the investigated operating conditions.

In connection with the consideration of additional thermal masses, redundant [Ku99] or parallel [KSK+14] LHPs are developed for the thermal control of complex electronic components. They are suitable for the heat transfer of distributed heat sources as an alternative to LHPs with multiple components, and contribute to an isothermal electronic component [Ku99]. If one LHP cannot transfer the desired amount of heat alone, parallel LHPs are an effective solution to raise the overall heat transport capability. By sharing both the heat source and the heat sink, there is an interaction between the self-regulating LHPs. Hence, their operation may become problematic when the heat distribution between both evaporators is uneven and a redistribution of the heat flows takes place. The mutual interaction between both evaporators across the thermal mass of the heat source has thus an impact on their individual startup moment and complicates the thermal control of the heat source due to the heat distribution rather than the amount of the total heat load itself [Ku99].

In the example of the thermal control of an LCT, two parallel LHPs are thermally coupled at their condensers and at their evaporators, as the silver structure on the LCT platform in Fig. 1.2 reveals. An illustration of such an advanced heat transport system with parallel LHPs is also given in Fig. 2.1.

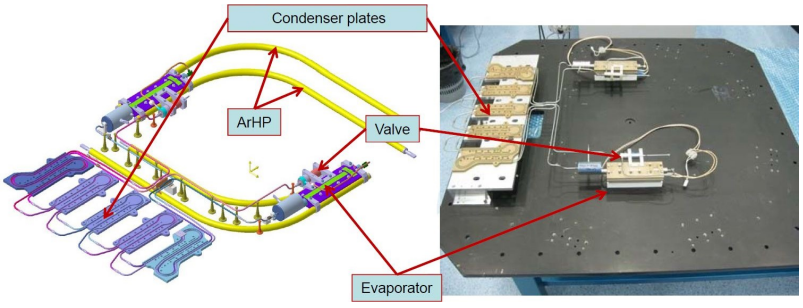

Figure 2.1: Parallel LHPs with arterial heat pipes (ArHPs) for the thermal control of an LCT (adapted from [RMT16])

Both condensers share a radiator as the heat sink and run in parallel through the condenser plates, which are mounted on the heat sink body. The body of the LCT serves as the coupling thermal mass between the evaporators of both LHPs. In addition to the connecting thermal mass, four arterial heat pipes (ArHPs) are attached to the evaporators to collect the dissipated

heat of the distributed heat sources (cf. [RMT16], [MKHW19]). These ArHPs are sealed hermetically like the LHP itself, and the heat exchange takes place via the thermal coupling instead of a mass exchange. In [RMT16], a valve in each VL controls the vapor flow to the condenser. Control heaters with PID controllers on the CCs can be used as backup controllers in the case of a valve failure. Nevertheless, the impact of the thermal mass and the individual OT control of both coupled LHPs must be also considered in the design of adequate control algorithms to improve the startup of both LHPs and to reduce phenomena like temperature oscillations.

A closer look on the occurrence and causes of temperature oscillations in the considered LHP systems and in connection with an additional thermal mass at the evaporator is given in the next section.

2.4 Temperature Oscillations in Loop Heat Pipe Systems

A known but undesirable phenomenon during the operation of LHP systems is the appearance of temperature oscillations. Typically, the OT of an LHP reaches a steady state under constant operating conditions. Even if the heat load or the sink temperature changes, the OT usually finds a new steady state eventually [KOK+01]. However, the OT can oscillate under certain operating conditions. Two relevant types of temperature oscillations of a conventional LHP without OT control are specified in [Ku03]: oscillations with a high frequency and a low amplitude (HFLA) with a period of seconds to minutes and an amplitude on the order of one Kelvin as well as oscillations with a low frequency and a high amplitude (LFHA) with a period and an amplitude on the order of hours and tens of Kelvin, respectively. HFLA oscillations are connected to the liquid-vapor front in the condenser and its inability to find a stable position inside the condenser under certain operating conditions. Thus, the liquid-vapor interface oscillates at either the condenser inlet, when a high heat load is applied at the evaporator, or the condenser outlet, when a low heat load and a low sink temperature exist [Ku03]. In contrast, LFHA oscillations occur because of either an oscillating sink temperature at a constant heat load, which the CC temperature follows with a delay, or a large thermal mass at the evaporator combined with a low heat load and a sink temperature lower than the ambient temperature of the LHP [KR03]. The experimental descriptions of both oscillation phenomena are supported by two of the aforementioned numerical models. In [LPDJ07], the HFLA oscillations at the condenser outlet and the LFHA oscillations in connection with a thermal mass are reproduced in order to predict their frequencies and amplitudes in dependence on design and operational parameters. In order to investigate the connection between the internal flow and the HFLA oscillations at the condenser outlet more closely, another model with a focus on the vapor quality in the transport lines is developed in [AFN19]. It is noted that HFLA oscillations are already triggered when the two-phase flow in the condenser enters the LL once. Nevertheless, the investigated HFLA oscillations occur at very low or high heat loads, which are usually outside the intended operating range of the LHP. Furthermore, HFLA oscillations disappear when the liquid-vapor interface is kept inside the condenser over the entire operating range with an active OT control [Ku03].

Temperature oscillations in connection with an actively controlled conventional LHP are traced back again to the thermal mass at the evaporator. Especially an external heat input, e.g. with a control heater, promotes temperature oscillations due to the interacting heat and mass exchange processes inside the LHP [GGK+13]. In addition, the position of the controlled temperature sensor is also relevant for the control accuracy (cf. Sec. 2.1). Due to the time delay between the control action and the response of the cooled object, which is enlarged by the thermal mass at the evaporator, the design of an active OT control is hindered [GGK+13]. In [HB12], the authors come to the same conclusion by establishing a stability criterion for the LHP operation based on the theory of a mass-spring-damper system in the form of a Van der Pol oscillator [vdPvdM27]. In this approach, the combination of the phase transition processes, the heat and mass exchange processes, and the fluid dynamics in an LHP resemble the fluctuating energy exchange processes in a mass-spring-damper system. By strongly simplifying their former numerical model in [HK03], the nonlinear LHP dynamics are described by a Van der Pol oscillator to underline their stability theory. The condition for reaching a periodic state is transformed into a criterion that relates the stability of the LHP operation to the ratio of the thermal masses between the CC and the evaporator, a low OT, and a high vapor generation in the CC due to corresponding heat inputs, e.g. by a control heater. The theory is repeated, simplified, and generalized in further publications [HBM15], [HB16], [Hoa19] of the main author to support the experimental investigations of LFHA and HFLA oscillations in conventional LHPs without active control as well. By introducing the linear stability theory of nonlinear dynamical systems based on the linearization and perturbation in an equilibrium point, two more stability criteria for both oscillation types are derived. It is shown that both oscillation types are mutually exclusive and therefore do not appear simultaneously [Hoa19]. However, the established models catch the fundamental dynamic characteristics of an LHP, but are not suitable to simulate the LHP operation [HB12].

Another undesirable behavior is observed when the CC is heated actively by a control heater at a higher rate than the evaporator by the heat load accordingly. The rise of the evaporator temperature is delayed additionally by a large thermal mass at the evaporator due to the modulation of the net heat load. As explained in [Ku16], such situations result in a continuous LHP startup and shutdown cycle since both the temperature and the saturation pressure of the CC rise over those of the evaporator. The phenomenon is connected to a cold shock of the CC after the LHP startup, when a large amount of the subcooled liquid from the condenser enters the CC leading to a CC temperature decrease of several degrees. Immediately, the LHP is flooded with liquid and shuts down. The repeated interruption of the normal LHP operation presents itself as temperature oscillation. In contrast to the previously described temperature oscillations, however, the heat transfer between the heat source and the heat sink is interrupted periodically. Thus, a continuous heat transfer cannot be ensured and must be prevented by either an increase of the heat load or an adequate limitation of the control heater.

2.5 Conclusion and Research Gap

The preceding literature review demonstrates the need to investigate LHP-based multiphase heat transport systems from a control engineering perspective. Based on the highlighted research gaps in the previous sections, the corresponding objectives of this thesis concerning the two goals in Chapter 1 are stated in the following. The corresponding research question is derived subsequent to each paragraph that specifies the respective research gap.

In the field of thermal control with LHP systems, state-of-the-art controllers with a heuristic design are applied for the OT control so far. These show a certain lack of accuracy, stability, and structured design process. A model-based control design is a promising solution to mitigate the listed problems while reducing the high design efforts and costs of the existing controllers at the same time. Based on a control model, more sophisticated controllers can handle the complex performance characteristics of an LHP effectively. Especially with a control heater as the considered active control device, there is no model-based designed control algorithm for any LHP-based system to the best of the author's knowledge. Such a control heater on the CC with a variable power output impresses with his low failure risk and fast response to changes in the operating conditions, while only heating is indeed sufficient for the operating range of the considered LHP systems. Model-based control design for control heaters has the potential to improve the control accuracy, compensate temperature oscillations and control advanced LHP -based systems. This leads to the first research question:

1. Which model-based designed control structure is suitable to meet the performance requirements of an LHP the best?

As a basis for the desired control design approach, an adequate dynamical model of the LHP system must be established as it has not yet appeared in the literature. Thus, the modeling purpose in this thesis, i.e. for the control design, differs from the ones in the literature, but has a clear focus on the temperature dynamics. A deeper view of the dynamics of the system through the states is pursued with a physically motivated control model as defined in Def. 2.1. This control model is based on the adaption, extension, and combination of the reviewed LHP models which have been available in the literature at the start of this thesis. The desired control model should simulate the transient performance of the LHP temperatures during the ongoing operation with a continuous heat transfer. Furthermore, the existing stability theory of an LHP can be extended to the corresponding closed-loop LHP systems to support a stable controller performance in general. This leads to the second research question:

2. Which level of detail is necessary for control models of LHP-based heat transport systems to allow a successful control design?

A next step is the extension of the desired models and controllers of a conventional LHP to more advanced LHP systems, which provides another challenge to handle the dynamic behavior of LHP-based multiphase heat transport systems. The OT control of advanced LHP systems with control heaters on the CCs are investigated. In these systems, an increased thermal mass at the evaporator and parallel LHPs, as they can be found in the heat transport system of the introduced LCT, are considered. This leads to the third research question:

3. How can the extensions of advanced LHP systems be integrated into the corresponding models and controllers?

Besides the general improvement of the temperature control performance of the different LHP-based systems, temperature oscillations during the continuous LHP operation are highly unwelcome and must be prevented by the controller. Against this phenomenon, an appropriate modeling and control approach is necessary to reach a better performance than with the state-of-the-art controllers. This leads to the fourth research question:

4. Which control algorithms are able to eliminate temperature oscillations during the continuous LHP operation?

The remainder of this thesis is structured as follows: The thermodynamic preliminaries of the multiphase heat and mass transfer and the fundamentals of LHP OT control are illustrated in Chapter 3. On this basis, a complex and a simplified LHP model including different levels of detail, together with corresponding model-based control designs, are established in Chapter 4 and Chapter 5 for a conventional LHP. Subsequently, the complex model and its controllers are extended for the advanced LHP-based heat transport systems in Chapter 6. The validation and comparison of all models and controllers, also in the context of reducing temperature oscillations, is elaborated in Chapter 7, where the results are discussed and answers to the research questions are given. In Chapter 8, the conclusions of this thesis are stated.

3 Thermodynamic Preliminaries and Loop Heat Pipe Characteristics

In this chapter, the fundamental thermodynamic preliminaries and the LHP characteristics are described shortly while introducing the abbreviations and symbols used in the subsequent descriptions and equations of the LHP. The first section goes into detail about the laws of conservation, the heat transfer, and the basics of multiphase systems, which are relevant for the understanding of the thermodynamic processes in an LHP. In the second section, the characteristic working principle of temperature-controlled LHPs is explained.

3.1 Thermodynamic Preliminaries

The modeling approaches of the LHP in this thesis are based on conservation and balance equations. Combined with the fundamental equations of the phase change in multiphase systems, the model equations of the LHP are derived. The following thermodynamic preliminaries are mainly based on [BK16], [BS19], [HMS16], [Nat18], [Str14], and [vBW17].

3.1.1 Laws of Conservation

Energy Conservation

One of the key variables for describing the physical phenomena of a dynamic system is the energy. Energy cannot be created or destroyed in a system, but energy appears in different forms, which can be transformed into each other by corresponding processes [Str14, p. 33]. Furthermore, energy can be stored in a system and transferred between systems while changing the systems' state [vBS15, p. 90]. The dynamic behavior of the state of a system is closely connected to the energy in the system. Hence, a specific system behavior is achieved by controlling the state of a system. The state can be stabilized and altered by the supplied energy of a control system.

Starting from the basics of physics, the total energy of a mechanical system without energy exchange with the surroundings remains constant, i.e. energy is conserved, and the *law of conservation of energy* holds [HMS16, p. 55]:

$$E_{sys} = E_{kin} + E_{pot} = \text{constant}. \tag{3.1}$$

The total energy E_{sys} of a mechanical system is the sum of the kinetic energy E_{kin} and the potential energy E_{pot}. Both energies are a function of the mass m of the system:

$$E_{kin} = \frac{1}{2} \cdot m \cdot c^2, \tag{3.2}$$

$$E_{pot} = m \cdot g \cdot w, \tag{3.3}$$

with the velocity c of the system, the gravitational constant g, and the height w of the system above a reference level. Compared to the total energy of a mechanical system in (3.1), the total energy of an isolated system in thermodynamics includes the internal energy U_{sys} additionally, which describes the energy of a system in rest [BK16, p. 41]:

$$E_{sys} = E_{kin} + E_{pot} + U_{sys} = \text{constant}. \tag{3.4}$$

Equation (3.4) describes the *first law of thermodynamics for isolated systems*. In general, the total energy of an isolated system, i.e. the sum of all forms of energy within the system, is constant. Based on his experience, Hermann von Helmholtz concluded that there is no machine that works continuously without absorbing energy in any form [HMS16, p. 174]. Such a perpetual motion machine of the first kind would contradict the first law of thermodynamics and the law of conservation of energy in general.

In contrast to an isolated system, a closed system is able to exchange energy over its borders with another system in consideration of the first law of thermodynamics. Hence, the system's energy changes depending on not only the work[1] W done on the system but also the heat[2] Q added to the system [BK16, p. 47]:

$$\Delta E_{sys} = \Delta E_{kin} + \Delta E_{pot} + \Delta U_{sys} = W + Q. \tag{3.5}$$

Here, Δ denotes the difference between the energies in the initial and the final state of the system. The energy balance equation (3.5) presents the *first law of thermodynamics for closed systems*. It describes the quasi-stationary process of the heat and work transfer to a closed system, which finds an equilibrium state at the starting and the end point of the process.

Taking into account the time dependency of an instationary process, the temporal change of the total energy of the closed system is described by the power balance equation

$$\frac{\mathrm{d}E_{sys}}{\mathrm{d}t} = P + \dot{Q}, \tag{3.6}$$

with the derivative $\mathrm{d}E_{sys}/\mathrm{d}t$ of the total energy E_{sys} with respect to the time t, the power P as the time derivative of the work W, and the heat flow rate $\dot{Q}$ as the time derivative of the heat Q.

Another possibility to transport energy over system borders is connected with the mass flow of a fluid. The internal energy of the mass flow, which enters and leaves an open system,

[1] In the English literature on thermodynamics, the sign of the work W in the energy balance equation (3.5) is often negative, indicating the work done by the system (cf. [Sto07, p. 81]).

[2] The sign convention for the heat Q in the energy balance equation (3.5) defines that positive heat is received by a system and negative heat is released by a system.

increases and decreases the total energy of the system. This energy is called enthalpy H. In the flow process, additional moving boundary work is done on the fluid to be transported in and out of the system. Hence, the enthalpy H of a fluid is defined as the sum of its internal energy U and the moving boundary work, which is the product of the pressure p and the volume V of the fluid [LKLT17, p. 103]:

$$H = U + p \cdot V. \tag{3.7}$$

In addition, the enthalpy is expressed by the mass m and the specific enthalpy h of the fluid, which results from the specific internal energy u and the specific volume v:

$$H = h \cdot m = (u + p \cdot v) \cdot m. \tag{3.8}$$

In thermodynamics, the specific property is a special class of the intensive property with respect to the corresponding mass. An intensive variable, in contrast to an extensive variable, is independent of the size of the system [Str14, p. 14]. Accordingly, the extensive enthalpy flow rate $\dot{H}$ is calculated by the extensive mass flow rate $\dot{m}$ and the intensive specific enthalpy h:

$$\dot{H} = h \cdot \dot{m}. \tag{3.9}$$

With the kinetic and potential energies of the entering (index i) and leaving (index o) fluid flows, the general form of the *first law of thermodynamics for open systems* is derived [BK16, p. 78]:

$$\frac{\mathrm{d}E_{sys}}{\mathrm{d}t} = \sum_j P_j + \sum_k \dot{Q}_k + \sum_i \dot{m}_i \cdot \left(h_i + g \cdot w_i + \frac{1}{2} \cdot c_i^2 \right) - \sum_o \dot{m}_o \cdot \left(h_o + g \cdot w_o + \frac{1}{2} \cdot c_o^2 \right). \tag{3.10}$$

The mechanical energies of the fluid on the right side of (3.10), which correspond to the kinetic energy in (3.2) and the potential energy in (3.3), can often be neglected compared to the enthalpy of the fluid in (3.8) [LKLT17, p. 89]. On the left side of (3.10), the mechanical energies E_{kin} and E_{pot} in the total energy E_{sys} of the thermodynamic system according to (3.4) are negligible [vBW17, p. 9]. Both assumptions are also valid for the LHP. Hence, (3.10) can often be rewritten as

$$\frac{\mathrm{d}U}{\mathrm{d}t} = \sum_j P_j + \sum_k \dot{Q}_k + \sum_i \dot{m}_i \cdot h_i - \sum_o \dot{m}_o \cdot h_o. \tag{3.11}$$

The different forms of the heat flow $\dot{Q}$ are explained in detail in Sec. 3.1.2. The specific enthalpy h of the fluid is expressed as a function of the temperature T and the pressure p, also known as *caloric equation of state* [Str14, p. 103]:

$$h = h(T, p). \tag{3.12}$$

The total differential of the specific enthalpy is

$$\mathrm{d}h = \left.\frac{\partial h}{\partial T}\right|_p \mathrm{d}T + \left.\frac{\partial h}{\partial p}\right|_T \mathrm{d}p. \tag{3.13}$$

The first partial derivative in (3.13) is defined as the isobaric specific heat capacity $c_p(T, p)$. It is used in the calculation of specific enthalpy differences at the same pressure level p:

$$h(T_2, p) - h(T_1, p) = \int_{T_1}^{T_2} c_p(T, p)\, \mathrm{d}T. \tag{3.14}$$

For small temperature differences, the temperature dependency of $c_p(T, p)$ can be neglected [BK16, p. 85], and the integral in (3.14) is approximated by the mean isobaric specific heat capacity $\bar{c}$. Thus, (3.14) is given by

$$h(T_2, p) - h(T_1, p) = \bar{c}_{2,1} \cdot (T_2 - T_1)\,, \tag{3.15}$$

where $\bar{c}_{2,1}$ is determined by the arithmetic mean of the specific heat capacities at T_1 and T_2:

$$\bar{c}_{2,1} = \frac{c_p(T_1, p) + c_p(T_2, p)}{2}. \tag{3.16}$$

In order to ease notation, the isobaric subscript p is replaced in (3.15) by the subscripts of the two temperatures T_1 and T_2 of the corresponding temperature difference. The calculation of the individual specific enthalpies for the different phases of a fluid is presented in Sec. 3.1.3.

Mass Conservation

Similar to the law of conservation of energy, mass can neither be created nor destroyed. Thus, the total mass m in a closed system is constant and does not change in time t. Hence, the following *law of conservation of mass* for closed systems holds:

$$\frac{\mathrm{d}m}{\mathrm{d}t} = 0. \tag{3.17}$$

In open systems, mass can be transferred across the system's boundaries as mass flows between the systems. The mass balance equation

$$\frac{\mathrm{d}m}{\mathrm{d}t} = \sum_i \dot{m}_i - \sum_o \dot{m}_o \tag{3.18}$$

describes the relation between the temporal change of the total mass m of the open system and the mass flows $\dot{m}$ into (index i) and out of (index o) the system. [BK16, p. 73]

Momentum Conservation

Besides the energy and the mass, the law of conservation also applies to the momentum. Isaac Newton stated in his *second law of motion* that a force F acting on a system equals the temporal change of the momentum B of a system [HMS16, p. 44]:

$$\frac{\mathrm{d}\boldsymbol{B}}{\mathrm{d}t} = \boldsymbol{F}. \tag{3.19}$$

Since the direction of the momentum B is parallel to the force F, both physical variables are expressed in bold font as the vectors $\boldsymbol{B}$ and $\boldsymbol{F}$. The momentum vector $\boldsymbol{B}$ is defined by the product of the mass m and the velocity vector $\boldsymbol{c}$:

$$\boldsymbol{B} = m \cdot \boldsymbol{c}. \tag{3.20}$$

In open thermodynamic systems like pipes, the mass transfer across the boundaries of the system includes a momentum flux in and out of the system. Hence, the conservation of momentum of a fluid flow in a pipe is described by the following balance equation:

$$\frac{\mathrm{d}\boldsymbol{B}}{\mathrm{d}t} + \boldsymbol{B}_o - \boldsymbol{B}_i - \sum_j \boldsymbol{F}_j = 0. \tag{3.21}$$

The force vector $\boldsymbol{F}$ acts on the fluid volume along the direction of motion. Hence, $\boldsymbol{F}$ is perpendicular to the cross-sectional area A of the pipe and its normal component is given by

$$F = p \cdot A. \tag{3.22}$$

The longitudinal section of an elevated pipe is illustrated in Fig. 3.1.

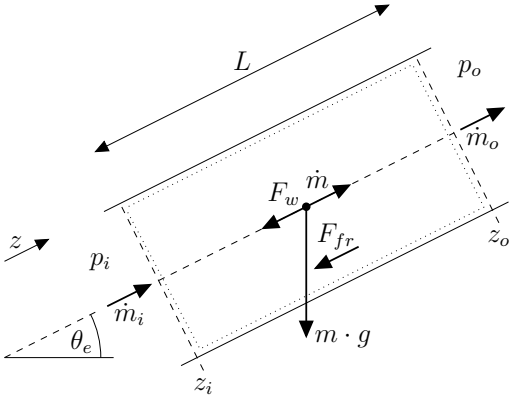

Figure 3.1: Momentum conservation for a fluid in an elevated pipe (cf. [Cha14, p. 43])

According to [Cha14, p. 44], the one-dimensional, differential form of the *law of conservation of momentum* for the transient fluid flow through a pipe of infinitesimal length in z-direction is given by

$$\frac{\partial\left(\rho A c\right)}{\partial t} + \frac{\partial\left(\rho A c^2\right)}{\partial z} + \frac{\partial F}{\partial z} + \frac{\partial F_w}{\partial z} + \frac{\partial F_{fr}}{\partial z} = 0, \tag{3.23}$$

with the density ρ and the velocity c of the fluid. The terms in (3.23) from the left to the right correspond to the temporal and local change of the momentum B of the fluid in the pipe, and the local changes of the pressure force F, the z-component F_w of the fluid weight, and the pressure force F_{fr} due to friction. Assuming a constant density ρ of the fluid, (3.23) is rewritten as

$$\frac{\partial \dot{m}}{\partial t} + \frac{1}{\rho A} \cdot \frac{\partial \dot{m}^2}{\partial z} + \frac{\partial F}{\partial z} + \frac{\partial F_w}{\partial z} + \frac{\partial F_{fr}}{\partial z} = 0, \tag{3.24}$$

where the mass flow rate $\dot{m}$ is expressed by the product of the fluid density ρ, the cross-sectional area A, and the fluid velocity c:

$$\dot{m} = \rho \cdot A \cdot c. \tag{3.25}$$

The length L of the pipe in Fig. 3.1 is given by the difference between the positions of the outlet at z_o and the inlet at z_i:

$$\Delta z = z_o - z_i = L. \tag{3.26}$$

By integrating (3.23) over L, the following equation is obtained:

$$L \cdot \frac{\mathrm{d}\dot{m}}{\mathrm{d}t} + \frac{1}{\rho A} \cdot \dot{m}_o^2 - \frac{1}{\rho A} \cdot \dot{m}_i^2 + A \cdot p_o - A \cdot p_i + \Delta F_w + \Delta F_{fr} = 0. \tag{3.27}$$

The pressure force difference ΔF_{fr} due to friction losses results from (3.22):

$$\Delta F_{fr} = A \cdot \Delta p_{fr}. \tag{3.28}$$

For laminar flow, the pressure drop in smooth pipes can be calculated by the *Hagen-Poiseuille law* [WGWS10, p. 1057]:

$$\Delta p_{fr} = \frac{32 \mu c L}{D_i^2} = \frac{32 \mu \dot{m} L}{\rho A D_i^2}. \tag{3.29}$$

In (3.29), D_i represents the inner diameter of a pipe with circular cross section:

$$A = \pi \cdot \frac{D_i^2}{4}. \tag{3.30}$$

The dynamic viscosity μ depends on the average temperature between the inlet and outlet of the pipe at z_i and z_o. The corresponding weight difference of the fluid against the z-direction is given by

$$\Delta F_w = \rho \cdot g \cdot A \cdot L \cdot \sin(\theta_e). \tag{3.31}$$

The elevation of the pipe toward the horizontal is described by the elevation angle θ_e. The corresponding term in (3.23) vanishes if the pipe is horizontal, i.e. θ_e is zero and the weight has no z-component.

3.1.2 Heat Transfer

Nature always strives to balance temperature differences and establish a thermal equilibrium. According to the *first law of thermodynamics* and in addition to (3.4), the equilibrium temperature in an isolated system is the same everywhere in the system. If any temperature deviation is present, energy in the form of heat is transferred across the boundaries of the subsystems with the different temperatures. While the first law of thermodynamics describes the energy conversion between the two subsystems, it does not determine the direction of the heat flow. In fact, the restriction of the heat flow is stated in the *second law of thermodynamics* by introducing the extensive quantity, the entropy S. The entropy in an isolated system is

maximized when it reaches a stable equilibrium state. Mathematically speaking, the change of the entropy in an isolated system is always greater or equal to zero [Str14, p. 56]:

$$\frac{\mathrm{d}S}{\mathrm{d}t} = \dot{S}_g \geq 0, \tag{3.32}$$

where $\dot{S}_g$ is the entropy generation rate within the system.

Similar to the power balance equation of the first law of thermodynamics in (3.6), the corresponding entropy balance equation of a closed system that exchanges heat with the surroundings is given by the following equation [Str14, p. 57]:

$$\frac{\mathrm{d}S}{\mathrm{d}t} = \frac{\dot{Q}}{T} + \dot{S}_g. \tag{3.33}$$

In the example of a heat conductor connected to two reservoirs at different temperatures, as presented in [Str14, p. 63], both heat and entropy are exchanged because of a temperature difference. Thus, the heat conductor receives the heat flows $\dot{Q}_h$ and $\dot{Q}_l$ from the corresponding reservoirs at the higher temperature T_h and the lower temperature T_l. According to (3.6) and (3.33), the respective steady-state balance equations of the heat conductor are given by

$$\dot{Q}_h = -\dot{Q}_l = \dot{Q} \tag{3.34}$$

and thus

$$\dot{Q} \cdot \left(\frac{1}{T_l} - \frac{1}{T_h} \right) = \dot{S}_g \geq 0. \tag{3.35}$$

According to [Str14, p. 64], the inequality (3.35) only holds if

$$T_h > T_l, \quad \text{for } \dot{Q} > 0 \text{ and } T \geq 0. \tag{3.36}$$

Thus, the heat flow $\dot{Q}$ is only possible from the subsystem with the higher temperature to the subsystem with the lower temperature. For a more detailed determination of the heat flow $\dot{Q}$, the three fundamental heat transfer modes are elucidated in the next sections: heat conduction, convection, and thermal radiation [Nat18, p. 1]. While heat conduction and thermal radiation occur independently, the heat transfer process of convection always includes heat conduction [vBW17, p. 3].

Heat Conduction

Heat conduction occurs in materials where a temperature gradient exists. Nearby molecules carry out an energy transfer among themselves. This energy transfer presents itself as the conduction of heat and is characterized by the temperature. Accordingly, the basic law of heat conduction is described by *Fourier's law* [BS19, p. 6]:

$$\dot{\boldsymbol{q}} = -\lambda_{th} \cdot \nabla T. \tag{3.37}$$

The gradient ∇T of the temperature T multiplied by the thermal conductivity λ_{th} equals the vector of the heat flux $\dot{q}$. The minus sign relates to the heat flow direction based on the second law of thermodynamics.

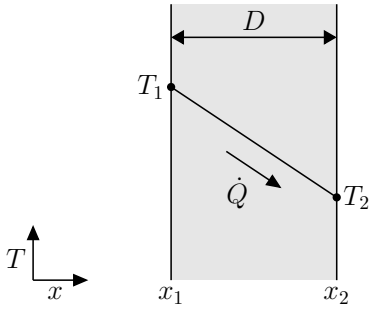

Figure 3.2: Heat conduction in a wall

Based on Fig 3.2, the equation for the mean steady-state one-dimensional heat conduction in a wall with thickness D and heat transfer surface area A_s is derived from (3.37) [BS19, p. 6]:

$$\dot{Q} = \dot{q} \cdot A_s = \lambda_{th} \cdot \frac{\Delta T}{D} \cdot A_s = \frac{\lambda_{th} A_s}{D} \cdot (T_1 - T_2)\,, \tag{3.38}$$

with the difference ΔT of the temperatures T_1 and T_2 on both sides of the wall. The thermal conductivity λ_{th} is substance-specific and both temperature- and pressure-dependent. Hence, its value is usually determined via appropriate measurements.

Convection

Convection describes the energy transport in fluids in the form of heat. In addition to heat conduction in the fluid itself, heat is transferred via the macroscopic motion of the fluid. The kinetic energy and the enthalpy of the fluid is released as heat to the passing solid matter due to friction. For this reason, the velocity and the temperature of the fluid in the boundary layer near the solid matter differ from the values in the center of the fluid flow. Besides the physical properties of the fluid and the geometry of the solid matter, the transferred heat depends on the local temperature and velocity fields. [BS19, p. 10]

According to *Newton's law of cooling*, the convective heat flow rate $\dot{Q}$ to the surface of an area A_s can be approximated by the following equation to average the local dependencies [Nat18, p. 12]:

$$\dot{Q} = \alpha \cdot A_s \cdot \Delta T = \alpha \cdot A_s \cdot (T_1 - T_2)\,, \tag{3.39}$$

with the mean convective heat transfer coefficient α and the temperature difference ΔT between the temperature T_1 of the fluid and the temperature T_2 of the surface (see Fig. 3.3). The convective heat transfer coefficient α describes the complex relations in the boundary layer. Because of its dependency on the local velocity and the temperature fields, the exact convective heat transfer coefficient can only be determined by application-specific measurements. In this context, the known dimensionless variables of fluid dynamics are introduced to specify and facilitate the determination process of the coefficient α if necessary (see e.g. [BS19, p. 17]).

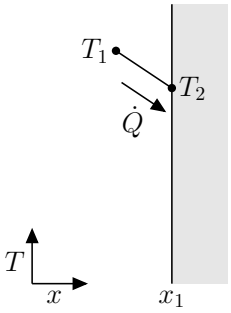

Figure 3.3: Convective heat transfer

Thermal Radiation

The thermal radiation of a body results from the emission of thermal energy in the form of electromagnetic waves to its surroundings. A body converts its internal energy into energy that can be transported without matter. Hence, the energy transport in vacuum is possible [BS19, p. 28]. The decisive factor of thermal radiation is not a linear temperature gradient as with the other two heat transfer modes, but the thermodynamic temperature of the body itself since every body with a temperature above absolute zero (at $0\,\mathrm{K}$ or $-273.15\,^{\circ}\mathrm{C}$) emits thermal radiation [vBW17, p. 226]. According to the *Stefan-Boltzmann law*, the emitted heat flow via the thermal radiation of a body with temperature T and surface area A_s is given by

$$\dot{Q} = \epsilon(T) \cdot \sigma \cdot A_s \cdot T^4, \tag{3.40}$$

with the Stefan-Boltzmann constant σ [Nat18, p. 15]:

$$\sigma = 5.67 \times 10^{-8}\,\mathrm{W/m^2K^4}. \tag{3.41}$$

The temperature-dependent surface emissivity ϵ describes the ability of a body to emit thermal radiation and depends mainly on the physical properties of the material but also on the nature of the surface. In comparison with an ideal emitter, which is a black body with

$$\epsilon = 1, \tag{3.42}$$

the surface emissivity is

$$\epsilon(T) \leq 1. \tag{3.43}$$

for all other emitters [BS19, p. 29].

Since all bodies above absolute zero emit thermal radiation, the radiative heat exchange between a body at T and its surroundings is summed up by the net radiative heat flow

$$\dot{Q} = \epsilon(T) \cdot \sigma \cdot A_s \cdot \left(T_{amb}^4 - T^4\right), \tag{3.44}$$

where the surroundings of the body behave like a black body at the ambient temperature T_{amb} [Nat18, p. 15]. The equation holds under the assumption based on *Kirchhoff's law of thermal radiation* that the emission ratio equals the absorption ratio of a body with a diffuse surface [BS19, p. 643].

Combined Heat Transfer Considering Electrical Analogy

Typical heat transfer processes include the heat exchange between several fluids or layers by a combination of all three heat transfer modes, which are described in the previous sections. Hence, the total heat transfer process is determined by a combination of (3.38), (3.39), and (3.44). For a consistent description of such heat transfer processes, the heat transfer modes are unified, and their calculations are facilitated by the analogy between the heat transfer and the energy transfer in electrical circuits. As a result, models of heat transfer processes are illustrated as thermal circuits [Sid15, p. 3], thereby representing lumped thermal parameters by circuit elements.

Already with the LHP in mind, the example of the heat transfer in pipes is chosen to illustrate the aforementioned combination of the heat transfer modes, as depicted in Fig. 3.4.

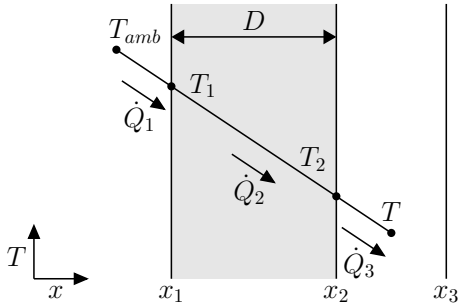

Figure 3.4: Combined heat transfer in a pipe

The working fluid inside the pipes exchanges heat through the pipe wall with the surroundings. When heat is exchanged between a fluid in a pipe at T and the surroundings at T_{amb}, convection and thermal radiation take place in parallel on the outside of the pipe at T_1 [BS19, p. 31]. Hence, the heat flows (3.39) and (3.44) of both heat transfer modes are added up:

$$\dot{Q}_1 = \alpha_1 \cdot A_{s,1} \cdot (T_{amb} - T_1) + \epsilon(T_1) \cdot \sigma \cdot A_{s,1} \cdot \left(T_{amb}^4 - T_1^4\right). \tag{3.45}$$

With the linearization of the radiation part (see [Nat18, p. 15]), (3.45) is rewritten and the heat transfer coefficients are combined:

$$\dot{Q}_1 = (\alpha_1 + \alpha_{rad}) \cdot A_{s,1} \cdot (T_{amb} - T_1), \tag{3.46}$$

where the effective radiation heat transfer coefficient α_{rad} is defined by

$$\alpha_{rad} = \epsilon(T_1) \cdot \sigma \cdot \left(T_{amb}^2 + T_1^2\right) \cdot (T_{amb} + T_1). \tag{3.47}$$

In the pipe wall, the heat is transferred from the outside at T_1 to the inside at T_2 via heat conduction:

$$\dot{Q}_2 = \frac{\lambda_{th} A_{s,2}}{D} \cdot (T_1 - T_2). \tag{3.48}$$

Finally, the heat is exchanged with the fluid at T inside the pipe via convection:

$$\dot{Q}_3 = \alpha_3 \cdot A_{s,3} \cdot (T_2 - T)\,. \tag{3.49}$$

With the thermal analogy of *Ohm's law*, the calculation of the separate heat flows $\dot{Q}_1$, $\dot{Q}_2$, and $\dot{Q}_3$ are unified with the thermal resistance R_{th}:

$$\dot{Q}_i = \frac{1}{R_{th,i}} \cdot \Delta T_i \quad \text{with } i = 1, 2, 3. \tag{3.50}$$

Hence, the heat flow corresponds to the electrical current, whereas the temperature difference corresponds to the electrical potential difference or voltage. The reciprocals of the heat transfer coefficients of the different heat transfer modes in (3.46), (3.48), and (3.49) correspond to their respective thermal resistances:

$$R_{th,1} = \frac{1}{(\alpha_1 + \alpha_{rad})\, A_{s,1}}, \tag{3.51}$$

$$R_{th,2} = \frac{D}{\lambda_{th} A_{s,2}}, \tag{3.52}$$

$$R_{th,3} = \frac{1}{\alpha_3 A_{s,3}}. \tag{3.53}$$

Continuing with the analogy, the rules of electrical circuits can also be applied to the thermal domain. Since the resistors $R_{th,1}$, $R_{th,2}$, and $R_{th,3}$ are connected in series, the separate heat flows $\dot{Q}_1$, $\dot{Q}_2$, and $\dot{Q}_3$ must be equal:

$$\dot{Q}_1 = \dot{Q}_2 = \dot{Q}_3 = \dot{Q}. \tag{3.54}$$

In addition, the total temperature difference ΔT between the fluid and the surroundings is given by the sum of the separate temperature differences:

$$\Delta T = (T_{amb} - T) = (T_{amb} - T_1) + (T_1 - T_2) + (T_2 - T)\,. \tag{3.55}$$

Hence, the total heat transfer from the surroundings through the wall to the fluid is given by

$$\dot{Q} = \frac{1}{R_{th,4}} \cdot (T_{amb} - T) = k_{th} \cdot A_{s,4} \cdot (T_{amb} - T)\,, \tag{3.56}$$

with the overall heat transfer coefficient k_{th} and the effective surface area $A_{s,4}$ [BS19, p. 35]. Because $R_{th,1}$, $R_{th,2}$, and $R_{th,3}$ are connected in series, the total thermal resistance $R_{th,4}$ is determined by their sum:

$$R_{th,4} = R_{th,1} + R_{th,2} + R_{th,3}. \tag{3.57}$$

Analogous to the electrical conductance, the reciprocal of the thermal resistance R_{th} corresponds to the thermal conductance U_{th} [Nat18, p. 184]:

$$U_{th} = \frac{1}{R_{th}}. \tag{3.58}$$

Since the heat transfers always expand over entire areas, the temperatures in the respective temperature differences are averaged over the area. The fluid temperature T in (3.56) is also assumed to be homogeneous over $A_{s,4}$. To consider a one-dimensional temperature gradient along the pipe length, which would extend into the third dimension in Fig. 3.4, based on the heat exchange with the surroundings, the temperature difference in (3.56) is substituted by the logarithmic mean temperature difference ΔT_m for heat exchanger [vBW17, p. 254]:

$$\dot{Q} = U_{th} \cdot \Delta T_m \tag{3.59}$$

with

$$\Delta T_m = \frac{(T_{amb} - T_i) - (T_{amb} - T_o)}{\ln\left(\frac{T_{amb}-T_i}{T_{amb}-T_o}\right)} \tag{3.60}$$

if

$$T_i < T_o < T_{amb} \tag{3.61}$$

with the inlet temperature T_i and the outlet temperature T_o of the pipe in flow direction holds. According to (3.11), the absorbed heat flow rate $\dot{Q}$ of the fluid equals the enthalpy flow rate difference of the fluid in the pipe for stationary processes. Hence, the following equation holds:

$$U_{th} \cdot \Delta T_m = \dot{m} \cdot \bar{c}_{o,i} \cdot (T_o - T_i)\,. \tag{3.62}$$

Thus, the outlet temperature T_o is calculated by

$$T_o = T_{amb} + (T_i - T_{amb}) \cdot \exp\left(-\frac{U_{th}}{\dot{m}\bar{c}_{o,i}}\right). \tag{3.63}$$

If T_{amb} is smaller than the fluid temperatures in the pipe, the fluid releases heat to the surroundings. In this case, (3.63) still holds.

For instationary heat transfer processes, the electrical analogy is also applied to the description of the temporal change of the total energy E_{sys} stored in a system, which does not experience any phase change processes [Sid15, p. 41]:

$$\frac{\mathrm{d}E_{sys}(t)}{\mathrm{d}t} = C_{th} \cdot \frac{\mathrm{d}T(t)}{\mathrm{d}t}. \tag{3.64}$$

The thermal capacity of the system is interpreted as the thermal capacitance C_{th}, which is given by the product of the constant density ρ, the constant volume V, and the constant specific heat capacity c_p [Nat18, p. 55]:

$$C_{th} = \rho \cdot V \cdot c_p. \tag{3.65}$$

A graphical approach to model the heat transfer between several systems is the construction of a nodal network, where each system is characterized by one temperature node. According to (3.50) and (3.64), the corresponding differential equations of the temperature nodes are established based on the electrical analogy, as presented in Example 3.1.

Example 3.1:

Two temperature nodes $T_1(t)$ and $T_2(t)$ of the thermal network in Fig. 3.5 are connected via a thermal resistance $R_{th,12}$ to exchange energy in the form of heat.

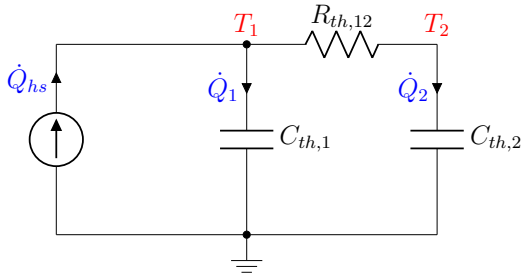

Figure 3.5: Thermal network with two temperature nodes T_1 and T_2 in the electrical circuit representation

The energy change in a system with temperature node $T_1(t)$ or $T_2(t)$ depends on the respective thermal capacitance $C_{th,1}$ or $C_{th,2}$. The dissipated heat $\dot{Q}_{hs}(t)$ of the heat source in the shape of an ideal current source enters the system characterized by $T_1(t)$. Similar to Kirchhoff's current law, the sum of the entering and leaving heat flows at a temperature node must be zero. Hence, the dynamics of the temperatures $T_1(t)$ and $T_2(t)$ are modeled by the following first-order differential equations:

$$C_{th,1} \cdot \frac{\mathrm{d}T_1(t)}{\mathrm{d}t} = -\frac{1}{R_{th,12}} \cdot \big(T_1(t) - T_2(t)\big) + \dot{Q}_{hs}(t), \tag{3.66}$$

$$C_{th,2} \cdot \frac{\mathrm{d}T_2(t)}{\mathrm{d}t} = \frac{1}{R_{th,12}} \cdot \big(T_1(t) - T_2(t)\big). \tag{3.67}$$

For a general thermal network with n temperature nodes $T_i(t)$ $(i = 1, ..., n)$ and q external heat inputs $\dot{Q}_{hs,j}(t)$ $(j = 1, ..., q)$, the following differential equation in matrix notation is derived:

$$\dot{\boldsymbol{x}}_{tn}(t) = \boldsymbol{A}_{tn} \cdot \boldsymbol{x}_{tn}(t) + \boldsymbol{B}_{tn} \cdot \boldsymbol{u}_{tn}(t), \tag{3.68}$$

with $\boldsymbol{x}_{tn}(t) = [T_1(t), ..., T_n(t)]^\top$, $\boldsymbol{u}_{tn}(t) = [\dot{Q}_{hs,1}(t), ..., \dot{Q}_{hs,q}(t)]^\top$, $\boldsymbol{A}_{tn} \in \mathbb{R}^{n \times n}$, and $\boldsymbol{B}_{tn} \in \mathbb{R}^{n \times q}$. In the case of an available temperature measurement for each node, the dynamics of the thermal network are described by the following dynamical state-space model according to Def. 2.2:

$$\dot{\boldsymbol{x}}_{tn}(t) = \boldsymbol{A}_{tn} \cdot \boldsymbol{x}_{tn}(t) + \boldsymbol{B}_{tn} \cdot \boldsymbol{u}_{tn}(t), \tag{3.69a}$$

$$\boldsymbol{y}_{tn}(t) = \boldsymbol{x}_{tn}(t), \tag{3.69b}$$

with $\boldsymbol{y}_{tn}(t) \in \mathbb{R}^{n \times 1}$. With every temperature node and corresponding thermal capacitance, the dimension of the state-space model (3.69) rises, which can result in a high computational effort. Therefore, further network simplifications can be necessary to keep the number of dimensions low and to be able to handle the matrices efficiently.

The previous equations refer to the single-phase heat transfer in thermodynamic systems. These fundamental equations are extended in the next section to multiphase systems.

3.1.3 Multiphase Systems

In the modeling process of complex control systems, one of the first steps is the delimitation of subsystems as parts of the total system to divide the complex modeling task into several simpler subtasks. Transferred to the field of thermodynamics, this means that heterogeneous systems are preferably divided into homogeneous subsystems, where all intensive and specific variables have a constant value in the equilibrium state throughout the subsystem [SSSM13, p. 10]. A phase is such a homogeneous subsystem in a multiphase system with an ambiguous meaning: While a phase may refer to different components in a multicomponent system, it can also stand for the different states of matter in a single-component multiphase system. The LHP is a multiphase system of the latter type with a working fluid in two states of matter: liquid and gas. These states are transformed into each other by condensation and evaporation. In this case, the gas phase is also called vapor phase to emphasize the experienced phase transition. The subsystems of the LHP are filled with either a single-phase fluid (liquid or vapor) or a two-phase fluid (liquid and vapor). While model equations for the subsystems can be established based on the previous laws of conservation in Section 3.1.1, the composition of the fluid in the subsystems has to be considered additionally since the laws and the values of the physical properties of the working fluid differ in both phases. The two relevant phases and their respective boundary in a single-component multiphase system, such as the LHP, are presented by the vapor-pressure curve in the pressure-temperature (p-T) diagram in Fig. 3.6a.

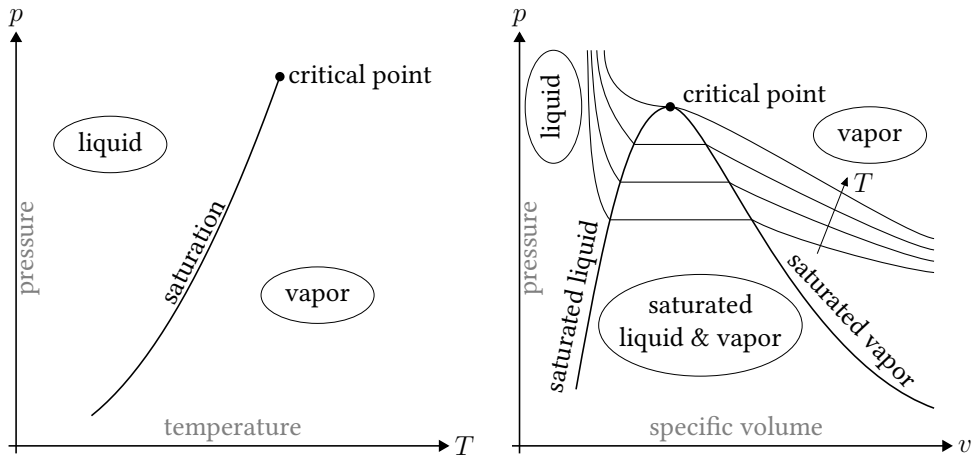

(a) Pressure-temperature diagram with the vapor-pressure curve

(b) Pressure-specific volume diagram

Figure 3.6: Phase diagrams of a single-component multiphase system (cf. [Str14, pp. 109, 111])

There only exists an equilibrium between the vapor and the liquid phase for pressures and temperatures below the critical point. Hence, the phase-changing processes condensation and vaporization on the vapor-pressure curve occur for temperatures lower than the temperature at the substance-specific critical point. Temperatures and pressures on the vapor-pressure curve between the liquid and the vapor phase are in a saturated equilibrium state since both phases coexist [BK16, p. 145].

The slope of the vapor-pressure curve in Fig. 3.6a is described by the *Clapeyron equation* [Str14, p. 408]:

$$\frac{\mathrm{d}p_s}{\mathrm{d}T_s} = \frac{\Delta h^v}{T_s \left(v^v - v^l\right)}, \tag{3.70}$$

with the saturation temperature T_s, the saturation pressure p_s, and the specific volumes v^v and v^l of the saturated vapor and the saturated liquid. The specific enthalpy difference Δh^v of the phase transition is called latent heat of evaporation and is defined by the difference between the specific enthalpy h^v of vapor and the specific enthalpy h^l of liquid at the saturation temperature T_s:

$$\Delta h^v = h^v - h^l. \tag{3.71}$$

Since the specific volume v is the reciprocal of the density ρ, (3.70) can be rewritten:

$$\frac{\mathrm{d}p_s}{\mathrm{d}T_s} = \frac{\Delta h^v}{T_s \left(\frac{1}{\rho^v} - \frac{1}{\rho^l}\right)} = \frac{\Delta h^v \rho^v \rho^l}{T_s \left(\rho^l - \rho^v\right)}. \tag{3.72}$$

For the direct calculation of the vapor pressure on the vapor-pressure curve, the author of [Ant88] derived a relation between the saturation pressure p_s and the saturation temperature T_s, which can be traced back to the Clapeyron equation (3.72) (cf. [BK16, p. 196]). The common form of the *Antoine equation* with the empirical substance-specific constants A_{wf}, B_{wf}, and C_{wf} is given by

$$p_s = \exp\left(A_{wf} - \frac{B_{wf}}{C_{wf} + T_s}\right). \tag{3.73}$$

Accordingly, the corresponding temperature T_s is calculated by

$$T_s = -\frac{B_{wf}}{\ln(p_s) - A_{wf}} - C_{wf}. \tag{3.74}$$

On the vapor-pressure curve, both phases coexist in the saturation state. The differentiation between the saturated liquid and the saturated vapor becomes visible in the pressure-specific volume (p-v) diagram in Fig. 3.6b. Here, a third area exists besides the single-phase areas of the liquid and the vapor. Below the saturation lines, the two-phase area contains both vapor and liquid in saturation state. In this area, the phase transition is isobaric and isothermal. It takes place under constant pressure and constant temperature, while the specific volume varies according to the volume ratio of the vapor and the liquid.

Combining both diagrams, the pressure p is a function of both the temperature T and the specific volume v, also called the *thermal equation of state* [Str14, p. 22]:

$$p = p(T, v). \tag{3.75}$$

At the boundaries between the single-phase areas and the two-phase area, (3.75) is not continuously differentiable with respect to the specific volume v. Hence, there is no pressure function for the total area. Instead, the subfunctions must be approximated separately for each phase by appropriate measurements of the temperature T, the pressure p, and the specific volume v. At least in the vapor area, the pressure coincides with the ideal gas law assuming small pressures [BK16, p. 203]:

$$p = \frac{RT}{v} = R \cdot T \cdot \rho, \tag{3.76}$$

with the specific gas constant R. In the two-phase area, the extensive variables, e.g. the mass m, the volume V, and the enthalpy H, equal the sum of their corresponding parts of the saturated liquid phase and the saturated vapor phase [BK16, p. 197]:

$$m = m^l + m^v, \tag{3.77}$$

$$V = V^l + V^v = v^l \cdot m^l + v^v \cdot m^v, \tag{3.78}$$

$$H = H^l + H^v = h^l \cdot m^l + h^v \cdot m^v, \tag{3.79}$$

with the masses m^v and m^l, the specific volumes v^v and v^l, and the specific enthalpies h^v and h^l of the saturated vapor and the saturated liquid, respectively.

In the case of the specific enthalpy, its calculation also differs in the corresponding phase. According to (3.15), the absolute specific enthalpy h^l of the subcooled liquid at the temperature T_1 up to the saturation temperature T_s is calculated by

$$h^l(T_1) = h^l(T_{ref}) + \bar{c}^l_{1,ref} \cdot (T_1 - T_{ref}) \tag{3.80}$$

or in abbreviated form

$$h^l_1 = h^l_{ref} + \bar{c}^l_{1,ref} \cdot (T_1 - T_{ref})\,. \tag{3.81}$$

Equations (3.80) and (3.81) are based on the constant reference temperature T_{ref}, which is often arbitrarily chosen according to the corresponding problem [BS19, p. 2]. Accordingly, the absolute specific enthalpy h^v of saturated vapor at the saturation temperature T_s is given by

$$h^v_s = h^l_{ref} + \bar{c}^l_{s,ref} \cdot (T_s - T_{ref}) + \Delta h^v. \tag{3.82}$$

In the vapor area, the vapor may reach temperatures above the saturation temperature T_s and thus is superheated. Therefore, the absolute specific enthalpy h^v of the superheated vapor at the temperature T_2 is calculated by

$$h^v_2 = h^l_{ref} + \bar{c}^l_{s,ref} \cdot (T_s - T_{ref}) + \Delta h^v + \bar{c}^v_{2,s} \cdot (T_2 - T_s)\,. \tag{3.83}$$

When considering the different kinds of a fluid in the calculation of the mean specific heat capacity $\bar{c}$ in (3.15), the specific heat capacity c^l_p of an incompressible liquid is approximated by

$$c^l_p = c^l_p(T), \tag{3.84}$$

while the specific heat capacity c^v_p of the vapor is independent of the pressure p in general assuming ideal gases [BK16, p. 86]:

$$c^v_p = c^v_p(T). \tag{3.85}$$

With the definition of the specific enthalpies, the thermodynamic preliminaries are sufficient to describe the LHP behavior in necessary detail. The important variables and expressions are introduced for the subsequent sections and chapters. The next section goes into detail about the specific characteristics of the multiphase system under investigation, the LHP.

3.2 Loop Heat Pipe Characteristics

The heat transport effectiveness of the LHP is based on its complex characteristics. Various thermodynamic and fluid-dynamic processes interact in an LHP on a microscopic scale, which makes the deduction of the macroscopic, control-relevant dynamics more difficult. To start the modeling process from a basic knowledge of the LHP operation, the fundamental working principle of the LHP is described in detail in Sec. 3.2.1. Afterwards, the characteristic behavior of the OT is explained in Sec. 3.2.2, which gives a closer look on the characteristics of the temperature-controlled LHP.

3.2.1 Working Principle

LHPs are especially known for their passive, two-phase working principle [Ku99]. The passivity of the LHP refers to the generation of a mass flow in the pipes by capillary forces in a porous wick [May05]. Thus, active mass transport components like power-consuming, error-prone mechanical pumps are avoided for a reliable heat transport. Furthermore, an effective heat transport is achieved by continuously changing the phase of the working fluid through evaporation and condensation. With the use of the latent heat during these phase transitions, the two-phase LHP reaches a higher heat transfer coefficient than single-phase heat transport systems. Accordingly, the overall thermal conductance and resistance of the LHP are high and low respectively [AAV+12]. In addition, the LHP sustains the required pressure difference and therefore their high heat transfer coefficient despite its orientation in the gravity field because of the local separation of the evaporation and the condensation. Apart from each other, the liquid and the vapor mass flow follow their own transport lines between the LHP components for evaporation and condensation. The corresponding reduced pressure drops in the transport lines together with a fine-pored primary wick enable a heat transport against gravity forces and over long distances up to several meters compared to conventional heat pipes without separation [May05].

The following description of the structure and the operation cycle of the LHP is illustrated by the two-dimensional schematic of the LHP in Fig. 3.7 for a better understanding of the challenges of controlling the LHP. The considered LHP is divided into five components. As their names imply, the evaporation and the condensation of the working fluid take place in the cylindric, multilayered evaporator (EV) and the condenser pipe (CO) accordingly. The transport lines include the liquid line (LL) and the vapor line (VL) corresponding to their contained phases. The last component of the LHP, the two-phase compensation chamber (CC), is attached to the evaporator and contributes to the stability of the LHP operation.

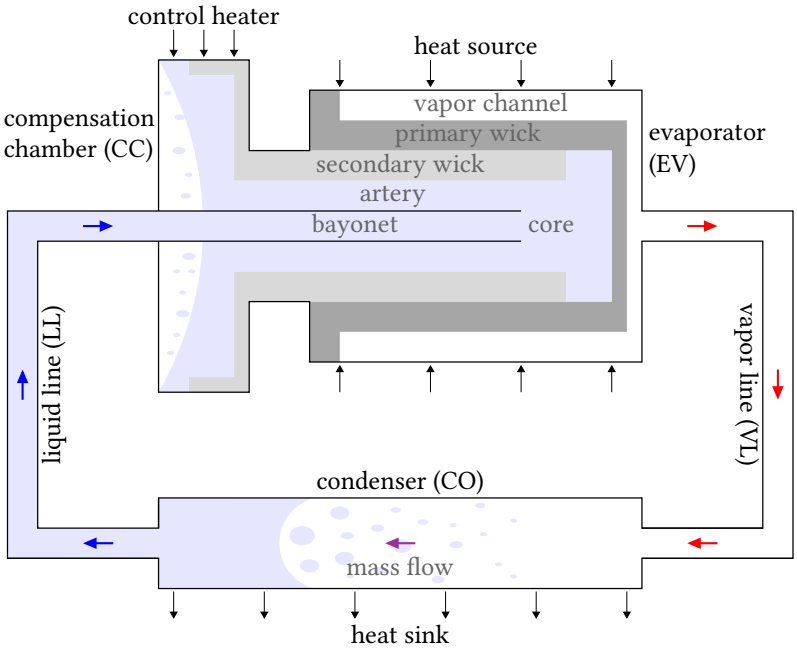

Figure 3.7: Structure of an LHP with its internal geometries and its fluid distribution (cf. [Ku99])

The LHP operation cycle starts in the evaporator when the liquid evaporates at the primary wick's outer surface due to the heat load at the evaporator generated by the heat source. During the evaporation of the liquid at the liquid-vapor interface, curved surfaces or menisci are formed in the pores of the primary wick, which develop capillary forces [Ku99]. These forces drive the accumulating vapor through the vapor channels to the outlet of the evaporator. On its way, the vapor absorbs additional heat from the heat load until it leaves the evaporator as superheated vapor. After the evaporator, the vapor is guided through the VL to the condenser. In the condenser, the vapor is cooled down to saturation temperature by the heat sink, condensates and releases its latent heat to the heat sink during the phase transition. Depending on the position of the liquid-vapor interface in the condenser, the condensed liquid is subcooled by the heat sink in the remaining length from the liquid-vapor interface to the outlet of the condenser. The subcooled liquid continues through the LL to the CC, where it is guided through a bayonet into the evaporator core. Here, the LHP operation cycle closes, as the returning liquid replenishes the primary wick for repeated evaporation by the heat load again. In short, the heat source induces the circulation of the working fluid in the loop, where the primary wick works as passive capillary pump.

A reliable and efficient heat transport of the LHP relies on a continuous evaporation of the liquid in the primary wick inside the evaporator. If the returning liquid from the condenser does not moisten the primary wick sufficiently, a dryout of the primary wick will disrupt the fluid circulation and thus the continuous operation of the LHP. Therefore, a secondary

wick with larger pores than the primary wick for a bidirectional liquid exchange connects the evaporator core with the liquid reservoir in the CC [Ku99]. This secondary wick in the CC ensures a sufficient supply of liquid to the primary wick at all times [CHKK98]. Furthermore, as a result of changing operating conditions, the CC as a two-phase reservoir counterbalances the movement of the liquid-vapor interface in the condenser and therefore the mass distribution in the entire loop in transient states. When the liquid-vapor interface in the condenser proceeds to the outlet of the condenser due to a high evaporation at high heat loads, the liquid column between the liquid-vapor interfaces in the condenser and the CC shifts toward the CC. In the process, excess liquid is transported through the secondary wick to be stored in the CC. If vapor is generated in the evaporator core because of high heat loads thereby blocking the direct liquid transport from the LL to the primary wick, it is discharged through the arteries into the CC. Thus, the CC has a direct impact on the LHP operation. It governs the OT of the LHP and supports a smooth LHP startup [Ku99]. To clarify the dependence of the LHP behavior on the external influences, a detailed description of the behavior of the OT and its control is given in Sec. 3.2.2.

3.2.2 Active Operating Temperature Control

The OT of an LHP is characterized by the temperature level, which the LHP adjusts itself at the current operating conditions [Ku99]. This equilibrium state ensures the necessary pressure distribution, at which a mass flow persists for a continuous heat transport during an on-going LHP operation. Usually, the OT refers to the vapor temperature at the evaporator [CVM07]. That is why the temperature sensor on the evaporator is usually used by the LHP end user to check the requirements of the thermal interface between the LHP and the cooled object to be met by the LHP manufacturer. The thermal interface and therefore the OT at this measuring point depend on many parameters and conditions [CM05]. A detailed characterization of its complex behavior follows in this section to determine the relevant influences on the LHP OT control under investigation.

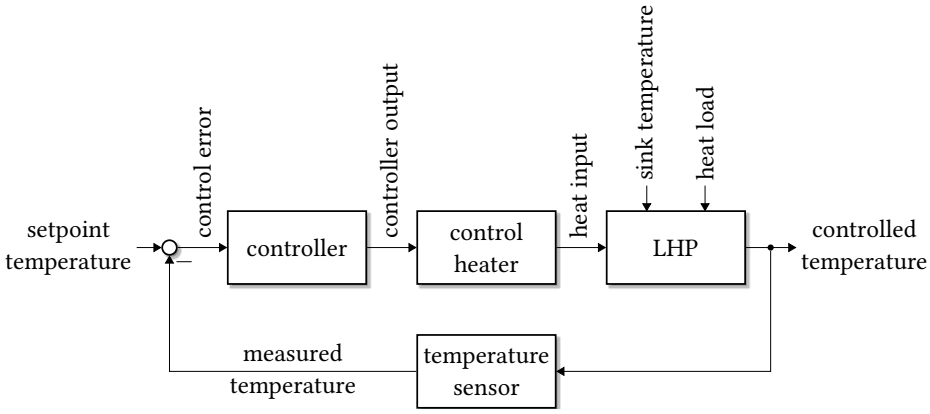

Figure 3.8: Active closed-loop OT control of an LHP with a control heater

The general temperature control loop of an LHP with a control heater (see Fig. 3.7) is depicted in Fig. 3.8, including the used signal names.

By measuring the controlled temperature with a temperature sensor, the control error as input of the controller to be designed is obtained as the difference between the measured temperature and the setpoint temperature. The controller output is transformed by the control heater into the corresponding heat input to the CC of the LHP, which adapts the controlled temperature in return. Depending on the variable operating conditions of the LHP, which are defined by the sink temperature and the heat load, the heat input must be determined in such a way that the controlled temperature remains as close as possible to the setpoint temperature over the entire operating range.

As the OT of the LHP is governed by the saturation temperature of the CC, the maintaining of a desired OT by controlling the CC temperature actively at a corresponding setpoint temperature with a control heater is commonly preferred [Ku08]. Instead of controlling the evaporator temperature as the nearest temperature to the cooled object, the control of the CC temperature provides the most stable temperatures and less temperature oscillations at low heat loads [KPM11a]. A small amount of external heat to the CC of the LHP is already enough to control the OT compared to the expected heat load at the evaporator supplied by the heat source. The heat of the control heater is able to alter the steady state of the CC and therefore the OT of the LHP by providing an additional changeable term to the energy balance in the CC. The CC energy balance is mainly influenced by the subcooling of the returning liquid from the LL and the heat leak from the evaporator to the CC as part of the heat load [Ku08]. With the additional heat of the control heater, the steady states at the desired setpoint temperature dependent on both the sink temperature and the heat load can be reached. Thus, the hardware design of the control system includes the adequate selection of the control heater with enough output power to cover the entire operating range of the LHP.

Besides the power limits of the control heater itself, another restriction regarding the self-sufficient working principle of the LHP must be considered when controlling the CC temperature with a control heater. To ensure a continuous heat transfer during LHP operation, the circulation of the working fluid has to be guaranteed. However, the mass circulation may stop if the CC is heated too quickly and its temperature rises above the evaporator temperature. In this case, the required pressure difference between the CC and the evaporator collapses. Consequently, the evaporator is flooded with liquid, and no vapor continues to the condenser for dissipation. If the CC is further heated, repeated startup and shutdown cycles may follow, as described in Sec. 2.4. In order to prevent the interruption of the mass flow in the LHP, the temperature gradient in the CC must be restricted by limiting the output of the control heater during operation. A practical approach is the adequate limitation of the controller gains since the LHP temperatures react very sensitively to changes of the control heater output. A deliberate LHP shutdown by excessive CC heating, in contrast, is sometimes used to prevent a continuous heat transport and therefore the temperature of the cooled object from dropping too low when no heat is to be dissipated, e.g. in situations where the cooled object has no power. [Ku99]

As mentioned before, the controlled OT of the LHP is subject to different external influences, mainly the sink temperature and the heat load. These influences evoke different processes at the same time due to the coupling of all LHP components in a loop. However, the complex

operating characteristics of the LHP can be comprehended by regarding the static characteristics of the LHP in the form of the steady-state operating temperature (SSOT) as a function of the heat load and the sink temperature. Thus, the equilibrium point of the LHP system in a steady state depends on the external influences. The natural SSOT over the heat load $\dot{Q}_{ev}$ for a given sink temperature T_{sk} forms a straight line if the ambient temperature T_{amb} in the surroundings of the LHP is lower than T_{sk}. In contrast, the LHP-typical U-shaped curve of the SSOT in Fig. 3.9 is generated if T_{amb} is higher than T_{sk}. In this case, the heat flow from the surroundings has an essential influence on the LL. [Chu03]

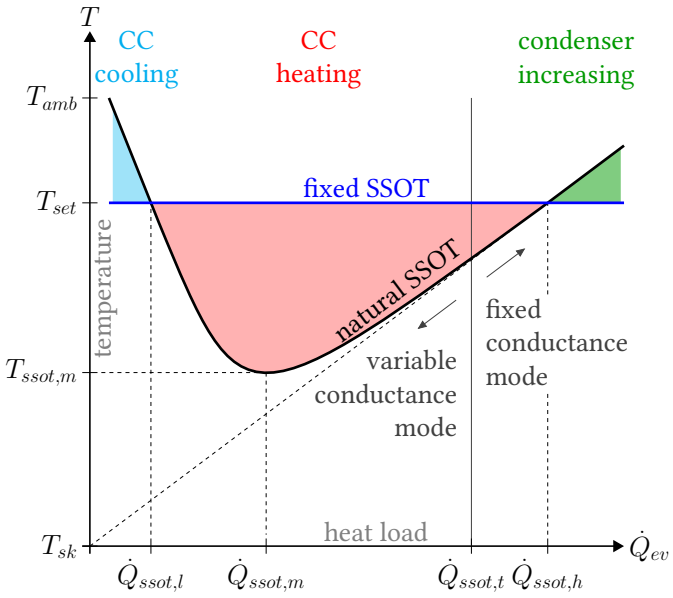

Figure 3.9: Typical curve of the steady-state operating temperature (SSOT) of an LHP over the heat load $\dot{Q}_{ev}$ for a sink temperature T_{sk} below the ambient temperature T_{amb} (cf. [Ku08], [Chu03])

Following the graph from the left to the right, a low heat load $\dot{Q}_{ev}$ causes little liquid to evaporate in the evaporator. Thus, the menisci in the primary wick generate low capillary forces, and the mass flow rates in the VL as well as the LL are small. The subcooled liquid enters the LL from the condenser at almost the temperature T_{sk} of the heat sink. As the liquid flows slowly through the LL, the rather large temperature difference to the surroundings compared to the conditions at the VL heats up the liquid since the ambient temperature T_{amb} is higher than the sink temperature T_{sk}. Consequently, the liquid reaches the CC with less subcooling, i.e. with a higher temperature, than when it left the condenser. Therefore, the liquid in the LL contributes naturally to an increased CC temperature and SSOT (black line) accordingly. The higher the heat load, the higher the evaporation, and the higher the mass flow rates. Hence, the residence time of the liquid in the LL decreases leaving less time to absorb heat from the surroundings. More subcooling shifts the energy balance in the CC to a lower natural SSOT. At the same time with more vapor generated, the liquid-vapor interface

in the condenser proceeds in the direction of the condenser outlet. The length for subcooling between the liquid-vapor interface and the condenser outlet shrinks. With not enough space for cooling the liquid down to near sink temperature, the liquid leaves the condenser with higher temperatures, which finally contribute to a rising natural SSOT. [Ku99]

At the heat load $\dot{Q}_{ssot,m}$, the minimal natural SSOT $T_{ssot,m}$ is reached caused by a low condenser outlet temperature and a low mass flow-dependent heat gain at the LL. When the heat load passes $\dot{Q}_{ssot,t}$, the LHP operation mode changes from a variable thermal conductance to a fixed thermal conductance. The LHP operation mode refers to the overall thermal conductance of the LHP, which depends on the overall heat transfer coefficient and the difference between the SSOT and the sink temperature. In the *variable conductance mode*, not only condensation but also subcooling takes place in the condenser. Hence, the condenser is not fully utilized, and the LHP has not yet reached its maximal heat transport capability. In the *fixed conductance mode*, the liquid-vapor interface is located at the condenser outlet leaving no space for subcooling. The LHP operates with its maximal overall heat transfer coefficient and the natural SSOT rises linearly with increasing heat load. [Chu03]

In Fig. 3.9, the extension of the straight line of the natural SSOT in the fixed conductance mode intersects the temperature axis at the sink temperature. When the sink temperature changes, the slope of the natural SSOT in the fixed conductance mode stays the same since the overall heat transfer coefficient of an LHP is constant. Only the curve of the natural SSOT in the variable conductance mode changes. When the sink temperature rises toward the ambient temperature, the size of the area in the graph, in which the natural SSOT is in variable conductance mode, decreases, until the sink temperature passes the ambient temperature, and the LHP operates only in fixed conductance mode with a linear natural SSOT. [Chu03]

In order to control the natural SSOT at a fixed SSOT (blue line) at the setpoint temperature T_{set}, various actions are required depending on the amount of heat load at the evaporator [Ku08]. For heat loads between $\dot{Q}_{ssot,l}$ and $\dot{Q}_{ssot,h}$, the CC is heated to reach the fixed SSOT (red area). Typically, the LHP is designed for this area, where a control heater is sufficient to control the OT of the LHP actively at a desired setpoint temperature over the entire operating range of the given heat source. Then, the lowest heat load $\dot{Q}_{ssot,l}$ coincides with the minimal dissipated excess heat of the heat source on standby, and the highest heat load $\dot{Q}_{ssot,h}$ with the heat source operating at maximum power. The amount of necessary heat input to the CC from the control heater does not correspond to the distances between the natural and the fixed SSOT in Fig. 3.9 because of the dependencies of the mass flow rates on the heat load [Ku99]. If required by the operating conditions, the CC must be cooled (blue area) to keep the setpoint temperature for heat loads lower than $\dot{Q}_{ssot,l}$. From a practical point of view, the condenser would need to be enlarged constructively in the design process for heat loads higher than $\dot{Q}_{ssot,h}$ (green area) to loose the excessive heat to the heat sink while preventing the rise of the total temperature level of the LHP [Ku08].

3.3 Summary

In this chapter, the basics of thermodynamics, heat transfer, and multiphase systems have been introduced, which are relevant for the dynamical modeling of LHP-based heat transport systems. Starting from the fundamental laws of conservation, the elementary equations to describe the heat transfer in single- and multiphase systems have been stated, and the electrical analogy has been illustrated to facilitate the modeling process. On this basis, the LHP working principle has been elucidated, and the specific challenges of modeling and controlling the OT of the LHP have been identified. In the following chapters, these findings are considered in the development of adequate model-based control designs for LHP-based heat transport systems.

4 Nonlinear Model-Based Control Designs for Loop Heat Pipes

The core of this thesis is based on the physically motivated modeling of a conventional LHP for the subsequent model-based design of controllers for the control heater. Because of the different focuses of the LHP models in the literature on the characterization of the LHP's working principle and the design of LHP components, a new modeling approach is necessary, which concentrates on the fundamental LHP dynamics influenced by the system's inputs. By physically describing the system's dynamics based on the thermodynamic preliminaries in Sec. 3.1 with differential equations in an explicit form, a dynamical state-space model according to Def. 2.1 is established that connects the system's inputs with its outputs. Based on this low-dimensional model, adequate controllers are designed methodically for an improved performance and an easy adaption to different thermal control applications on ground, in the air, or in space.

The investigated LHP in this thesis with its considered actuators and sensors is used for the thermal control of LCTs in space applications, as introduced in Chapter 1. Under consideration of the limited access to the interior of the LHP, the model-based control design is oriented toward the mentioned circumstances. In particular, the internal structures of the CC and the evaporator are often known to a limited extent to the LHP end user, and their direct determination is only achievable with great effort. Thus, related internal parameters, which are used in some of the transient LHP models in the literature (see Sec. 2.2), are not always known to the LHP end user and the thermal control engineer, respectively. However, for the desired state-space modeling of an LHP, an alternative modeling approach is sufficient, in which as few model parameters as possible are included to be determined from the outside with the available measurements. In addition, the model equations are designed in such a modular way that they can be adapted easily to applications with different actuator and sensor concepts.

For the specific hardware concept in this thesis, the input and output variables of the subsequent dynamical LHP state-space model are adapted to the available actuators and sensors. This state-space model was introduced in [GSO+20] and extended in [GMSH20b] to model the system dynamics between all actuators and sensors. The locations of these actuators and sensors on the considered LHP are shown in Fig. 4.1.

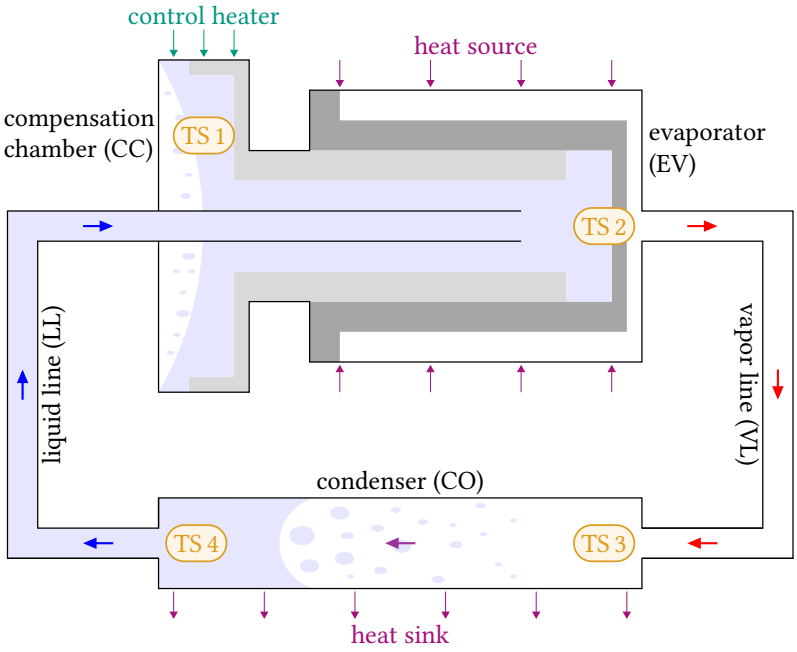

Figure 4.1: Structure of an LHP with the temperature sensors (TS 1 to TS 4) in orange, the actuator in green, and the external influences in violet

The LHP is equipped with four superficial temperature sensors TS 1 to TS 4 to monitor the LHP operation. For the desired OT control (see Sec. 3.2.2), one superficial control heater is installed on the CC. The operating range of the considered LHP is defined by the value ranges of the input variables, which are the dissipated heat $\dot{Q}_{hs}$ of the heat source, the sink temperature T_{sk} at the condenser, and the control heater output $\dot{Q}_{cc}$ at the CC. Their value ranges according to LCT specifications are listed in Table 4.1.

Variable	Minimum value	Maximum value
$\dot{Q}_{cc}$	0 W	10 W
$\dot{Q}_{hs}$	20 W	100 W
T_{sk}	−25 °C	15 °C

Table 4.1: Considered operating range of the running LHP given by the value ranges of the control heater output $\dot{Q}_{cc}$, the dissipated heat $\dot{Q}_{hs}$ of the heat source, and the sink temperature T_{sk}

In the considered operating range, the LHP works in the variable conductance mode since the condenser is never fully used (see Sec. 3.2.2). To maintain the OT at a desired setpoint temperature in this operating range, it is sufficient to heat the CC with the control heater. The control heater enables the suppression of the disturbances of the LHP, namely the sink

temperature T_{sk} and the dissipated heat $\dot{Q}_{hs}$ of the heat source. The disturbances influence not only the curvature of the natural SSOT in Fig. 3.9, but also the transient behavior of the temperatures during LHP operation. Thus, the LHP can be described as a controlled system with one input, four outputs, and two disturbances (see Fig. 4.2).

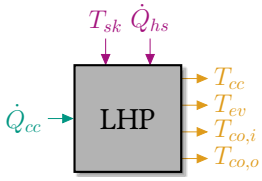

Figure 4.2: System view of an LHP with the input variable $\dot{Q}_{cc}$ in green, the output variables T_{cc}, T_{ev}, $T_{co,i}$, and $T_{co,o}$ in orange, and the disturbance variables T_{sk} and $\dot{Q}_{hs}$ in violet

The complex dynamics of the LHP require the combination of different engineering areas to derive a suitable control model of this multiphase heat transport system in state-space form. Besides the description of the thermodynamic processes with the fundamental laws of thermodynamics, the heat transfer presents another important domain. The consideration of the different heat transfer modes needs to be included to reproduce the measured temperatures of the LHP precisely. Because of the essential movement of the working fluid, flow dynamics have an impact on the system's behavior and play a major role in capturing the two-phase heat transport process of the LHP. By combining the basic equations of all domains, the LHP model reproduces the response of the measured temperatures to input changes accurately to be used in the model-based control design with an improved controller performance compared to the state-of-the-art controllers. In addition to the desired control design, the model is able to track the liquid-vapor interface in the condensation area as one of the important indicators of the operating status of the LHP and the occurrence of undesirable phenomena (see Sec. 2.4).

To separate the various dynamics for the modeling process, the LHP is divided into individual subsystems in the next section. For each subsystem, adequate model equations are derived from the fundamental laws of conservation and the balance equations in Sec. 3.1 to build the state-space model of the LHP. Subsequently, the control design based on the introduced state-space model is presented.

4.1 Complex Dynamical Modeling

A first step to facilitate the complex dynamical modeling is the delimitation of the multiphase LHP system into smaller subsystems as explained in Sec. 3.1.3. Hence, the LHP structure in Fig. 4.3 is divided into five subsystems. These subsystems include the two-phase compensation chamber (CC) in red, the single-phase evaporator (EV) in green, the single-phase vapor line (VL) in orange, the single-phase liquid line (LL) in blue, and the two-phase condenser (CO) in violet.

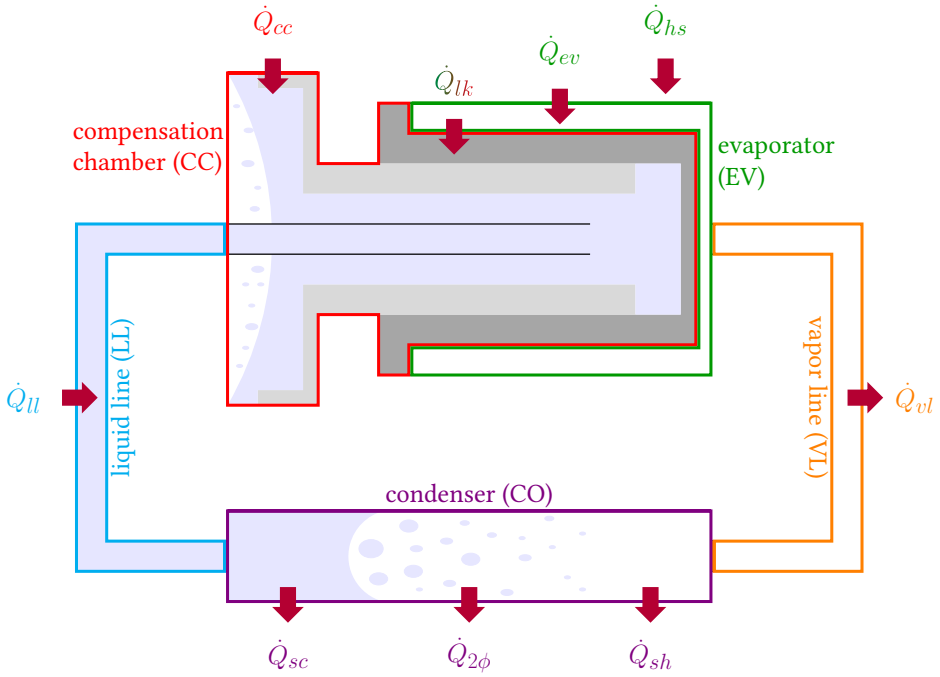

Figure 4.3: LHP subsystems with their corresponding main heat flows

The division of the LHP system into these five subsystems is based on the boundaries between the LHP components except for the boundary between the CC and the evaporator subsystems. In the CC-evaporator assembly, where the capillary pump of the LHP is situated, the boundary between both subsystems coincides with the liquid-vapor interface at the outer surface of the primary wick. In this way, the modeling of the LHP has the following advantage: The CC subsystem includes the evaporator core since they both reach the same absolute pressure during steady LHP operation [Ku99], while the evaporator subsystem is only vapor-filled.

In addition to the colored boundaries of the LHP subsystems, the fundamental heat flows across the boundaries of each subsystem are presented in Fig. 4.3. The heat load $\dot{Q}_{ev}$ is applied to the evaporator subsystem by the heat source and results from the dissipated heat $\dot{Q}_{hs}$. Besides the heat input $\dot{Q}_{cc}$ by the control heater to the CC subsystem, the heat leak $\dot{Q}_{lk}$ is exchanged between the CC subsystem and the evaporator subsystem. Furthermore, both transport lines exchange heat with the surroundings considering an ambient temperature between the liquid and the vapor temperatures (see Sec. 3.2.2). The cold liquid from the condenser is heated by the heat flow $\dot{Q}_{ll}$ to the LL. At the VL, the temperature of the superheated vapor is reduced by the heat flow $\dot{Q}_{vl}$. The total heat flow from the condenser to the heat sink results from the sum of the heat flows $\dot{Q}_{sh}$ and $\dot{Q}_{sc}$ in the superheated and the subcooled single-phase regions, and the heat flow $\dot{Q}_{2\phi}$ in the two-phase condensation region.

4.1.1 Model Assumptions

Before the individual equations of the subsystems are established, general assumptions are stated in this section for modeling the LHP with the objective of a model-based control design based on Def. 2.1. In the course of the model description in the next sections, these assumptions are referenced at the respective locations in the text to highlight their impact and necessity.

Assumption 4.1. *The sink temperature T_{sk} is considered to be spatially constant.*

Assumption 4.2. *The thermal and the fluid inertia are neglected for the single-phase subsystems.*

Assumption 4.3. *The homogeneous fluid in the CC and the two-phase region of the condenser is in saturation state at all times.*

Assumption 4.4. *The vapor is assumed to be an ideal gas, the liquid is incompressible.*

Assumption 4.5. *The physical properties of the working fluid are functions of the respective subsystem temperatures in the operating point (OP).*

Assumption 4.6. *The homogeneous flow regime of the liquid working fluid in the pipes of the LHP is laminar in the considered operating range.*

Discussion of the Assumptions

Assumption 4.1 is based on experimental data from the LHP test bench described in [MKHW19]. The data show that the temperature gradient along the condenser length varies only by few degrees Kelvin. Assumption 4.2 applies to the single-phase subsystems with a small pipe diameter, i.e. the evaporator and the transport lines. It is assumed that neither heat nor mass are stored in these subsystems since the corresponding temperature measurements show almost no delay between the inlet and the outlet of each subsystem compared to the temperature dynamics[3]. Assumption 4.3 is ensured by the LHP manufacturer through the size of the CC and the fluid inventory of the LHP. For a reliable operation in the considered operating range, an LHP is charged with such an amount of working fluid that the CC is always filled with liquid and vapor in saturation state under all operating conditions [Ku99]. It follows from Assumption 4.4 that the density of the liquid and the specific heat capacities of the liquid and the vapor are assumed to be independent of the pressure. In addition to Assumption 4.5, the temperature derivatives of the physical properties of the working fluid are neglected, as their temperature dependencies are small in the considered LHP operating range. This does not hold for the temperature derivative of the vapor density to consider the vapor's compressibility. Assumption 4.6 is verified in the numerical LHP simulation of [MKHW19].

[3] A delay on the order of seconds versus a settling time on the order of a quarter of an hour according to measurements.

4.1.2 Compensation Chamber

The CC has an important role when it comes to the OT control of the LHP (see Sec. 3.2.1). In this LHP component, the subcooling of the liquid returning from the condenser meets the heat input by the heat leak of the evaporator. The resulting temperature level in the CC governs the OT of the LHP. To control this temperature level, the additional heat input by the control heater on the CC is adapted, while the continuous heat transport between the heat source and the heat sink is maintained. During LHP operation, the primary and the secondary wick in the CC subsystem are assumed to be soaked with liquid at all times, i.e. the fluid enters and leaves the CC in liquid state. The CC contains both a liquid and a vapor phase in saturation state (Assumption 4.3). In order to model the dynamics of the CC, it is common practice to evaluate the mass and the energy balance of the fluid inside the two-phase CC subsystem (see [LPDJ07], [VR08], [MKHW19]). The difference of these CC modeling approaches lies in the individual establishment of the balance equations and the numerical solution method of the distributed-parameter systems (see Sec. 2.2). In this thesis, an own modeling approach with lumped parameters is derived in detail based on the mentioned CC submodels to obtain the necessary model accuracy with regard to the desired low-dimensional state-space form.

The total mass $m_{cc}^{2\phi}(t)$ in the two-phase CC is defined by the following sum of the liquid and the vapor masses $m_{cc}^{l}(t)$ and $m_{cc}^{v}(t)$:

$$m_{cc}^{2\phi}(t) = m_{cc}^{l}(t) + m_{cc}^{v}(t). \tag{4.1}$$

The mass balance in (3.18) implies that the change of the total mass $m_{cc}^{2\phi}(t)$ equals the difference of the mass flows across the boundary of the CC subsystem. Therefore, the CC mass balance is described by the following equation:

$$\frac{\mathrm{d}m_{cc}^{2\phi}(t)}{\mathrm{d}t} = \dot{m}^{l}(t) - \dot{m}^{v}(t), \tag{4.2}$$

where $\dot{m}^{l}(t)$ denotes the liquid mass flow rate, which enters the CC, and $\dot{m}^{v}(t)$ denotes the mass flow rate that evaporates at the outer surface of the primary wick and leaves the CC.

The liquid and the vapor mass $m_{cc}^{l}(t)$ and $m_{cc}^{v}(t)$ in the CC are expressed by

$$m_{cc}^{l}(t) = \rho_{cc}^{l} \cdot V_{cc}^{l}(t), \tag{4.3}$$

$$m_{cc}^{v}(t) = \rho_{cc}^{v}(t) \cdot V_{cc}^{v}(t), \tag{4.4}$$

with the corresponding densities ρ_{cc}^{l} and $\rho_{cc}^{v}(t)$[4] (see Assumption 4.5). The liquid volume $V_{cc}^{l}(t)$ and the vapor volume $V_{cc}^{v}(t)$ in the CC are determined by their volume fraction ratio $\beta(t)$:

$$V_{cc}^{l}(t) = \beta(t) \cdot V_{cc}, \tag{4.5}$$

$$V_{cc}^{v}(t) = \big(1 - \beta(t)\big) \cdot V_{cc}. \tag{4.6}$$

[4] The time dependency of $\rho_{cc}^{v}(t)$ results from its temperature dependency, i.e. $\rho_{cc}^{v}\big(T(t)\big)$, which is abbreviated to ease notation.

Their sum equals the total fluid volume V_{cc} in the CC subsystem:

$$V_{cc} = V_{cc}^{l}(t) + V_{cc}^{v}(t). \tag{4.7}$$

According to Assumption 4.4, the ideal gas law (3.76) is applied to the vapor density $\rho_{cc}^{v}(t)$ of the CC subsystem:

$$\rho_{cc}^{v}(t) = \frac{p_{cc}(t)}{RT_{cc}(t)}. \tag{4.8}$$

Hence, the time derivative of $\rho_{cc}^{v}(t)$ yields:

$$\frac{\mathrm{d}\rho_{cc}^{v}(t)}{\mathrm{d}t} = \frac{1}{RT_{cc}(t)} \cdot \frac{\mathrm{d}p_{cc}(t)}{\mathrm{d}t} - \frac{p_{cc}(t)}{R\big(T_{cc}(t)\big)^{2}} \cdot \frac{\mathrm{d}T_{cc}(t)}{\mathrm{d}t}, \tag{4.9}$$

where the time derivative of the saturation pressure $p_{cc}(t)$ on the right hand side is expressed by its temperature derivative:

$$\frac{\mathrm{d}\rho_{cc}^{v}(t)}{\mathrm{d}t} = \frac{1}{RT_{cc}(t)} \cdot \frac{\mathrm{d}p_{cc}(t)}{\mathrm{d}T_{cc}(t)} \cdot \frac{\mathrm{d}T_{cc}(t)}{\mathrm{d}t} - \frac{p_{cc}(t)}{R\big(T_{cc}(t)\big)^{2}} \cdot \frac{\mathrm{d}T_{cc}(t)}{\mathrm{d}t}, \tag{4.10}$$

By inserting (4.8) and the Clapeyron equation (3.72) into (4.10), the time derivative of $\rho_{cc}^{v}(t)$ is defined as a function of the time derivative of $T_{cc}(t)$:

$$\frac{\mathrm{d}\rho_{cc}^{v}(t)}{\mathrm{d}t} = \left(\frac{\Delta h_{cc}^{v} \rho_{cc}^{l} \rho_{cc}^{v}(t)}{R\big(T_{cc}(t)\big)^{2}\big(\rho_{cc}^{l} - \rho_{cc}^{v}(t)\big)} - \frac{\rho_{cc}^{v}(t)}{T_{cc}(t)} \right) \cdot \frac{\mathrm{d}T_{cc}(t)}{\mathrm{d}t}, \tag{4.11}$$

where Δh_{cc}^{v} denotes the specific heat of evaporation at a fixed T_{cc}. With (4.3), (4.4), (4.7), and (4.11), the CC mass balance in (4.2) takes the following form:

$$\begin{aligned} &\big(\rho_{cc}^{l} - \rho_{cc}^{v}(t)\big) \cdot \frac{\mathrm{d}\beta(t)}{\mathrm{d}t} \cdot V_{cc} \\ &\quad + \left(\frac{\Delta h_{cc}^{v} \rho_{cc}^{l} \rho_{cc}^{v}(t)}{R\big(T_{cc}(t)\big)^{2}\big(\rho_{cc}^{l} - \rho_{cc}^{v}(t)\big)} - \frac{\rho_{cc}^{v}(t)}{T_{cc}(t)} \right) \cdot \frac{\mathrm{d}T_{cc}(t)}{\mathrm{d}t} \cdot \big(1 - \beta(t)\big) \cdot V_{cc} \\ &\quad = \dot{m}^{l}(t) - \dot{m}^{v}(t). \end{aligned} \tag{4.12}$$

Thus, the change of the mass in the CC in (4.12) is a function of the homogeneous saturation temperature $T_{cc}(t)$ and the volume fraction ratio $\beta(t)$, their change rates, and the vapor density $\rho_{cc}^{v}(t)$.

Based on the first law of thermodynamics in (3.11), the thermal energy balance of the CC is given by

$$\frac{\mathrm{d}H_{cc}^{l}(t)}{\mathrm{d}t} + \frac{\mathrm{d}H_{cc}^{v}(t)}{\mathrm{d}t} - \frac{\mathrm{d}}{\mathrm{d}t}\big(p_{cc}(t) \cdot V_{cc}\big) = \dot{H}_{cc,i}^{l}(t) - \dot{H}_{cc}^{l}(t) + \dot{Q}_{cc}(t) + \dot{Q}_{lk}(t). \tag{4.13}$$

In (4.13), the left-hand side (LHS) describes the change of the internal energy $U_{cc}(t)$ in the CC. The moving boundary work defined in (3.7) is required for pushing the fluid out of the

CC. Following (3.8), (3.81), and (3.82), the enthalpies $H^l_{cc}(t)$ and $H^v_{cc}(t)$ of the liquid and the vapor phase are established as follows:

$$\begin{aligned} H^l_{cc}(t) &= m^l_{cc}(t) \cdot h^l_{cc}(t) \\ &= \rho^l_{cc} \cdot \beta(t) \cdot V_{cc} \cdot \left(h^l_{ref} + \bar{c}^l_{cc,ref} \cdot (T_{cc}(t) - T_{ref})\right), \end{aligned} \tag{4.14}$$

$$\begin{aligned} H^v_{cc}(t) &= m^v_{cc}(t) \cdot h^v_{cc}(t) \\ &= \rho^v_{cc}(t) \cdot \left(1 - \beta(t)\right) \cdot V_{cc} \cdot \left(h^l_{ref} + \bar{c}^l_{cc,ref} \cdot (T_{cc}(t) - T_{ref}) + \Delta h^v_{cc}\right). \end{aligned} \tag{4.15}$$

The right-hand side (RHS) of (4.13) describes the energy flows across the boundary of the subsystem as depicted in Fig. 4.3. According to (3.9), the enthalpy flow rates $\dot{H}^l_{cc,i}(t)$ at the CC inlet temperature $T_{cc,i}(t)$ and $\dot{H}^l_{cc}(t)$ at $T_{cc}(t)$ in and out of the CC depend on the corresponding mass flow rates $\dot{m}^l$ and $\dot{m}^v$:

$$\dot{H}^l_{cc,i}(t) = \dot{m}^l(t) \cdot h^l_{cc,i}(t) = \dot{m}^l(t) \cdot \left(h^l_{ref} + \bar{c}^l_{cc,i,ref} \cdot (T_{cc,i}(t) - T_{ref})\right), \tag{4.16}$$

$$\dot{H}^l_{cc}(t) = \dot{m}^v(t) \cdot h^l_{cc}(t) = \dot{m}^v(t) \cdot \left(h^l_{ref} + \bar{c}^l_{cc,ref} \cdot (T_{cc}(t) - T_{ref})\right). \tag{4.17}$$

The heat flow $\dot{Q}_{cc}(t)$ is applied to the CC by the control heater. The variable $\dot{Q}_{lk}(t)$ denotes the heat flow, which leaks from the evaporator subsystem at $T_{ev}(t)$ to the CC subsystem at $T_{cc}(t)$ by heat conduction through the wicks. This internal heat flow is approximated with the thermal resistance R_{lk} using (3.50) to

$$\dot{Q}_{lk} = \frac{1}{R_{lk}} \cdot \left(T_{ev}(t) - T_{cc}(t)\right). \tag{4.18}$$

With (4.14) and (4.15), the LHS of the CC energy balance equation (4.13) is rewritten:

$$\begin{aligned} \text{LHS:} \quad & \rho^l_{cc} \cdot \frac{\mathrm{d}\beta(t)}{\mathrm{d}t} \cdot V_{cc} \cdot \left(h^l_{ref} + \bar{c}^l_{cc,ref} \cdot (T_{cc}(t) - T_{ref})\right) \\ & + \rho^l_{cc} \cdot \beta(t) \cdot V_{cc} \cdot \bar{c}^l_{cc,ref} \cdot \frac{\mathrm{d}T_{cc}(t)}{\mathrm{d}t} \\ & + \frac{\mathrm{d}\rho^v_{cc}(t)}{\mathrm{d}t} \cdot \left(1 - \beta(t)\right) \cdot V_{cc} \cdot \left(h^l_{ref} + \bar{c}^l_{cc,ref} \cdot (T_{cc}(t) - T_{ref}) + \Delta h^v_{cc}\right) \\ & - \rho^v_{cc}(t) \cdot \frac{\mathrm{d}\beta(t)}{\mathrm{d}t} \cdot V_{cc} \cdot \left(h^l_{ref} + \bar{c}^l_{cc,ref} \cdot (T_{cc}(t) - T_{ref}) + \Delta h^v_{cc}\right) \\ & + \rho^v_{cc}(t) \cdot \left(1 - \beta(t)\right) \cdot V_{cc} \cdot \bar{c}^l_{cc,ref} \cdot \frac{\mathrm{d}T_{cc}(t)}{\mathrm{d}t} - V_{cc} \cdot \frac{\mathrm{d}p_{cc}(t)}{\mathrm{d}t}. \end{aligned} \tag{4.19}$$

The time derivative of the saturation pressure $p_{cc}(t)$ can be expressed by its temperature derivative. Inserting (3.72) and (4.11) into (4.19), the LHS yields:

$$\begin{aligned}\text{LHS:}\quad & \left[\left(\rho_{cc}^{l}\cdot\beta(t)+\rho_{cc}^{v}(t)\cdot\big(1-\beta(t)\big)\right)\cdot\bar{c}_{cc,ref}^{l}-\frac{\Delta h_{cc}^{v}\rho_{cc}^{l}\rho_{cc}^{v}(t)}{T_{cc}(t)\big(\rho_{cc}^{l}-\rho_{cc}^{v}(t)\big)}\right]\cdot V_{cc}\\ &\cdot\frac{\mathrm{d}T_{cc}(t)}{\mathrm{d}t}+\big(\rho_{cc}^{l}-\rho_{cc}^{v}(t)\big)\cdot\frac{\mathrm{d}\beta(t)}{\mathrm{d}t}\cdot V_{cc}\cdot\big(h_{ref}^{l}+\bar{c}_{cc,ref}^{l}\cdot(T_{cc}(t)-T_{ref})\big)\\ &-\ \rho_{cc}^{v}(t)\cdot\frac{\mathrm{d}\beta(t)}{\mathrm{d}t}\cdot V_{cc}\cdot\Delta h_{cc}^{v}+\left(\frac{\Delta h_{cc}^{v}\rho_{cc}^{l}\rho_{cc}^{v}(t)}{R\big(T_{cc}(t)\big)^{2}\big(\rho_{cc}^{l}-\rho_{cc}^{v}(t)\big)}-\frac{\rho_{cc}^{v}(t)}{T_{cc}(t)}\right)\\ &\cdot\frac{\mathrm{d}T_{cc}(t)}{\mathrm{d}t}\cdot\big(1-\beta(t)\big)\cdot V_{cc}\cdot\big(h_{ref}^{l}+\bar{c}_{cc,ref}^{l}\cdot(T_{cc}(t)-T_{ref})+\Delta h_{cc}^{v}\big)\,. \end{aligned}\tag{4.20}$$

The RHS of the CC energy balance equation (4.13) is reshaped with (4.16) and (4.17):

$$\begin{aligned}\text{RHS:}\quad & \dot{m}^{l}(t)\cdot\big(h_{ref}^{l}+\bar{c}_{cc,i,ref}^{l}\cdot(T_{cc,i}(t)-T_{ref})\big)\\ &-\ \dot{m}^{v}(t)\cdot\big(h_{ref}^{l}+\bar{c}_{cc,ref}^{l}\cdot(T_{cc}(t)-T_{ref})\big)+\dot{Q}_{cc}(t)+\dot{Q}_{lk}(t).\end{aligned}\tag{4.21}$$

By inserting the CC mass balance equation (4.12) into (4.21), the RHS is given by

$$\begin{aligned}\text{RHS:}\quad & \dot{m}^{l}(t)\cdot\big(h_{ref}^{l}+\bar{c}_{cc,i,ref}^{l}\cdot(T_{cc,i}(t)-T_{ref})\big)-\left[\dot{m}^{l}(t)-\big(\rho_{cc}^{l}-\rho_{cc}^{v}(t)\big)\cdot\frac{\mathrm{d}\beta(t)}{\mathrm{d}t}\right.\\ &\left.\cdot V_{cc}-\left(\frac{\Delta h_{cc}^{v}\rho_{cc}^{l}\rho_{cc}^{v}(t)}{R\big(T_{cc}(t)\big)^{2}\big(\rho_{cc}^{l}-\rho_{cc}^{v}(t)\big)}-\frac{\rho_{cc}^{v}(t)}{T_{cc}(t)}\right)\cdot\frac{\mathrm{d}T_{cc}(t)}{\mathrm{d}t}\cdot\big(1-\beta(t)\big)\cdot V_{cc}\right]\\ &\cdot\big(h_{ref}^{l}+\bar{c}_{cc,ref}^{l}\cdot(T_{cc}(t)-T_{ref})\big)+\dot{Q}_{cc}(t)+\dot{Q}_{lk}(t)\end{aligned}\tag{4.22}$$

and

$$\begin{aligned}\text{RHS:}\quad & \dot{m}^{l}(t)\cdot\bar{c}_{cc,i,cc}^{l}\cdot\big(T_{cc,i}(t)-T_{cc}(t)\big)+\left[\big(\rho_{cc}^{l}-\rho_{cc}^{v}(t)\big)\cdot\frac{\mathrm{d}\beta(t)}{\mathrm{d}t}\cdot V_{cc}\right.\\ &\left.+\left(\frac{\Delta h_{cc}^{v}\rho_{cc}^{l}\rho_{cc}^{v}(t)}{R\big(T_{cc}(t)\big)^{2}\big(\rho_{cc}^{l}-\rho_{cc}^{v}(t)\big)}-\frac{\rho_{cc}^{v}(t)}{T_{cc}(t)}\right)\cdot\frac{\mathrm{d}T_{cc}(t)}{\mathrm{d}t}\cdot\big(1-\beta(t)\big)\cdot V_{cc}\right]\\ &\cdot\big(h_{ref}^{l}+\bar{c}_{cc,ref}^{l}\cdot(T_{cc}(t)-T_{ref})\big)+\dot{Q}_{cc}(t)+\dot{Q}_{lk}(t),\end{aligned}\tag{4.23}$$

respectively. By recombining (4.20) and (4.23), the following equation is established:

$$\begin{aligned}&\left[\left(\rho_{cc}^{l}\cdot\beta(t)+\rho_{cc}^{v}(t)\cdot\big(1-\beta(t)\big)\right)\cdot\bar{c}_{cc,ref}^{l}-\frac{\Delta h_{cc}^{v}\rho_{cc}^{l}\rho_{cc}^{v}(t)}{T_{cc}(t)\big(\rho_{cc}^{l}-\rho_{cc}^{v}(t)\big)}\right.\\ &\left.+\left(\frac{\Delta h_{cc}^{v}\rho_{cc}^{l}\rho_{cc}^{v}(t)}{R\big(T_{cc}(t)\big)^{2}\big(\rho_{cc}^{l}-\rho_{cc}^{v}(t)\big)}-\frac{\rho_{cc}^{v}(t)}{T_{cc}(t)}\right)\cdot\big(1-\beta(t)\big)\cdot\Delta h_{cc}^{v}\right]\\ &\cdot V_{cc}\cdot\frac{\mathrm{d}T_{cc}(t)}{\mathrm{d}t}-\rho_{cc}^{v}(t)\cdot\frac{\mathrm{d}\beta(t)}{\mathrm{d}t}\cdot V_{cc}\cdot\Delta h_{cc}^{v}\\ &=\dot{m}^{l}(t)\cdot\bar{c}_{cc,i,cc}^{l}\cdot\big(T_{cc,i}(t)-T_{cc}(t)\big)+\dot{Q}_{cc}(t)+\dot{Q}_{lk}(t).\end{aligned}\tag{4.24}$$

Finally, the differential equations (4.12) and (4.24) are rearranged resulting in the time derivatives of the CC temperature $T_{cc}(t)$ and the volume fraction ratio $\beta(t)$:

$$\begin{aligned}\frac{\mathrm{d}T_{cc}(t)}{\mathrm{d}t} = &\frac{1}{C_{cc}(t)} \cdot \Bigg[\dot{m}^l(t) \cdot \bar{c}^l_{cc,i,cc} \cdot \big(T_{cc,i}(t) - T_{cc}(t)\big) + \dot{Q}_{cc}(t) + \dot{Q}_{lk}(t) \\ &+ \frac{\rho^v_{cc}(t)\Delta h^v_{cc}}{\rho^l_{cc} - \rho^v_{cc}(t)} \cdot \big(\dot{m}^l(t) - \dot{m}^v(t)\big)\Bigg], \end{aligned} \tag{4.25}$$

$$\begin{aligned}\frac{\mathrm{d}\beta(t)}{\mathrm{d}t} = &\frac{1}{V_{cc}\big(\rho^l_{cc} - \rho^v_{cc}(t)\big)} \cdot \big[\dot{m}^l(t) - \dot{m}^v(t) \\ &- \left(\frac{\Delta h^v_{cc}\rho^l_{cc}\rho^v_{cc}(t)}{R\big(T_{cc}(t)\big)^2\big(\rho^l_{cc} - \rho^v_{cc}(t)\big)} - \frac{\rho^v_{cc}(t)}{T_{cc}(t)}\right) \cdot \big(1 - \beta(t)\big) \cdot V_{cc} \cdot \frac{\mathrm{d}T_{cc}(t)}{\mathrm{d}t}\Bigg], \end{aligned} \tag{4.26}$$

with the thermal capacity

$$\begin{aligned}C_{cc}(t) = &\Bigg[\Big(\rho^l_{cc} \cdot \beta(t) + \rho^v_{cc}(t) \cdot \big(1 - \beta(t)\big)\Big) \cdot \bar{c}^l_{cc,ref} - \frac{\Delta h^v_{cc}\rho^l_{cc}\rho^v_{cc}(t)}{T_{cc}(t)\big(\rho^l_{cc} - \rho^v_{cc}(t)\big)} \\ &+ \left(\frac{\Delta h^v_{cc}\rho^l_{cc}\rho^v_{cc}(t)}{R\big(T_{cc}(t)\big)^2\big(\rho^l_{cc} - \rho^v_{cc}(t)\big)} - \frac{\rho^v_{cc}(t)}{T_{cc}(t)}\right) \cdot \big(1 - \beta(t)\big) \cdot \Delta h^v_{cc} \\ &+ \frac{\rho^v_{cc}(t)\Delta h^v_{cc}}{\rho^l_{cc} - \rho^v_{cc}(t)} \cdot \left(\frac{\Delta h^v_{cc}\rho^l_{cc}\rho^v_{cc}(t)}{R\big(T_{cc}(t)\big)^2\big(\rho^l_{cc} - \rho^v_{cc}(t)\big)} - \frac{\rho^v_{cc}(t)}{T_{cc}(t)}\right) \cdot \big(1 - \beta(t)\big)\Bigg] \cdot V_{cc}. \end{aligned} \tag{4.27}$$

4.1.3 Evaporator

The closest LHP component to the heat source is the evaporator. The liquid working fluid from the CC is evaporated in the primary wick in the evaporator body. Because of the capillary effect, menisci in the pores of the primary wick form themselves to drive the working fluid through the LHP system. Due to the chosen delimitation in Fig. 4.3, the evaporator subsystem contains only a single phase of superheated vapor. Following the first law of thermodynamics in (3.11), the thermal energy balance of the evaporator subsystem yields

$$\frac{\mathrm{d}U_{ev}(t)}{\mathrm{d}t} = \dot{m}^l(t) \cdot h^l_{cc}(t) - \dot{m}^v(t) \cdot h^v_{ev}(t) + \dot{Q}_{ev}(t) - \dot{Q}_{lk}(t). \tag{4.28}$$

In the evaporator subsystem, the enthalpy flows are determined by the incoming mass flow $\dot{m}^l(t)$ of the liquid from the CC subsystem, which evaporates instantly at the liquid-vapor interface in the primary wick, and the outgoing mass flow $\dot{m}^v(t)$ of the vapor. The heat flows across the boundary of the evaporator subsystem include the leaving heat leak $\dot{Q}_{lk}(t)$ and the incoming heat flow $\dot{Q}_{ev}(t)$ from the heat source.

Following Assumption 4.2, neither mass nor heat are stored in the evaporator subsystem. Hence, the incoming and outgoing mass flow rates $\dot{m}^l$ and $\dot{m}^v$ are the same. Since the transported amount of material is determined by the evaporation process [Ses19, p. 29], the

equation to describe the vapor mass flow rate $\dot{m}^v(t)$ is derived from the steady-state energy balance of the evaporator subsystem:

$$0 = \dot{m}^v(t) \cdot h^l_{cc}(t) - \dot{m}^v(t) \cdot h^v_{ev}(t) + \dot{Q}_{ev}(t) - \dot{Q}_{lk}(t), \tag{4.29}$$

$$\begin{aligned} 0 = \dot{m}^v(t) \cdot \big[& h^l_{ref} + \bar{c}^l_{cc,ref} \cdot (T_{cc} - T_{ref}) - \big(h^l_{ref} + \bar{c}^l_{ev,s,ref} \cdot (T_{ev,s} - T_{ref}) \\ & + \Delta h^v_{ev} + \bar{c}^v_{ev,ev,s} \cdot (T_{ev} - T_{ev,s}) \big) \big] + \dot{Q}_{ev}(t) - \dot{Q}_{lk}(t), \end{aligned} \tag{4.30}$$

with the mean evaporator temperature $T_{ev}(t)$ and the specific heat of evaporation Δh^v_{ev} at the saturation temperature $T_{ev,s}$. Hence, the equation of the vapor mass flow rate $\dot{m}^v(t)$ is given by

$$\dot{m}^v(t) = \frac{\dot{Q}_{ev}(t) - \dot{Q}_{lk}(t)}{\bar{c}^l_{ev,s,cc} \cdot \big(T_{ev,s}(t) - T_{cc}(t)\big) + \Delta h^v_{ev} + \bar{c}^v_{ev,ev,s} \cdot \big(T_{ev}(t) - T_{ev,s}(t)\big)}. \tag{4.31}$$

According to (3.74), the saturation temperature $T_{ev,s}(t)$ is a function of the saturation pressure $p_{ev}(t)$ in the evaporator subsystem since the temperature and the pressure are linked to each other in the saturation state:

$$T_{ev,s}(t) = -\frac{B_{wf}}{\ln\big(p_{ev}(t)\big) - A_{wf}} - C_{wf}, \tag{4.32}$$

where the specific parameters A_{wf}, B_{wf}, and C_{wf} of the working fluid are given in Appendix A.1. In contrast to [LPDJ07], the saturation pressure $p_{ev}(t)$ is calculated from the saturation pressure $p_{cc}(t)$ in the CC subsystem and not from the pressure in the VL to form an explicit equation system for the desired state-space form. This is due to the pressure drop along the loop between the evaporator and the CC, which is balanced by the pressure difference Δp_{ca} across the liquid-vapor interface caused by the capillary action in the pores of the primary wick. Thus, $p_{ev}(t)$ is given by

$$p_{ev}(t) = p_{cc}(t) + \Delta p_{ca}, \tag{4.33}$$

where $p_{cc}(t)$ results from (3.73):

$$p_{cc}(t) = \exp\left(A_{wf} - \frac{B_{wf}}{C_{wf} + T_{cc}(t)}\right). \tag{4.34}$$

The formula for the capillary pressure Δp_{ca} of the primary wick is given in [Ku99]:

$$\Delta p_{ca} = \frac{2\sigma \cos(\theta_c)}{R_p}, \tag{4.35}$$

with the surface tension σ of the liquid working fluid in saturation state (see Appendix A.1), the wick pore radius R_p, and the contact angle θ_c between the liquid-vapor interface and the wick. Formula (4.35) is based on the nonlinear partial differential *Young-Laplace equation* for artery wicks (see [Zoh16, p. 52]). The maximum capillary pressure is reached with the minimum contact angle $\theta_c = 0°$. As the pore radius R_p of the wick in the considered LHP is unknown, it is chosen as $R_p = 1\,\mu\text{m}$ by means of literature values [Chu03], [KG06], [RWH07].

While the saturated vapor flows through the vapor channels to the evaporator outlet, it absorbs more heat from the heat source, and its temperature rises. Thus, the lumped thermal resistance R_{sh} is introduced to describe the temperature difference between the superheated temperature $T_{ev}(t)$ and $T_{ev,s}(t)$, which itself is a function of the CC saturation temperature $T_{cc}(t)$. Based on Sec. 3.1.2, the respective thermal network of the evaporator subsystem, as depicted in Fig. 4.4, is constructed to derive the equation for $T_{ev}(t)$.

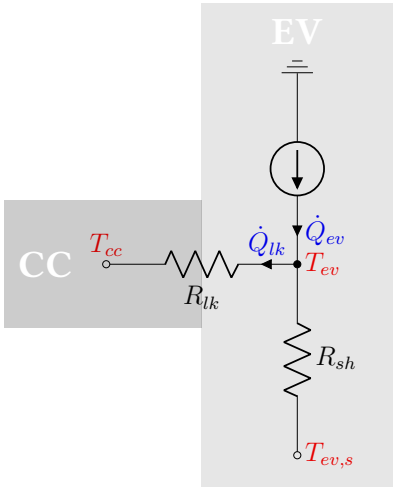

Figure 4.4: Thermal network representation of the evaporator subsystem

According to Kirchhoff's current law, the superheated mean evaporator temperature $T_{ev}(t)$ is calculated from the heat load $\dot{Q}_{ev}(t)$, the heat leak $\dot{Q}_{lk}(t)$ and the saturation temperature $T_{ev,s}(t)$:

$$T_{ev}(t) = T_{ev,s}(t) + R_{sh} \cdot \left(\dot{Q}_{ev}(t) - \dot{Q}_{lk}(t) \right). \tag{4.36}$$

The difference between $\dot{Q}_{ev}(t)$ and $\dot{Q}_{lk}(t)$ forms the heat flow, which evaporates the liquid in the primary wick to raise the vapor mass flow rate $\dot{m}^v(t)$ in (4.31). By inserting (4.18) into (4.36), the following equation is obtained:

$$T_{ev}(t) = T_{ev,s}(t) + R_{sh} \cdot \dot{Q}_{ev}(t) - \frac{R_{sh}}{R_{lk}} \cdot T_{ev}(t) + \frac{R_{sh}}{R_{lk}} \cdot T_{cc}(t). \tag{4.37}$$

Finally, the evaporator temperature $T_{ev}(t)$ is explicitly given by

$$T_{ev}(t) = \frac{R_{lk}}{R_{lk} + R_{sh}} \cdot \left(T_{ev,s}(t) + R_{sh} \cdot \dot{Q}_{ev}(t) + \frac{R_{sh}}{R_{lk}} \cdot T_{cc}(t) \right). \tag{4.38}$$

4.1.4 Transport Lines

The transport lines include the VL and the LL (see Fig. 4.3). These lines are made of thin pipes, which are typical features of LHP systems. Compared to compact heat pipe systems,

the separation of the fluid flows in LHPs makes it possible to transport the heat between the evaporator near the heat source and the condenser near the heat sink over several meters. Because of their great length in comparison with their width, the temperature gradients of the fluid in the transport lines caused by the heat exchanges with the surroundings are considered in the calculations of the temperatures in both subsystems.

Liquid Line

Especially in the LL, the heat input $\dot{Q}_{ll}(t)$ to the subcooled liquid has a significant impact on the behavior of the OT forming its characteristic U-shaped curve in Fig. 3.9, as explained in Sec. 3.2.2. According to Assumption 4.2, the thermal and fluid inertia in the transport lines are neglected since the transport delay is relatively small compared to the temperature dynamics due to the small diameter of the pipes. Therefore, additional states are not necessary, and the LHP state-space model is kept low-dimensional. The temperature gradient between the inlet and the outlet of a pipe is approximated by the logarithmic mean temperature difference ΔT_m in (3.60) instead. Thus, the temperature decreases exponentially along the LL, and the CC inlet temperature $T_{cc,i}(t)$, which corresponds to the LL outlet temperature, is calculated using (3.63):

$$T_{cc,i}(t) = T_{amb} + (T_{co,o}(t) - T_{amb}) \cdot \exp\left(-\frac{U_{ll}}{\dot{m}^l(t)\overline{c}^l_{cc,i,co,o}}\right), \tag{4.39}$$

where the thermal conductance U_{ll} of the LL is defined by

$$U_{ll} = k_{ll} \cdot A_{s,ll} = k_{ll} \cdot \pi \cdot D_p \cdot L_{ll}, \tag{4.40}$$

with the heat transfer coefficient k_{ll} of the LL, the heat transfer surface area $A_{s,ll}$ of the LL, the pipe diameter D_p of the transport lines, and the length L_{ll} of the LL. In the VL, the superheated vapor from the evaporator subsystem exchanges heat with the surroundings until it reaches the inlet of the condenser.

Vapor Line

The same approach for heat exchanger like the LL is applied to the VL considering the heat flow $\dot{Q}_{vl}(t)$. The inlet temperature $T_{co,i}(t)$ of the condenser is approximated by

$$T_{co,i}(t) = T_{amb} + (T_{ev}(t) - T_{amb}) \cdot \exp\left(-\frac{U_{vl}}{\dot{m}^v(t)\overline{c}^v_{ev,co,i}}\right). \tag{4.41}$$

Accordingly, the thermal conductance U_{vl} of the VL is given by

$$U_{vl} = k_{vl} \cdot A_{s,vl} = k_{vl} \cdot \pi \cdot D_p \cdot L_{vl}, \tag{4.42}$$

with the heat transfer coefficient k_{vl} of the VL, the heat transfer surface area $A_{s,vl}$ of the VL, and the length L_{vl} of the VL.

4.1.5 Condenser

In order to model the dynamic behavior in the two-phase condenser, the condenser is further subdivided into three regions. Following the flow direction in the loop, the first region in the condenser is the superheated region. As stated in Sec. 4.1.4, the superheated vapor enters the condenser coming from the VL and is cooled down to the saturation temperature of the condenser. Next to the superheated region, the saturated, two-phase region is located, whose saturation temperature and pressure are assumed to be homogeneous, as pure substances condense at constant pressure and temperature. Finally, the subcooled region is located near the outlet of the condenser subsystem, where the liquid leaves the condenser at almost sink temperature depending on the operating status of the LHP (see Sec. 3.2.2). To illustrate the spatial phase and temperature distribution of the condenser subsystem, Fig. 4.5 shows the two-dimensional schematic of the condenser with its three regions and the relevant parameters and variables.

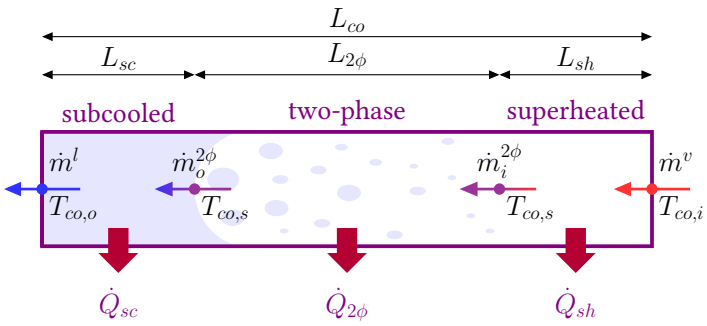

Figure 4.5: Condenser subsystem with the corresponding temperatures, mass flow rates, heat flows and lengths

For the condenser subsystem, the condensation model of [WBB78] with a two-phase and a subcooled region, which is also used in [LPDJ07], is extended to consider the superheated region as well. This zero-dimensional, transient condensation model enables the tracking of the liquid-vapor interface in the condenser. By describing the point of complete condensation as well as the liquid mass flow rate $\dot{m}^l$ at the outlet of the condenser as a function of the vapor mass flow rate $\dot{m}^v$ at the inlet of the condenser, the position of the liquid-vapor interface is determined, when the vapor enters the condenser in saturation state. The advantage of this model is that it is a dynamical, lumped-parameter model that needs only one constant, which is the heat transfer coefficient $k_{2\phi}$ of the two-phase region.

To calculate the temperatures, lengths, and mass flow rates of all three regions in the condenser subsystem, as depicted in Fig. 4.5, the behavior of the condenser is assumed to be governed by mass and energy conservation principles, while the minor influences of the momentum are neglected with a mean void fraction [WBB78, p. 101]. The distance between the condenser inlet at $T_{co,i}$ and the point, where the vapor flow reaches the saturation temperature $T_{co,s}$ of the condenser subsystem, is described by L_{sh}. The length L_{sh} correlates with the length of the superheated region in the condenser as part of the total condenser length L_{co}. Furthermore,

$L_{2\phi}$ denotes the distance between the end of the superheated region and the point of complete condensation and corresponds to the length of the two-phase region. In the remaining distance L_{sc}, the condensed liquid is further subcooled.

The mass balance in (3.18) for the two-phase region yields

$$\frac{\mathrm{d}}{\mathrm{d}t}\big(\rho^{2\phi} \cdot A_p \cdot L_{2\phi}(t)\big) = \dot{m}_i^{2\phi}(t) - \dot{m}_o^{2\phi}(t), \tag{4.43}$$

with the cross-sectional area A_p of the condenser pipe, the inlet mass flow rate $\dot{m}_i^{2\phi}(t)$ and the outlet mass flow rate $\dot{m}_o^{2\phi}(t)$. The variable $\dot{m}_o^{2\phi}(t)$ denotes the mass flow rate, which flows across the moving liquid-vapor interface between the two-phase region and the subcooled region, while $\dot{m}_i^{2\phi}(t)$ flows across the moving interface between the superheated region and the two-phase region (see Fig. 4.5). In order to simplify the transient problem, the condenser model neglects the change of the fluid momentum by assuming a homogeneous density $\rho^{2\phi}$ in the two-phase region [WBB78]:

$$\rho^{2\phi} = \rho_{co}^{l} \cdot (1 - \bar{\gamma}) + \rho_{co}^{v} \cdot \bar{\gamma}, \tag{4.44}$$

with the mean void fraction $\bar{\gamma}$ and the time-invariant densities ρ_{co}^{l} and ρ_{co}^{v} of the saturated liquid and the saturated vapor flow in the two-phase region. According to the calculations of [WBB78] based on experimental data while assuming steady condensing flow conditions, an approximated value of

$$\bar{\gamma} = 0.82 \tag{4.45}$$

is appropriate for the condensation process in the LHP.

According to the first law of thermodynamics in (3.11), the energy balance of the two-phase region is given by

$$\begin{aligned}\frac{\mathrm{d}}{\mathrm{d}t}\Big(\big(\rho_{co}^{l} \cdot h_{co}^{l} \cdot (1 - \bar{\gamma}) + \rho_{co}^{v} \cdot h_{co}^{v} \cdot \bar{\gamma}\big) \cdot A_p \cdot L_{2\phi}(t)\Big) \\ = -\dot{Q}_{2\phi}(t) + h_{co}^{v} \cdot \dot{m}_i^{2\phi}(t) - h_{co}^{l} \cdot \dot{m}_o^{2\phi}(t),\end{aligned} \tag{4.46}$$

where the LHS describes the change of homogeneous enthalpy in the subsystem and the RHS stands for the enthalpy flows of the entering vapor flow and the leaving condensate minus the heat flow $\dot{Q}_{2\phi}(t)$. The variable $\dot{Q}_{2\phi}(t)$ denotes the heat flow, which is released during condensation and is transferred to the heat sink by heat convection and heat conduction. It is expressed by

$$\dot{Q}_{2\phi}(t) = k_{2\phi} \cdot \pi \cdot D_p \cdot L_{2\phi}(t) \cdot \big(T_{co,s}(t) - T_{sk}(t)\big), \tag{4.47}$$

with the aforementioned heat transfer coefficient $k_{2\phi}$ of the two-phase region. The sink temperature $T_{sk}(t)$ is assumed to be constant along the condenser (see Assumption 4.1).

Combining (4.43), (4.44), and (4.46), the following equations are obtained:

$$\begin{aligned}&\big(\rho_{co}^{l} \cdot h_{co}^{l} \cdot (1 - \bar{\gamma}) + \rho_{co}^{v} \cdot h_{co}^{v} \cdot \bar{\gamma}\big) \cdot A_p \cdot \frac{\mathrm{d}L_{2\phi}(t)}{\mathrm{d}t} \\ &\quad = -\dot{Q}_{2\phi}(t) + h_{co}^{v} \cdot \dot{m}_i^{2\phi}(t) - h_{co}^{l} \cdot \dot{m}_i^{2\phi}(t) + h_{co}^{l} \cdot \rho^{2\phi} \cdot A_p \cdot \frac{\mathrm{d}L_{2\phi}(t)}{\mathrm{d}t}\end{aligned} \tag{4.48}$$

and

$$\begin{aligned}&\left(\rho_{co}^{l}\cdot h_{co}^{l}\cdot(1-\bar{\gamma})+\rho_{co}^{v}\cdot h_{co}^{v}\cdot\bar{\gamma}-\rho_{co}^{l}\cdot h_{co}^{l}\cdot(1-\bar{\gamma})-\rho_{co}^{v}\cdot h_{co}^{l}\cdot\bar{\gamma}\right)\cdot A_p\cdot\frac{\mathrm{d}L_{2\phi}(t)}{\mathrm{d}t}\\&\quad=-\dot{Q}_{2\phi}(t)+\Delta h_{co}^{v}\cdot\dot{m}_i^{2\phi}(t),\end{aligned}\tag{4.49}$$

with the specific heat of evaporation Δh_{co}^{v} at the fixed saturation temperature $T_{co,s}$. Thus, with (4.47), the differential equation for $L_{2\phi}(t)$ is obtained [WBB78]:

$$\frac{\mathrm{d}L_{2\phi}(t)}{\mathrm{d}t}=-\frac{k_{2\phi}\pi D_p\left(T_{co,s}(t)-T_{sk}(t)\right)}{\rho_{co}^{v}\bar{\gamma}A_p\Delta h_{co}^{v}}\cdot L_{2\phi}(t)+\frac{1}{\rho_{co}^{v}\bar{\gamma}A_p}\cdot\dot{m}_i^{2\phi}(t).\tag{4.50}$$

In contrast to [WBB78] and [LPDJ07], a third length $L_{sh}(t)$ and a second interface mass flow rate $\dot{m}_i^{2\phi}(t)$ are introduced together with the superheated region. The length $L_{sh}(t)$ depends on the required distance between the inlet of the condenser and the start of the two-phase region to cool the superheated vapor flow down to the saturation temperature $T_{co,s}(t)$. As a hermetically sealed system with a fixed working fluid charge, the mass distribution in the loop changes with the varying operating conditions. Correspondingly, the lengths of the regions in the LHP condenser automatically adapt to new operating conditions. To determine the lengths of all three regions, it is sufficient to establish two equations for the two lengths $L_{2\phi}(t)>0$ and $L_{sh}(t)\geq 0$, while the third length $L_{sc}(t)\geq 0$ is calculated from the fixed total length L_{co} of the condenser:

$$L_{sc}(t)=L_{co}-L_{2\phi}(t)-L_{sh}(t).\tag{4.51}$$

Thus, the equation for the mass balance of the subcooled region is given by

$$\frac{\mathrm{d}}{\mathrm{d}t}\Big(\rho_{co}^{l}\cdot A_p\cdot\big(L_{co}-L_{2\phi}(t)-L_{sh}(t)\big)\Big)=\dot{m}_o^{2\phi}-\dot{m}^{l}.\tag{4.52}$$

Due to the smaller length[5] and lower density of the superheated region in comparison with the other two regions, the impact of the fluid inertia in the superheated region on the phase distribution in the condenser subsystem is neglected. Hence, the change in $L_{sh}(t)$ equals zero, and the mass balance of the superheated region yields

$$\frac{\mathrm{d}}{\mathrm{d}t}\big(\rho_{co}^{v}\cdot A_p\cdot L_{sh}(t)\big)=\dot{m}^{v}(t)-\dot{m}_i^{2\phi}(t)=0.\tag{4.53}$$

Thus, the following equation holds:

$$\dot{m}_i^{2\phi}(t)=\dot{m}^{v}(t).\tag{4.54}$$

With this approximation, (4.52) is simplified:

$$-\rho_{co}^{l}\cdot A_p\cdot\frac{\mathrm{d}L_{2\phi}(t)}{\mathrm{d}t}=\dot{m}_o^{2\phi}(t)-\dot{m}^{l}(t).\tag{4.55}$$

[5] A maximum of about 16 % of the total condenser length is occupied by the superheated region in the considered LHP operating range according to the numerical LHP simulation of [MKHW19].

Furthermore, (4.43) is inserted into (4.55):

$$-\rho_{co}^{l} \cdot A_p \cdot \frac{1}{\rho_{2\phi} A_p} \left(\dot{m}^v(t) - \dot{m}_o^{2\phi}(t) \right) = \dot{m}_o^{2\phi}(t) - \dot{m}^l(t). \tag{4.56}$$

Finally, the interface mass flow rate $\dot{m}_o^{2\phi}(t)$ is expressed by the following equation (cf. [LPDJ07]):

$$\dot{m}_o^{2\phi}(t) = \dot{m}^v(t) - \frac{\dot{m}^v(t) - \dot{m}^l(t)}{1 - \frac{\rho_{co}^l}{\rho^{2\phi}}}. \tag{4.57}$$

Both the superheated region and the subcooled region are single-phase regions, where a single-phase heat exchange with the heat sink takes place. While the temperature $T_{co,s}(t)$ of the two-phase region is spatially constant (see Fig. 3.6b), the temperatures in the superheated and the subcooled region decrease along their lengths due to the heat flows $\dot{Q}_{sh}(t)$ and $\dot{Q}_{sc}(t)$ to the heat sink. Hence, the heat exchanger approach in Sec. 4.1.4 is also established for these two regions. The following equation of the saturation temperature $T_{co,s}(t)$ results:

$$T_{co,s}(t) = T_{sk}(t) + \left(T_{co,i}(t) - T_{sk}(t) \right) \cdot \exp\left(- \frac{\pi D_p k_{sh}}{\dot{m}^v(t) \bar{c}_{co,s,co,o}^l} \cdot L_{sh}(t) \right), \tag{4.58}$$

with the heat transfer coefficient k_{sh} of the superheated region. By rearranging (4.58), the length $L_{sh}(t)$ of the superheated region is determined:

$$L_{sh}(t) = \ln\left(\frac{T_{co,s}(t) - T_{sk}(t)}{T_{co,i}(t) - T_{sk}(t)} \right) \cdot \frac{-\dot{m}^v(t) \bar{c}_{co,s,co,o}^l}{\pi D_p k_{sh}}. \tag{4.59}$$

Analogously, the condenser outlet temperature $T_{co,o}(t)$ is calculated by

$$T_{co,o}(t) = T_{sk}(t) + \left(T_{co,s}(t) - T_{sk}(t) \right) \cdot \exp\left(- \frac{\pi D_p k_{sc}}{\dot{m}^l(t) \bar{c}_{co,s,co,o}^l} \cdot L_{sc}(t) \right), \tag{4.60}$$

with the heat transfer coefficient k_{sc} of the subcooled region. In order to determine the saturation temperature $T_{co,s}(t)$, the steady-state energy and mass balance of the two-phase region in (4.43) and (4.46) are evaluated:

$$T_{co,s}(t) = T_{sk}(t) + \frac{\Delta h_{co}^v}{k_{2\phi} \pi D_p L_{2\phi}(t)} \cdot \dot{m}_o^{2\phi}(t), \tag{4.61}$$

where $\dot{m}_o^{2\phi}(t)$ is determined in (4.57) as a function of the vapor mass flow rate $\dot{m}^v(t)$ in (4.31) and the liquid mass flow rate $\dot{m}^l(t)$. In order to close the system of equations and to establish the desired LHP state-space model, the liquid mass flow rate $\dot{m}^l(t)$ is derived in the next section.

4.1.6 Liquid Column

The movements of the liquid-vapor interfaces in the CC and the condenser, which are defined by the dynamics of the CC volume fraction ratio $\beta(t)$ in (4.26) and the length $L_{2\phi}(t)$ of

the two-phase condenser region in (4.50), are directly connected to the movement of the total liquid column in the LHP for transient operating conditions. According to (3.19), the momentum of the liquid column is influenced by the forces of the interfaces on both sides of the column. Furthermore, the position of the interfaces determine the total length of the column, which extends over three subsystems: the condenser, the LL, and the CC subsystem. In contrast to [LPDJ07], the length of the liquid column in the CC is neglected in this thesis. This is due to the fact that, on the one hand, the exact interior of the CC for determining the total length of the column is not always known to the LHP end user (see Chapter 1). On the other hand, the effective length of the liquid column in the CC is relatively small in comparison with the lengths in the LL and the condenser. Accordingly, the dynamic influence of the liquid-vapor interface in the CC on the column through the variation of the volume fraction ratio $\beta(t)$ is negligible compared to the other influences. Hence, the considered liquid column ranges from the end of the two-phase region in the condenser subsystem to the end of the LL.

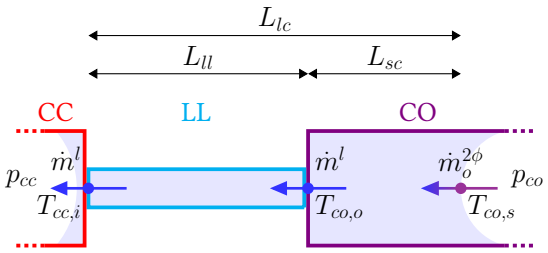

Figure 4.6: Liquid column in the condenser, the LL, and the CC with the corresponding temperatures, mass flow rates, pressures, and lengths

As shown in Fig. 4.6, the time-variant length $L_{lc}(t) \geq L_{ll}$ of the liquid column is calculated to

$$L_{lc}(t) = L_{sc}(t) + L_{ll}. \tag{4.62}$$

The effects on the liquid column can be described by the transient form of the law of conservation of momentum in Sec. 3.1.1. According to Assumption 4.6, the one-dimensional form for laminar flow in a pipe in (3.27) is adapted to the momentum of the liquid column in an LHP. Since the components of the considered LHP are on the same level, no inclination is regarded, i.e. $\theta_e = 0°$. From Fig. 4.6, the following equation results:

$$\begin{aligned} L_{lc}(t) \cdot \frac{\mathrm{d}\dot{m}^l(t)}{\mathrm{d}t} + \frac{1}{\rho^l_{cc,i} A_p} \cdot \left(\dot{m}^l(t)\right)^2 - \frac{1}{\rho^l_{co} A_p} \cdot \left(\dot{m}^{2\phi}_o(t)\right)^2 + A_p \cdot p_{cc}(t) \\ - A_p \cdot p_{co}(t) + \frac{32 \mu^l_{co,o} \dot{m}^l(t) L_{lc}(t)}{\rho^l_{co,o} D_p^2} \\ = 0, \end{aligned} \tag{4.63}$$

with the dynamic viscosity μ^l of the liquid defined in Appendix A.1 and the cross-sectional area A_p of the liquid column in the pipes[6]. Thus, the differential equation for the incompressible liquid mass flow rate $\dot{m}^l(t)$ (see Assumption 4.4) is obtained by rearranging (4.63):

$$\frac{\mathrm{d}\dot{m}^l(t)}{\mathrm{d}t} = \frac{1}{L_{lc}(t)} \cdot \left(\frac{\left(\dot{m}_o^{2\phi}(t)\right)^2}{\rho_{co}^l A_p} - \frac{\left(\dot{m}^l(t)\right)^2}{\rho_{cc,i}^l A_p} + A_p \cdot p_{co}(t) - A_p \cdot p_{cc}(t) - \frac{32\mu_{co,o}^l \dot{m}^l(t) L_{lc}(t)}{\rho_{co,o}^l D_p^2} \right), \tag{4.64}$$

with $\rho_{cc,i}^l$, $\rho_{co,o}^l$, and $\mu_{co,o}^l$ being the densities and the dynamic viscosity of the liquid at the inlet of the CC subsystem and the outlet of the condenser subsystem, respectively. Similar to $p_{cc}(t)$ in (4.34), the saturation pressure $p_{co}(t)$ in the two-phase region of the condenser subsystem is calculated by the Antoine equation (3.73) with the saturation temperature $T_{co,s}(t)$ defined in (4.61):

$$p_{co}(t) = \exp\left(A_{wf} - \frac{B_{wf}}{C_{wf} + T_{co,s}(t)} \right). \tag{4.65}$$

After establishing the mass and energy balance equations of the subsystems in the previous sections, the system of equations for the LHP state-space model is now closed by the momentum balance equation of the liquid column across the subsystems with the differential equation for the liquid mass flow rate $\dot{m}^l$ in (4.64). Consequently, the resulting LHP state-space model is constructed in the next section.

4.1.7 State-Space Representation of Loop Heat Pipes

After the thermodynamic and hydraulic modeling of each LHP subsystem in the previous sections, the established differential and algebraic equations are combined to build the desired LHP model in state-space form. For an explicit first-order differential equation system in dependence on inputs, states, and parameters only, the established state- and disturbance-dependent algebraic equations must be inserted into the four differential equations (4.25), (4.26), (4.50), and (4.64). As a result, the novel dynamical model of the LHP is given by the following nonlinear, four-dimensional state-space model:

$$\dot{\boldsymbol{x}}(t) = \boldsymbol{f}\big(\boldsymbol{x}(t), u(t), \boldsymbol{d}(t)\big), \tag{4.66a}$$

$$\boldsymbol{y}(t) = \boldsymbol{g}\big(\boldsymbol{x}(t), \boldsymbol{d}(t)\big), \tag{4.66b}$$

with $\boldsymbol{x}(t) = [T_{cc}(t), L_{2\phi}(t), \beta(t), \dot{m}^l(t)]^\top$, $u(t) = \dot{Q}_{cc}(t)$, $\boldsymbol{d}(t) = [\dot{Q}_{ev}(t), T_{sk}(t)]^\top$, and $\boldsymbol{y}(t) = [T_{cc}(t), T_{ev}(t), T_{co,i}(t), T_{co,o}(t)]^\top$. The four state variables in the state vector $\boldsymbol{x}(t)$ correspond to the temperature $T_{cc}(t)$ in the CC, the length $L_{2\phi}(t)$ of the two-phase region in the condenser, the volume fraction ratio $\beta(t)$ in the CC, and the liquid mass flow rate $\dot{m}^l(t)$. The four temperatures in the output vector $\boldsymbol{y}(t)$ coincide with the temperature sensors TS 1 to TS 4 in Fig. 4.1. The heat flow $\dot{Q}_{cc}(t)$ from the control heater to the CC is the single input

[6] It should be noted that in contrast to the depiction in Fig. 4.6 in the style of Fig. 4.3, the condenser and the transport lines have the same pipe diameter D_p and therefore the same pipe cross-sectional area A_p.

variable $u(t)$ of the system. The disturbance vector $\boldsymbol{d}(t)$ is characterized by the heat load $\dot{Q}_{ev}(t)$ at the evaporator and the sink temperature $T_{sk}(t)$ at the condenser as the two external disturbance inputs of the system. The functions f_1, f_2, f_3, and f_4 in the vector function $\boldsymbol{f}$ of the state equation (4.66a) are given as follows:

$$f_1 = \frac{1}{C_{cc}(t)} \cdot \left[\dot{m}^l(t) \cdot \bar{c}^l_{cc,i,cc} \cdot \big(T_{cc,i}(t) - T_{cc}(t)\big) + \dot{Q}_{cc}(t) + \dot{Q}_{lk}(t) + \frac{\rho^v_{cc}(t)\Delta h^v_{cc}}{\rho^l_{cc} - \rho^v_{cc}(t)} \cdot \big(\dot{m}^l(t) - \dot{m}^v(t)\big) \right], \tag{4.67}$$

$$f_2 = -\frac{k_{2\phi}\pi D_p\big(T_{co,s}(t) - T_{sk}(t)\big)}{\rho^v_{co}\bar{\gamma}A_p\Delta h^v_{cond}} \cdot L_{2\phi}(t) + \frac{1}{\rho^v_{co}\bar{\gamma}A_p} \cdot \dot{m}_i^{2\phi}(t), \tag{4.68}$$

$$f_3 = \frac{1}{V_{cc}\big(\rho^l_{cc} - \rho^v_{cc}(t)\big)} \cdot \left\{ \dot{m}^l(t) - \dot{m}^v(t) - \left(\frac{1}{\big(T_{cc}(t)\big)^2} \cdot \frac{\rho^l_{cc}}{R} \cdot \frac{\rho^v_{cc}(t)\Delta h^v_{cc}}{\rho^l_{cc} - \rho^v_{cc}(t)} - \frac{\rho^v_{cc}(t)}{T_{cc}(t)} \right) \cdot \big(1 - \beta(t)\big) \cdot \frac{V_{cc}}{C_{cc}(t)} \cdot \left[\dot{m}^l(t) \cdot \bar{c}^l_{cc,i,cc} \cdot \big(T_{cc,i}(t) - T_{cc}(t)\big) + \dot{Q}_{cc}(t) + \dot{Q}_{lk}(t) + \frac{\rho^v_{cc}(t)\Delta h^v_{cc}}{\rho^l_{cc} - \rho^v_{cc}(t)} \cdot \big(\dot{m}^l(t) - \dot{m}^v(t)\big) \right] \right\}, \tag{4.69}$$

$$f_4 = \frac{1}{L_{lc}(t)} \cdot \left(\frac{\big(\dot{m}_o^{2\phi}(t)\big)^2}{\rho^l_{co}A_p} - \frac{\big(\dot{m}^l(t)\big)^2}{\rho^l_{cc,i}A_p} + p_{co}(t) \cdot A_p - p_{cc}(t) \cdot A_p - \frac{32\mu^l_{co,o}\dot{m}^l(t)L_{lc}(t)}{\rho^l_{co,o}D_p^2} \right). \tag{4.70}$$

Similarly, the functions g_1, g_2, g_3, and g_4 in the vector function $\boldsymbol{g}$ of the output equation (4.66b) are the following:

$$g_1 = T_{cc}(t), \tag{4.71}$$

$$g_2 = \frac{R_{lk}}{R_{lk} + R_{sh}} \cdot \left(T_{ev,s}(t) + R_{sh} \cdot \dot{Q}_{ev}(t) + \frac{R_{sh}}{R_{lk}} \cdot T_{cc}(t) \right), \tag{4.72}$$

$$g_3 = T_{amb} + (T_{ev}(t) - T_{amb}) \cdot \exp\left(-\frac{k_{vl}\pi D_p L_{vl}}{\dot{m}^v(t)\bar{c}^v_{ev,co,i}} \right), \tag{4.73}$$

$$g_4 = T_{sk}(t) + \big(T_{co,s}(t) - T_{sk}(t)\big) \cdot \exp\left(-\frac{\pi D_p k_{sc}}{\dot{m}^l(t)\bar{c}^l_{co,s,co,o}} \cdot L_{sc}(t) \right). \tag{4.74}$$

For the sake of readability, not all state- and disturbance-dependent equations are inserted into one another to form the functions (4.67), (4.68), (4.69), and (4.70), as well as (4.71), (4.72), (4.73), and (4.74) explicitly. Instead, the dependencies of the different variables are presented individually:

$$p_{cc}(t) = f\big(T_{cc}(t)\big), \tag{4.75}$$

$$T_{ev,s}(t) = f\big(T_{cc}(t)\big), \tag{4.76}$$

$$\dot{Q}_{lk}(t) = f\left(T_{cc}(t), \dot{Q}_{ev}(t)\right), \tag{4.77}$$

$$\dot{m}^{v}(t) = f\left(T_{cc}(t), \dot{Q}_{ev}(t)\right), \tag{4.78}$$

$$T_{co,s}(t) = f\left(T_{cc}(t), L_{2\phi}(t), \dot{m}^{l}(t), \dot{Q}_{ev}(t), T_{sk}(t)\right), \tag{4.79}$$

$$p_{co}(t) = f\left(T_{cc}(t), L_{2\phi}(t), \dot{m}^{l}(t), \dot{Q}_{ev}(t), T_{sk}(t)\right), \tag{4.80}$$

$$L_{lc}(t) = f\left(T_{cc}(t), L_{2\phi}(t), \dot{m}^{l}(t), \dot{Q}_{ev}(t), T_{sk}(t)\right), \tag{4.81}$$

$$T_{cc,i}(t) = f\left(T_{cc}(t), L_{2\phi}(t), \dot{m}^{l}(t), \dot{Q}_{ev}(t), T_{sk}(t)\right). \tag{4.82}$$

Simplification of the Nonlinear Model

In addition to their presentation, the mathematical analysis of the model equations in the subsequent sections is complicated due to their size and algebraic complexity. That's why numerical solutions are also pursued in the following for a first statement. Besides the dependencies of the exponential functions in (4.39), (4.41), and (4.60) on the state and input variables, the complexity results from the nested logarithm and exponential functions in (4.32) and (4.76), respectively. However, this nonlinear state-space model (4.66) has the desired model form as described in Def. 2.1 for a model-based control design. The model is able to predict the dynamic behavior of the LHP over the complete operating range of the running LHP according to the input and output variables in Fig. 4.2. The internal state variables represent the system's change in time. This change includes the dynamics of the CC temperature $T_{cc}(t)$ and the liquid mass flow rate $\dot{m}^{l}(t)$. In addition, the dynamics of the liquid-vapor interfaces in the CC and the condenser are traceable through the remaining two state variables $\beta(t)$ and $L_{2\phi}(t)$. The seven model parameters R_{lk}, $k_{2\phi}$, k_{sc}, k_{ll}, k_{vl}, k_{sh}, and R_{sh} in the established LHP state-space model depend on flow regimes, velocity-dependent pressure losses, and spatial variation. In accordance with Assumption 4.5, these parameters are assumed to be constant over the considered LHP operating range and are determined in the individual OP of the LHP systems under investigation.

Due to the fundamental derivation of the CC modeling with a variable volume fraction ratio $\beta(t)$ in Sec. 4.1.2, a deeper insight into the numerical LHP models related to this thesis is possible. At the same time, it becomes clear which dominant dynamics must be considered for the desired control system modeling of the LHP. While a varying $\beta(t)$ is considered in the CC modeling approach in [LPDJ07] as well, the differential equation for the CC temperature $T_{cc}(t)$ in [VR08] and [MKHW19] for the transient modeling of the LHP temperatures can be reproduced from (4.25) by fixing β. This means that the total mass $m_{cc}^{2\phi}(t)$ of the CC in (4.1) depends mainly on the vapor density $\rho_{cc}^{v}(t)$ in (4.4). Consequently, a reduction of the order of the four-dimensional state-space model (4.66) is possible since the variation of the third state $\beta(t)$ has only a negligible impact on the LHP dynamics. Indeed, $\beta(t)$ only influences the first state equation (4.67) through the thermal capacity $C_{cc}(t)$ given in (4.27).

Furthermore, both the dependency of $C_{cc}(t)$ on $\beta(t)$ and on $T_{cc}(t)$ are weak. For this reason, a thermal capacity is often chosen as a fixed parameter (cf. [vBW17, p. 10]), which is fitted to the investigated system. Especially when the exact interior of the CC is unknown and the total fluid volume is approximated by the exterior dimensions of the CC, as it is the case in this work, a fixed thermal capacity must be adapted to measurements. Analogous to (3.64), the thermal capacity $C_{cc}(t)$ in (4.27) is thus approximated by a constant thermal capacitance C_{cc}^{op} of the CC subsystem in the OP with a fixed volume fraction ratio β^{op} and temperature T_{cc}^{op} of the saturated two-phase CC:

$$C_{cc}^{op} = \Bigg[\left(\rho_{cc}^{l} \cdot \beta^{op} + \rho_{cc}^{v,op} \cdot (1-\beta^{op})\right) \cdot \bar{c}_{cc,ref}^{l} - \frac{\Delta h_{cc}^{v} \rho_{cc}^{l} \rho_{cc}^{v,op}}{T_{cc}^{op}\left(\rho_{cc}^{l} - \rho_{cc}^{v,op}\right)} + \left(\frac{\Delta h_{cc}^{v} \rho_{cc}^{l} \rho_{cc}^{v,op}}{R (T_{cc}^{op})^2 \left(\rho_{cc}^{l} - \rho_{cc}^{v,op}\right)} - \frac{\rho_{cc}^{v,op}}{T_{cc}^{op}} \right) \cdot (1-\beta^{op}) \cdot \Delta h_{cc}^{v} \Bigg] \cdot V_{cc}. \tag{4.83}$$

Since (4.26) cannot be solved for β^{op} in steady state, i.e. where $\dot{m}^{l}(t) = \dot{m}^{v}(t)$, it is fitted to experimental data of the investigated system. In doing so, the dynamics of the CC temperature, which are governed by (4.83), are adapted to the CC dynamics of the investigated LHP system.

From a control engineering point of view, not only the system order is reduced with a constant β^{op}, but also the introduction of an additional unobservable state due to the simultaneous connection between (4.25) and (4.26) is prevented for the subsequent model-based control design. The order reduction is further evaluated in Sec. 7.2.4 by comparing the results of both state-space models.

In conclusion, the final three-dimensional LHP state-space model for the subsequent model-based control design is derived:

$$\dot{\boldsymbol{x}}(t) = \boldsymbol{f}\big(\boldsymbol{x}(t), u(t), \boldsymbol{d}(t)\big), \tag{4.84a}$$

$$\boldsymbol{y}(t) = \boldsymbol{g}\big(\boldsymbol{x}(t), \boldsymbol{d}(t)\big), \tag{4.84b}$$

with $\boldsymbol{x}(t) = [T_{cc}(t), L_{2\phi}(t), \dot{m}^{l}(t)]^{\top}$, $u(t) = \dot{Q}_{cc}(t)$, $\boldsymbol{d}(t) = [\dot{Q}_{ev}(t), T_{sk}(t)]^{\top}$, and $\boldsymbol{y}(t) = [T_{cc}(t), T_{ev}(t), T_{co,i}(t), T_{co,o}(t)]^{\top}$. The functions f_1, f_2, and f_3 of the state equation (4.84a) are given by

$$f_1 = \frac{1}{C_{cc}^{op}} \cdot \left[\dot{m}^{l}(t) \cdot \bar{c}_{cc,i,cc}^{l} \cdot \big(T_{cc,i}(t) - T_{cc}(t)\big) + \dot{Q}_{cc}(t) + \dot{Q}_{lk}(t) \right], \tag{4.85}$$

$$f_2 = -\frac{k_{2\phi} \pi D_p \big(T_{co,s}(t) - T_{sk}(t)\big)}{\rho_{co}^{v} \bar{\gamma} A_p \Delta h_{cond}^{v}} \cdot L_{2\phi}(t) + \frac{1}{\rho_{co}^{v} \bar{\gamma} A_p} \cdot \dot{m}_{i}^{2\phi}(t), \tag{4.86}$$

$$f_3 = \frac{1}{L_{lc}(t)} \cdot \left(\frac{\big(\dot{m}_{o}^{2\phi}(t)\big)^2}{\rho_{co}^{l} A_p} - \frac{\big(\dot{m}^{l}(t)\big)^2}{\rho_{cc,i}^{l} A_p} + p_{co}(t) \cdot A_p - p_{cc}(t) \cdot A_p - \frac{32 \mu_{co,o}^{l} \dot{m}^{l}(t) L_{lc}(t)}{\rho_{co,o}^{l} D_p^2} \right). \tag{4.87}$$

The corresponding output equation (4.84b) is the same as for the four-dimensional model (4.66).

With the formulation of the LHP state-space model (4.84), the desired dynamical modeling of a conventional LHP is finished. Based on this model structure, the following section concentrates on the design of adequate controllers for the OT control of LHPs.

4.2 Nonlinear Control Designs Based on the Complex Model

For the nonlinear state-space model (4.84), nonlinear controllers for the CC temperature and the evaporator temperature are designed in the following sections. It becomes clear from (4.84) that the state-space model is an input-affine single-input-multiple-output (SIMO) system:

$$\dot{\boldsymbol{x}}(t) = \boldsymbol{a}\big(\boldsymbol{x}(t), \boldsymbol{d}(t)\big) + \boldsymbol{b} \cdot u(t), \tag{4.88a}$$

$$\boldsymbol{y}(t) = \boldsymbol{c}\big(\boldsymbol{x}(t), \boldsymbol{d}(t)\big), \tag{4.88b}$$

where the control heater output $\dot{Q}_{cc}(t)$ as system input $u(t)$ appears linearly in the system equations. The unforced part $\boldsymbol{a}$ of (4.88a) is defined by

$$a_1 = \frac{1}{C_{cc}^{op}} \cdot \left[\dot{m}^l(t) \cdot \bar{c}^l_{cc,i,cc} \cdot \big(T_{cc,i}(t) - T_{cc}(t)\big) + \dot{Q}_{lk}(t) \right], \tag{4.89}$$

$$a_2 = -\frac{k_{2\phi} \pi D_p \big(T_{co,s}(t) - T_{sk}(t)\big)}{\rho^v_{co} \bar{\gamma} A_p \Delta h^v_{cond}} \cdot L_{2\phi}(t) + \frac{1}{\rho^v_{co} \bar{\gamma} A_p} \cdot \dot{m}_i^{2\phi}(t), \tag{4.90}$$

$$\begin{aligned} a_3 = {} & \frac{1}{L_{lc}(t)} \cdot \left(\frac{\big(\dot{m}_o^{2\phi}(t)\big)^2}{\rho^l_{co} A_p} - \frac{\big(\dot{m}^l(t)\big)^2}{\rho^l_{cc,i} A_p} + p_{co}(t) \cdot A_p - p_{cc}(t) \cdot A_p \right. \\ & \left. - \frac{32 \mu^l_{co,o} \dot{m}^l(t) L_{lc}(t)}{\rho^l_{co,o} D_p^2} \right). \end{aligned} \tag{4.91}$$

Accordingly, the forced part $\boldsymbol{b}$ has the form of the vector

$$\boldsymbol{b} = \begin{bmatrix} \frac{1}{C_{cc}^{op}} \\ 0 \\ 0 \end{bmatrix}. \tag{4.92}$$

In the output equation (4.88b), the vector function $\boldsymbol{c}$ is equal to $\boldsymbol{g}$ in (4.84b):

$$c_1 = T_{cc}(t), \tag{4.93}$$

$$c_2 = \frac{R_{lk}}{R_{lk} + R_{sh}} \cdot \left(T_{ev,s}(t) + R_{sh} \cdot \dot{Q}_{ev}(t) + \frac{R_{sh}}{R_{lk}} \cdot T_{cc}(t) \right), \tag{4.94}$$

$$c_3 = T_{amb} + \big(T_{ev}(t) - T_{amb}\big) \cdot \exp\left(-\frac{k_{vl} \pi D_p L_{vl}}{\dot{m}^v(t) \bar{c}^v_{ev,co,i}} \right), \tag{4.95}$$

$$c_4 = T_{sk}(t) + \big(T_{co,s}(t) - T_{sk}(t)\big) \cdot \exp\left(-\frac{\pi D_p k_{sc}}{\dot{m}^l(t) \bar{c}^l_{co,s,co,o}} \cdot L_{sc}(t) \right). \tag{4.96}$$

The described system property is exploited in the subsequent model-based control designs, which stabilize the LHP in the OP as desired equilibrium point, i.e. where $\boldsymbol{x}^{op} = [T_{cc}^{op}, L_{2\phi}^{op}, \dot{m}^{l,op}]^\top$, $u^{op} = \dot{Q}_{cc}^{op}$, $\boldsymbol{d}^{op} = [\dot{Q}_{ev}^{op}, T_{sk}^{op}]^\top$ holds.

4.2.1 Nonlinear PI State Feedback Control Based on Exact Input-Output Linearization

In this section, a nonlinear PI state feedback controller for the CC temperature is introduced based on exact linearization [Isi95, p. 147], also called exact input-output linearization [Ada18, p. 314] or partial feedback linearization [Kha15, p. 219], to control the nonlinear dynamics of the LHP and stabilize the LHP in the OP at a fixed setpoint. Thus, the corresponding LHP control model forms a single-input-single-output (SISO) system based on (4.88) since the CC temperature $T_{cc}(t)$ is the controlled output variable $y(t)$ (cf. (4.71)):

$$\dot{\boldsymbol{x}}(t) = \boldsymbol{a}\big(\boldsymbol{x}(t), \boldsymbol{d}(t)\big) + \boldsymbol{b} \cdot u(t), \tag{4.97a}$$

$$y(t) = c_1\big(\boldsymbol{x}(t)\big). \tag{4.97b}$$

The nonlinear PI state feedback controller with exact input-output linearization avoids a control design based on the classical linearization of the system equations about the OP, but compensates the relevant nonlinear dynamics with a feedback controller to achieve a linear input-output behavior over the entire state space. The corresponding control loop with a fixed setpoint is presented in Fig. 4.7.

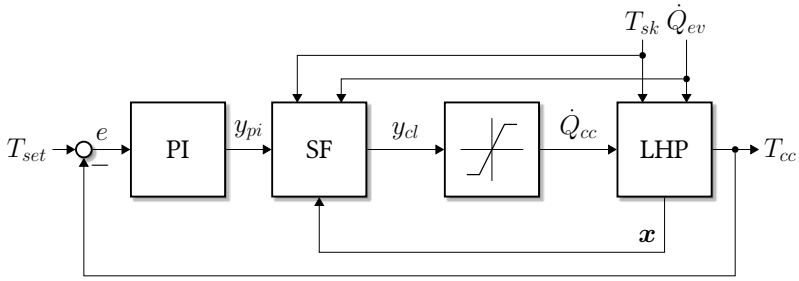

Figure 4.7: Control loop of an LHP with a PI controller and a nonlinear state feedback control (SF) with fixed setpoint

For the subsequent design of the nonlinear PI state feedback controller, the state vector $\boldsymbol{x}$ of the LHP state-space model (4.97) is initially considered to be known. Since only the first state, the CC temperature T_{cc}, is indeed measured in the real application, the other two states, namely the length $L_{2\phi}$ of the two-phase region in the condenser and the liquid mass flow rate $\dot{m}^l$, has to be estimated. An adequate state estimation method is introduced later on in Sec. 4.2.3 to fill this gap in the control loop. In a first attempt, the availability of the sink temperature T_{sk} and the heat load $\dot{Q}_{ev}$ is assumed for the control design.

In the case of the nonlinear LHP dynamics, the exact input-output linearization does not require an initial transformation of the system into the *Byrnes-Isidori normal form* (see [AG93])

since the LHP control model (4.97) is already given in this form. Therefore, the division of the three-dimensional system state $\boldsymbol{x}(t)$ into an external part with the state variable $x_{ex}(t)$ and an internal part with the two-dimensional state vector $\boldsymbol{x}_{in}(t)$ is already recognizable from the state equation (4.97a):

$$\boldsymbol{x}(t) = \begin{bmatrix} T_{cc}(t) \\ L_{2\phi}(t) \\ \dot{m}^l(t) \end{bmatrix} = \begin{bmatrix} x_{ex}(t) \\ \boldsymbol{x}_{in}(t) \end{bmatrix}. \tag{4.98}$$

Accordingly, the first row of (4.97a) corresponds to the external dynamics of the LHP, i.e. the dynamics of the CC temperature $T_{cc}(t)$, which are directly influenced by the system input $u(t) = \dot{Q}_{cc}(t)$:

$$\dot{x}_{ex}(t) = \dot{T}_{cc}(t) = a_1\big(x_{ex}(t), \boldsymbol{x}_{in}(t), \boldsymbol{d}(t)\big) + b_1 \cdot u(t). \tag{4.99}$$

The nonlinearity of (4.99) will be canceled by the intended exact input-output linearization in the form of a state feedback controller. The other two rows of (4.97a), i.e. the dynamics of the length $L_{2\phi}(t)$ and the mass flow rate $\dot{m}^l(t)$, belong to the internal dynamics of the LHP:

$$\dot{\boldsymbol{x}}_{in}(t) = \begin{bmatrix} \dot{L}_{2\phi}(t) \\ \ddot{m}^l(t) \end{bmatrix} = \begin{bmatrix} a_2\big(x_{ex}(t), \boldsymbol{x}_{in}(t), \boldsymbol{d}(t)\big) \\ a_3\big(x_{ex}(t), \boldsymbol{x}_{in}(t), \boldsymbol{d}(t)\big) \end{bmatrix}. \tag{4.100}$$

While the internal dynamics (4.100) are not taken into account by the state feedback controller, their stability is necessary for the stability of the overall control system and is examined after the control design. The stability of the external dynamics is ensured by the selection of adequate controller gains.

A first step of designing the exact input-output linearization is the determination of the *relative degree* δ of (4.97). Based on the Byrnes-Isidori normal form, δ is equal to the dimension of the external dynamics, i.e.

$$\delta = 1. \tag{4.101}$$

In addition, δ corresponds exactly to the time derivative of the output $y(t)$, which depends explicitly on the input $u(t)$ for the first time [AG93]. For (4.97), the first time derivative of the CC temperature $T_{cc}(t)$ depends on the control heater output $\dot{Q}_{cc}(t)$. Thus, δ is the smallest natural number for which the following equation holds [AG93]:

$$L_{\boldsymbol{b}} L_{\boldsymbol{a}}^{\delta-1} c_1\big(\boldsymbol{x}(t)\big) \neq 0. \tag{4.102}$$

The operator L in (4.102) is called *Lie derivative* and is defined as follows:

Definition 4.1 (Lie derivative [Ada18, p. 310])
The Lie derivative is the gradient of a scalar function $f(\boldsymbol{x})$ multiplied by the vector field $\boldsymbol{g}(\boldsymbol{x})$:

$$L_{\boldsymbol{g}} f(\boldsymbol{x}) = \frac{\partial f(\boldsymbol{x})}{\partial \boldsymbol{x}} \boldsymbol{g}(\boldsymbol{x}) = \operatorname{grad}^\top f(\boldsymbol{x}) \cdot \boldsymbol{g}(\boldsymbol{x}). \tag{4.103}$$

According to Def. 4.1, (4.102) can be resolved:

$$L_{\boldsymbol{b}} c_1\big(\boldsymbol{x}(t)\big) = \frac{1}{C_{cc}^{op}} \neq 0. \tag{4.104}$$

The relative degree δ is well-defined since (4.104) holds for all $\boldsymbol{x}(t) \in \mathbb{R}^n$ [Ada18, p. 315]. Thus, the static state feedback controller $u\big(\boldsymbol{x}(t)\big)$ can be designed to achieve an exact input-output linearization [AG93]:

$$u\big(\boldsymbol{x}(t)\big) = \frac{v(t) - L_{\boldsymbol{a}}^{\delta} c_1\big(\boldsymbol{x}(t)\big)}{L_{\boldsymbol{b}} L_{\boldsymbol{a}}^{\delta-1} c_1\big(\boldsymbol{x}(t)\big)} - \frac{\sum_{i=1}^{\delta} \eta_{i-1} L_{\boldsymbol{a}}^{i-1} c_1\big(\boldsymbol{x}(t)\big)}{L_{\boldsymbol{b}} L_{\boldsymbol{a}}^{\delta-1} c_1\big(\boldsymbol{x}(t)\big)}, \tag{4.105}$$

with the new input variable $v(t)$ and the scalar coefficients η_i. The input-output behavior of the linearized external dynamics is given by the transfer function $G(s)$ with the complex variable s in the Laplace domain according to (2.11):

$$G(s) = \frac{y(s)}{v(s)} = \frac{1}{\eta_\delta s^\delta + \eta_{\delta-1} s^{\delta-1} + \ldots + \eta_1 s + \eta_0}. \tag{4.106}$$

The poles of (4.106) can be specified by an appropriate choice of the coefficients η_i [AG93].

Considering (4.101), the formula in (4.105) yields the state feedback controller[7] $y_{cl}(t)$ according to the control model (4.97):

$$y_{cl}(t) = \frac{v(t) - L_{\boldsymbol{a}} c_1\big(\boldsymbol{x}(t)\big) - \eta_0 c_1\big(\boldsymbol{x}(t)\big)}{L_{\boldsymbol{b}} c_1\big(\boldsymbol{x}(t)\big)} = \frac{v(t) - a_1\big(\boldsymbol{x}(t), \boldsymbol{d}(t)\big) - \eta_0 c_1\big(\boldsymbol{x}(t)\big)}{b_1}. \tag{4.107}$$

Based on (4.106) with $v(t) = y_{pi}(t)$ or by inserting (4.107) into (4.97) and transferring the resulting system dynamics into the Laplace domain, the transfer function $G(s)$ of the linearized external dynamics is derived:

$$G(s) = \frac{T_{cc}(s)}{y_{pi}(s)} = \frac{1}{s + \eta_0}. \tag{4.108}$$

For an improved stationary accuracy, the current exact input-output linearized control loop in (4.108) is extended by a PI controller:

$$C(s) = \frac{y_{pi}(s)}{e(s)} = K_p + K_i \cdot \frac{1}{s}, \tag{4.109}$$

with the proportional gain K_p, the integral gain K_i, and the Laplace-transformed control error $e(s)$. The control error $e(t)$ in the time domain is calculated by the difference between the setpoint temperature T_{set} and the CC temperature $T_{cc}(t)$:

$$e(t) = T_{set} - T_{cc}(t). \tag{4.110}$$

By introducing an integrator to the control loop with (4.109), the stationary accuracy is improved by reducing the control error asymptotically. This control error is due to the mismatch between the model and the real system and the influence of the disturbances.

[7] The nonlinear LHP controller based on a control Lyapunov function in [GSO+20] corresponds to the control law in (4.107) if the state feedback controller is extended by a prefilter $v(t) = \eta_0 \cdot T_{set}$

After the design of the PI state feedback controller, the stability of the overall control loop is examined. A stable overall control loop does not follow from the stability of the linearizing feedback controller (4.107) in general. Instead, the stability of the internal dynamics (4.100) must be verified additionally. Since the internal dynamics are strongly nonlinear, the stability of equilibrium points is evaluated. For this purpose, the analysis of the *zero dynamics* of (4.100) at the balanced OP is sufficient (see [Ada18, p. 345]):

$$\dot{\boldsymbol{x}}_{in}(t) = \begin{bmatrix} a_2(x_{ex}^{op}, \boldsymbol{x}_{in}(t), \boldsymbol{d}^{op}) \\ a_3(x_{ex}^{op}, \boldsymbol{x}_{in}(t), \boldsymbol{d}^{op}) \end{bmatrix}. \tag{4.111}$$

The stability of the OP of the zero dynamics[8] (4.111) is determined according to Theorem 4.1.

Theorem 4.1 (Lyapunov's indirect method (cf. [Kha15, p. 56]))
Consider the system

$$\dot{\boldsymbol{x}} = \boldsymbol{f}(\boldsymbol{x}) \tag{4.112}$$

with the equilibrium point $\boldsymbol{x} = \boldsymbol{x}^{op}$ and $\boldsymbol{f}$ being continuously differentiable around the equilibrium point. Then, the eigenvalues λ_i ($i = 1, ..., n$) of the Jacobian of $\boldsymbol{f}$

$$\boldsymbol{J} = \left.\frac{\partial \boldsymbol{f}(\boldsymbol{x})}{\partial \boldsymbol{x}}\right|_{\boldsymbol{x}=\boldsymbol{x}^{op}} \tag{4.113}$$

determine the stability characteristics of (4.112) *according to the following conditions:*

1. *The OP is exponentially stable if and only if* $\mathrm{Re}\{\lambda_i\} < 0$ *for all* i,
2. *The OP is unstable if* $\mathrm{Re}\{\lambda_i\} > 0$ *for at least one* i.

Since a_2 becomes independent of $L_{2\phi}$ when inserting (4.61) into (4.90), the *Jacobian* $\boldsymbol{J}$ of (4.111) is given by

$$\boldsymbol{J} = \left[\begin{array}{cc} 0 & \dfrac{\partial a_2(x_{ex}^{op}, \boldsymbol{x}_{in}(t), \boldsymbol{d}^{op})}{\partial \dot{m}^l(t)} \\ \dfrac{\partial a_3(x_{ex}^{op}, \boldsymbol{x}_{in}(t), \boldsymbol{d}^{op})}{\partial L_{2\phi}(t)} & \dfrac{\partial a_3(x_{ex}^{op}, \boldsymbol{x}_{in}(t), \boldsymbol{d}^{op})}{\partial \dot{m}^l(t)} \end{array}\right]\Bigg|_{\boldsymbol{x}_{in}=\boldsymbol{x}_{in}^{op}}. \tag{4.114}$$

For the determination of the eigenvalues λ_1 and λ_2 of (4.114), the corresponding characteristic polynomial is constructed:

$$\det(\lambda \cdot \boldsymbol{I} - \boldsymbol{J}) = \lambda^2 + \gamma_1 \cdot \lambda + \gamma_0 = 0, \tag{4.115}$$

with the coefficient γ_0 and γ_1. If (4.115) is a *Hurwitz polynomial* according to Theorem A.1 in Appendix A.2, all eigenvalues have a negative real part. Since (4.115) is a second-order polynomial, the first Hurwitz condition is already necessary and sufficient [Unb08, p. 145].

[8] The explicit transformation of the OP into the origin for the creation of a vanishing output variable $y(t) = x_{ex}(t) = 0$ as input variable of the internal dynamics (4.100) is skipped in (4.111).

According to (4.115), $\gamma_2 = 1$ is always positive. Hence, the coefficients γ_0 and γ_1 must be positive as well for an exponentially stable OP of the zero dynamics (4.111). Thus, only these two coefficients must be further analyzed. A numerical solution of the inequalities in Theorem A.1 is pursued by inserting the values of x_{ex}^{op}, $\boldsymbol{x}_{in}^{op}$, and $\boldsymbol{d}^{op}$ and the model parameters. Hence, the positive solution of random OPs within the LHP operating range enables practically the verification of the stability of the internal dynamics and thus of the LHP control loop over the entire LHP operating range. The corresponding numerical results are positive, as presented in Sec. 7.4.4. Furthermore, the overall stability of the control loop is also verified in the simulations presented in Sec. 7.4.

Because of the power limitation of the control heater (see Table 4.1), the introduced integral action may cause an undesired dynamic behavior of the LHP control loop, i.e. when the integration in the PI controller winds up. This effect makes it necessary to implement an anti-windup (AW) strategy after the design process of the actual stable controller [Ort13, p. 27]. First, the state feedback control (SF) in (4.107) and the PI controller in (4.109) with the integral action are designed without considering the limitation and the corresponding windup. In a second step, the control loop is extended with a suitable AW structure. Therefore, the block diagram in Fig. 4.7 is extended by the AW structure below the saturation block to consider the limitation of the control heater. The overall control loop with a fixed setpoint is presented in Fig. 4.8.

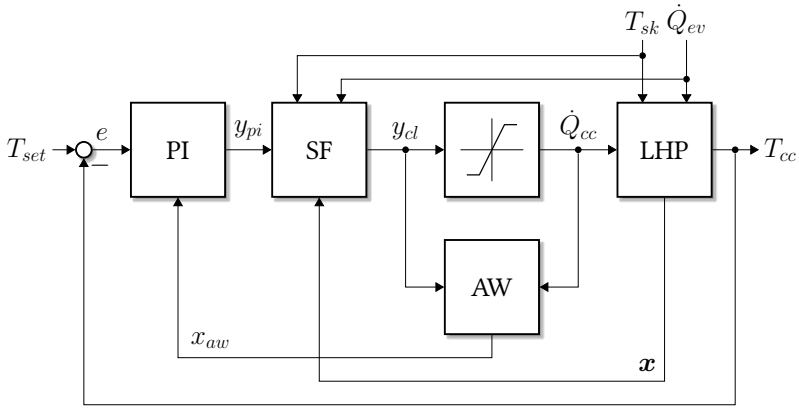

Figure 4.8: Control loop of an LHP with a PI controller, a nonlinear state feedback control (SF), a fixed setpoint, and an AW structure

The back-calculation method is one of the standard tracking AW strategies [BA95]. This AW strategy allows for a simple implementation in the control loop to achieve the desired limitation of the integral action. As depicted in Fig. 4.8, this classical AW structure is based on the additional feedback of the difference between the controller output values before and after the saturation. To prevent the windup of the integral term of the PI controller, the difference between $y_{cl}(t)$ and $\dot{Q}_{cc}(t)$ is multiplied by a feedback gain K_{aw} to form the output x_{aw} of

the AW structure that is subtracted from the integrator input:

$$x_{aw}(t) = K_{aw} \cdot \left(y_{cl}(t) - \dot{Q}_{cc}(t) \right), \tag{4.116}$$

$$y_{pi}(t) = K_p \cdot e(t) + K_i \cdot \int \big(e(t) - x_{aw}(t) \big) \, \mathrm{d}t. \tag{4.117}$$

The feedback gain of the back-calculation method is set to the inverse of the proportional gain K_p of the PI controller [GKU+03]:

$$K_{aw} = 1/K_p. \tag{4.118}$$

This is the end of the controller design for the CC temperature control of an LHP. The implementation of the algorithm in the real application is shortly presented in Appendix A.3. Thus, the discrete PI controller with the chosen AW strategy is given by

$$x_{aw}(k) = K_{aw} \cdot \left(y_{cl}(k-1) - \dot{Q}_{cc}(k-1) \right), \tag{4.119}$$

$$i_{pi}(k) = K_i \cdot T_{st} \cdot \big(e(k) - x_{aw}(k) \big) + i_{pi}(k-1), \tag{4.120}$$

$$y_{pi}(k) = K_p \cdot e(k) + i_{pi}(k), \tag{4.121}$$

with the sampling time T_{st}, the time constant k, and the discrete control error $e(k)$:

$$e(k) = T_{set} - T_{cc}(k). \tag{4.122}$$

Accordingly, the discrete state feedback control is given by

$$y_{cl}(k) = \frac{y_{pi}(k) - a_1\big(\boldsymbol{x}(k), \boldsymbol{d}(k)\big) - \eta_0 c_1\big(\boldsymbol{x}(k)\big)}{b_1}. \tag{4.123}$$

After the design of the CC control loop with the nonlinear PI state feedback controller, this controller is adapted in the next section to include the control of the evaporator temperature.

4.2.2 Nonlinear PI State Feedback Cascade Control Based on Exact Input-Output Linearization

In the previously designed control loop, the CC temperature, which governs the OT of the LHP, is the controlled temperature as it is common practice (see Sec. 3.2.2). However, changes in the dissipated heat at the heat source still have a direct impact on the evaporator temperature. This temperature is the nearest measurable LHP temperature to the cooled object that varies while keeping the CC temperature at a fixed setpoint temperature. Since the CC temperature control yields the most stable temperatures and the least risk for temperature oscillations at low powers compared to directly controlling the evaporator temperature (see Sec. 3.2.2), the model-based design of a cascade control makes it possible to control both the CC and the evaporator temperature simultaneously. By stabilizing the evaporator temperature, temperature changes of the cooled object are also further reduced. The structure of the nonlinear PI state feedback cascade control for LHPs is presented in Fig. 4.9.

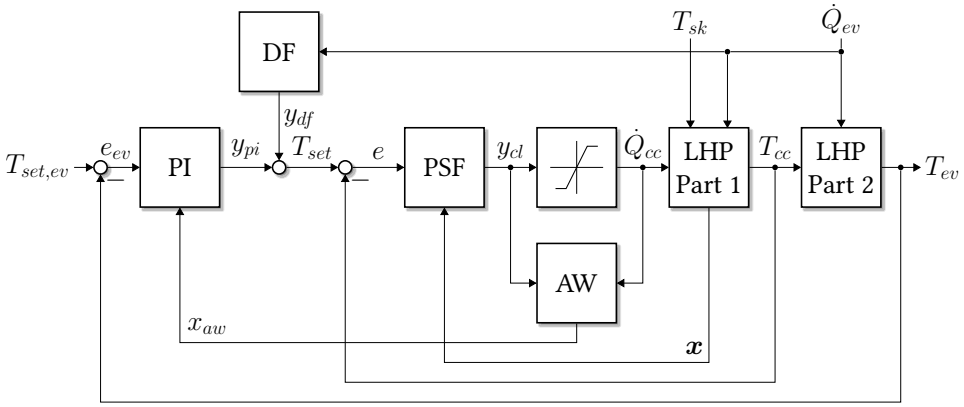

Figure 4.9: Cascade control loop of an LHP with a PI controller, a disturbance feedforward control (DF), and a nonlinear P state feedback control (PSF), the divided system parts LHP Part 1 and LHP Part 2, and an AW structure

The inner loop of the cascade control in Fig. 4.9 controls the CC temperature T_{cc}, while the outer loop controls the evaporator temperature T_{ev}. If the inner control loop reacts faster to changes than the outer control loop, the inner control loop can be regarded as a static transfer element for the design of the controller in the outer loop [Lun20a, p. 602]. Thus, the controllers in both loops can be designed in an iterative model-based design process. To reduce the residual control error of the evaporator temperature and to improve its stationary accuracy, an integral term in the outer controller of the cascade is sufficient [Vis06, p. 252]. That is why the nonlinear PI state feedback control in Sec. 4.2.1 is reduced to a nonlinear P state feedback control in the inner loop of the cascade control, while the integral term is incorporated in the linear controller of the outer loop. Hence, the inner control loop consists of the submodel LHP Part 1, represented by the SISO model (4.97), and the corresponding nonlinear P state feedback control, for which the state feedback control (4.107) is extended by a P controller $C_1(s)$ with $v(t) = y_p(t)$:

$$C_1(s) = \frac{y_p(s)}{e(s)} = K_{p1}, \tag{4.124}$$

with the proportional gain K_{p1}.

For the model-based control design of the PI controller in the outer control loop, the transfer function $G_1(s)$ of the total inner control loop is first established. It is composed of the transfer functions (4.106) and (4.124) in a feedback structure:

$$G_1(s) = \frac{T_{cc}(s)}{T_{set}(s)} = \frac{C_1(s)G(s)}{1 + C_1(s)G(s)} = \frac{\frac{K_{p1}}{s+\eta_0}}{1 + \frac{K_{p1}}{s+\eta_0}} = \frac{K_{p1}}{s + (\eta_0 + K_{p1})}. \tag{4.125}$$

Accordingly, the transfer function $G_2(s)$ of the submodel LHP Part 2 in Fig. 4.9 describes the transfer behavior between the controlled temperatures $T_{cc}(s)$ and $T_{ev}(s)$. This behavior is

modeled in (4.38) based on the thermal network of the LHP's evaporator in Fig. 4.4. Linearizing (4.38) around the OP with the Taylor series expansion and neglecting the higher-order terms, the linearized equation of $T_{ev}(t)$ is given by the following equation:

$$\Delta T_{ev}(t) = \mathcal{Z} \cdot \frac{R_{lk}}{R_{lk} + R_{sh}} \cdot \Delta T_{cc}(t) + \frac{R_{lk} R_{sh}}{R_{lk} + R_{sh}} \cdot \Delta \dot{Q}_{ev}(t), \tag{4.126}$$

with the parameter $\mathcal{Z}$:

$$\mathcal{Z} = \frac{R_{sh}}{R_{lk}} + \frac{B_{wf}^2 \cdot p_{cc}^{op}}{\left(A_{wf} - \ln\left(p_{ev}^{op}\right)\right)^2 \cdot \left(T_{cc}^{op} + C_{wf}\right)^2 \cdot p_{ev}^{op}}. \tag{4.127}$$

The respective pressures in (4.127) are calculated in the OP using (4.33) and (4.34):

$$p_{ev}^{op} = p_{cc}^{op} + \Delta p_{ca}, \tag{4.128}$$

$$p_{cc}^{op} = \exp\left(A_{wf} - \frac{B_{wf}}{C_{wf} + T_{cc}^{op}}\right). \tag{4.129}$$

The differences are defined as follows:

$$\Delta T_{ev}(t) = T_{ev}(t) - T_{ev}^{op}, \tag{4.130}$$

$$\Delta T_{cc}(t) = T_{cc}(t) - T_{cc}^{op}, \tag{4.131}$$

$$\Delta \dot{Q}_{ev}(t) = \dot{Q}_{ev}(t) - \dot{Q}_{ev}^{op}. \tag{4.132}$$

Transferring the system dynamics into the Laplace domain yields the transfer function $G_2(s)$:

$$G_2(s) = \frac{T_{ev}(s)}{T_{cc}(s)} = \mathcal{Z} \cdot \frac{R_{lk}}{R_{lk} + R_{sh}}. \tag{4.133}$$

Thus, the linear transfer behavior between $T_{cc}(s)$ and $T_{ev}(s)$ is a proportional gain since the inertia of the evaporator subsystem is neglected in the LHP control model (4.84) according to Assumption 4.2. The final transfer function $G_3(s)$ of the controlled subsystem in the outer control loop is obtained by the series connection of (4.125) and (4.133):

$$G_3(s) = \frac{T_{ev}(s)}{T_{set}(s)} = G_1(s) \cdot G_2(s) = \frac{K_{p1}}{s + (\eta_0 + K_{p1})} \cdot \mathcal{Z} \cdot \frac{R_{lk}}{R_{lk} + R_{sh}}. \tag{4.134}$$

Similar to (4.109), the transfer function $C_2(s)$ of the PI controller in the outer control loop is established by the following equation:

$$C_2(s) = \frac{T_{set}(s)}{e_{ev}(s)} = K_{p2} + K_{i2} \cdot \frac{1}{s}, \tag{4.135}$$

with the transformed evaporator control error $e_{ev}(s)$ being defined as the difference between the transformed evaporator setpoint temperature $T_{set,ev}(s)$ and the transformed evaporator temperature $T_{ev}(s)$:

$$e_{ev}(s) = T_{set,ev}(s) - T_{ev}(s). \tag{4.136}$$

The controller gains K_{p2} and K_{i2} in (4.135) are determined based on (4.134) with the method described in the previous section.

The disturbance transfer behavior between $\dot{Q}_{ev}(t)$ and $T_{ev}(t)$ in (4.126) is modeled by the corresponding transfer function $G_4(s)$:

$$G_4(s) = \frac{T_{ev}(s)}{\dot{Q}_{ev}(s)} = \frac{R_{lk}R_{sh}}{R_{lk} + R_{sh}}. \tag{4.137}$$

For an improved disturbance response, a disturbance feedforward control (see [Lun20a, p. 596]) is suggested, as depicted in Fig. 4.9. Based on (4.137), the transfer function $K_q(s)$ of the feedforward component is determined by the quotient of (4.134) and (4.137).

$$K_q(s) = \frac{G_4(s)}{G_3(s)} = \frac{R_{sh} \cdot \big(s + (\eta_0 + K_{p1})\big)}{K_{p1} \cdot \mathcal{Z}}. \tag{4.138}$$

Since the degree of the numerator is smaller than the degree of the denominator in (4.138), only a stationary disturbance feedforward control is technically realizable, i.e. for $s = 0$ [Lun20a, p. 597]:

$$K_q = \frac{R_{sh} \cdot (\eta_0 + K_{p1})}{K_{p1} \cdot \mathcal{Z}}. \tag{4.139}$$

For the sake of completeness, the total nonlinear PI state feedback cascade controller is given in the discrete domain for the real implementation by

$$y_{cl}(k) = \frac{y_p(k) - a_1\big(\boldsymbol{x}(k), \boldsymbol{d}(k)\big) - \eta_0 c_1\big(\boldsymbol{x}(k)\big)}{b_1}, \tag{4.140}$$

with the P controller

$$y_p(k) = K_{p1} \cdot e(k) \tag{4.141}$$

and the discrete control error

$$e(k) = T_{set}(k) - T_{cc}(k). \tag{4.142}$$

The discrete PI controller with AW structure and disturbance feedforward control is given by

$$x_{aw}(k) = K_{aw} \cdot \Big(y_{cl}(k-1) - \dot{Q}_{cc}(k-1)\Big), \tag{4.143}$$

$$i_{pi}(k) = K_{i2} \cdot T_{st} \cdot \big(e_{ev}(k) - x_{aw}(k)\big) + i_{pi}(k-1), \tag{4.144}$$

$$y_{ff}(k) = -K_q \cdot \dot{Q}_{ev}(k-1), \tag{4.145}$$

$$T_{set}(k) = K_{p2} \cdot e_{ev}(k) + i_{pi}(k) + y_{ff}(k). \tag{4.146}$$

As mentioned before, both the cascade controller and the single-loop controller in the previous section based on the exact input-output linearization depend on the availability of all three LHP states. The determination of the unmeasured states in the control loop is presented in the next section.

4.2.3 Nonlinear State and Parameter Estimation

The designed nonlinear state feedback controllers (4.123) and (4.140) are functions of the system's states. For the control design, the states have been assumed to be available so far. Now, since not all states are measurable in the considered LHP system, an adequate state estimation method is proposed for the operation of the controller in the real application.

First of all, the observability of the nonlinear LHP model (4.84) is investigated. According to [Ada18, p. 526], a general nonlinear system in the form of (2.1) is said to be *observable* if all initial states $\boldsymbol{x}_0$ are uniquely determinable from the input vector $\boldsymbol{u}(t)$ and the output vector $\boldsymbol{y}(t)$ for all inputs $\boldsymbol{u}$ in finite time. If the determination of $\boldsymbol{x}_0$ is only possible in the neighborhood of a point in the state space for all points, the system is said to be *weakly observable*.

Since the relative degree δ of the input-affine LHP model (4.97) is smaller than the system order, i.e. $\delta < n$ in accordance with (4.101), the observability of (4.97) cannot be deduced from the equality of both numbers (see Theorem 87 in [Ada18, p. 540]). Instead, the criterion in Theorem 4.2 based on [Ada18, p. 538] enables the investigation of the observability.

Theorem 4.2 (Weak observability of an input-affine system)
An input-affine system

$$\dot{\boldsymbol{x}} = \boldsymbol{a}(\boldsymbol{x}) + \boldsymbol{b}(\boldsymbol{x}) \cdot u, \tag{4.147a}$$

$$y = c(\boldsymbol{x}). \tag{4.147b}$$

is said to be weakly observable if the following condition holds for all $\boldsymbol{x}$ and u:

$$\operatorname{rank}\left(\boldsymbol{Q}_{obs}\right) = n \tag{4.148}$$

with the observability matrix

$$\boldsymbol{Q}_{obs} = \begin{bmatrix} \frac{\partial c(\boldsymbol{x})}{\partial \boldsymbol{x}} \\ \frac{\partial L_{\boldsymbol{a}} c(\boldsymbol{x})}{\partial \boldsymbol{x}} + \frac{\partial L_{\boldsymbol{b}} c(\boldsymbol{x})}{\partial \boldsymbol{x}} u \\ \frac{\partial L_{\boldsymbol{a}}^2 c(\boldsymbol{x})}{\partial \boldsymbol{x}} + \frac{\partial L_{\boldsymbol{b}} L_{\boldsymbol{a}} c(\boldsymbol{x})}{\partial \boldsymbol{x}} u + \frac{\partial L_{\boldsymbol{a}} L_{\boldsymbol{b}} c(\boldsymbol{x})}{\partial \boldsymbol{x}} u + \frac{\partial L_{\boldsymbol{b}}^2 c(\boldsymbol{x})}{\partial \boldsymbol{x}} u^2 + \frac{\partial L_{\boldsymbol{b}} c(\boldsymbol{x})}{\partial \boldsymbol{x}} \dot{u} \\ \vdots \\ \frac{\partial L_{\boldsymbol{a}}^{n-1} c(\boldsymbol{x})}{\partial \boldsymbol{x}} + \frac{\partial L_{\boldsymbol{b}} L_{\boldsymbol{a}}^{n-2} c(\boldsymbol{x})}{\partial \boldsymbol{x}} u + \ldots + \frac{\partial L_{\boldsymbol{b}} c(\boldsymbol{x})}{\partial \boldsymbol{x}} u^{(n-2)} \end{bmatrix}. \tag{4.149}$$

For the LHP model (4.97), the following $\boldsymbol{Q}_{obs}$ results from the evaluation of the Lie derivatives in (4.149):

$$\boldsymbol{Q}_{obs} = \begin{bmatrix} 1 & 0 & 0 \\ \dfrac{\mathrm{d}a_1}{\mathrm{d}T_{cc}} & \dfrac{\mathrm{d}a_1}{\mathrm{d}L_{2\phi}} & \dfrac{\mathrm{d}a_1}{\mathrm{d}\dot{m}^l} \\ \dfrac{\mathrm{d}\left(\frac{\partial \boldsymbol{a}}{\mathrm{d}\boldsymbol{x}}\right)}{\mathrm{d}T_{cc}} + \dfrac{\mathrm{d}\left(\frac{\mathrm{d}a_1}{\mathrm{d}T_{cc}} b_1\right)}{\mathrm{d}T_{cc}} u & \dfrac{\mathrm{d}\left(\frac{\partial \boldsymbol{a}}{\mathrm{d}\boldsymbol{x}}\right)}{\mathrm{d}L_{2\phi}} + \dfrac{\mathrm{d}\left(\frac{\mathrm{d}a_1}{\mathrm{d}T_{cc}} b_1\right)}{\mathrm{d}L_{2\phi}} u & \dfrac{\mathrm{d}\left(\frac{\partial \boldsymbol{a}}{\mathrm{d}\boldsymbol{x}}\right)}{\mathrm{d}\dot{m}^l} + \dfrac{\mathrm{d}\left(\frac{\mathrm{d}a_1}{\mathrm{d}T_{cc}} b_1\right)}{\mathrm{d}\dot{m}^l} u \end{bmatrix}. \tag{4.150}$$

A statement about the rank of (4.150) is possible through a numerical analysis with values for the states $T_{cc}(t)$, $L_{2\phi}(t)$, and $\dot{m}^l(t)$ as well as the inputs $\dot{Q}_{cc}(t)$, $\dot{Q}_{ev}(t)$, and $T_{sk}(t)$ distributed over the LHP operating range. This numerical analysis, as presented in Appendix A.4, has not yielded any exception to the condition (4.148). Thus, it suggests that (4.150) has indeed a full rank inside the operating range, and therefore, the LHP model is assumed to be weakly observable. The functionality of an LHP state estimation is additionally verified in the simulations in Sec. 7.4.1.

For the nonlinear estimation of the LHP states, the *square-root unscented Kalman filter* (SRUKF) in [vdMW01] is chosen based on the following considerations (cf. [GMSH20b]). The classical Kalman filter was originally developed for the state estimation of linear systems [Kal60]. For nonlinear systems, the extended Kalman filter (EKF) is commonly used, which linearizes the nonlinear transformation of the states around the OP [QSWL18]. For the strongly nonlinear LHP state-space model (4.84), the state estimation with an EKF does not converge due to the constrained local validity of the disturbed linearized model over the entire operating range. Therefore, the unscented Kalman filter (UKF) [JU97] is often the preferred Kalman filter for nonlinear systems, which replaces the linearization with the unscented transformation (UT). The UT transforms the mean and the covariance of a random state vector directly based on a set of deterministic vectors, the so-called *sigma points*. Their ensemble mean and covariance equal the mean and covariance of the random state vector [Sim06, p. 441]. Hence, the UKF provides a derivative-free alternative to the EKF. In addition, the square-root form of the UKF enables an efficient implementation and an improved numerical stability by directly updating the matrix square root of the state covariance instead of the entire covariance itself [vdMW01].

According to the SRUKF algorithm given in Appendix A.5 with the estimated state vector $\hat{\boldsymbol{x}}$, the sigma points of the states and outputs are calculated and transformed in every discrete time step k. Thus, the continuous progression of the states of the LHP state-space model (4.84) must be approximated by a finite number of points in time. For such an approximation of the continuous LHP model, *Euler's forward method* is usually utilized because of its simplicity. This time discretization method forms a system of difference equations via the numerical integration of the time derivative in (4.84a):

$$\begin{aligned} \boldsymbol{x}(k) &= \boldsymbol{x}(k-1) + \int_{(k-1)T_{st}}^{kT_{st}} \boldsymbol{f}\big(\boldsymbol{x}(t), u(t), \boldsymbol{d}(t)\big)\,\mathrm{d}t \\ &\approx\ \boldsymbol{x}(k-1) + T_{st} \cdot \boldsymbol{f}\big(\boldsymbol{x}(k-1), u(k-1), \boldsymbol{d}(k-1)\big). \end{aligned} \tag{4.151}$$

In the case of the LHP, a peculiarity of the ordinary differential equation system (4.84) becomes apparent when simulating (4.151) discretized by the explicit one-step Euler method. A very small fixed step size in the range of $T_{st} = 0.1\,\mathrm{ms}$ is required to resolve the differential equation of $\dot{m}^l$ correctly, although a step size of $T_{st} = 1\,\mathrm{s}$ is sufficient for the other two differential equations. The small step size is connected to the fact that the CC temperature T_{cc} as first state and the length of the two-phase region $L_{2\phi}$ as second state show higher change rates on the order of $1 \times 10^{-2}\,\mathrm{K\,s^{-1}}$ and $1 \times 10^{-3}\,\mathrm{m\,s^{-1}}$, respectively, while the liquid mass flow rate $\dot{m}^l$ varies to a much smaller extend on the order of $2 \times 10^{-6}\,\mathrm{kg\,s^{-2}}$. In other words, the dynamics of the three states differ strongly. This property of the underlying ordinary differential equation system is called *stiffness* [Ada18, p. 52]. Due to the small step size consistent with the shortest time constant, a high number of calculations and therefore an excessive simulation time of the stiff LHP model results. The elevated computation time may also jeopardize the real-time capability of Euler's forward method for the LHP application. Furthermore, the temperature sensors of the LHP are usually sampled in the range of seconds similar to the cycle time of the control algorithm. Thus, a multi-rate framework is necessary to integrate the discretized state-space model with a smaller step size into the control algorithm. In the framework, the final states for the controller in one cycle correspond to the last discrete time step of the repeatedly solved difference equation (4.151).

A great impact on the states has the heat load $\dot{Q}_{ev}$, which directly influences the superheated evaporator temperature T_{ev} according to (4.38). The size of the impact depends on the introduced thermal resistance R_{sh}, which is exposed to fluctuations over the LHP operating range due to the complex flow dynamics inside the evaporator. Based on the measurement of T_{ev} and the availability of $\dot{Q}_{ev}$, the parameter R_{sh} can be adjusted to the varying operating conditions to improve the consistency between the model results and the measurements. For this purpose, the thermal resistance R_{sh} in the output equation (4.72) is estimated by minimizing the error between the calculated and the measured evaporator temperature T_{ev}. An adequate parameter estimation method for the LHP control loop follows directly from the state estimation based on the SRUKF. The corresponding algorithm to calculate the estimated parameter $\hat{p}$ is detailed in Appendix A.5.2.

The combined estimation of the state variables T_{cc}, $L_{2\phi}$, and $\dot{m}^l$ and the parameter R_{sh} of the state-space model (4.84) and its integration into the final control loop are presented in Fig. 4.10 using the example of the nonlinear PI state feedback controller in Sec. 4.2.1.

With the application of the SRUKFs, the model-based control design based on the established nonlinear LHP state-space model (4.84) is completed. The SRUKFs as well as both controllers are evaluated in simulations in Sec. 7.4.1. A short conclusion of this chapter is given in the following section.

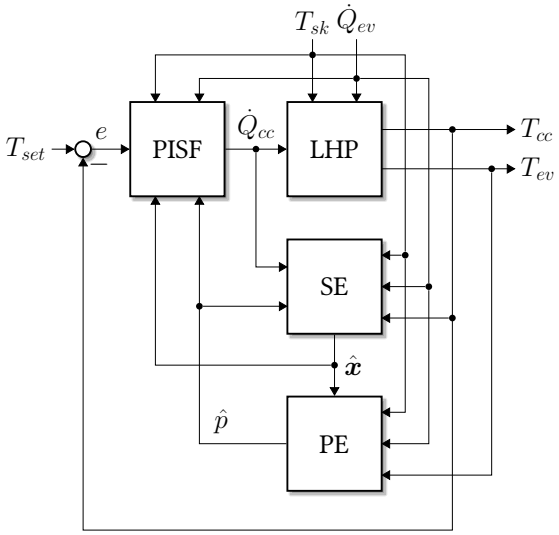

Figure 4.10: Control loop of an LHP with a state- and parameter-dependent nonlinear PI state feedback controller (PISF) and two square-root unscented Kalman filters (SRUKFs) for the nonlinear state (SE) and parameter estimation (PE)

4.3 Conclusion

In contrast to the state of the art, the presented nonlinear LHP model with lumped parameters includes all the equations necessary to physically model the significant dynamics of a multi-phase heat transport system with in fact distributed parameters, such as the LHP. Only by modeling the relevant mass flow dynamics and phase transitions with the liquid mass flow rate $\dot{m}^l$ and the length of the two-phase region $L_{2\phi}$, the variations of the uncontrollable inputs, namely the disturbances $\dot{Q}_{ev}$ and T_{sk}, can be incorporated. Thus, an efficient simulation of the dynamics of the measured LHP temperatures is possible. Furthermore, the desired state-space form for the model-based design of controllers for the control heaters of LHPs has been met.

The proposed nonlinear model-based designed controller based on the exact input-output linearization simplifies the nonlinear external dynamics of the governing CC temperature T_{cc} including the impact of the disturbances, while the internal dynamics of $\dot{m}^l$ and $L_{2\phi}$ have no impact on the controlled T_{cc}. Instead, their stability has been investigated for a stable overall control loop. With every change of the inputs, a new OP is targeted. Thus, the local stability of the multiple equilibrium points of the internal dynamics has been investigated and verified with Lyapunov's indirect method.

Due to the model-based design approach, the development of a cascade control for the LHP is possible. The cascade control is able to control the evaporator temperature as closest temperature to the cooled object besides the CC temperature for a smoother temperature

curve of the object. Furthermore, the precise modeling of the disturbance influence enables a disturbance feedforward control when controlling the evaporator temperature.

For the unmeasured states, a nonlinear state estimation in form of an SRUKF is necessary. It has been proven that the LHP model is already weakly observable with the controlled CC temperature as single output variable. The integrated parameter estimation, also based on an SRUKF, adapts the state estimation to the measured evaporator temperature to consider the influence of the unmodeled flow dynamics on the heat transfer in the evaporator.

By simplifying the model equations, a different state-space representation is formed in the next chapter for the model-based design of controllers with lower complexity and hardware requirements for a simplified application.

5 Simplified Model-Based Control Designs for Loop Heat Pipes

Considering the limitation of energy demand and mass in aerospace systems, a model-based design of controllers for the temperature control of LHPs with minor algebraic complexity and reduced computational effort is preferred. For this reason, a simplified modeling approach based on further model assumptions is introduced in this chapter. By concentrating on the control-relevant system dynamics, not only the modeling approach is simplified with regard to the analytical solvability of the complex equations, but also the number of model parameters is reduced to save expensive test bench time for parameter determination. In the resulting simplified control model, the dynamics of the measurable states are modeled leading to the model-based design of the state-of-the-art controllers and further extensions with low computational effort for the efficient use in aerospace or terrestrial applications. In this way, LHP systems already delivered with state-of-the-art control software can be re-parameterized and extended with little effort since no hardware adjustments are necessary. In the first section, the simplified modeling approach is presented. In the second section, the model-based designs of the state-of-the-art LHP controller and LHP-specific extended controllers based on the simplified model are derived.

5.1 Simplified Dynamical Modeling

The result of the simplified modeling approach, which is based on [GSHH18], is a three-dimensional LHP state-space model. With further assumptions, the complex LHP control model in Sec. 4 is adapted to derive a simplified control model, in which the dynamics of the basic temperatures of the LHP are decoupled from the fluid dynamics reducing the mathematical complexity. In doing so, the validity of the simplified control model is restricted to the OP, while incorporating only measurable temperatures as state variables for a simplified control design. Similar to the modeling approach in Sec. 4, the fundamental equations of the simplified model are still established based on the relevant thermodynamic principles presented in Sec. 3.1.

5.1.1 Model Assumptions

In addition to the assumptions in Sec. 4.1.1, further simplifications are necessary to reduce the complexity of the LHP control model for simplified model-based control designs.

Assumption 5.1. *The mass flow rates $\dot{m}^l$ and $\dot{m}^v$ between the condenser and the CC-evaporator assembly are equal in transient states.*

Assumption 5.2. *The temperature change between the evaporator output and the CC input can be simplified by one temperature node T_{co}.*

Assumption 5.3. *Superheating is neglected.*

Discussion of the Assumptions

In steady state, the mass flow rates $\dot{m}^l$ and $\dot{m}^v$ are equal, and the temperatures reach their equilibria. Assumption 5.1 transfers this property to transient states since the imbalance of the mass flow rates $\dot{m}^l$ and $\dot{m}^v$ caused by temperature changes can be neglected [LWL10]. Furthermore, they only change with the OP, as the fluid inertia has a smaller impact on the temperature profiles than the thermal inertia [KPGT08]. Assumption 5.2 results from the fact that the controlled variable of the LHP is the CC temperature T_{cc}. In addition, a temperature sensor at the input of the CC for parameter approximation is not available in the considered LHP setting. Since little superheating takes place in the considered LHP operating range (see [MKHW19]), Assumption 5.3 applies. Hence, the vapor in the evaporator is assumed to be in a saturation state at all times.

Delimitation of the Subsystems

In accordance with Sec. 3.1.3, the LHP is subdivided in such a way that the evaporator (EV) only contains a vapor phase, and the compensation chamber (CC) and the condenser (CO) are two-phase subsystems at all times. In Fig. 5.1, the respective boundaries of the three subsystems are depicted in color.

In comparison with the subdivision in Sec. 4, the boundary between the CC and the evaporator subsystems persists at the liquid-vapor interface in the primary wick. However, the condenser subsystem combines the transport lines with the condenser based on Assumption 5.2. Hence, the heat exchange of the working fluid with the heat sink and the surroundings is described with one overall heat flow $\dot{Q}_{co}$. The remaining heat flows in Fig. 5.1 correspond to the heat flows described in Sec. 4.1.

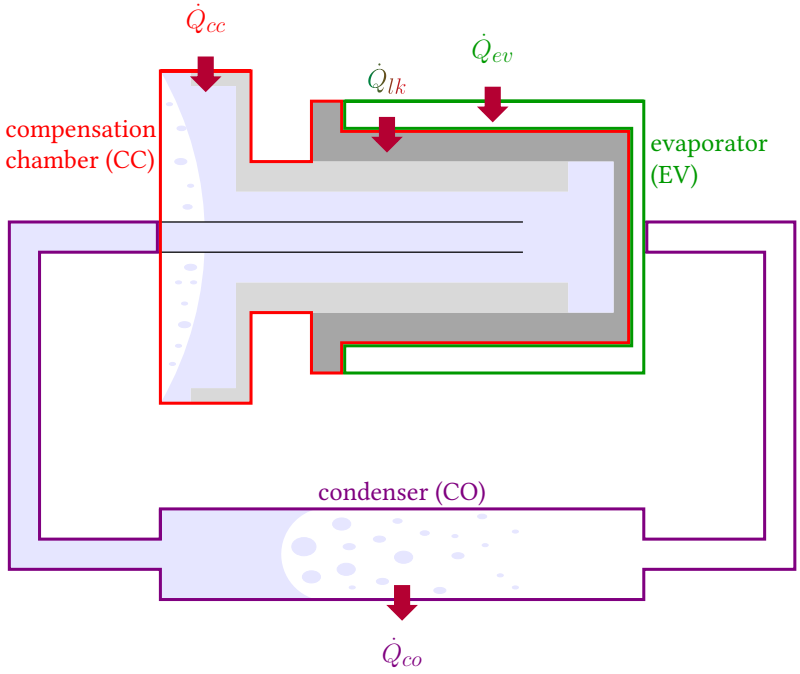

Figure 5.1: Simplified LHP subsystems with their corresponding main heat flows

5.1.2 Simplified State-Space Representation of Loop Heat Pipes

After the division of the LHP into three subsystems in the previous section, the respective balance equations are established independently based on the first law of thermodynamics in (3.11). One by one, the equations of the CC subsystem, the evaporator subsystem, and the condenser subsystem are derived and combined to the simplified state-space model of the LHP.

Compensation Chamber

According to Assumption 5.1, the mass flow $\dot{m}^l(t)$ and $\dot{m}^v(t)$ of the liquid phase and the vapor phase of the simplified model coincide with one overall constant mass flow $\dot{m}$:

$$\dot{m}^v(t) = \dot{m}^l(t) = \dot{m}. \tag{5.1}$$

Hence, the energy balance equation of the CC in (4.13) is rewritten for the simplified model since the same boundary of the CC subsystem is chosen in both models (see Fig 4.3 and Fig. 5.1):

$$\frac{\mathrm{d}U_{cc}(t)}{\mathrm{d}t} = \dot{m} \cdot \left(h^l_{co}(t) - h^l_{cc}(t)\right) + \dot{Q}_{cc}(t) + \dot{Q}_{lk}(t), \tag{5.2}$$

where the inlet of the CC subsystem corresponds to the outlet of the condenser subsystem. The heat leak $\dot{Q}_{lk}(t)$ is defined in (4.18). With (5.1), the total mass $m_{cc}^{2\phi}(t)$ of the two-phase fluid in the CC subsystem does not change following the law of conservation of mass in (3.18):

$$\frac{\mathrm{d}m_{cc}^{2\phi}(t)}{\mathrm{d}t} = 0. \tag{5.3}$$

With a fixed ratio β between the volumes of the liquid and the vapor phase in the two-phase CC in saturation state, no work is done on the boundary between both phases, and the internal energy $U_{cc}(t)$ of the CC subsystem reduces to the sum of the enthalpies of the saturated phases (see (3.79)):

$$U_{cc}(t) = H_{cc}(t) = h_{cc}^{l}(t) \cdot m_{cc}^{l} + h_{cc}^{v}(t) \cdot m_{cc}^{v}. \tag{5.4}$$

Considering (5.3), the time derivative of the enthalpy $H_{cc}(t)$ is a function of the time derivative of the mean temperature $T_{cc}(t)$ in the CC subsystem:

$$\frac{\mathrm{d}U_{cc}(t)}{\mathrm{d}t} = \frac{\mathrm{d}H_{cc}(t)}{\mathrm{d}t} = \frac{\mathrm{d}H_{cc}(t)}{\mathrm{d}T_{cc}(t)} \cdot \frac{\mathrm{d}T_{cc}(t)}{\mathrm{d}t}. \tag{5.5}$$

Applying the electrical analogy in Sec. 3.1.2 and the determination of the specific enthalpies in Sec. 3.1, (5.2) is rewritten as

$$C_{cc}^{op} \cdot \frac{\mathrm{d}T_{cc}(t)}{\mathrm{d}t} = \dot{m} \cdot \bar{c}_{co,cc}^{l} \cdot \big(T_{co}(t) - T_{cc}(t)\big) + \dot{Q}_{cc}(t) + \dot{Q}_{lk}(t), \tag{5.6}$$

with the thermal capacitance C_{cc}^{op}. Under consideration of Assumption 4.5, C_{cc}^{op} results from (3.81), (3.82), (4.3) - (4.6), and (4.11) in the OP:

$$\begin{aligned} C_{cc}^{op} = {} & V_{cc} \cdot \bar{c}_{cc,ref}^{l} \cdot \left(\beta^{op} \cdot \rho_{cc}^{l} + (1-\beta^{op}) \cdot \rho_{cc}^{v,op}\right) \\ & + V_{cc} \cdot (1-\beta^{op}) \cdot \left(\frac{\Delta h_{cc}^{v} \rho_{cc}^{l} \rho_{cc}^{v,op}}{R(T_{cc}^{op})^2 \left(\rho_{cc}^{l} - \rho_{cc}^{v,op}\right)} - \frac{\rho_{cc}^{v,op}}{T_{cc}^{op}}\right) \\ & \cdot \left(h_{ref}^{l} + \bar{c}_{cc,ref}^{l} \cdot (T_{cc}^{op} - T_{ref}) + \Delta h_{cc}^{v}\right). \end{aligned} \tag{5.7}$$

Evaporator

For the single-phase evaporator, the energy balance equation in (4.28) holds for the simplified model as well due to the equally selected delimitation of the evaporator subsystems in both models (see Fig 4.3 and Fig. 5.1). Considering Assumption 5.1 and Assumption 5.3, the specific enthalpy in (4.28) is resolved based on (3.82) and (5.1) as follows:

$$\frac{\mathrm{d}U_{ev}(t)}{\mathrm{d}t} = \dot{m} \cdot \left(\bar{c}_{cc,ev}^{l} \cdot \big(T_{cc}(t) - T_{ev}(t)\big) - \Delta h_{ev}^{v}\right) + \dot{Q}_{ev}(t) - \dot{Q}_{lk}(t). \tag{5.8}$$

Finally, the internal energy U_{ev}(t) is rewritten with the thermal capacitance C_{ev}^{op} in the OP:

$$C_{ev}^{op} \cdot \frac{\mathrm{d}T_{ev}(t)}{\mathrm{d}t} = \dot{m} \cdot \left(\bar{c}_{cc,ev}^{l} \cdot \big(T_{cc}(t) - T_{ev}(t)\big) - \Delta h_{ev}^{v}\right) + \dot{Q}_{ev}(t) - \dot{Q}_{lk}(t). \tag{5.9}$$

The thermal capacitance C_{ev}^{op} is derived from (5.7) considering the saturated, vapor-filled evaporator:

$$\begin{aligned} C_{ev}^{op} = {} & V_{ev} \cdot \bar{c}_{ev,ref}^{l} \cdot \rho_{ev}^{v,op} \\ & + V_{ev} \cdot \left(\frac{\Delta h_{ev}^{v} \rho_{ev}^{l} \rho_{ev}^{v,op}}{R (T_{ev}^{op})^2 \left(\rho_{ev}^{l} - \rho_{ev}^{v,op} \right)} - \frac{\rho_{ev}^{v,op}}{T_{ev}^{op}} \right) \\ & \cdot \left(h_{ref}^{l} + \bar{c}_{ev,ref}^{l} \cdot (T_{ev}^{op} - T_{ref}) + \Delta h_{ev}^{v} \right). \end{aligned} \tag{5.10}$$

Condenser

Similar to the previous two energy balance equations, the energy balance equation of the condenser subsystem is obtained by applying the first law of thermodynamics in (3.11):

$$C_{co}^{op} \cdot \frac{\mathrm{d}T_{co}(t)}{\mathrm{d}t} = \dot{m} \cdot \left(\bar{c}_{ev,co}^{l} \cdot \left(T_{ev}(t) - T_{co}(t) \right) + \Delta h_{ev}^{v} \right) - \dot{Q}_{co}(t), \tag{5.11}$$

where the incoming enthalpy flow of the vapor from the evaporator and the outgoing enthalpy flow of the liquid to the CC along with the overall heat flow $\dot{Q}_{co}(t)$ determine the change of the internal energy of the condenser subsystem. The overall heat flow $\dot{Q}_{co}(t)$, which describes the heat exchange of the condenser subsystem with the heat sink and the surroundings, is approximated with (3.50):

$$\dot{Q}_{co}(t) = \frac{1}{R_{co}} \cdot \left(\frac{T_{ev}(t) + T_{co}(t)}{2} - T_{sk}(t) \right), \tag{5.12}$$

where the arithmetic mean of the evaporator temperature $T_{ev}(t)$ and the condenser temperature $T_{co}(t)$ is taken as the average temperature in the condenser subsystem. The thermal capacitance C_{co}^{op} is calculated similar to (5.7) in the OP:

$$\begin{aligned} C_{co}^{op} = {} & V_{co} \cdot \bar{c}_{co,ref}^{l} \cdot \left(\beta_{co}^{op} \cdot \rho_{co}^{l} + (1 - \beta_{co}^{op}) \cdot \rho_{co}^{v,op} \right) \\ & + V_{co} \cdot (1 - \beta_{co}^{op}) \cdot \left(\frac{\Delta h_{co}^{v} \rho_{co}^{l} \rho_{co}^{v,op}}{R (T_{co}^{op})^2 \left(\rho_{co}^{l} - \rho_{co}^{v,op} \right)} - \frac{\rho_{co}^{v,op}}{T_{co}^{op}} \right) \\ & \cdot \left(h_{ref}^{l} + \bar{c}_{co,ref}^{l} \cdot (T_{co}^{op} - T_{ref}) + \Delta h_{co}^{v} \right), \end{aligned} \tag{5.13}$$

with the fixed volume fraction ratio β_{co}^{op}.

Simplified LHP State-Space Model

The simplified dynamical model of the LHP forms the following nonlinear, three-dimensional state-space model according to Def. 2.1:

$$\dot{\boldsymbol{x}}(t) = \boldsymbol{f}\big(\boldsymbol{x}(t), u(t), \boldsymbol{d}(t)\big), \tag{5.14a}$$

$$\boldsymbol{y}(t) = \boldsymbol{x}(t), \tag{5.14b}$$

with $\boldsymbol{x}(t) = [T_{cc}(t), T_{ev}(t), T_{co}(t)]^\top$, $u(t) = \dot{Q}_{cc}(t)$, and $\boldsymbol{d}(t) = [\dot{Q}_{ev}(t), T_{sk}(t)]^\top$. The three state variables in the state vector $\boldsymbol{x}(t)$ correspond to the temperatures $T_{cc}(t)$ at the CC, $T_{ev}(t)$ at the evaporator, and $T_{co}(t)$ at the condenser outlet. These three state variables are related to the three temperature sensors TS 1, TS 2, and TS 4 in Fig. 4.1 and form the output vector $\boldsymbol{y}(t)$ as well. The heat flow $\dot{Q}_{cc}(t)$ from the control heater to the CC is the single input variable $u(t)$ of the system. The disturbance vector $\boldsymbol{d}(t)$ is characterized by the heat load $\dot{Q}_{ev}(t)$ at the evaporator and the sink temperature $T_{sk}(t)$ at the condenser as the two external disturbance inputs to the system. The state equation (5.14a) of the simplified LHP state-space model is obtained by combining the previously established first-order differential equations (5.6), (5.9), and (5.12) in the vector function $\boldsymbol{f} = [f_1, f_2, f_3]^\top$ as follows[9]:

$$f_1 = \frac{1}{C_{cc}^{op}} \cdot \left(\dot{m} \cdot \bar{c}_{co,cc}^{l} \cdot (T_{co} - T_{cc}) + \dot{Q}_{cc} + \frac{1}{R_{lk}} \cdot (T_{ev} - T_{cc}) \right), \tag{5.15}$$

$$f_2 = \frac{1}{C_{ev}^{op}} \cdot \left(\dot{m} \cdot \left(\bar{c}_{cc,ev}^{l} \cdot (T_{cc} - T_{ev}) - \Delta h_{ev}^{v} \right) + \dot{Q}_{ev} - \frac{1}{R_{lk}} \cdot (T_{ev} - T_{cc}) \right), \tag{5.16}$$

$$f_3 = \frac{1}{C_{co}^{op}} \cdot \left(\dot{m} \cdot \left(\bar{c}_{ev,co}^{l} \cdot (T_{ev} - T_{co}) + \Delta h_{ev}^{v} \right) - \frac{1}{R_{co}} \cdot \left(\frac{T_{ev} + T_{co}}{2} - T_{sk} \right) \right). \tag{5.17}$$

Besides the physical properties of the working fluid, which are the mean specific heat capacities $\bar{c}$ and the specific heat of evaporation Δh^v, six parameters are included in the simplified dynamical model. The three thermal capacitances C_{cc}^{op}, C_{ev}^{op}, and C_{co}^{op} of the three subsystems determine the dynamics of the corresponding temperatures. The two thermal resistances R_{lk} and R_{co} define the heat leak and the heat flow to the heat sink, respectively. As the last parameter, the steady-state mass flow rate $\dot{m}$ governs the enthalpy exchange between the subsystems.

For the subsequent linear control designs, the nonlinear LHP state-space model (5.14) is linearized about the steady-state OP. By performing the Taylor series expansion of the state about the OP, while neglecting the higher-order terms, the linear approximation of (5.14) yields the linearized simplified LHP state-space model according to Def. 2.2:

$$\Delta\dot{\boldsymbol{x}}(t) = \boldsymbol{A}_{lin} \cdot \Delta\boldsymbol{x}(t) + \boldsymbol{b}_{lin} \cdot \Delta u(t) + \boldsymbol{E}_{lin} \cdot \Delta\boldsymbol{d}(t), \tag{5.18a}$$

$$\Delta\boldsymbol{y}(t) = \boldsymbol{C}_{lin} \cdot \Delta\boldsymbol{x}(t) \tag{5.18b}$$

with

$$\Delta\boldsymbol{x}(t) = \begin{bmatrix} T_{cc}(t) - T_{cc}^{op} \\ T_{ev}(t) - T_{ev}^{op} \\ T_{co}(t) - T_{co}^{op} \end{bmatrix}, \tag{5.19}$$

$$\Delta u(t) = \dot{Q}_{cc}(t) - \dot{Q}_{cc}^{op}, \tag{5.20}$$

$$\Delta\boldsymbol{d}(t) = \begin{bmatrix} \dot{Q}_{ev}(t) - \dot{Q}_{ev}^{op}, \\ T_{sk}(t) - T_{sk}^{op}. \end{bmatrix}. \tag{5.21}$$

With the separation of the disturbance variables $\dot{Q}_{ev}$ and T_{sk} from the input variable $\dot{Q}_{cc}$, the state disturbance matrix $\boldsymbol{E}_{lin}$ is established besides the system matrix $\boldsymbol{A}_{lin}$, the input vector

[9] In order to ease notation, time dependencies are dropped.

$\boldsymbol{b}_{lin}$, and the output matrix $\boldsymbol{C}_{lin}$:

$$\boldsymbol{A}_{lin} = \begin{bmatrix} -\frac{1}{C_{cc}^{op}}\left(\bar{c}_{co,cc}^{l}\dot{m} + \frac{1}{R_{lk}}\right) & \frac{1}{C_{cc}^{op}R_{lk}} & \frac{1}{C_{cc}^{op}}\left(\bar{c}_{co,cc}^{l}\dot{m}\right) \\ \frac{1}{C_{ev}^{op}}\left(\bar{c}_{cc,ev}^{l}\dot{m} + \frac{1}{R_{lk}}\right) & -\frac{1}{C_{ev}^{op}}\left(\bar{c}_{cc,ev}^{l}\dot{m} + \frac{1}{R_{lk}}\right) & 0 \\ 0 & \frac{1}{C_{co}^{op}}\left(\bar{c}_{ev,co}^{l}\dot{m} - \frac{1}{2R_{co}}\right) & -\frac{1}{C_{co}^{op}}\left(\bar{c}_{ev,co}^{l}\dot{m} + \frac{1}{2R_{co}}\right) \end{bmatrix}, \tag{5.22}$$

$$\boldsymbol{b}_{lin} = \begin{bmatrix} \frac{1}{C_{cc}^{op}} \\ 0 \\ 0 \end{bmatrix}, \tag{5.23}$$

$$\boldsymbol{E}_{lin} = \begin{bmatrix} 0 & 0 \\ \frac{1}{C_{ev}^{op}} & 0 \\ 0 & \frac{1}{C_{co}^{op}R_{co}} \end{bmatrix}, \tag{5.24}$$

$$\boldsymbol{C}_{lin} = \begin{bmatrix} 1 & 0 & 0 \\ 0 & 1 & 0 \\ 0 & 0 & 1 \end{bmatrix}. \tag{5.25}$$

5.2 Control Designs Based on the Simplified Model

According to the state of the art in Sec. 2, heuristic PID controllers are commonly used for the LHP temperature control due to their comparatively simple application and adequate performance in most systems. To replace the individual heuristic tuning approach with a systematic parameterization, the first model-based design of this linear LHP controller is proposed in the following. Based on the simplified LHP model in the previous section, further extensions of the PID controller and a nonlinear controller are presented, which are especially suitable for the LHP temperature control in applications with low computational power.

5.2.1 PI Controller with Anti-Windup Strategy

Due to its simple structure and low computational effort, the PID controller is most commonly used in the industry for automation processes since it provides a stable control result in most applications and an acceptable disturbance behavior [Vis06, p. 1]. In contrast to the elaborate heuristic PID control design, the model-based design of this controller with the introduced simplified LHP model in Sec. 5.1.2 is presented here. Thus, the general advantages of the model-based approach (see Sec. 1) are exploited when designing PID controllers for the LHP temperature control. In fact, the design of a PI controller without a derivative term is sufficient for LHP temperature control. This is due to the required limitation of the temperature dynamics of the control loop for a continuous heat transport, which is described in detail in Sec. 3.2.2. Besides this controller constraint, the windup effect in the PI controller has to be considered. As stated in Sec. 4.2.1, the commonly used back-calculation AW method is also suitable for the PI controller and will be adapted after the design of the controller gains. The final control loop containing the LHP system, the PI controller and the AW structure is depicted in Fig. 5.2.

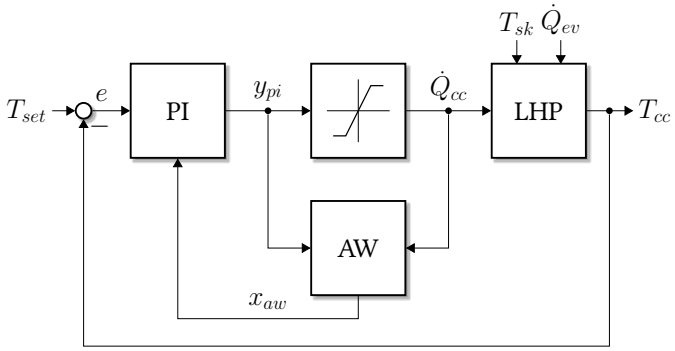

Figure 5.2: Control loop of an LHP with a PI controller and an AW structure

The PI controller in the corresponding block in Fig. 5.2 sees the LHP as an SISO system. The controlled output variable $y(t)$ is equivalent to the state variable $T_{cc}(t)$ and the output matrix $\boldsymbol{C}_{lin}$ of the linearized LHP state-space model (5.18) reduces to the output vector $\boldsymbol{c}_{lin}^{\top}$:

$$\boldsymbol{c}_{lin}^{\top} = \begin{bmatrix} 1 & 0 & 0 \end{bmatrix}. \tag{5.26}$$

In accordance with (2.11), the transfer function $G(s)$ of the linearized LHP state-space model (5.18) in the Laplace domain with the complex variable s is defined by the ratio of the transformed output $T_{cc}(s)$ and the transformed input $y_{pi}(s)$:

$$G(s) = \frac{T_{cc}(s)}{\dot{Q}_{cc}(s)} = \frac{T_{cc}(s)}{y_{pi}(s)} = \boldsymbol{c}_{lin}^{\top} \cdot (s \cdot \boldsymbol{I} - \boldsymbol{A}_{lin})^{-1} \cdot \boldsymbol{b}_{lin}, \tag{5.27}$$

with the identity matrix $\boldsymbol{I} \in \mathbb{R}^{3\times 3}$. Inserting (5.22), (5.23), and (5.26) into (5.27) yields:

$$G(s) = \frac{\mathcal{A} \cdot s^2 + \mathcal{B} \cdot s + \mathcal{C}}{\mathcal{D} \cdot s^3 + \mathcal{E} \cdot s^2 + \mathcal{F} \cdot s + \mathcal{G}}. \tag{5.28}$$

with the parameters $\mathcal{A}$ to $\mathcal{G}$:

$$\mathcal{A} = 2 \cdot C_{co}^{op} \cdot C_{ev}^{op} \cdot R_{co} \cdot R_{lk}, \tag{5.29}$$

$$\begin{aligned} \mathcal{B} = {} & 2 \cdot C_{co}^{op} \cdot R_{co} + C_{ev}^{op} \cdot R_{lk} + 2 \cdot C_{co}^{op} \cdot R_{co} \cdot R_{lk} \cdot \bar{c}_{cc,ev}^{l} \cdot \dot{m} \\ & + 2 \cdot C_{ev}^{op} \cdot R_{co} \cdot R_{lk} \cdot \bar{c}_{ev,co}^{l} \cdot \dot{m}, \end{aligned} \tag{5.30}$$

$$\mathcal{C} = 2 \cdot R_{co} \cdot \bar{c}_{ev,co}^{l} \cdot \dot{m} + R_{lk} \cdot \bar{c}_{cc,ev}^{l} \cdot \dot{m} + 2 \cdot R_{co} \cdot R_{lk} \cdot \bar{c}_{cc,ev}^{l} \cdot \bar{c}_{ev,co}^{l} \cdot \dot{m}^2 + 1, \tag{5.31}$$

$$\mathcal{D} = 2 \cdot C_{cc}^{op} \cdot C_{co}^{op} \cdot C_{ev}^{op} \cdot R_{co} \cdot R_{lk}, \tag{5.32}$$

$$\begin{aligned} \mathcal{E} = {} & 2 \cdot C_{cc}^{op} \cdot C_{co}^{op} \cdot R_{co} + 2 \cdot C_{co}^{op} \cdot C_{ev}^{op} \cdot R_{co} + C_{cc}^{op} \cdot C_{ev}^{op} \cdot R_{lk} \\ & + 2 \cdot C_{cc}^{op} \cdot C_{co}^{op} \cdot R_{co} \cdot R_{lk} \cdot \bar{c}_{cc,ev}^{l} \cdot \dot{m} + 2 \cdot C_{co}^{op} \cdot C_{ev}^{op} \cdot R_{co} \cdot R_{lk} \cdot \bar{c}_{co,cc}^{l} \cdot \dot{m} \\ & + 2 \cdot C_{cc}^{op} \cdot C_{ev}^{op} \cdot R_{co} \cdot R_{lk} \cdot \bar{c}_{ev,co}^{l} \cdot \dot{m}, \end{aligned} \tag{5.33}$$

$$\begin{aligned}\mathcal{F} = {} & C_{cc}^{op} + C_{ev}^{op} + 2 \cdot C_{co}^{op} \cdot R_{co} \cdot \bar{c}_{co,cc}^{l} \cdot \dot{m} + 2 \cdot C_{cc}^{op} \cdot R_{co} \cdot \bar{c}_{ev,co}^{l} \cdot \dot{m} \\ & + 2 \cdot C_{ev}^{op} \cdot R_{co} \cdot \bar{c}_{ev,co}^{l} \cdot \dot{m} + C_{cc}^{op} \cdot R_{lk} \cdot \bar{c}_{cc,ev}^{l} \cdot \dot{m} + C_{ev}^{op} \cdot R_{lk} \cdot \bar{c}_{co,cc}^{l} \cdot \dot{m} \\ & + 2 \cdot C_{co}^{op} \cdot R_{co} \cdot R_{lk} \cdot \bar{c}_{co,cc}^{l} \cdot \bar{c}_{cc,ev}^{l} \cdot \dot{m}^2 + 2 \cdot C_{cc}^{op} \cdot R_{co} \cdot R_{lk} \cdot \bar{c}_{cc,ev}^{l} \cdot \bar{c}_{ev,co}^{l} \cdot \dot{m}^2 \\ & + 2 \cdot C_{ev}^{op} \cdot R_{co} \cdot R_{lk} \cdot \bar{c}_{co,cc}^{l} \cdot \bar{c}_{ev,co}^{l} \cdot \dot{m}^2, \end{aligned} \tag{5.34}$$

$$\mathcal{G} = 2 \cdot R_{lk} \cdot \bar{c}_{co,cc}^{l} \cdot \bar{c}_{cc,ev}^{l} \cdot \dot{m}^2 + 2 \cdot \bar{c}_{co,cc}^{l} \cdot \dot{m}. \tag{5.35}$$

According to (5.28), the transfer function $G(s)$ of the LHP includes no integral term. Hence, the integral term for stationary accuracy has to be included in the controller, i.e. the integral gain K_i of the PI controller transfer function $C(s)$ must not be zero:

$$C(s) = \frac{y_{pi}(s)}{e(s)} = K_p + K_i \cdot \frac{1}{s}. \tag{5.36}$$

The transformed control error $e(s)$ is defined as the difference between the transformed setpoint temperature $T_{set}(s)$ and the transformed CC temperature $T_{cc}(s)$ as output variable of the system:

$$e(s) = T_{set}(s) - T_{cc}(s). \tag{5.37}$$

For the model-based tuning of the controller gains K_p and K_i in (5.36), the robust response time algorithm [Mat20b, p. 12-85] in the Control System Toolbox in MATLAB is used, as introduced in Sec. 4.2.2. As mentioned at the beginning of this section, the performance of the PI controller has to be constrained since a continuous heat transfer of the LHP depends on the change rate of the controlled CC temperature (see Sec. 3.2.2). By adapting the response time in the algorithm, a suitable rise time of the controlled CC temperature is set, and the PI gains are determined within the temperature-rate restriction accordingly.

For the implementation of the PI controller in the real application, (5.36) is transformed into the discrete time domain according to Appendix A.3, which yields the discrete control law $y_{pi}(k)$:

$$\Delta i_{pi}(k) = K_i \cdot T_{st} \cdot \Delta e(k) + \Delta i_{pi}(k-1), \tag{5.38}$$

$$y_{pi}(k) = K_p \cdot \Delta e(k) + \Delta i_{pi}(k) + y_{pi}^{op}, \tag{5.39}$$

with the discrete time k, the integral term $\Delta i_{pi}(k)$ of the PI controller, the sampling time T_{st}, and the discrete control error $\Delta e(k)$. After determining the PI controller and its gains for the LHP control heater, the strategy against the windup of the integral term of the PI controller in saturation, described in Sec. 4.2.1, is added to the control loop as follows:

$$\Delta x_{aw}(k) = K_{aw} \cdot \Big(\big(y_{pi}(k-1) - y_{pi}^{op} \big) - \Delta \dot{Q}_{cc}(k-1) \Big), \tag{5.40}$$

$$\Delta i_{pi}(k) = K_i \cdot T_{st} \cdot \big(\Delta e(k) - \Delta x_{aw}(k) \big) + \Delta i_{pi}(k-1), \tag{5.41}$$

$$y_{pi}(k) = K_p \cdot \Delta e(k) + \Delta i_{pi}(k) + y_{pi}^{op}. \tag{5.42}$$

This past section enables the implementation and first model-based parameterization of the state-of-the-art controller for the OT control of an LHP under consideration of the control

heater limits. This controller and all controllers that follow in this chapter are applied in simulations in Sec. 7.4.1. The performance of the AW strategy is verified in the third subsection of Sec. 7.4.1. For the specific improvement of its disturbance rejection, the state-of-the-art controller is extended in the next section.

5.2.2 PI Controller with Disturbance Feedforward Control

The performance of the designed PI controller is adjusted in Sec. 5.2.1 by determining the controller gains based on the simplified LHP state-space model. To further improve the disturbance performance of the PI controller in particular, which is most important for the LHP temperature control, the control structure is extended by a disturbance feedforward control, as suggested in [GMK+18]. The resulting controller has a two-degree-of-freedom structure, where the total control law $y_{cl}(k)$ is defined by the superposition of the PI controller output $y_{pi}(k)$ and the disturbance feedforward control output $y_{df}(k)$:

$$y_{cl}(k) = y_{pi}(k) + y_{df}(k). \tag{5.43}$$

A two-degree-of-freedom control achieves a stable temperature control and an improved reaction to disturbances. Due to the separation of the response to setpoint changes from the response to disturbances, both control objectives can be adjusted independently by two controller parts [AT03]. The combination of a disturbance feedforward control with another controller is indeed reasonable in order to compensate the low robustness of the feedforward component against model uncertainties [Lun20b, p. 190]. The two-degree-of-freedom control structure for the LHP is shown in Fig. 5.3.

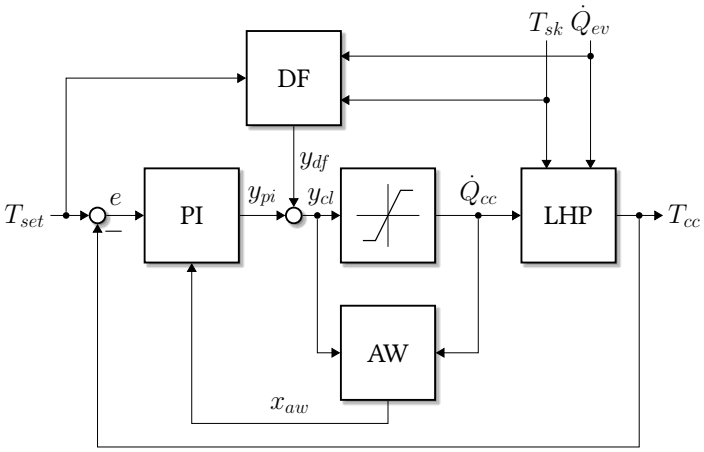

Figure 5.3: Control loop of an LHP with a PI controller, a disturbance feedforward control (DF), and an AW structure

The first degree of freedom is determined by the proposed PI controller with anti-windup strategy in Sec. 5.2.1. For the second degree of freedom, the classical disturbance feedforward

control (see [Lun20b, p. 190]) based on the linearized LHP state-space model (5.18) is given by the following equation in discrete time:

$$y_{df}(k) = -\left(\boldsymbol{b}_{lin}^{\top} \cdot \boldsymbol{b}_{lin}\right)^{-1} \cdot \boldsymbol{b}_{lin}^{\top} \cdot \boldsymbol{E}_{lin} \cdot \Delta \boldsymbol{d}(k) + y_{df}^{op} = \begin{bmatrix} 0 \\ 0 \end{bmatrix} \cdot \Delta \boldsymbol{d}(k) + y_{df}^{op}. \tag{5.44}$$

The resulting gain vector in (5.44) based on (5.23) and (5.24) is a zero vector. The disturbances have no influence on the controller input, since the control input $\dot{Q}_{cc}$ and the measurable disturbances $\dot{Q}_{ev}$ and T_{sk} do not have a direct impact on the same state in the simplified model. Therefore, the proposed disturbance feedforward control for LHPs in this thesis is based on the numerical disturbance-dependent determination of the stationary control heater output. A vivid description of the stationary control heater output being the heat input to the CC is the heat gap between the natural and the desired SSOT (see Sec. 3.2.1). This basic heat input is necessary to compensate the subcooling of the liquid returning to the CC. Adequate stationary LHP models are already commonly used to improve the characterization and the design of LHP components, as described in Sec. 2.2. In order to improve the LHP temperature control performance, these stationary LHP models are harnessed to predict the stationary control heater output and balance the influences of the disturbances on the LHP system through the disturbance feedforward control.

For an efficient online implementation of the disturbance feedforward control, a repeated online prediction of the required control heater output value with a stationary LHP model can be replaced by reading the value from a lookup table. Such a multi-dimensional lookup table can be created offline from the stationary model results according to the number of the relevant disturbances and the setpoint temperature. The more accurate the modeled steady-state values are over the LHP operating range, the more the PI controller can focus on the disturbance response, which results in a better overall control performance. The data for the lookup table could also be determined from measurements of the investigated LHP on a test bench. However, a huge number of measurements would be necessary to cover the whole operating range in a suitable accuracy, which would consume a lot of expensive test bench time. Therefore, the use of stationary models fitted to a smaller number of measurements is preferable.

As presented in [GMK+18], a numerical stationary model is used for the disturbance feedforward control, which has already been developed for the experimental and numerical thermal characterization of an LHP on a test bench in [MKHW19] (see also Sec. 2.2). This stationary model calculates the steady states of the LHP temperatures depending on the control heater output and the disturbances. It relies on energy balance equations of the principal LHP components and on the relevant heat transfer kinetics. For the disturbance feedforward control, the stationary system model is easily inverted by introducing another optimization loop. Thus, the necessary stationary control heater output is determined for a desired CC temperature at given disturbances.

In [GGK+13], the stationary control heater output at the CC is determined as a function of the heat load to be compared to different heat input locations for electrical energy consumption minimization. In this thesis, however, the required stationary control heater output $y_{df}(k)$ is not only a function f of the heat load $\dot{Q}_{ev}(k)$. It depends also on the sink temperature

$T_{sk}(k)$ and the setpoint temperature $T_{set}(k)$ to extend the accuracy of the predicted stationary control heater output over the entire operating range of the LHP:

$$y_{df}(k) = f\left(\dot{Q}_{ev}(k), T_{sk}(k), T_{set}(k)\right). \tag{5.45}$$

As an example, the corresponding three-dimensional graph of y_{df} for a fixed $T_{set} = 27\,^{\circ}\mathrm{C}$ and different values of $\dot{Q}_{ev}$ and T_{sk} in consideration of the power limitation is presented in Fig. 5.4.

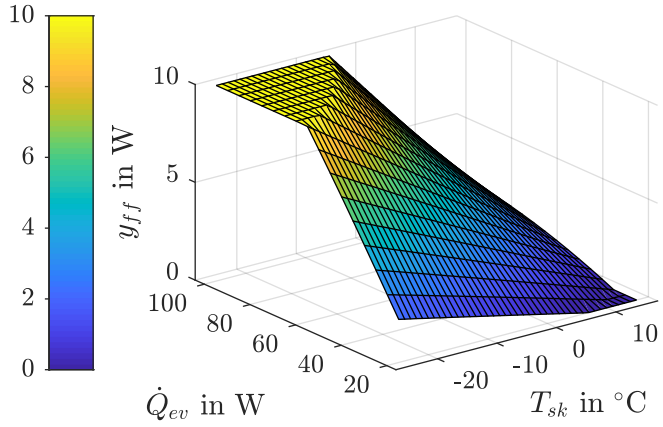

Figure 5.4: Surface plot of the modeled stationary control heater output y_{df} as a function of the heat load $\dot{Q}_{ev}$ and the sink temperature T_{sk} for a fixed setpoint temperature $T_{set} = 27\,^{\circ}\mathrm{C}$

Over the larger part of the operating range, the available control heater output is sufficient to control the CC temperature at the setpoint temperature. The limits of the control heater output at 0 W and 10 W are only reached at the extreme ends of the operating range in the lower right and the upper left corner of the graph in Fig. 5.4. These extreme ends correspond to the highest sink temperatures at the lowest heat loads and the lowest sink temperatures at the highest heat loads, respectively. With a closer look on the stationary behavior of LHPs in Fig. 3.9 in Sec. 3.2.1, the LHP operation mode in this operating range is the variable conductance mode since the condenser at the highest heat load is not yet fully utilized. In addition, the decreasing surface supports the statement in Sec. 3.2.1 that the amount of necessary control heater output does not correspond to the distance between the natural and the fixed SSOT in Fig. 3.9.

5.2.3 PI Output Feedback Control

Both previous controllers focus on one controlled variable, the CC temperature T_{cc}, whose feedback closes the SISO control loop. A powerful alternative to PID controllers for the control

of linear system's dynamics is the state feedback control

$$y_{of}(t) = -\boldsymbol{K}_x \cdot \Delta\boldsymbol{x}(t) + y_{of}^{op} = -\boldsymbol{K}_x \cdot \begin{bmatrix} \Delta T_{cc}(t) \\ \Delta T_{ev}(t) \\ \Delta T_{co}(t) \end{bmatrix} + y_{of}^{op}, \tag{5.46}$$

with the state feedback gain matrix $\boldsymbol{K}_x \in \mathbb{R}^{1\times 3}$ and the three states $\Delta T_{cc}(t)$, $\Delta T_{ev}(t)$, and $\Delta T_{co}(t)$ of the linearized LHP state-space model (5.18). The advantage of state feedback control is the possibility to place the poles of the closed control loop at desired positions in the complex plane provided that the system is fully controllable [Lun20b, p. 256]. Since all three states in $\Delta\boldsymbol{x}(t)$ are measurable temperatures, as shown by the output matrix $\boldsymbol{C}_{lin}$ in (5.25), the full-state feedback control of the LHP in (5.46) coincides with the output feedback control:

$$y_{of}(t) = -\boldsymbol{K}_x \cdot \Delta\boldsymbol{y}(t) + y_{of}^{op} = -\boldsymbol{K}_x \cdot \boldsymbol{C}_{lin} \cdot \begin{bmatrix} \Delta T_{cc}(t) \\ \Delta T_{ev}(t) \\ \Delta T_{co}(t) \end{bmatrix} + y_{of}^{op} = -\boldsymbol{K}_x \cdot \Delta\boldsymbol{x}(t) + y_{of}^{op}. \tag{5.47}$$

By enhancing the output feedback control with the proposed PI controller with anti-windup strategy of Sec. 5.2.1, the resulting two-degree-of-freedom control achieves an accurate LHP temperature control with disturbance rejection:

$$y_{cl}(t) = y_{of}(t) + y_{pi}(t). \tag{5.48}$$

The simple but efficient structure of this PI output feedback control is displayed in Fig. 5.5.

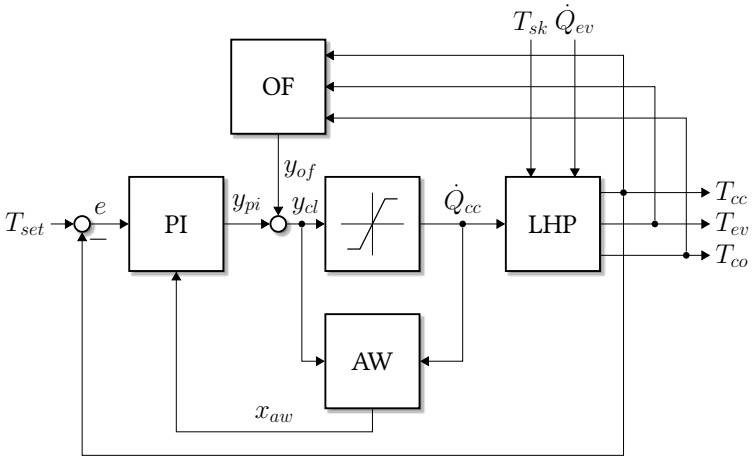

Figure 5.5: Control loop of an LHP with a PI controller, an output feedback control (OF), and an AW structure

The design of the PI output feedback control is similar to the design of a sole state feedback control, when the linearized system (5.18) is extended by the control error $e(t)$ [Föl16, p. 375]:

$$\begin{bmatrix} \Delta\dot{T}_{cc}(t) \\ \Delta\dot{T}_{ev}(t) \\ \Delta\dot{T}_{co}(t) \\ \Delta\dot{e}(t) \end{bmatrix} = \underbrace{\begin{bmatrix} \boldsymbol{A}_{lin} & \boldsymbol{0} \\ -\boldsymbol{c}_{lin}^{\top} & 0 \end{bmatrix}}_{\boldsymbol{A}_{ex}} \cdot \begin{bmatrix} \Delta T_{cc}(t) \\ \Delta T_{ev}(t) \\ \Delta T_{co}(t) \\ \Delta e(t) \end{bmatrix} + \underbrace{\begin{bmatrix} \boldsymbol{b}_{lin} \\ 0 \end{bmatrix}}_{\boldsymbol{b}_{ex}} \cdot \Delta\dot{Q}_{cc}(t) + \begin{bmatrix} \boldsymbol{E}_{lin} \\ \boldsymbol{0} \end{bmatrix} \cdot \begin{bmatrix} \Delta\dot{Q}_{ev}(t) \\ \Delta T_{sk}(t) \end{bmatrix}, \quad (5.49)$$

with the zero matrix $\boldsymbol{0}$, the extended system matrix $\boldsymbol{A}_{ex} \in \mathbb{R}^{4\times4}$, and the extended input vector $\boldsymbol{b}_{ex} \in \mathbb{R}^{4\times1}$ consisting of the matrices and vectors defined in (5.22), (5.23), (5.24) and (5.26), respectively. The condition for adjusting the closed-loop dynamics with a state feedback control is the controllability of the extended control system (5.49). According to Kalman's criteria (see [Föl16, p. 292]), the former linear system (5.18) with $\boldsymbol{A}_{lin} \in \mathbb{R}^{3\times3}$, $\boldsymbol{b}_{lin} \in \mathbb{R}^{3\times1}$, and $\boldsymbol{c}_{lin}^{\top} \in \mathbb{R}^{1\times3}$ is fully controllable if its controllability matrix $\boldsymbol{Q}_{ctr}$ is full rank:

$$\operatorname{rank}(\boldsymbol{Q}_{ctr}) = \operatorname{rank}\left(\begin{bmatrix} \boldsymbol{b}_{lin} & \boldsymbol{A}_{lin}\cdot\boldsymbol{b}_{lin} & \boldsymbol{A}_{lin}^{2}\cdot\boldsymbol{b}_{lin} \end{bmatrix}\right) = n = 3. \quad (5.50)$$

The general controllability matrix $\boldsymbol{Q}_{ctr}$ of a linear state-space system (2.9) is defined in [Föl16, p. 293]:

$$\boldsymbol{Q}_{ctr} = \begin{bmatrix} \boldsymbol{B}_{lin} & \boldsymbol{A}_{lin}\cdot\boldsymbol{B}_{lin} & \dots & \boldsymbol{A}_{lin}^{n-1}\cdot\boldsymbol{B}_{lin} \end{bmatrix}. \quad (5.51)$$

In addition to (5.50), it must also hold [Föl16, p. 375]:

$$\operatorname{rank}\left(\begin{bmatrix} \boldsymbol{A}_{lin} & \boldsymbol{b}_{lin} \\ \boldsymbol{c}_{lin}^{\top} & 0 \end{bmatrix}\right) = n + q = 4. \quad (5.52)$$

Since both conditions (5.50) and (5.52) are fulfilled, the extended control system (5.49) is indeed controllable. Hence, the PI output feedback control is determined by applying the state feedback control law with the gain matrices $\boldsymbol{K}_{ex} \in \mathbb{R}^{1\times4}$ and $\boldsymbol{K}_{s} \in \mathbb{R}^{1\times3}$ to the extended control system (5.49):

$$y_{cl}(t) = -\boldsymbol{K}_{ex}\cdot\begin{bmatrix} \Delta T_{cc}(t) \\ \Delta T_{ev}(t) \\ \Delta T_{co}(t) \\ \Delta e(t) \end{bmatrix} + y_{cl}^{op} = -\begin{bmatrix} \boldsymbol{K}_{s} & -K_i \end{bmatrix}\cdot\begin{bmatrix} \Delta T_{cc}(t) \\ \Delta T_{ev}(t) \\ \Delta T_{co}(t) \\ \Delta e(t) \end{bmatrix} + y_{cl}^{op}, \quad (5.53)$$

where the extended state feedback gain matrix $\boldsymbol{K}_{ex}$ is determined via pole placement. Here, *Ackermann's formula* is applied [Lun20b, p. 254]:

$$\boldsymbol{K}_{ex} = \begin{bmatrix} a_0 & a_1 & a_2 & a_3 & 1 \end{bmatrix}\cdot\begin{bmatrix} \boldsymbol{q}_{ctr,ex}^{\top} \\ \boldsymbol{q}_{ctr,ex}^{\top}\boldsymbol{A}_{ex} \\ \boldsymbol{q}_{ctr,ex}^{\top}\boldsymbol{A}_{ex}^{2} \\ \boldsymbol{q}_{ctr,ex}^{\top}\boldsymbol{A}_{ex}^{3} \\ \boldsymbol{q}_{ctr,ex}^{\top}\boldsymbol{A}_{ex}^{4} \end{bmatrix}, \quad (5.54)$$

with $\boldsymbol{q}_{ctr,ex}^{\top}$ being the last row of the inverse controllability matrix $\boldsymbol{Q}_{ctr,ex}^{-1}$ of the extended control system (5.49):

$$\boldsymbol{q}_{ctr,ex}^{\top} = \begin{bmatrix} 0 & 0 & 0 & 1 \end{bmatrix}\cdot\boldsymbol{Q}_{ctr,ex}^{-1} = \begin{bmatrix} 0 & 0 & 0 & 1 \end{bmatrix}\cdot\begin{bmatrix} \boldsymbol{b}_{ex} \\ \boldsymbol{A}_{ex}\boldsymbol{b}_{ex} \\ \boldsymbol{A}_{ex}^{2}\boldsymbol{b}_{ex} \\ \boldsymbol{A}_{ex}^{3}\boldsymbol{b}_{ex} \end{bmatrix}^{-1}. \quad (5.55)$$

The parameters a_0 to a_3 in (5.54) correspond to the coefficients of the characteristic equation of $\boldsymbol{A}_{ex}$:

$$\det\left(\lambda \cdot \boldsymbol{I} - \boldsymbol{A}_{ex}\right) = \lambda^4 + a_3 \cdot \lambda^3 + a_2 \cdot \lambda^2 + a_1 \cdot \lambda + a_0 = 0. \tag{5.56}$$

The characteristic equation is solved with the desired eigenvalues $\lambda_1, ..., \lambda_4$ of the closed-loop system. After the design of $\boldsymbol{K}_{ex}$, the separate gains K_p and K_i of the PI controller and $\boldsymbol{K}_x$ of the output feedback control can be derived from $\boldsymbol{K}_{ex}$. According to (5.53), K_i corresponds to the last element of $\boldsymbol{K}_{ex}$:

$$K_i = -K_{ex}(4). \tag{5.57}$$

The state feedback gain matrix $\boldsymbol{K}_x$ and the proportional gain K_p are calculated under the condition of a static feedforward control according to [Klu13] using

$$K_p = -\left(\boldsymbol{c}_{lin}^{\top} \cdot \boldsymbol{A}_{lin}^{-1} \cdot \boldsymbol{b}_{lin}\right)^{-1}, \tag{5.58}$$

$$\boldsymbol{K}_x = \boldsymbol{K}_s - K_p \cdot \boldsymbol{c}_{lin}^{\top}. \tag{5.59}$$

With the extension of the AW structure in Sec. 5.2.1, the discrete PI output feedback control is finalized for the LHP temperature control:

$$\Delta x_{aw}(k) = K_{aw} \cdot \left(\left(y_{pi}(k-1) - y_{pi}^{op}\right) - \Delta\dot{Q}_{cc}(k-1)\right), \tag{5.60}$$

$$\Delta i_{pi}(k) = K_i \cdot T_{st} \cdot \left(\Delta e(k) - \Delta x_{aw}(k)\right) + \Delta i_{pi}(k-1), \tag{5.61}$$

$$y_{pi}(k) = K_p \cdot \Delta e(k) + \Delta i_{pi}(k) + y_{pi}^{op}, \tag{5.62}$$

$$y_{cl}(k) = -\boldsymbol{K}_x \cdot \Delta\boldsymbol{y}(k) + y_{of}^{op} + y_{pi}(k). \tag{5.63}$$

5.2.4 Nonlinear Model Identification Adaptive Control

For the previous control designs, the selection of the OP plays a major role in adjusting the controller performance over the entire operating range of the LHP. The nonlinear simplified control model, described in Sec. 5.1, is linearized about the OP for a linear control design. Thus, the accuracy of the simplified model is limited to the proximity around the steady state given by the OP. Consequently, the performance of the corresponding linear controllers varies over the entire operating range. Furthermore, the model parameters are determined and fixed in the OP. However, the disturbances that define the LHP operating range (see Table 4.1) have a direct impact on the model parameters. Thus, the model parameters do change over time in the real application due to the disturbances and in addition to the variable heat and mass transfer. To detach from the dependencies on the fixed OP, two approaches are combined in an adaptive control structure, as presented in [GZSH19]: In a first approach, a nonlinear controller is designed based on the nonlinear simplified control model (5.14). This controller is based on a so-called control Lyapunov function as defined in Def. 5.1.

Definition 5.1 (Control Lyapunov function [Ada18, p. 411])
Consider the system

$$\dot{\boldsymbol{x}} = \boldsymbol{f}(\boldsymbol{x}, \boldsymbol{u}) \tag{5.64}$$

with the equilibrium point $\boldsymbol{x} = \boldsymbol{0}$ for $\boldsymbol{u} = \boldsymbol{0}$. Then, a continuously differentiable function $V_{ly}(\boldsymbol{x})$ is called control Lyapunov function, if the following conditions are met:

1. $V_{ly}(\boldsymbol{0}) = 0$,
2. $V_{ly}(\boldsymbol{x}) > 0$ *for all* $\boldsymbol{x} \neq \boldsymbol{0}$,
3. $V_{ly}(\boldsymbol{x}) \to \infty$ *for* $\boldsymbol{x} \to \infty$,
4. *There exists a* $\boldsymbol{u}(\boldsymbol{x})$, *so that* $\dot{V}_{ly}(\boldsymbol{x}) < 0$ *for all* $\boldsymbol{x} \neq \boldsymbol{0}$.

The existence of a control Lyapunov function ensures in turn the existence of a stabilizing state feedback control for the nonlinear system according to Lyapunov's direct method stated in Theorem 5.1.

Theorem 5.1 (Lyapunov's direct method [Ada18, p. 97])
The differential equation $\dot{\boldsymbol{x}} = \boldsymbol{f}(\boldsymbol{x})$ with the equilibrium point $\boldsymbol{x} = \boldsymbol{0}$ has a continuous and unique solution for each initial state in the domain $Z_1(\boldsymbol{0})$ that contains the origin. If there exists a function $V_{ly}(\boldsymbol{x})$ with continuous partial derivatives in the domain $Z_2(\boldsymbol{0}) \subseteq Z_1(\boldsymbol{0})$, and the following conditions hold:

1. $V_{ly}(\boldsymbol{0}) = 0$,
2. $V_{ly}(\boldsymbol{x}) > 0$, $\boldsymbol{x} \neq \boldsymbol{0}$,
3. $\dot{V}_{ly}(\boldsymbol{x}) < 0$, $\boldsymbol{x} \neq \boldsymbol{0}$,

then the equilibrium point $\boldsymbol{x} = \boldsymbol{0}$ is asymptotically stable.

If the second and third condition in Theorem 5.1 hold globally for all $\boldsymbol{x}$ in the state space, and $V_{ly}(\boldsymbol{x})$ is radially unbounded according to the third condition in Def. 5.1, then the equilibrium point is globally asymptotically stable [Ada18, p. 98]. Based on this nonlinear design approach, the linearization of the system equations about the OP for a linear control design as in the previous sections is avoided. However, the nonlinear controller alone shows a low robustness when using the fixed model parameters of the OP, as investigated in [GSO+20]. Therefore, the relevant model parameters are identified online and the states are predicted in a second approach to cover the variations of these parameters and their influences on the states for continuous adaption of the state-dependent controller over the entire LHP operating range.

The resulting nonlinear model identification adaptive control (nMIAC) structure for the temperature control of the LHP is depicted in Fig. 5.6.

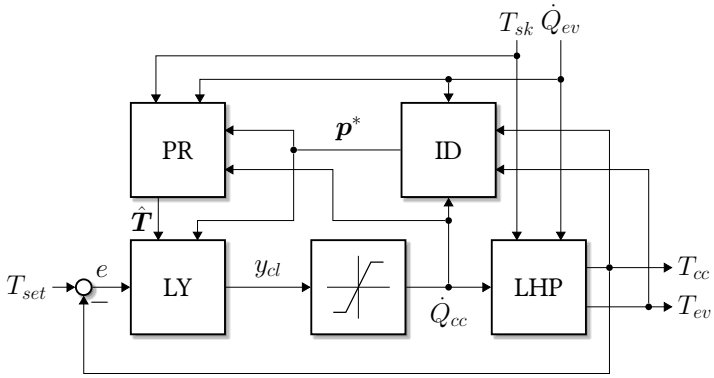

Figure 5.6: Control loop of an LHP with an nMIAC consisting of an online parameter identification (ID), a state prediction (PR), and a nonlinear Lyapunov-based controller (LY)

The influences of the time-variant disturbances on the model parameters are as follows. The heat load $\dot{Q}_{ev}(t)$ at the evaporator has a significant, direct impact on the mass flow rate $\dot{m}$ and the lumped thermal resistance R_{lk}. The sink temperature $T_{sk}(t)$ influences the lumped thermal resistance R_{co}. Hence, the model error of (5.14) grows with rising distance to the fixed OP values of the model parameters. By including the time dependencies of the parameters in the nonlinear simplified control model in (5.14), the emerging state-space model forms a nonlinear parameter-varying (NPV) system[10]:

$$\dot{\boldsymbol{x}}(t) = \boldsymbol{A}_{npv}\big(\boldsymbol{p}(t)\big) \cdot \boldsymbol{x}(t) + \boldsymbol{b}_{npv} \cdot u(t) + \boldsymbol{f}_{npv}\big(\boldsymbol{p}(t), \boldsymbol{d}(t)\big), \tag{5.65a}$$

$$\boldsymbol{y}(t) = \boldsymbol{x}(t), \tag{5.65b}$$

with the time-variant parameter vector $\boldsymbol{p}(t)$ under consideration of (3.58):

$$\boldsymbol{p}(t) = \begin{bmatrix} U_{lk}(t) \\ \dot{m}(t) \\ U_{co}(t) \end{bmatrix}. \tag{5.66}$$

The matrix $\boldsymbol{A}_{npv}\big(\boldsymbol{p}(t)\big)$ is derived from the differential equations of the simplified control model in (5.14) as follows:

$$\boldsymbol{A}_{npv}\big(\boldsymbol{p}(t)\big) = \begin{bmatrix} -\mathcal{I} & \frac{U_{lk}(t)}{C_{cc}^{op}} & \frac{1}{C_{cc}^{op}}\left(\bar{c}_{co,cc}^{l}\dot{m}(t)\right) \\ \mathcal{H} & -\mathcal{H} & 0 \\ 0 & \frac{1}{C_{co}^{op}}\left(\bar{c}_{ev,co}^{l}\dot{m}(t) - \frac{U_{co}(t)}{2}\right) & -\frac{1}{C_{co}^{op}}\left(\bar{c}_{ev,co}^{l}\dot{m}(t) + \frac{U_{co}(t)}{2}\right) \end{bmatrix}, \tag{5.67}$$

with the parameters $\mathcal{H}$ and $\mathcal{I}$:

$$\mathcal{H} = \frac{1}{C_{ev}^{op}} \cdot \left(\bar{c}_{cc,ev}^{l} \cdot \dot{m}(t) + U_{lk}(t)\right), \tag{5.68}$$

$$\mathcal{I} = \frac{1}{C_{cc}^{op}} \cdot \left(\bar{c}_{co,cc}^{l} \cdot \dot{m}(t) + U_{lk}(t)\right). \tag{5.69}$$

[10] For the simplification of the subsequent identification problem, all fractions in (5.14) containing a thermal resistance are substituted by their corresponding thermal conductance, as introduced in (3.58).

Accordingly, the vector $\boldsymbol{b}_{npv}$ and the vector function $\boldsymbol{f}_{npv}\big(\boldsymbol{p}(t), \boldsymbol{d}(t)\big)$ are given by

$$\boldsymbol{b}_{npv} = \begin{bmatrix} \frac{1}{C_{cc}^{op}} \\ 0 \\ 0 \end{bmatrix} \tag{5.70}$$

and

$$\boldsymbol{f}_{npv}\left(\boldsymbol{p}(t), \boldsymbol{d}(t)\right) = \begin{bmatrix} 0 \\ \frac{1}{C_{ev}^{op}}\Big(\dot{Q}_{ev}(t) - \Delta h_{ev}^{v}\dot{m}(t)\Big) \\ \frac{1}{C_{co}^{op}}\big(U_{co}(t)T_{sk}(t) + \Delta h_{ev}^{v}\dot{m}(t)\big) \end{bmatrix}. \tag{5.71}$$

Nonlinear Control Design

The subsequent nonlinear control design takes advantage of the natural connection between the temperatures in the LHP. As stated in Sec. 3.2.2, the behavior of the OT is governed by the CC temperature $T_{cc}(t)$, which is commonly controlled instead. Similar to the complex LHP control model (4.97) with output variable $T_{cc}(t)$ in Chapter 4, the simplified LHP control model in the form of the NPV system (5.65) for the desired control design is also given in Byrnes-Isidori normal form with its relative degree $\delta_{npv} = 1$:

$$\begin{bmatrix} \dot{x}_{ex}(t) \\ \dot{\boldsymbol{x}}_{in}(t) \end{bmatrix} = \boldsymbol{A}_{npv}\big(\boldsymbol{p}(t)\big) \cdot \begin{bmatrix} x_{ex}(t) \\ \boldsymbol{x}_{in}(t) \end{bmatrix} + \boldsymbol{b}_{npv} \cdot u(t) + \boldsymbol{f}_{npv}\big(\boldsymbol{p}(t), \boldsymbol{d}(t)\big), \tag{5.72a}$$

$$\boldsymbol{y}(t) = x_{ex}(t). \tag{5.72b}$$

The nonlinear controller in Fig. 5.6 is designed based on the external dynamics of (5.72). The external dynamics correspond to the dynamics of the CC subsystem. For the initial design process, the saturation block is neglected, i.e. $u(t) = \dot{Q}_{cc}(t) \triangleq y_{cl}(t)$. The corresponding input-affine state equation of the controlled $T_{cc}(t)$ is given by

$$\begin{aligned} \dot{x}_{ex}(t) = \dot{T}_{cc}(t) = &-\mathcal{I} \cdot T_{cc}(t) + \frac{1}{C_{cc}^{op}} \cdot y_{cl}(t) \\ &+ \frac{U_{lk}(t)}{C_{cc}^{op}} \cdot T_{ev}(t) + \frac{1}{C_{cc}^{op}} \cdot \big(\bar{c}_{co,cc}^{l} \cdot \dot{m}(t)\big) \cdot T_{co}(t). \end{aligned} \tag{5.73}$$

To stabilize $T_{cc}(t)$ in the OP at the setpoint temperature T_{set}, the control error

$$e(t) = T_{set} - T_{cc}(t) \tag{5.74}$$

is eliminated by the desired nonlinear controller. According to Theorem 5.1, a candidate for a positive definite control Lyapunov function $V_{ly}(t)$ must be chosen for an asymptotically stable equilibrium point. The following candidate consists of the squared control error $e(t)$ to meet the first three conditions of Def. 5.1:

$$V_{ly}(t) = \frac{1}{2} \cdot \big(e(t)\big)^2. \tag{5.75}$$

The control law for the control heater is determined by ensuring a negative definite derivative of the control Lyapunov function $V_{ly}(t)$ according to the fourth condition of Def. 5.1. Thus, the $V_{ly}(t)$ decreases outside T_{set} along every trajectory $e(t)$. The derivative of the control Lyapunov function (5.75) is given by

$$\dot{V}_{ly}(t) = e(t) \cdot \dot{e}(t) = \big(T_{set} - T_{cc}(t)\big) \cdot \Big(-\dot{T}_{cc}(t)\Big). \tag{5.76}$$

The requirement for a negative derivative (5.76) is met by choosing the following condition:

$$\dot{T}_{cc}(t) = \lambda_{ly} \cdot \big(T_{set} - T_{cc}(t)\big), \tag{5.77}$$

with

$$\lambda_{ly} > 0. \tag{5.78}$$

The parameter λ_{ly} sets the rate of decrease of the control Lyapunov function (5.75) and is adjusted to the system's dynamics to achieve the desired controller performance. Inserting (5.73) into (5.77) results in the following control law $y_{cl}(t)$ for the control heater of the LHP:

$$\begin{aligned} y_{cl}(t) &= C_{cc}^{op} \cdot \Bigg(\lambda_{ly} \cdot \big(T_{set} - T_{cc}(t)\big) + \mathcal{I} \cdot T_{cc}(t) \\ &\quad - \frac{U_{lk}(t)}{C_{cc}^{op}} \cdot T_{ev}(t) - \frac{1}{C_{cc}^{op}} \cdot \big(\bar{c}_{co,cc}^{l} \cdot \dot{m}(t)\big) \cdot T_{co}(t) \Bigg) \\ &= C_{cc}^{op} \cdot \lambda_{ly} \cdot \big(T_{set} - T_{cc}(t)\big) - U_{lk}(t) \cdot \big(T_{ev}(t) - T_{cc}(t)\big) \\ &\quad - \dot{m}(t) \cdot \bar{c}_{co,cc}^{l} \cdot \big(T_{co}(t) - T_{cc}(t)\big). \end{aligned} \tag{5.79}$$

For a stable overall control system, stable internal dynamics must be present according to Sec. 4.2.1. Therefore, the stability of the OP of the zero dynamics of the simplified LHP control model (5.72) are investigated in the following. By setting $x_{ex}(t)$ as input variable of the internal dynamics to its OP value, the zero dynamics are determined:

$$\begin{aligned} \dot{\boldsymbol{x}}_{in}(t) = &\begin{bmatrix} -\mathcal{H} & 0 \\ \frac{1}{C_{co}^{op}} \Big(\bar{c}_{ev,co}^{l} \dot{m}(t) - \frac{U_{co}(t)}{2} \Big) & -\frac{1}{C_{co}^{op}} \Big(\bar{c}_{ev,co}^{l} \dot{m}(t) + \frac{U_{co}(t)}{2} \Big) \end{bmatrix} \cdot \boldsymbol{x}_{in}(t) \\ &+ \begin{bmatrix} \mathcal{H} \\ 0 \end{bmatrix} \cdot x_{ex}^{op} + \begin{bmatrix} \frac{1}{C_{ev}^{op}} \Big(\dot{Q}_{ev}(t) - \Delta h_{ev}^{v} \dot{m}(t) \Big) \\ \frac{1}{C_{co}^{op}} \big(U_{co}(t) T_{sk}(t) + \Delta h_{ev}^{v} \dot{m}(t) \big) \end{bmatrix}. \end{aligned} \tag{5.80}$$

For the stability analysis of the equilibrium point of (5.80), Theorem 4.1 is applied. The Jacobian of (5.80) is given by

$$\boldsymbol{J} = \begin{bmatrix} -\mathcal{H} & 0 \\ \frac{1}{C_{co}^{op}} \Big(\bar{c}_{ev,co}^{l} \dot{m}^{op} - \frac{U_{co}^{op}}{2} \Big) & -\frac{1}{C_{co}^{op}} \Big(\bar{c}_{ev,co}^{l} \dot{m}^{op} + \frac{U_{co}^{op}}{2} \Big) \end{bmatrix} \Bigg|_{\boldsymbol{x}_{in} = \boldsymbol{x}_{in}^{op}}. \tag{5.81}$$

Since (5.81) is a lower triangular matrix, its eigenvalues λ_1 and λ_2 based on the characteristic polynomial (4.115) correlate with its diagonal elements (see [TT13, pp. 283, 333]):

$$\begin{aligned}\lambda_1 &= -\mathcal{H} \\ &= -\frac{1}{C_{ev}^{op}} \cdot \left(\bar{c}_{cc,ev}^{l} \cdot \dot{m}^{op} + U_{lk}^{op}\right), \end{aligned} \tag{5.82}$$

$$\lambda_2 = -\frac{1}{C_{co}^{op}} \cdot \left(\bar{c}_{ev,co}^{l} \cdot \dot{m}^{op} + \frac{U_{co}^{op}}{2}\right). \tag{5.83}$$

All parameters in (5.82) and (5.83) are positive during the normal LHP operation over the entire operating range. Thus, the eigenvalues λ_1 and λ_2 have negative real parts, and the zero dynamics (5.80) are consequently exponentially stable. Furthermore, the control loop with the nonlinear Lyapunov-based controller (5.79) is indeed stable around the OP.

A suitable online identification method for the adaption of the model parameters in (5.79) in the form of the nMIAC is designed and integrated into the control loop in the following section.

Online Parameter Identification

The nonlinear Lyapunov-based controller in (5.79) depends on the time-variant model parameters $U_{lk}(t)$ and $\dot{m}(t)$. However, the dynamics of both model parameters are unknown. Since these parameters are not directly measured or determinable in the considered LHP setup (see Chapter 1), they are estimated quasi-continuously from the available superficial temperature measurements for the adaption of the controller to the varying operating conditions. The discrete form of (5.79) is given by

$$\begin{aligned} y_{cl}(k) = C_{cc}^{op} \cdot \lambda_{ly} \cdot \big(T_{set} - T_{cc}(k)\big) - U_{lk}(k) \cdot \big(T_{ev}(k) - T_{cc}(k)\big) \\ - \dot{m}(k) \cdot \bar{c}_{co,cc}^{l} \cdot \big(T_{co}(k) - T_{cc}(k)\big). \end{aligned} \tag{5.84}$$

The parameters $U_{lk}(k)$ and $\dot{m}(k)$ are identified from the two measured temperatures $T_{cc}(k)$ and $T_{ev}(k)$ as depicted in Fig. 5.6. The parameter vector $\boldsymbol{p}(k)$ to be identified is given by

$$\boldsymbol{p}(k) = \begin{bmatrix} U_{lk}(k) \\ \dot{m}(k) \end{bmatrix}. \tag{5.85}$$

Due to Assumption 5.1, the time-variant parameter vector $\boldsymbol{p}(k)$ in (5.85) is considered quasi-continuous over time. Hence, both parameters in the parameter vector are estimated from the measured temperatures $T_{cc,m}(k)$ and $T_{ev,m}(k)$ of the CC and the evaporator in every discrete time step k. For the online parameter identification, the differential equations of the relevant measured temperature states in (5.65a) are discretized with Euler's forward method and the sampling time constant T_{st} and transformed into the following form:

$$\begin{bmatrix} T_{cc}(k) \\ T_{ev}(k) \end{bmatrix} = T_{st} \cdot \boldsymbol{p}(k-1) \cdot \boldsymbol{N}(k-1) + \begin{bmatrix} T_{cc}(k-1) + T_{st} \frac{1}{C_{cc}^{op}} \dot{Q}_{cc}(k-1) \\ T_{ev}(k-1) + T_{st} \frac{1}{C_{ev}^{op}} \dot{Q}_{ev}(k-1) \end{bmatrix}, \tag{5.86}$$

with the identification matrix $\boldsymbol{N}$ being defined by

$$\boldsymbol{N}(k) = \begin{bmatrix} N_{11}(k) & N_{12}(k) \\ N_{21}(k) & N_{22}(k) \end{bmatrix}, \tag{5.87}$$

with

$$N_{11}(k) = \frac{T_{ev}(k) - T_{cc}(k)}{C_{cc}^{op}}, \tag{5.88}$$

$$N_{12}(k) = \frac{\bar{c}_{co,cc}^{l}\big(T_{co}(k) - T_{cc}(k)\big)}{C_{cc}^{op}}, \tag{5.89}$$

$$N_{21}(k) = \frac{T_{cc}(k) - T_{ev}(k)}{C_{ev}^{op}}, \tag{5.90}$$

$$N_{22}(k) = \frac{\bar{c}_{cc,ev}^{l}\big(T_{cc}(k) - T_{ev}(k)\big) - \Delta h_{ev}^{v}}{C_{ev}^{op}}. \tag{5.91}$$

The parameter identification problem is posed as a nonlinear unconstrained optimization problem for the identification error vector $\boldsymbol{e}_{id}(k)$ between the measured temperatures $T_{cc,m}(k)$ and $T_{ev,m}(k)$, and the calculated temperature outputs in (5.86):

$$\boldsymbol{e}_{id}(k) = \begin{bmatrix} T_{cc,m}(k) \\ T_{ev,m}(k) \end{bmatrix} - \begin{bmatrix} T_{cc}(k) \\ T_{ev}(k) \end{bmatrix}. \tag{5.92}$$

In every time step k, the optimal parameter vector $\boldsymbol{p}^*(k)$ denotes the argument, for which the square of the identification error vector (5.92) is minimized:

$$\boldsymbol{p}^*(k) = \begin{bmatrix} U_{lk}^*(k) \\ \dot{m}^*(k) \end{bmatrix} = \underset{\boldsymbol{p}(k)}{\arg\min}\, \boldsymbol{e}_{id}^{\top}(k) \cdot \boldsymbol{e}_{id}(k). \tag{5.93}$$

The minimization problem (5.93) is solved with the direct search method of [LRWW98], an extended version of the simplex method of [NM65]. For its computation, the available MATLAB implementation is used (see [Mat20d, p. 9-4]). The initial parameter vector in every time step k is taken from the OP, which is also an equilibrium point of the NPV system (5.65).

State Prediction

With the online identification of the time-variant parameters in the previous section, only the determination of the states $T_{cc}(k)$, $T_{ev}(k)$, and $T_{co}(k)$ in the state vector $\boldsymbol{x}(k)$ in (5.84) is left to complete the equations of the nMIAC structure in Fig. 5.6. These are determined by predicting the temperatures with the NPV system (5.65). The differential equations in (5.65a) are discretized with Euler's forward method resulting in the following discrete form of (5.65a) with (5.67), (5.70), and (5.71):

$$\begin{aligned} \boldsymbol{x}(k) = {} & T_{st} \cdot \boldsymbol{A}_{npv}\big(\boldsymbol{p}(k-1)\big) \cdot \boldsymbol{x}(k-1) + T_{st} \cdot \boldsymbol{b}_{npv} \cdot u(k-1) \\ & + T_{st} \cdot \boldsymbol{f}_{npv}\big(\boldsymbol{p}(k-1), \boldsymbol{d}(k-1)\big) + \boldsymbol{x}(k-1). \end{aligned} \tag{5.94}$$

The model parameter U_{co} is fixed in the OP. The parameter vector $\boldsymbol{p}(k-1)$ with the two model parameters $U_{lk}(k-1)$ and $\dot{m}(k-1)$ is determined by the online parameter estimation method in the previous section.

The performance of the state prediction and parameter identification, integrated in the proposed nMIAC, are evaluated in simulations in the fourth subsection of Sec. 7.4.1 and with measurement data in [GZSH19]. The nMIAC in this section and the LHP controllers in the previous sections control the CC temperature. Their simulation results are presented in the first subsection of Sec. 7.4.1. To additionally control the evaporator temperature, corresponding cascade controls are introduced in the next section.

5.2.5 Cascade Control

The benefits of the cascade control for the temperature control of the LHP are already highlighted in Sec. 4.2.2. Here, the cascaded extensions of the previous controllers based on the simplified model are introduced. For the PI controller in Sec. 5.2.1, it is shown in [GH20] that the influences on the evaporator temperature during LHP operation are decreased in a PI cascade control compared to the direct PI control of the evaporator temperature in a single control loop. However, the cascade control design in [GH20] based on the linearized simplified LHP state-space model (5.18) facilitates not only the extension of the single PI control loop, but also of all other previous single-loop controllers in Sec. 5.2.2 to 5.2.4. In each case, both control loops are adapted to each other for a provably stable overall control system by a model-based design approach. Thus, the advantages of controlling the CC temperature as governing temperature are not only preserved, but the evaporator temperature as the nearest measurable LHP temperature to the heat source is also controlled.

The general structure of the PI cascade control for LHPs is depicted in Fig. 5.7.

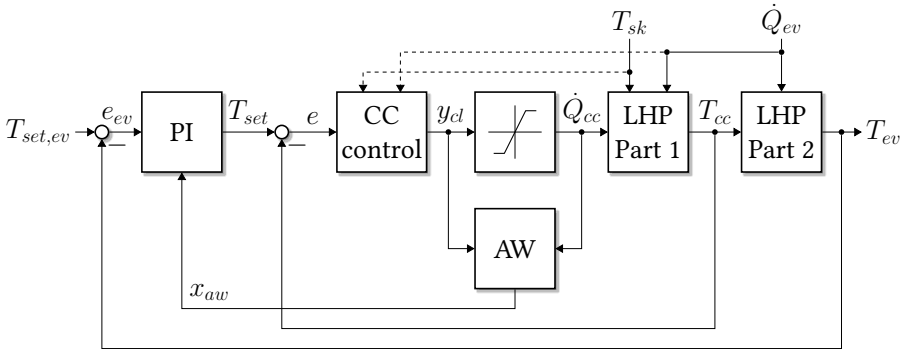

Figure 5.7: Cascade control loop of an LHP with a PI controller and a CC controller, the divided system parts LHP Part 1 and LHP Part 2, and an AW structure

As the inner control loop in Fig. 5.7, one of the previously designed control loops in Sec. 5.2.1 to Sec. 5.2.4 can be chosen according to the design requirements. From the PI controller's

point of view, the controlled system in the outer control loop consists therefore not only of the system part LHP Part 2 but also of the chosen inner control loop.

For the determination of LHP Part 2, its transfer function $G_2(s)$ is derived from the linearized differential equation for T_{ev} in (5.18):

$$\Delta\dot{T}_{ev}(t) = \mathcal{R} \cdot \Delta T_{cc}(t) - \mathcal{R} \cdot \Delta T_{ev}(t) + \frac{1}{C_{ev}^{op}} \cdot \Delta\dot{Q}_{ev}(t), \tag{5.95}$$

$$\Delta\dot{T}_{ev}(t) + \mathcal{R} \cdot \Delta T_{ev}(t) = \mathcal{R} \cdot \Delta T_{cc}(t) + \frac{1}{C_{ev}^{op}} \cdot \Delta\dot{Q}_{ev}(t), \tag{5.96}$$

with the parameter $\mathcal{R}$:

$$\mathcal{R} = \frac{1}{C_{ev}^{op}} \cdot \left(\bar{c}_{cc,ev}^{l} \cdot \dot{m} + \frac{1}{R_{lk}} \right). \tag{5.97}$$

The Laplace transformation of (5.96) yields

$$s \cdot T_{ev}(s) + \mathcal{R} \cdot T_{ev}(s) = \mathcal{R} \cdot T_{cc}(s) + \frac{1}{C_{ev}^{op}} \cdot \dot{Q}_{ev}(s), \tag{5.98}$$

$$(s + \mathcal{R}) \cdot T_{ev}(s) = \mathcal{R} \cdot T_{cc}(s) + \frac{1}{C_{ev}^{op}} \cdot \dot{Q}_{ev}(s), \tag{5.99}$$

$$T_{ev}(s) = \frac{\mathcal{R}}{s + \mathcal{R}} \cdot T_{cc}(s) + \frac{\frac{1}{C_{ev}^{op}}}{s + \mathcal{R}} \cdot \dot{Q}_{ev}(s). \tag{5.100}$$

Hence, the transfer function $G_2(s)$ is determined as

$$G_2(s) = \frac{T_{ev}(s)}{T_{cc}(s)} = \frac{\mathcal{R}}{s + \mathcal{R}} = \frac{\frac{1}{C_{ev}^{op}} \left(\bar{c}_{cc,ev}^{l} \dot{m} + \frac{1}{R_{lk}} \right)}{s + \frac{1}{C_{ev}^{op}} \left(\bar{c}_{cc,ev}^{l} \dot{m} + \frac{1}{R_{lk}} \right)}. \tag{5.101}$$

Combined with the transfer function $G_3(s)$ of the chosen inner control loop, the transfer function $G_4(s)$ of the controlled system in the outer control loop is established:

$$G_4(s) = \frac{T_{ev}(s)}{T_{set}(s)} = G_3(s) \cdot G_2(s). \tag{5.102}$$

The transfer function $G_4(s)$ is controlled by the PI controller $C_2(s)$ in the outer control loop, which has the following form:

$$C_2(s) = \frac{T_{set}(s)}{e_{ev}(s)} = K_{p2} + K_{i2} \cdot \frac{1}{s}, \tag{5.103}$$

with the controller gains K_{p2} and K_{i2}. This controller determines the setpoint temperature T_{set} for the CC controller in the inner control loop. Besides the transformed control error $e(s)$ of the inner control loop in (5.37), the transformed evaporator control error $e_{ev}(s)$ is defined as the difference between the transformed setpoint temperature $T_{set,ev}(s)$ of the evaporator and the transformed evaporator temperature $T_{ev}(s)$:

$$e_{ev}(s) = T_{set,ev}(s) - T_{ev}(s). \tag{5.104}$$

Analogous to Sec. 5.2.1, the AW structure is attached to the integral term of $C_2(s)$ to finalize the entire cascade control in Fig. 5.7. The condition of a separate design process with a faster inner control loop than the outer control loop must be considered during the determination of the control parameters K_{p2} and K_{i2} with the mentioned methods in Sec. 5.2.1. According to the chosen inner-loop controller, this is done by choosing either the poles of the inner control loop to the left of the poles of the outer control loop in the complex plane, i.e. with a smaller real part, or a smaller robust response time and a greater cutoff frequency for the inner control loop, respectively.

In the following subsections, the individual transfer function $G_3(s)$ of the different inner control loops is formed from the adapted CC control loops in the previous sections. The performance of these cascade controls is presented in the fifth subsection of Sec. 7.4.1.

Cascade Control Based on PI Controllers

The designs of the LHP cascade controls based on the PI controllers in Sec. 5.2.1 and Sec. 5.2.2 are similar since the disturbance feedforward control is designed independently, as mentioned in Sec. 5.2.2. Hence, both cascade controls consist of two linear SISO controllers, as depicted in Fig. 5.8.

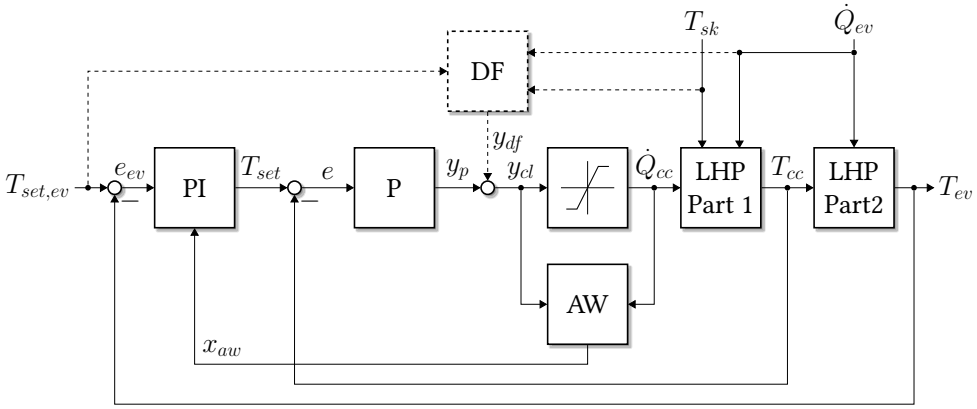

Figure 5.8: Cascade control loop of an LHP with a PI controller and a P controller with an optional disturbance feedforward control (DF), the divided system parts LHP Part 1 and LHP Part 2, and an AW structure

As presented in Fig. 5.8, the combination of a PI and a P controller is commonly used in the industry for its good performance [KRJD90]. For the stationary accuracy of the entire cascade control loop, an integral term in the linear controllers of the outer loop is sufficient [Vis06, p. 252]. Hence, the inner control loop for the CC temperature must be redesigned by using a P controller. The transfer function $G_1(s)$ of LHP Part 1 is already given in (5.28), i.e.

$$G_1(s) = \frac{T_{cc}(s)}{\dot{Q}_{cc}(s)} = G(s) = \frac{\mathcal{A} \cdot s^2 + \mathcal{B} \cdot s + \mathcal{C}}{\mathcal{D} \cdot s^3 + \mathcal{E} \cdot s^2 + \mathcal{F} \cdot s + \mathcal{G}}, \tag{5.105}$$

with the parameters $\mathcal{A}$ to $\mathcal{G}$ in (5.29) to (5.35). For the inner control loop, the transfer function of the P controller $C_1(s)$ is constructed according to (5.36):

$$C_1(s) = \frac{\dot{Q}_{cc}(s)}{e(s)} = K_{p1}, \tag{5.106}$$

with the transformed P controller output $y_p(s)$ and the controller gain K_{p1}. Then, the transfer function

$$G_3(s) = \frac{T_{cc}(s)}{T_{set}(s)} = \frac{C_1(s)G_1(s)}{1 + C_1(s)G_1(s)} \tag{5.107}$$

of the inner control loop is established.

The disturbance feedforward control in block DF in Fig. 5.8 is adapted from Sec. 5.2.2 to its corresponding cascade control in such a way that the predicted stationary control heater output $y_{df}(k)$ is not a function f of the CC setpoint temperature T_{set}, as in (5.45), but of the evaporator setpoint temperature $T_{set,ev}$:

$$y_{df}(k) = f\left(\dot{Q}_{ev}(k), T_{sk}(k), T_{set,ev}(k)\right). \tag{5.108}$$

Cascade Control Based on the PI Output Feedback Control

Since an integral term in one of the controllers in the cascade control loop in Fig. 5.7 is sufficient, the PI output feedback control in Sec. 5.2.3 is adapted for the inner control loop of the corresponding cascade control by designing a P output feedback control without integral part:

$$y_{cl}(t) = y_{of}(t) + y_p(t), \tag{5.109}$$

with (5.47) and

$$\begin{aligned} y_p(t) &= K_{p1} \cdot \Delta e(t) + y_p^{op} \\ &= K_{p1} \cdot \left(\Delta T_{set}(t) - \Delta T_{cc}(t)\right) + y_p^{op} \\ &= K_{p1} \cdot \left(\Delta T_{set}(t) - \boldsymbol{c}_{lin}^{\top} \cdot \Delta \boldsymbol{x}(t)\right) + y_p^{op} \\ &= -K_{p1} \cdot \boldsymbol{c}_{lin}^{\top} \cdot \Delta \boldsymbol{x}(t) + K_{p1} \cdot \Delta T_{set}(t) + y_p^{op}. \end{aligned} \tag{5.110}$$

With this control structure, the linearized system (5.18) does not have to be extended with the control error $e(t)$ for the application of Ackermann's formula, as it is the case in Sec. 5.2.3. Instead, the formula for the design of the state feedback control is directly applied to the linearized system (5.18) while considering the structure of the P output feedback control in (5.109):

$$y_{cl}(t) = -\left(\boldsymbol{K}_x + K_{p1} \cdot \boldsymbol{c}_{lin}^{\top}\right) \cdot \Delta \boldsymbol{x}(t) + y_{cl}^{op} = -\boldsymbol{K}_{s1} \cdot \Delta \boldsymbol{x}(t) + y_{cl}^{op}. \tag{5.111}$$

Thus, Ackermann's formula can be directly applied to determine the gain K_{s1} of the state feedback control in (5.111). By striving for a stationary disturbance rejection, the individual

gains K_{p1} and $\boldsymbol{K}_x$ are derived, as described in Sec. 5.2.3:

$$K_{p1} = -\left(\boldsymbol{c}_{lin}^{\top} \cdot \boldsymbol{A}_{lin}^{-1} \cdot \boldsymbol{b}_{lin}\right)^{-1}, \tag{5.112}$$

$$\boldsymbol{K}_x = \boldsymbol{K}_{s1} - K_{p1} \cdot \boldsymbol{c}_{lin}^{\top}. \tag{5.113}$$

Thus, the transfer function $G_3(s)$ of the closed control loop is established by inserting (5.109) into the linearized system (5.18):

$$\begin{aligned}\Delta\dot{\boldsymbol{x}}(t) = \boldsymbol{A}_{lin} \cdot \Delta\boldsymbol{x}(t) + \boldsymbol{b}_{lin} \cdot \left(-\left(\boldsymbol{K}_x + K_{p1} \cdot \boldsymbol{c}_{lin}^{\top}\right) \cdot \Delta\boldsymbol{x}(t) + K_{p1} \cdot \Delta T_{set}(t)\right) \\ + \boldsymbol{E}_{lin} \cdot \Delta\boldsymbol{d}(t).\end{aligned} \tag{5.114}$$

Subsequently, the system dynamics in (5.114) are transformed into the Laplace domain:

$$\begin{aligned}G_3(s) &= \frac{T_{cc}(s)}{T_{set}(s)} \\ &= \boldsymbol{c}_{lin}^{\top} \cdot \left(s \cdot \boldsymbol{I} - \left(\boldsymbol{A}_{lin} - \boldsymbol{b}_{lin} \cdot \left(\boldsymbol{K}_x + K_{p1} \cdot \boldsymbol{c}_{lin}^{\top}\right)\right)\right)^{-1} \cdot \boldsymbol{b}_{lin} \cdot K_{p1}.\end{aligned} \tag{5.115}$$

Cascade Control Based on the Nonlinear Model Identification Adaptive Control

For the determination of the transfer function $G_3(s)$ of the inner control loop based on the nMIAC in Sec. 5.2.4, the control law (5.79) is inserted into the nonlinear subsystem equation (5.73):

$$\begin{aligned}\dot{T}_{cc}(t) &= -\mathcal{I} \cdot T_{cc}(t) + \frac{1}{C_{cc}^{op}} \cdot \left(C_{cc}^{op} \cdot \left(\lambda_{ly} \cdot \left(T_{set} - T_{cc}(t)\right) + \mathcal{I} \cdot T_{cc}(t)\right.\right. \\ &\quad \left.\left. - \frac{U_{lk}(t)}{C_{cc}^{op}} \cdot T_{ev}(t) - \frac{1}{C_{cc}^{op}} \cdot \left(\bar{c}_{co,cc}^{l} \cdot \dot{m}(t)\right) \cdot T_{co}(t)\right)\right) \\ &\quad + \frac{U_{lk}(t)}{C_{cc}^{op}} \cdot T_{ev}(t) + \frac{1}{C_{cc}^{op}} \cdot \left(\bar{c}_{co,cc}^{l} \cdot \dot{m}(t)\right) \cdot T_{co}(t) \\ &= \lambda_{ly} \cdot \left(T_{set} - T_{cc}(t)\right)\end{aligned} \tag{5.116}$$

Transforming (5.116) into the Laplace domain yields

$$s \cdot T_{cc}(s) = \lambda_{ly} \cdot \left(T_{set}(s) - T_{cc}(s)\right). \tag{5.117}$$

Thus, the transfer function of the inner control loop results:

$$G_3(s) = \frac{T_{cc}(s)}{T_{set}(s)} = \frac{\lambda_{ly}}{\lambda_{ly} + s}. \tag{5.118}$$

5.3 Conclusion

In this chapter, a simplified LHP state-space model has been derived from the complex nonlinear LHP state-space model in Chapter 4. The simplified model is based on the first law of thermodynamics for open systems and includes the important mass flow rate as a model parameter. With that in mind, the state-of-the-art PI controller has been designed based on the simplified state-space model in the desired steady-state OP. Furthermore, several two-degree-of-freedom control structures have been proposed that exploit the optimization potential of the common PI controller under consideration of the given requirements. On the one hand, one of the common steady-state models in the literature has been adapted and incorporated in a disturbance feedforward control to improve the disturbance performance of the PI controller. Thus, the required stationary heater output is already set in the controller by modeling the power gap between the natural and the desired stationary behavior of the OT. On the other hand, the full-state feedback control has harnessed the measurability of all states which has not been given in the previous chapter. Thus, the need for elaborate state estimation methods, which place higher demands on the hardware, has been eliminated. However, the linear controllers have been designed for the local behavior around a fixed OP. To adapt the controller to the varying OPs and to incorporate the variation of the mass flow rate over the operating range due to changing operating conditions in the controller, an nMIAC has been designed based on Lyapunov's direct method. This nonlinear controller identifies the temporal progression of the mass flow rate and the thermal resistance of the heat leak from the measured temperatures. Thus, the controller is able to adapt the OP to the varying disturbances improving the precision of the LHP OT control.

All four controllers have been designed to control the CC temperature. For the control of the evaporator temperature as closest temperature to the cooled object, these controllers have been extended with an outer control loop. Thus, the direct control of the evaporator temperature with a PI controller, which may lead to an undesired dynamic behavior of the control loop as reported in the literature, has been circumvented by the cascade structure. This structure still reduces the temperature variations of an LHP-cooled object based on the close evaporator temperature.

Up to this point, the focus has been set on modeling and controlling a conventional LHP. In the next chapter, advanced LHP-based heat transport systems are investigated, which further extend the current structures and methods.

6 Nonlinear Model-Based Control Designs for Advanced Loop Heat Pipe Systems

In the previous chapters, a single LHP is modeled and controlled in order to design an effective thermal control system. The single LHP structure, as it is shown in Fig. 4.1, can be referred to as the basic LHP structure since it represents a conventional LHP with its five fundamental components. As reported in Sec. 2.3, different advanced heat transport systems are based on connecting a conventional LHP with further components. In this thesis, two relevant extensions are investigated. An attached heat source with significant thermal mass at the evaporator has a non-negligible impact on the dynamics of the LHP, which may cause temperature oscillations during LHP operation (see Sec. 2.4). These oscillations need to be prevented by adequate control algorithms. Another kind of extension is used for the thermal control of LCTs, where two parallel LHPs with ArHPs are thermally coupled to increase the overall heat transfer and contribute to an isothermal LCT platform. Thus, a multiple-input-multiple-output (MIMO) system is created in which two control heaters must be coordinated. Besides the modeling of these advanced heat transport systems, the model-based design of suitable control algorithms is in the focus of the next sections.

6.1 Complex Dynamical Modeling of Advanced Loop Heat Pipe Systems

A modular modeling approach is derived in this section to model advanced LHP systems, e.g. an LHP with an attached thermal mass or parallel LHPs of an LCT. For the overall dynamical state-space models of such complex systems, the theory of thermal networks in Sec. 3.1.2 is used to describe the structural extensions of the evaporators in these systems. The corresponding state-space representation of the application-specific thermal networks is created out of a given set of thermal resistances and capacitances. Combined with one or several LHP state-space models (4.84), formerly developed in Chapter 4, the overall dynamical model of the advanced LHP system is established.

First, the general state-space model (3.69) of a thermal network is adapted to the specific structures of the advanced LHP system with one or several LHPs. The total heat $\dot{Q}_{hs}$ of the heat source splits into q heat inputs $\dot{Q}_{sf}$ at the surfaces of the thermal masses in the thermal network. At the interfaces between the evaporators of the r LHPs and the thermal network, r heat loads $\dot{Q}^{l}_{ev}(t)$ ($l = 1, ..., r$) are functions of the corresponding surface temperatures

$T^l_{ev,sf}(t)$ and the fluid temperatures $T^l_{ev}(t)$ of the r evaporators:

$$\dot{Q}^l_{ev}(t) = \frac{1}{R^l_{sf}} \cdot \left(T^l_{ev,sf}(t) - T^l_{ev}(t)\right), \tag{6.1}$$

with the thermal resistance R_{sf} between the surface and the fluid of the evaporator. Inserting (4.38) into (6.1) and solving the resulting equation for the heat load $\dot{Q}^l_{ev}(t)$ yields a function of the LHP temperatures $T^l_{ev,s}(t)$ and $T^l_{cc}(t)$:

$$\begin{aligned}\dot{Q}^l_{ev}(t) &= \frac{\left(R^l_{sh} + R^l_{lk}\right) T^l_{ev,sf}(t) - R^l_{lk} T^l_{ev,s}(t) - R^l_{sh} T^l_{cc}(t)}{\underbrace{R^l_{sf}R^l_{lk} + R^l_{lk}R^l_{sh} + R^l_{sf}R^l_{sh}}_{=:\mathcal{J}^l}} \\ &= \underbrace{\frac{R^l_{sh} + R^l_{lk}}{\mathcal{J}^l}}_{=:\mathcal{K}^l} \cdot T^l_{ev,sf}(t) - \underbrace{\frac{R^l_{lk}}{\mathcal{J}^l}}_{=:\mathcal{L}^l} \cdot T^l_{ev,s}(t) - \underbrace{\frac{R^l_{sh}}{\mathcal{J}^l}}_{=:\mathcal{M}^l} \cdot T^l_{cc}(t),\end{aligned} \tag{6.2}$$

with the parameters $\mathcal{J}^l$ to $\mathcal{M}^l$. Consequently, a disturbance vector $\boldsymbol{d}_{tn}(t)$ extends the state-space model (3.69) by the LHP temperatures $T^l_{ev,s}(t)$ and $T^l_{cc}(t)$. In addition, the dimension of the output vector $\boldsymbol{y}_{tn}(t)$ changes due to the addition of the evaporator surface temperatures $T^l_{ev,sf}(t)$. With these modifications, the state equation (3.69a) and the output equation (3.69b) are adapted as follows:

$$\dot{\boldsymbol{x}}_{tn}(t) = \boldsymbol{A}_{tn} \cdot \boldsymbol{x}_{tn}(t) + \boldsymbol{B}_{tn} \cdot \boldsymbol{u}_{tn}(t) + \boldsymbol{E}_{tn} \cdot \boldsymbol{d}_{tn}(t), \tag{6.3a}$$

$$\boldsymbol{y}_{tn}(t) = \boldsymbol{C}_{tn} \cdot \boldsymbol{x}_{tn}(t) + \boldsymbol{F}_{tn} \cdot \boldsymbol{d}_{tn}(t), \tag{6.3b}$$

with the vectors

$$\boldsymbol{x}_{tn}(t) = \begin{bmatrix} T_1(t) & \cdots & T_n(t) \end{bmatrix}^\top, \tag{6.4}$$

$$\boldsymbol{u}_{tn}(t) = \begin{bmatrix} \dot{Q}_{sf,1}(t) & \cdots & \dot{Q}_{sf,q}(t) \end{bmatrix}^\top, \tag{6.5}$$

$$\boldsymbol{d}_{tn}(t) = \begin{bmatrix} T^1_{ev,s}(t) & T^1_{cc}(t) & \cdots & T^r_{ev,s}(t) & T^r_{cc}(t) \end{bmatrix}^\top, \tag{6.6}$$

$$\boldsymbol{y}_{tn}(t) = \begin{bmatrix} \dot{Q}^1_{ev}(t) & T^1_{ev,sf}(t) & \cdots & \dot{Q}^r_{ev}(t) & T^r_{ev,sf}(t) \end{bmatrix}^\top, \tag{6.7}$$

and the matrices $\boldsymbol{A}_{tn} \in \mathbb{R}^{n\times n}$, $\boldsymbol{B}_{tn} \in \mathbb{R}^{n\times q}$, $\boldsymbol{C}_{tn} \in \mathbb{R}^{2r\times n}$, $\boldsymbol{E}_{tn} \in \mathbb{R}^{n\times 2r}$, $\boldsymbol{F}_{tn} \in \mathbb{R}^{2r\times 2r}$.

Following the subsequent step-by-step instructions, the matrices of the state-space model (6.3) are constructed. These instructions describe the implemented algorithm that determines the matrices of arbitrary thermal networks attached to the evaporator of one or several LHPs automatically. Based on the given set of thermal resistances and conductances in the thermal network, the matrices of (6.3) are directly established according to the order of the variables in (6.4), (6.5), and (6.7). In this way, the construction of the differential equation system of the thermal network based on Kirchhoff's current law, as presented in Example 3.1, is skipped. For the system matrix $\boldsymbol{A}_{tn}$, graph theory is utilized to describe the thermal network mathematically. The developed instructions include the following steps:

1. Construction of an adjacency matrix $\boldsymbol{A}_{tn} \in \mathbb{R}^{n\times n}$ (cf. [TT13, p. 421]) from the finite undirected graph $\mathsf{G} = (\mathsf{T}, \mathsf{E})$ of the thermal network with the set of vertices $\mathsf{T} = \{T_1, ..., T_n\}$ and the set of edges $\mathsf{E} = \{\{T_1, T_1\}, \{T_1, T_2\}, ..., \{T_n, T_n\}\}$. Each vertex $T_i \in \mathsf{T}$ corresponds to the dedicated temperature node in the thermal network. The weights of the edges $\{T_i, T_j\} \in \mathsf{E}$ correspond to the reciprocals of the thermal resistances $R_{th,ij}$ between two vertices $T_i, T_j \in \mathsf{T}$:

$$A_{tn}(i,j) = \begin{cases} \frac{1}{R_{th,ij}}, & \text{if } \{T_i, T_j\} \in \mathsf{E}, \\ 0, & \text{else.} \end{cases} \tag{6.8}$$

2. Subtraction of the sum of all row elements $A_{tn}(i,j)$ in $\boldsymbol{A}_{tn}$ from the diagonal element $A_{tn}(i,i)$ in each row i:

$$A_{tn}(i,i) = A_{tn}(i,i) - \sum_{j=1}^{n} A_{tn}(i,j), \quad \forall i \in \{1, ..., n\}. \tag{6.9}$$

3. Subtraction of the coefficient $\mathcal{K}^l$ in (6.2) from the diagonal element $A_{tn}(i,i)$, to which $x_{tn,i}(t) = T^l_{ev,sf}(t)$ applies:

$$A_{tn}(i,i) = \begin{cases} A_{tn}(i,i) - \mathcal{K}^l, & \text{if } x_{tn,i}(t) = T^l_{ev,sf}(t),\ \forall l \in \{1, ..., r\}, \\ A_{tn}(i,i), & \text{else.} \end{cases} \tag{6.10}$$

4. Multiplication of the i-th row of $\boldsymbol{A}_{tn}$ with the corresponding reciprocal of the thermal capacitance $C_{th,i}$:

$$A_{tn}(i,j) = A_{tn}(i,j) \cdot \frac{1}{C_{th,i}}, \quad \forall i, j \in \{1, ..., n\}. \tag{6.11}$$

The construction of the input matrix $\boldsymbol{B}_{tn} \in \mathbb{R}^{n\times q}$ is given as follows:

1. For each external heat input $\dot{Q}_{sf,j}(t)$ to the temperature node $x_{tn,i}(t) = T_i(t)$, $B_{tn}(i,j) = 1$ holds, otherwise $B_{tn}(i,j) = 0$:

$$B_{tn}(i,j) = \begin{cases} 1, & \text{if } \dot{Q}_{sf,j}(t) \text{ to } x_{tn,i}(t) = T_i(t),\ \forall j \in \{1, ..., q\}, \\ 0, & \text{else.} \end{cases} \tag{6.12}$$

2. Multiplication of the i-th row of $\boldsymbol{B}_{tn}$ with the corresponding reciprocal of the thermal capacitance $C_{th,i}$:

$$B_{tn}(i,j) = B_{tn}(i,j) \cdot \frac{1}{C_{th,i}}, \quad \forall i \in \{1, ..., n\},\ j \in \{1, ..., q\}. \tag{6.13}$$

The matrix $\boldsymbol{C}_{tn} \in \mathbb{R}^{2r\times n}$ results from the following:

1. The element $C_{tn}(2 \cdot l - 1, i)$ equals the coefficient $\mathcal{K}^l$ in (6.2), for which $x_{tn,i}(t) = T^l_{ev,sf}(t)$ holds, otherwise $C_{tn}(2 \cdot l - 1, i) = 0$:

$$C_{tn}(2 \cdot l - 1, i) = \begin{cases} \mathcal{K}^l, & \text{if } x_{tn,i}(t) = T^l_{ev,sf}(t),\ \forall l \in \{1, ..., r\}, \\ 0, & \text{else.} \end{cases} \tag{6.14}$$

2. If the state $x_{tn,i}(t)$ corresponds to the evaporator surface temperature $T^l_{ev,sf}(t)$, then $C_{tn}(2 \cdot l, i) = 1$, otherwise $C_{tn}(2 \cdot l, i) = 0$:

$$C_{tn}(2 \cdot l, i) = \begin{cases} 1, & \text{if } x_{tn,i}(t) = T^l_{ev,sf}(t),\ \forall l \in \{1, ..., r\}, \\ 0, & \text{else.} \end{cases} \tag{6.15}$$

The matrix $\boldsymbol{E}_{tn} \in \mathbb{R}^{n \times 2r}$ is given as follows:

1. The element $E_{tn}(i, 2 \cdot l - 1)$ equals the coefficient $\mathcal{L}^l$ in (6.2), for which $x_{tn,i}(t) = T^l_{ev,sf}(t)$ holds:

$$E_{tn}(i, 2 \cdot l - 1) = \begin{cases} \mathcal{L}^l, & \text{if } x_{tn,i}(t) = T^l_{ev,sf}(t),\ \forall l \in \{1, ..., r\}, \\ 0, & \text{else.} \end{cases} \tag{6.16}$$

2. The element $E_{tn}(i, 2 \cdot l)$ equals the coefficient $\mathcal{M}^l$ in (6.2), for which $x_{tn,i}(t) = T^l_{ev,sf}(t)$ holds:

$$E_{tn}(i, 2 \cdot l) = \begin{cases} \mathcal{M}^l, & \text{if } x_{tn,i}(t) = T^l_{ev,sf}(t),\ \forall l \in \{1, ..., r\}, \\ 0, & \text{else.} \end{cases} \tag{6.17}$$

3. Multiplication of the i-th row of $\boldsymbol{E}_{tn}$ with the corresponding reciprocal of the thermal capacitance $C_{th,i}$:

$$E_{tn}(i, j) = E_{tn}(i, j) \cdot \frac{1}{C_{th,i}}, \quad \forall i \in \{1, ..., n\},\ j \in \{1, ..., 2 \cdot r\}. \tag{6.18}$$

The matrix $\boldsymbol{F}_{tn} \in \mathbb{R}^{2r \times 2r}$ is constructed as follows:

1. The element $F_{tn}(2 \cdot l - 1, 2 \cdot l - 1)$ equals the negative coefficient $\mathcal{L}^l$ in (6.2), otherwise $F_{tn}(2 \cdot l - 1, 2 \cdot l - 1) = 0$:

$$F_{tn}(2 \cdot l - 1, 2 \cdot l - 1) = \begin{cases} -\mathcal{L}^l, & \text{if } x_{tn,i}(t) = T^l_{ev,sf}(t),\ \forall l \in \{1, ..., r\}, \\ 0, & \text{else.} \end{cases} \tag{6.19}$$

2. The element $F_{tn}(2 \cdot l - 1, 2 \cdot l)$ equals the negative coefficient $\mathcal{M}^l$ in (6.2), otherwise $F_{tn}(2 \cdot l - 1, 2 \cdot l) = 0$:

$$F_{tn}(2 \cdot l - 1, 2 \cdot l) = \begin{cases} -\mathcal{M}^l, & \text{if } x_{tn,i}(t) = T^l_{ev,sf}(t),\ \forall l \in \{1, ..., r\}, \\ 0, & \text{else.} \end{cases} \tag{6.20}$$

These specific instructions enable a state-space modeling of arbitrary thermal networks connecting multiple LHPs. Based on this procedure, the corresponding state-space models of the considered advanced LHP systems in this thesis are constructed in the next sections.

6.1.1 Loop Heat Pipe with Attached Thermal Mass

For the consideration of the thermal behavior of an additional thermal mass at the evaporator and its impact on the LHP dynamics, the network representation of a thermal mass is attached to the thermal network of the evaporator subsystem in Fig. 4.4. Thus, the LHP state-space model is extended to form the overall state-space model of a conventional LHP with a critical total evaporator mass in relation to the total thermal mass of the CC (cf. [HB12]) by establishing the state-space model of the thermal network with the previous modular modeling approach. A schematic of the resulting LHP system and its corresponding thermal network are depicted in Fig. 6.1 and Fig. 6.2, respectively.

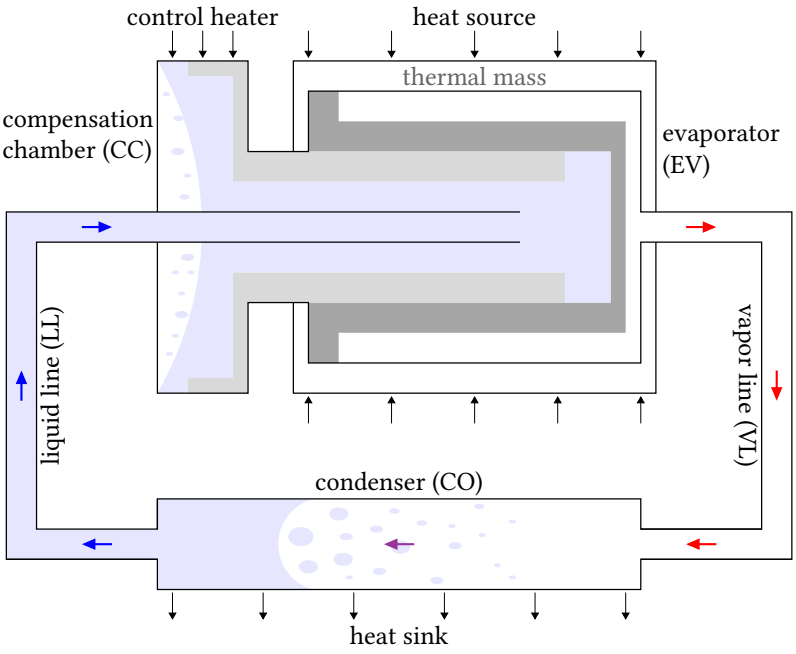

Figure 6.1: Structure of an LHP with attached thermal mass

With the extension at the evaporator, the initial impact point of the heat source moves further away from the working fluid. The heat input from the heat sources is applied directly to the thermal mass, which subsequently transfers the heat through the evaporator body into the working fluid for evaporation and further transport to the heat sink.

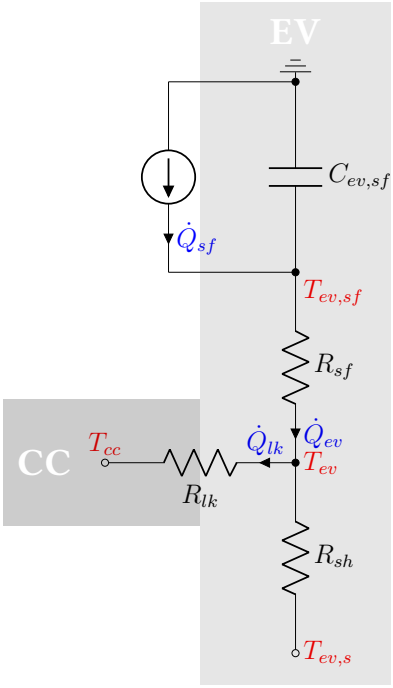

Figure 6.2: Thermal network representation of the evaporator subsystem with attached thermal mass

Using the above instructions, the following one-dimensional state-space model of the thermal mass network in Fig. 6.2 is established:

$$\dot{x}_{tn}(t) = a_{tn} \cdot x_{tn}(t) + b_{tn} \cdot u_{tn}(t) + \boldsymbol{e}_{tn} \cdot \boldsymbol{d}_{tn}(t), \tag{6.21a}$$

$$\boldsymbol{y}_{tn}(t) = \boldsymbol{c}_{tn} \cdot x_{tn}(t) + \boldsymbol{F}_{tn} \cdot \boldsymbol{d}_{tn}(t), \tag{6.21b}$$

with the variables and vectors $x_{tn}(t) = T_{ev,sf}(t)$, $u_{tn}(t) = \dot{Q}_{sf}(t)$, $\boldsymbol{d}_{tn}(t) = [T_{ev,s}(t), T_{cc}(t)]^\top$, and $\boldsymbol{y}_{tn}(t) = [\dot{Q}_{ev}(t), T_{ev,sf}(t)]^\top$.

The matrices in (6.21) are defined as follows:

$$a_{tn} = -\frac{1}{C_{ev,sf}}\mathcal{K}, \tag{6.22}$$

$$b_{tn} = \frac{1}{C_{ev,sf}}, \tag{6.23}$$

$$\boldsymbol{c}_{tn} = \begin{bmatrix} \mathcal{K} \\ 1 \end{bmatrix}, \tag{6.24}$$

$$\boldsymbol{e}_{tn} = \begin{bmatrix} \frac{1}{C_{ev,sf}}\mathcal{L} & \frac{1}{C_{ev,sf}}\mathcal{M} \end{bmatrix}, \tag{6.25}$$

$$\boldsymbol{F}_{tn} = \begin{bmatrix} -\mathcal{L} & -\mathcal{M} \\ 0 & 0 \end{bmatrix}, \tag{6.26}$$

with the thermal capacitance $C_{ev,sf}$, the thermal resistance R_{sf}, and the parameters $\mathcal{K}$, $\mathcal{L}$, and $\mathcal{M}$ defined in (6.2).

For the overall state-space model of the LHP with attached thermal mass, (6.21) is connected with the LHP state-space model (4.84) by merging both state spaces. Furthermore, the heat load $\dot{Q}_{ev}(t)$ in the overall state-space model results from the output of the extended thermal network in (6.21b). Thus, the final state-space model with the extended state vector $\boldsymbol{x}(t) = [T_{cc}(t), L_{2\phi}(t), \dot{m}^l(t), T_{ev,sf}(t)]^\top$, the same input variable $u(t) = \dot{Q}_{cc}(t)$, the new disturbance vector $\boldsymbol{d}(t) = [\dot{Q}_{sf}(t), T_{sk}(t)]^\top$, and the new output vector $\boldsymbol{y}(t) = [T_{cc}(t), T_{ev,sf}(t), T_{co,i}(t), T_{co,o}(t)]^\top$ results:

$$\dot{\boldsymbol{x}}(t) = \boldsymbol{f}\big(\boldsymbol{x}(t), u(t), \boldsymbol{d}(t)\big), \tag{6.27a}$$

$$\boldsymbol{y}(t) = \boldsymbol{g}\big(\boldsymbol{x}(t), \boldsymbol{d}(t)\big). \tag{6.27b}$$

While f_1 - f_3 in (6.27a) correspond to the previous state functions (4.85), (4.86), (4.87), the fourth state function is derived from (6.21a):

$$f_4 = -\frac{\mathcal{K}}{C_{ev,sf}} \cdot T_{ev,sf}(t) + \frac{1}{C_{ev,sf}} \cdot \dot{Q}_{sf}(t) + \frac{\mathcal{L}}{C_{ev,sf}} \cdot T_{ev,s}(t) + \frac{\mathcal{M}}{C_{ev,sf}} \cdot T_{cc}(t). \tag{6.28}$$

Accordingly, g_1, g_3, and g_4 in (6.27b) result from the previous output equation of (4.84), i.e. the output functions (4.71), (4.73), and (4.74), while the second output function g_2 corresponds to the second output of (6.21b).

With this model, the simulation of the LHP behavior under consideration of different sizes of the thermal mass at the evaporator is possible. Furthermore, the basis for a corresponding model-based control design to handle the possible nonlinear effects in form of temperature oscillations is set. The stability limit of (6.27) in the OP in dependence on $C_{ev,sf}$ can be determined based on Theorem 4.1. The resulting critical value of $C_{ev,sf}$ for the considered LHP system is calculated in Sec. 7.2.5.

In the following section, the introduced approach is extended to model two parallel LHPs.

6.1.2 Parallel Loop Heat Pipes with Arterial Heat Pipes

According to Fig. 2.1, the heat transport system of an LCT consists of parallel LHPs with ArHPs. Both LHPs spread across the structure that carries the LCT and make sure that the LCT is cooled homogeneously. Thus, a balanced temperature level is achieved that supports the optimal operation of the laser for high precision communications. For the modeling of the complex heat transport system with parallel LHPs, the LCT structure is regarded as one accumulated thermal mass, which is thermally coupled with the ArHPs and the evaporators of both LHPs. A schematic of LHP a and LHP b with their respective ArHPs on the LCT structure and its corresponding thermal network are presented in Fig. 6.3 and Fig. 6.4, respectively.

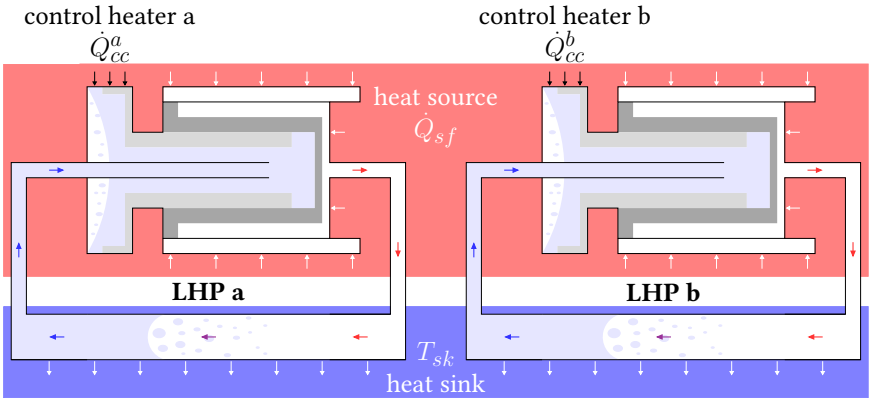

Figure 6.3: Structure of two parallel LHPs (LHP a and LHP b) each with two ArHPs mounted on the thermal mass of a heat source (e.g. an LCT)

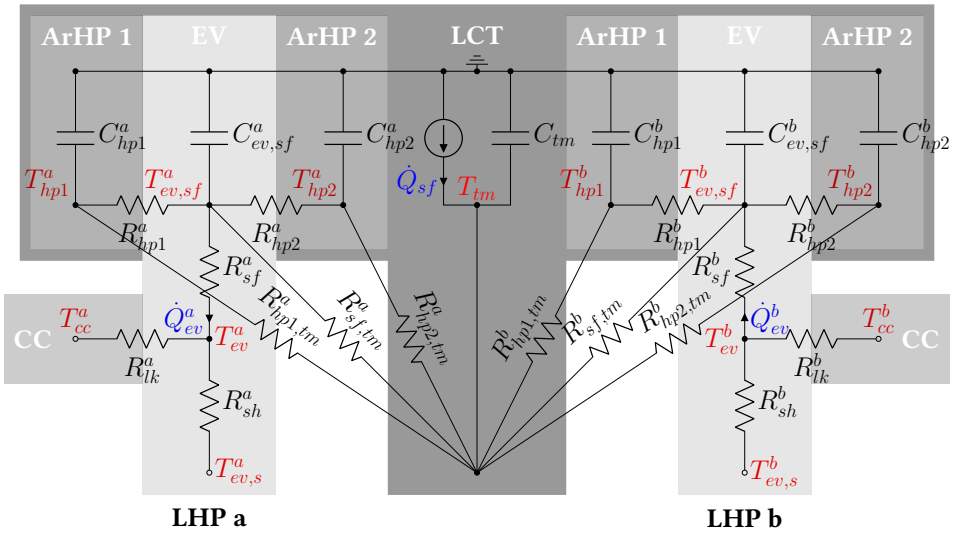

Figure 6.4: Thermal network representation of the evaporator subsystems of two parallel LHPs (LHP a and LHP b) each with two ArHPs mounted on the thermal mass of a heat source (e.g. an LCT)

Following the previous instructions, a thermal network is designed that is able to connect two parallel LHPs with a thermal mass. Before the dynamical models of the two LHPs are coupled to form the model of the advanced LCT heat transport system, the following assumption is made.

Assumption 6.1. *The heat exchange between the condenser lines of both LHPs in the condenser plates is neglected.*

Assumption 6.1 applies to the condenser plates of the LCT, as presented in Fig. 2.1, since the local temperature difference as the driving force of the heat exchange is smaller between both condenser lines than between each condenser line and the heat sink. In addition to perfect cooling conditions under consideration of Assumption 4.1, a thermal network between the heat source, the evaporators, and their respective ArHPs is established to model the heat transfer paths starting from the heat load $\dot{Q}_{sf}(t)$ at the surface of the thermal mass. The resulting seven-dimensional state-space model is given by

$$\dot{\boldsymbol{x}}_{tn}(t) = \boldsymbol{A}_{tn} \cdot \boldsymbol{x}_{tn}(t) + \boldsymbol{b}_{tn} \cdot u_{tn}(t) + \boldsymbol{E}_{tn} \cdot \boldsymbol{d}_{tn}(t), \tag{6.29a}$$

$$\boldsymbol{y}_{tn}(t) = \boldsymbol{C}_{tn} \cdot \boldsymbol{x}_{tn}(t) + \boldsymbol{F}_{tn} \cdot \boldsymbol{d}_{tn}(t), \tag{6.29b}$$

where

$$\boldsymbol{x}_{tn}(t) = \begin{bmatrix} T^a_{hp1}(t) & T^a_{hp2}(t) & T^a_{ev,sf}(t) & T^b_{hp1}(t) & T^b_{hp2}(t) & T^b_{ev,sf}(t) & T_{tm}(t) \end{bmatrix}^\top, \tag{6.30}$$

$$u_{tn}(t) = \dot{Q}_{sf}(t), \tag{6.31}$$

$$\boldsymbol{d}_{tn}(t) = \begin{bmatrix} T^a_{ev,s}(t) & T^a_{cc}(t) & T^b_{ev,s}(t) & T^b_{cc}(t) \end{bmatrix}^\top, \tag{6.32}$$

$$\boldsymbol{y}_{tn}(t) = \begin{bmatrix} \dot{Q}^a_{ev}(t) & T^a_{ev,sf}(t) & \dot{Q}^b_{ev}(t) & T^b_{ev,sf}(t) \end{bmatrix}^\top, \tag{6.33}$$

with the temperature $T_{tm}(t)$ and the thermal capacitance C_{tm} of the LCT structure. The superscripts a and b of the temperatures $T_{hp1}(t)$, $T_{hp2}(t)$, and $T_{ev,sf}(t)$ as well as of the heat load $\dot{Q}_{ev}(t)$ mark the affiliation with the respective LHP. The system matrix $\boldsymbol{A}_{tn} \in \mathbb{R}^{7\times7}$ contains the following diagonal elements:

$$A_{tn}(1,1) = -\frac{1}{C^a_{hp1}}\left(\frac{1}{R^a_{hp1}} + \frac{1}{R^a_{hp1,tm}}\right),$$

$$A_{tn}(2,2) = -\frac{1}{C^a_{hp2}}\left(\frac{1}{R^a_{hp2}} + \frac{1}{R^a_{hp2,tm}}\right),$$

$$A_{tn}(3,3) = -\frac{1}{C^a_{ev,sf}}\left(\frac{1}{R^a_{hp1}} + \frac{1}{R^a_{hp2}} + \frac{1}{R^a_{sf,tm}} + \mathcal{K}^a\right),$$

$$A_{tn}(4,4) = -\frac{1}{C^b_{hp1}}\left(\frac{1}{R^b_{hp1}} + \frac{1}{R^b_{hp1,tm}}\right),$$

$$A_{tn}(5,5) = -\frac{1}{C^b_{hp2}}\left(\frac{1}{R^b_{hp2}} + \frac{1}{R^b_{hp2,tm}}\right),$$

$$A_{tn}(6,6) = -\frac{1}{C^b_{ev,sf}}\left(\frac{1}{R^b_{hp1}} + \frac{1}{R^b_{hp2}} + \frac{1}{R^b_{sf,tm}} + \mathcal{K}^b\right),$$

$$A_{tn}(7,7) = -\frac{1}{C_{tm}}\left(\frac{1}{R^a_{hp1,tm}} + \frac{1}{R^a_{hp2,tm}} + \frac{1}{R^a_{sf,tm}} + \frac{1}{R^b_{hp1,tm}} + \frac{1}{R^b_{hp2,tm}} + \frac{1}{R^b_{sf,tm}}\right),$$

with the respective thermal resistances $R_{hp1,tm}$, $R_{hp2,tm}$, and $R_{sf,tm}$ of LHP a and LHP b. All other elements of $\boldsymbol{A}_{tn}$ are zero except for the following elements:

$$A_{tn}(1,3) = \frac{1}{R^a_{hp1}C^a_{hp1}}, \qquad A_{tn}(1,7) = \frac{1}{R^a_{hp1,tm}C^a_{hp1}},$$

$$A_{tn}(2,3) = \frac{1}{R^a_{hp2}C^a_{hp2}}, \qquad A_{tn}(2,7) = \frac{1}{R^a_{hp2,tm}C^a_{hp2}},$$

$$A_{tn}(3,1) = \frac{1}{R^a_{hp1}C^a_{ev,sf}}, \qquad A_{tn}(3,2) = \frac{1}{R^a_{hp2}C^a_{ev,sf}},$$

$$A_{tn}(3,7) = \frac{1}{R^a_{sf,tm}C^a_{ev,sf}}, \qquad A_{tn}(4,6) = \frac{1}{R^b_{hp1}C^b_{hp1}},$$

$$A_{tn}(4,7) = \frac{1}{R^b_{hp1,tm}C^b_{hp1}}, \qquad A_{tn}(5,6) = \frac{1}{R^b_{hp2}C^b_{hp2}},$$

$$A_{tn}(5,7) = \frac{1}{R^b_{hp2,tm}C^b_{hp2}}, \qquad A_{tn}(6,4) = \frac{1}{R^b_{hp1}C^b_{ev,sf}},$$

$$A_{tn}(6,5) = \frac{1}{R^b_{hp2}C^b_{ev,sf}}, \qquad A_{tn}(6,7) = \frac{1}{R^b_{sf,tm}C^b_{ev,sf}},$$

$$A_{tn}(7,1) = \frac{1}{R^a_{hp1,tm}C_{tm}}, \qquad A_{tn}(7,2) = \frac{1}{R^a_{hp2,tm}C_{tm}},$$

$$A_{tn}(7,3) = \frac{1}{R^a_{sf,tm}C_{tm}}, \qquad A_{tn}(7,4) = \frac{1}{R^b_{hp1,tm}C_{tm}},$$

$$A_{tn}(7,5) = \frac{1}{R^b_{hp2,tm}C_{tm}}, \qquad A_{tn}(7,6) = \frac{1}{R^b_{sf,tm}C_{tm}}.$$

The other matrices of the state-space model (6.29) are given by

$$\boldsymbol{b}_{tn} = \begin{bmatrix} 0 & 0 & 0 & 0 & 0 & 0 & \frac{1}{C_{tm}} \end{bmatrix}^\top, \tag{6.34}$$

$$\boldsymbol{C}_{tn} = \begin{bmatrix} 0 & 0 & \mathcal{K}^a & 0 & 0 & 0 & 0 \\ 0 & 0 & 1 & 0 & 0 & 0 & 0 \\ 0 & 0 & 0 & 0 & 0 & \mathcal{K}^b & 0 \\ 0 & 0 & 0 & 0 & 0 & 1 & 0 \end{bmatrix}, \tag{6.35}$$

$$\boldsymbol{E}_{tn} = \begin{bmatrix} 0 & 0 & 0 & 0 \\ 0 & 0 & 0 & 0 \\ \frac{1}{C^a_{ev,sf}}\mathcal{L}^a & \frac{1}{C^a_{ev,sf}}\mathcal{M}^a & 0 & 0 \\ 0 & 0 & 0 & 0 \\ 0 & 0 & 0 & 0 \\ 0 & 0 & \frac{1}{C^b_{ev,sf}}\mathcal{L}^b & \frac{1}{C^b_{ev,sf}}\mathcal{M}^b \\ 0 & 0 & 0 & 0 \end{bmatrix}, \tag{6.36}$$

$$\boldsymbol{F}_{tn} = \begin{bmatrix} -\mathcal{L}^a & -\mathcal{M}^a & 0 & 0 \\ 0 & 0 & 0 & 0 \\ 0 & 0 & -\mathcal{L}^b & -\mathcal{M}^b \\ 0 & 0 & 0 & 0 \end{bmatrix}. \tag{6.37}$$

Finally, the state-space model of the parallel LHPs with ArHPs is constructed by connecting (6.29) with two state-space models (4.84) for LHP a and LHP b. The combination results in the overall state-space model (6.38):

$$\dot{\boldsymbol{x}}(t) = \boldsymbol{f}\big(\boldsymbol{x}(t), \boldsymbol{u}(t), \boldsymbol{d}(t)\big), \tag{6.38a}$$

$$\boldsymbol{y}(t) = \boldsymbol{g}\big(\boldsymbol{x}(t), \boldsymbol{d}(t)\big), \tag{6.38b}$$

with the extended state vector

$$\boldsymbol{x}(t) = \begin{bmatrix} T^a_{cc}(t) & L^a_{2\phi}(t) & \dot{m}^{l,a}(t) & T^b_{cc}(t) & L^b_{2\phi}(t) & \dot{m}^{l,b}(t) & \boldsymbol{x}^\top_{tn}(t) \end{bmatrix}^\top, \tag{6.39}$$

the new input vector

$$\boldsymbol{u}(t) = \begin{bmatrix} \dot{Q}^a_{cc}(t) & \dot{Q}^b_{cc}(t) \end{bmatrix}^\top, \tag{6.40}$$

the disturbance vector

$$\boldsymbol{d}(t) = \begin{bmatrix} \dot{Q}_{sf}(t) & T_{sk}(t) \end{bmatrix}^\top, \tag{6.41}$$

and the new output vector

$$\boldsymbol{y}(t) = \begin{bmatrix} T^a_{cc}(t) & T^a_{ev,sf}(t) & T^a_{coi}(t) & T^a_{coo}(t) & T^b_{cc}(t) & T^b_{ev,sf}(t) & T^b_{coi}(t) & T^b_{coo}(t) \end{bmatrix}^\top. \tag{6.42}$$

Similar to the division of the vector functions of (2.1) into (2.3) to (2.5) and (2.6) to (2.8), the individual functions of $\boldsymbol{f}$ and $\boldsymbol{g}$ in (6.38) are derived from the LHP state-space model (4.84) and the thermal network model (6.29). The order of the functions is related to the order of the states in (6.39) and of the outputs in (6.42). Both the functions f_1 to f_3 for LHP a and f_4

to f_6 for LHP b in (6.38a) correspond to the previous state functions (4.85), (4.86), (4.87). The seven other functions f_7 to f_{13} are derived from the state equation (6.29a). Similarly, g_1, g_3, and g_4 for LHP a as well as g_5, g_7, and g_8 for LHP b in (6.38b) result from the previous output functions (4.71), (4.73), and (4.74) of the LHP state-space model (4.84). The output functions g_2 and g_5 correspond to the second and the fourth output of (6.29b).

The state-space model (6.38) enables the simulation of parallel LHPs with ArHPs as they can be found in the heat transport system of an LCT. Due to the coupling of both LHPs with the thermal mass of the LCT, the overall behavior of the advanced LHP system is significantly influenced. For the consideration of the coupling effects, an adequate MIMO controller is designed in the subsequent section.

6.2 Nonlinear Control Designs for Advanced Loop Heat Pipe Systems

For the model-based design of adequate controllers for the considered advanced LHP systems in Sec. 6.1.1 and 6.1.2, the nonlinear designs based on the exact input-output linearization in Sec. 4.2 are adapted. A nonlinear controller is designed for the LHP with attached thermal mass considering the new system equations. For the heat transport system with parallel LHPs, the nonlinear control design is extended to the MIMO case.

6.2.1 PI State Feedback Control Based on Exact Input-Output Linearization for Loop Heat Pipes with Attached Thermal Mass

The design of nonlinear controllers for the LHP with attached thermal mass results analogously from the approaches in Sec. 4.2. Both the CC controller and the cascade controller are designed for the new state-space model (6.27).

Compensation Chamber Control

The input-affine form of (6.27) for the desired CC control design is given by

$$\dot{\boldsymbol{x}}(t) = \boldsymbol{a}\big(\boldsymbol{x}(t), \boldsymbol{d}(t)\big) + \boldsymbol{b} \cdot u(t), \tag{6.43a}$$

$$y(t) = c_1\big(\boldsymbol{x}(t)\big) = T_{cc}(t), \tag{6.43b}$$

with the input vector

$$\boldsymbol{b} = \left[\tfrac{1}{C_{cc}^{op}} \quad 0 \quad 0 \quad 0\right]^\top. \tag{6.44}$$

Thus, the functions a_1, a_2, and a_3 of $\boldsymbol{a}$ correspond to (4.89), (4.90), and (4.91), while a_4 is equal to f_4 of (6.27a). The function c_1 in (6.43b) corresponds to g_1 in (6.27b).

According to (4.102), the well-defined relative degree $\delta = 1$ of (6.43) is determined from the condition

$$L_{\boldsymbol{b}} c_1\big(\boldsymbol{x}(t)\big) = \frac{1}{C_{cc}^{op}} \neq 0. \tag{6.45}$$

Thus, the first state corresponds to the external dynamics while the other three states describe the internal dynamics. The following state feedback controller $y_{cl}(t)$ is obtained from (4.105):

$$y_{cl}(t) = \frac{v(t) - a_1\big(\boldsymbol{x}(t), \boldsymbol{d}(t)\big) - \eta_0 c_1\big(\boldsymbol{x}(t)\big)}{b_1}, \tag{6.46}$$

where the new input variable $v(t)$ is calculated by a PI controller of the form (4.109) with AW strategy (cf. Sec. 4.2.1). The local stability of the OP of the internal dynamics is numerically evaluated in Sec. 7.4.4 according to Lyapunov's indirect method in Theorem 4.1 and Hurwitz criterion in Theorem A.1. In addition, it is verified in simulations in Sec. 7.4.2.

Evaporator Control

For the control of the evaporator temperature with the temperature sensor TS 2 in Fig. 4.1 on the surface of the evaporator mass, a cascade control is designed according to the approach in Sec. 4.2.2. Since the state $T_{ev,sf}$ corresponds to the measured evaporator temperature, the output equation of (6.43) is extended for the cascade control design according to (6.27b):

$$\boldsymbol{y}(t) = \begin{bmatrix} T_{cc}(t) \\ T_{ev,sf}(t) \end{bmatrix} \tag{6.47}$$

Based on (6.28), the differential equation for $T_{ev,sf}(t)$ is given by

$$\dot{T}_{ev,sf}(t) = -\frac{\mathcal{K}}{C_{ev,sf}} \cdot T_{ev,sf}(t) + \frac{1}{C_{ev,sf}} \cdot \dot{Q}_{sf}(t) + \frac{\mathcal{L}}{C_{ev,sf}} \cdot T_{ev,s}(t) + \frac{\mathcal{M}}{C_{ev,sf}} \cdot T_{cc}(t). \tag{6.48}$$

As before, (6.48) is linearized about the OP and transferred into the Laplace domain, which results in the transfer function $G_2(s)$ of LHP Part 2 (cf. Fig. 4.9):

$$G_2(s) = \frac{T_{ev,sf}(s)}{T_{cc}(s)} = \frac{\mathcal{N}}{s - \mathcal{O}}, \tag{6.49}$$

with the parameters $\mathcal{N}$ and $\mathcal{O}$:

$$\mathcal{N} = \frac{1}{C_{ev,sf}} \cdot \left(\mathcal{M} + \mathcal{L} \cdot \frac{B_{wf}^2 \cdot p_{cc}^{op}}{p_{ev}^{op} \cdot \big(A_{wf} - \ln\left(p_{ev}^{op}\right)\big)^2 \cdot (T_{cc}^{op} + C_{wf})^2} \right), \tag{6.50}$$

$$\mathcal{O} = -\frac{1}{C_{ev,sf}} \cdot \mathcal{K}. \tag{6.51}$$

The considered capacity of the thermal mass causes a linear behavior between $T_{cc}(t)$ and $T_{ev,sf}(t)$. This is described by the first-order transfer function (6.49). The transfer function

$G_1(s)$ of the inner control loop arises from the transfer function $G(s)$ of the exact input-output linearized external dynamics of (6.43) with the arbitrary coefficient η_0 extended by a P controller of the form (4.124) with proportional gain K_{p1}:

$$G_1(s) = \frac{T_{cc}(s)}{T_{set}(s)} = \frac{K_{p1}}{s + (\eta_0 + K_{p1})}. \tag{6.52}$$

The series connection of (6.49) and (6.52) describes the final transfer function $G_3(s)$ for the model-based PI control design of the outer control loop:

$$G_3(s) = \frac{T_{ev}(s)}{T_{set}(s)} = G_1(s) \cdot G_2(s) = \frac{K_{p1}}{s + (\eta_0 + K_{p1})} \cdot \frac{\mathcal{N}}{s - \mathcal{O}}. \tag{6.53}$$

The form of the PI controller is given in (4.135).

The disturbance transfer function $G_4(s)$ is derived from (6.48):

$$G_4(s) = \frac{T_{ev,sf}(s)}{\dot{Q}_{sf}(s)} = \frac{\mathcal{P}}{s - \mathcal{O}}, \tag{6.54}$$

with the parameter $\mathcal{P}$:

$$\mathcal{P} = \frac{1}{C_{ev,sf}}. \tag{6.55}$$

Similar to the approach in Sec. 4.2.2, a stationary disturbance feedforward control

$$y_{ff}(t) = K_q \cdot \dot{Q}_{sf}(t) \tag{6.56}$$

is added to the cascade controller. The gain K_q of the feedforward component is determined by the quotient of (6.53) and (6.54) with $s = 0$:

$$K_q = \frac{\mathcal{P}}{\mathcal{N}} \cdot \frac{\eta_0 + K_{p1}}{K_{p1}}. \tag{6.57}$$

The cascade controller is applied in simulations in Sec. 7.4.2. The parameterization and discretization of both previously designed controllers are carried out as presented in Sec. 4.2.1 and 4.2.2, respectively.

After the completion of the control designs for an LHP with attached thermal mass, the control design for parallel LHPs is presented in the following.

6.2.2 PI State Feedback Control Based on Exact Input-Output Linearization for Parallel Loop Heat Pipes with Arterial Heat Pipes

For the application of the exact input-output linearization to the advanced heat transport system with parallel LHPs and ArHPs, this section follows the MIMO case of the corresponding control design described in [Ada18, p. 371]. While the linear state-of-the-art controllers for

the two control heaters on both CCs consider only the linear transfer behavior between their individual inputs and outputs, the coupling of both LHP is neglected. An MIMO control design approach, however, incorporates the coupling to improve the controller performance as well as to handle corresponding nonlinear effects like undesirable temperature oscillations.

The input-affine form of (6.38) is given by the following state-space model:

$$\dot{\boldsymbol{x}}(t) = \boldsymbol{a}\big(\boldsymbol{x}(t), \boldsymbol{d}(t)\big) + \boldsymbol{B} \cdot \boldsymbol{u}(t), \tag{6.58a}$$

$$\boldsymbol{y}(t) = \begin{bmatrix} c_1\big(\boldsymbol{x}(t)\big) \\ c_2\big(\boldsymbol{x}(t)\big) \end{bmatrix} = \begin{bmatrix} T_{cc}^{a}(t) \\ T_{cc}^{b}(t) \end{bmatrix}, \tag{6.58b}$$

with the input matrix

$$\boldsymbol{B} = \begin{bmatrix} \boldsymbol{b}_1 & \boldsymbol{b}_2 \end{bmatrix} = \begin{bmatrix} \frac{1}{C_{cc}^{op,a}} & 0 \\ 0 & 0 \\ 0 & 0 \\ 0 & \frac{1}{C_{cc}^{op,b}} \\ 0 & 0 \\ 0 & 0 \\ 0 & 0 \\ 0 & 0 \\ 0 & 0 \\ 0 & 0 \\ 0 & 0 \\ 0 & 0 \\ 0 & 0 \end{bmatrix}. \tag{6.59}$$

The functions c_1 and c_2 in (6.58b) correspond to g_1 and g_5 of $\boldsymbol{g}$ in (6.38b), respectively. The state functions a_1, a_2, and a_3 representing LHP a and a_4, a_5, and a_6 representing LHP b of $\boldsymbol{a}$ in (6.58a) are equal to the functions (4.89), (4.90), and (4.91). Consequently, the other state functions a_7 to a_{13} of $\boldsymbol{a}$ are derived from the corresponding functions f_7 to f_{13} of $\boldsymbol{f}$ in (6.38a).

As before in Sec. 4.2.1, the Byrnes-Isidori normal form of (6.58) is directly derived from the model itself, since the external dynamics consists of the first and fourth state, while the other states form the state vector of the internal dynamics. For both output variables y_1 and y_2 in (6.58b), the relative degree δ_i ($i = 1, 2$) is defined by the smallest natural number which fulfills the following equation for at least one $j \in \{1, 2\}$ [Ada18, p. 347]:

$$L_{\boldsymbol{b}_j} L_{\boldsymbol{a}}^{\delta_i - 1} c_i\big(\boldsymbol{x}(t)\big) \neq 0. \tag{6.60}$$

For (6.58), it holds:

$$L_{\boldsymbol{b}_1} c_1\big(\boldsymbol{x}(t)\big) = \frac{1}{C_{cc}^{op,a}} \neq 0, \tag{6.61}$$

$$L_{\boldsymbol{b}_2} c_2\big(\boldsymbol{x}(t)\big) = \frac{1}{C_{cc}^{op,b}} \neq 0. \tag{6.62}$$

Thus, the relative degrees of both outputs are well-defined and given by

$$\delta_1 = 1, \tag{6.63}$$

$$\delta_2 = 1. \tag{6.64}$$

In order to apply the exact input-output linearization to the coupled model (6.58), the decoupling matrix $\boldsymbol{Z}$ must be regular [Ada18, p. 373]. For the coupled model, $\boldsymbol{Z}$ is defined as follows:

$$\boldsymbol{Z} = \begin{bmatrix} L_{\boldsymbol{b}_1} c_1\big(\boldsymbol{x}(t)\big) & 0 \\ 0 & L_{\boldsymbol{b}_2} c_2\big(\boldsymbol{x}(t)\big) \end{bmatrix} = \begin{bmatrix} \frac{1}{C_{cc}^{op,a}} & 0 \\ 0 & \frac{1}{C_{cc}^{op,b}} \end{bmatrix}. \tag{6.65}$$

The matrix condition is verified via the determinant of $\boldsymbol{Z}$:

$$\det\left(\boldsymbol{Z}\right) = \frac{1}{C_{cc}^{op,a} C_{cc}^{op,b}} \neq 0. \tag{6.66}$$

Since (6.66) is nonzero, $\boldsymbol{Z}$ is regular. Thus, the state feedback controller for the coupled model (6.58) can be constructed according to [Ada18, p. 373]:

$$y_{cl}(t) = -\boldsymbol{Z}^{-1} \cdot \begin{bmatrix} L_{\boldsymbol{a}} c_1\big(\boldsymbol{x}(t)\big) + \eta_{10} c_1\big(\boldsymbol{x}(t)\big) \\ L_{\boldsymbol{a}} c_2\big(\boldsymbol{x}(t)\big) + \eta_{20} c_2\big(\boldsymbol{x}(t)\big) \end{bmatrix} + \boldsymbol{Z}^{-1} \cdot \boldsymbol{v}(t), \tag{6.67}$$

with the scalar coefficients η_{10} and η_{20} as well as the new input vector $\boldsymbol{v}(t)$. Similar to Sec. 4.2.1, the state feedback controller is extended by two PI controllers of the form (4.109) with AW strategy (cf. Sec. 4.2.1) for improved robustness:

$$\boldsymbol{v}(t) = \begin{bmatrix} y_{pi}^{a}(t) \\ y_{pi}^{b}(t) \end{bmatrix}. \tag{6.68}$$

The total control loop for the heat transport system comprising the parallel LHPs with ArHPs is depicted in Fig. 6.5.

The local stability of the OP of the internal dynamics is numerically evaluated in Sec. 7.4.4 according to Lyapunov's indirect method in Theorem 4.1 and Hurwitz criterion in Theorem A.1 as well as verified in simulations in Sec. 7.4.3.

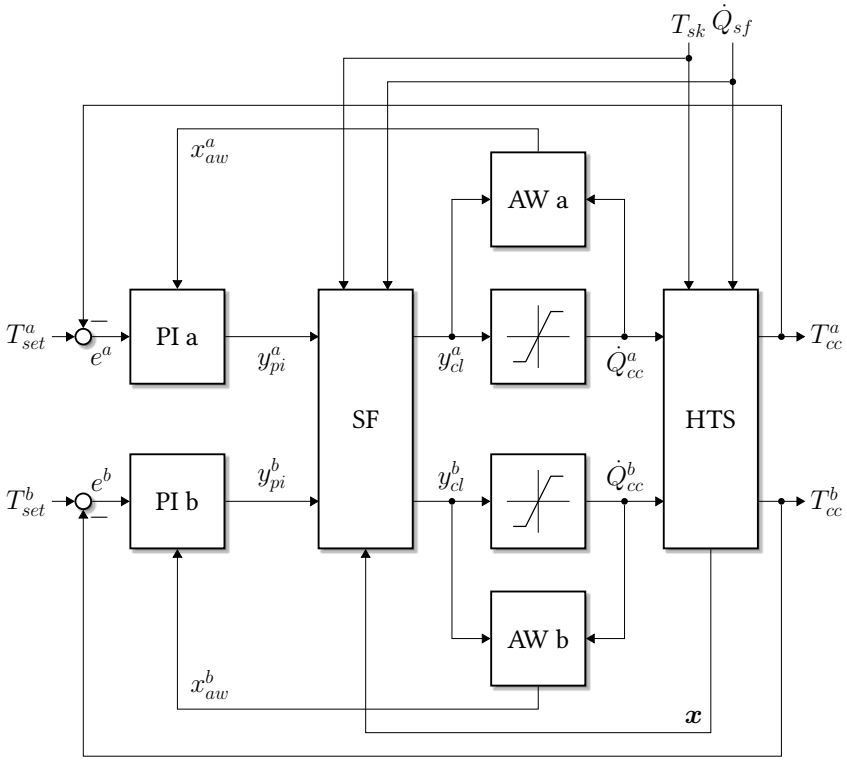

Figure 6.5: Coupled control loops of a heat transport system (HTS) consisting of parallel LHPs (LHP a and LHP b) with a PI controller each, a nonlinear state feedback control (SF), and the AW structures

6.3 Conclusion

For the modeling and control of advanced LHP-based heat transport systems, the complex model of a conventional LHP in Chapter 4 has been extended to include an attached thermal mass at the evaporator as well as to form a coupled model of two parallel LHPs with ArHPs. By using the electrical analogy of thermal networks, the model extensions have been described in a clear and comprehensible manner. Furthermore, the developed step-by-step instructions for thermal networks of LHPs enable the automatic construction of the matrices of the corresponding state-space model. In addition, the algorithm allows for the simple adaption of the model to further advanced LHP-based systems with a different thermal setting including one or several LHPs.

The simulation of LHP-based heat transport systems with additional thermal mass including its impact on the LHP dynamics is now possible. Due to the coupling of the thermal networks with the respective LHP systems, the heat load at the evaporators is influenced by both sides. Thus, the modulation of the net heat load at the evaporator has been modeled to consider

possible temperature oscillations in LHPs with increased thermal evaporator mass and the heat distribution between two parallel LHPs in simulations.

Besides the models, the previous model-based control designs based on the exact input-output linearization have been extended to the new system structures in order to consider their dynamics in the control design. While the increased thermal evaporator mass adds a new state to the previous complex model of an LHP, the coupled state-space model of parallel LHPs forms an MIMO system with two control inputs and two controlled outputs. For this reason, the model-based control designs introduced in Chapter 4 could also been applied to the LHP model with attached thermal mass. For parallel LHPs, however, the corresponding control design for MIMO systems has been used to consider the coupled model structure in contrast to the linear state-of-the-art controllers based on the main transfer paths.

In the next chapter, the comprehensive verification and validation of the introduced models and proposed controllers are given. Moreover, the advantages and disadvantages of the models and controllers are highlighted.

7 Validation and Comparison

For the comparison and the validation of the introduced state-space models and proposed controllers for the conventional LHP and the advanced LHP-based heat transport systems in the previous chapters, measurement data of three different LHP systems on two different test benches are available within the framework of the joint project on behalf of the DLR Space Administration. The first test bench was assembled temporarily during the aforementioned project for the thermal characterization of LHPs. On this test bench, two conventional LHPs (LHP 1 and LHP 2) of different manufacturers were tested and thermally characterized. The second test bench is situated in a vacuum chamber and used for the realization of qualification tests of ready-to-fly hardware such as the advanced heat transport system of an LCT consisting of parallel LHPs on an LCT dummy (LHP 3), as discussed in Sec. 6.1.2. Both test facilities were subject to limited availability, accessibility, and capacity. Thus, test campaigns had to be planned with progression in the early phase of this thesis. Regarding the slow LHP processes and the large amount of possible influences on the LHP operation, a limited range of operating points and conditions could be reached during the time-consuming test runs within this limited period. In later phases of this thesis, no test facility was accessible. Therefore, the available test results of the real application are utilized in this thesis to underline the validity of the state-space models selectively.

Extensive analysis and performance evaluations of the models and the corresponding controllers in this thesis are done using a validated simulation model. The numerical LHP model in [MKHW19], hereinafter referred to as SIM, is designed in close agreement with the experimental characterization of LHP 1. It is able to provide an LHP simulation solution to LHP end users for the evaluation of the performances and robustness of controllers. The corresponding publication [MKHW19] includes the detailed description of the numerical LHP model and the experimental test bench. As introduced in Sec. 2.2, the model uses the finite-difference method to solve the partial differential equations of the condenser for a precise prediction of the mass flows, the phase distribution, and the temperatures along the LHP cycle over the entire operating range. Thus, the results of this thesis can be further supported by the experimentally validated mathematical simulation of a conventional LHP as a safe test environment with unlimited access. In this way, not only arbitrary variations of the operating conditions can be considered, but also the curves of internal variables are available, which cannot be measured on the test benches due to the restriction to noninvasive temperature measurements on the surface of the hermetically sealed LHP.

Some small extensions are realized in order to fit the LHP simulation in [MKHW19] to the needs in this thesis. For the consideration of a control heater on the CC, the variable $\dot{Q}_{cc}$ representing the power input of the control heater is added to the corresponding CC energy balance equation as before in the introduced state-space models (cf. (4.13) or (5.2)). The heat flow $\dot{Q}_{ev}^{SIM}$ into the fluid inside the evaporator is approximated exponentially in [MKHW19]

by a limited growth function fitted to measurement data to model the transfer delay between the dissipated heat $\dot{Q}_{hs}$ of the heat source and the heat load $\dot{Q}_{ev}^{SIM}$. For this thesis, the limited growth function is substituted by a discrete first-order transfer function based on *Euler's backward method*. This approximates the exponential input-output behavior of the unidirectional heat transfer path for a user-friendly implementation of arbitrary heat load profiles in the LHP simulation SIM:

$$\dot{Q}_{ev}^{SIM}(k) = \frac{1}{1+\frac{T_d}{T_{st}}} \cdot \left(\dot{Q}_{hs}(k-1) - \dot{Q}_{ev}^{SIM}(k-1)\right) + \dot{Q}_{ev}^{SIM}(k-1), \tag{7.1}$$

with the delay time constant T_d. The same filter approach is applied to obtain the given heat loads of the state-space models which also experience a transfer delay between the dictated heating profiles of the heaters imitating heat sources on the test benches and the actual heat flows into the LHP systems. Hence, $\dot{Q}_{ev}$ of the conventional LHP and $\dot{Q}_{sf}$ of the advanced LHP systems are delayed by substituting $\dot{Q}_{ev}^{SIM}$ in (7.1), accordingly. The used time constant T_d of the delays is approximated by means of the delay of the measured temperatures. For the different LHP systems, the respective values of T_d are given in the following table:

Symbol	**SIM**	**LHP 1**	**LHP 2**	**LHP 3**
T_d	$500\,\mathrm{s}$	$250\,\mathrm{s}$	$222\,\mathrm{s}$	$2500\,\mathrm{s}$

Table 7.1: Values of the delay time constant T_d with regard to the different LHP systems SIM, LHP 1, LHP 2, and LHP 3

The controllers designed for the conventional LHP without additional thermal mass at the evaporator are tested in the LHP simulation SIM, which is implemented in MATLAB. For the verification of the controllers for advanced LHP-based heat transport systems, the introduced state-space models are implemented in SIMULINK. A simple controller startup routine is described in Appendix A.6 to drive the LHP gently into the desired OP without interrupting the LHP operation and to ensure a safe startup on the test benches.

The parameterization of the state-space models and controllers according to the introduced approaches in the previous chapters is performed in the next section.

7.1 Parameterization

The parameterization includes the repeated adaption of the state-space models and controllers to the different LHP systems SIM, LHP 1, LHP 2, and LHP 3. First, the model parameters are determined based on the respective measurements at steady-state conditions. For this purpose, the OP of each LHP system is defined in the individual equilibrium point of the same LHP system at the desired temperature levels. Since the equilibrium points vary with the controlled and uncontrolled inputs, OPs with values in the middle area of the operating range, which is given in Table 4.1, are chosen for the respective version of the state-space models. Second, the control parameters are calculated based on the parameterized models according to the introduced design approaches.

7.1.1 Model Parameters

The model parameters are calculated by means of the measured data of the investigated LHP systems. However, it is only possible to measure temperatures on the exterior surface of the LHP, and additionally, the interior is rarely known to LHP end user (see Chapter 1). Thus, the lumped model parameters, which describe distributed thermodynamic processes, are roughly deduced from the external geometries and by solving the derived steady-state equations in the OP. The other model parameters are manually adjusted within their physical limits to ensure that the model represents the values and the system dynamics according to the temperature measurements as closely as possible. With this parameter-determination method, the parameters of the LHP state-space models are easily adapted to different LHP setups without detailed LHP design information and extensive measuring effort for the LHP end user.

Complex LHP State-Space Model

The complex LHP state-space model (4.84), hereinafter called Model C, includes seven lumped model parameters R_{lk}, $k_{2\phi}$, k_{sc}, k_{ll}, k_{vl}, k_{sh}, and R_{sh}. For the determination of these parameters, the known data of the investigated LHP systems are used to solve an appropriate equation system in the OP. The data includes the input u^{op} and the disturbances d^{op} as well as the first state T_{cc}^{op}. Besides the CC temperature, more information is available with the three measured temperatures T_{ev}^{op}, $T_{co,i}^{op}$, and $T_{co,o}^{op}$. In the OP as equilibrium point of the system, the derivatives of the states are equal to zero. Hence, the steady-state equations of (4.84) yield the following three equations:

$$f_1^{op} = 0, \tag{7.2}$$

$$f_2^{op} = 0, \tag{7.3}$$

$$f_3^{op} = 0. \tag{7.4}$$

Furthermore, it holds that the mass flow rates $\dot{m}^{l,op}$ and $\dot{m}^{v,op}$ in the OP are equal. The second state $L_{2\phi}^{op}$ remains undefined and therefore enlarges the number of parameters. Thus, an eight-dimensional system of equations is necessary, for which the previous three steady-state equations (7.2) to (7.4) are already present. Three of the remaining five equations are obtained by building the difference between the output equations (4.72), (4.73), and (4.74) in the OP and the measured temperatures T_{ev}^{op}, $T_{co,i}^{op}$, and $T_{co,o}^{op}$:

$$T_{ev}^{op} - g_2^{op} = 0, \tag{7.5}$$

$$T_{co,i}^{op} - g_3^{op} = 0, \tag{7.6}$$

$$T_{co,o}^{op} - g_4^{op} = 0. \tag{7.7}$$

With the differences between (4.39) and the CC inlet temperature $T_{cc,i}^{op}$ as well as between (4.61) and the condenser saturation temperature $T_{co,s}^{op}$, the system of equations is completed:

$$T_{cc,i}^{op} - \left(T_{amb} + \left(T_{co,o}^{op} - T_{amb} \right) \cdot \exp\left(-\frac{k_{ll} \pi D_p L_{ll}}{\dot{m}^{l,op} \bar{c}_{cc,i,co,o}^{l}} \right) \right) = 0, \tag{7.8}$$

$$T_{co,s}^{op} - \left(T_{sk}^{op} + \frac{\Delta h_{co}^{v}}{k_{2\phi} \pi D_p L_{2\phi}^{op}} \cdot \dot{m}_{o}^{2\phi,op} \right) = 0. \tag{7.9}$$

The temperatures $T_{cc,i}^{op}$ and $T_{co,s}^{op}$ are either available based on the thermal characterization of the investigated system or narrowed down by the heat transfer kinetics of the LL and by the distribution of the saturated pressures during LHP operation. The same procedure applies to the contact angle θ_c^{op} to set the pressure difference (4.35).

The complexity of the equations mentioned in Sec. 4.1.7 impedes an analytical solution for the parameters. Hence, the values of the parameters are optimized by means of the least squares method. For this purpose, the square sum of the previous equations is minimized. By an appropriate choice of the initial parameter values, the optimization yields the OP values of the parameters. Since the third state $\dot{m}^l$ takes the smallest values in the area of 10^{-5}, an extremely small deviation from zero in (7.4) in the area of 10^{-12} is desirable. This precision has been achieved with an optimization based on the direct search method applied in Sec. 5.2.4. For the tuning of the model's dynamics, β^{op} is finally adapted in such a way that the dynamics of the CC temperature fit to the measured $\dot{Q}_{cc}$ step response. The different values of the variables and parameters of Model C in the respective OPs of SIM, LHP 1, and LHP 2 are given in Table 7.2.

During the parameter tuning, the focus is set on a good agreement between the measured and the simulated temperatures. While SIM and LHP 1 are based on the same LHP design, the dimensions of the LHP components of LHP 2 differ slightly which has a small impact on the OP values of the model parameters and variables. Thus, the length $L_{2\phi}^{op}$ of the two-phase region in the larger condenser of LHP 2 is greater than for the other two systems. Another difference is the sink temperature T_{sk}^{op}. Due to the higher T_{sk}^{op}, a lower control heater output $\dot{Q}_{cc}^{op}$ is sufficient to reach the same setpoint temperature. For the same reason, the temperature $T_{co,o}^{op}$ of the condenser outlet and the temperature $T_{cc,i}^{op}$ of the CC inlet are higher according to T_{sk}^{op}. The similar heat loads $\dot{Q}_{ev}^{op}$ cause a similar mass flow rate $\dot{m}^{l,op}$ in all three systems, which are designed for the same LHP operating range. All systems operate in the variable conductance mode since the condenser is not fully used, and the subcooling area is sufficiently large to cool the liquid temperature $T_{co,o}^{op}$ down to near sink temperature T_{sk}^{op}. Furthermore, most of the OP values between SIM and LHP 1 agree well. However, the CC dynamics are slightly faster in the numerical simulation. That is why the volume fraction ratio β^{op} and thus the thermal capacitance C_{cc}^{op} of the CC for SIM is smaller than for LHP 1. Another slight difference occurs in the heat transfer coefficients k_{sh}, $k_{2\phi}$, and k_{sc} of the condenser regions, which result from the different temperatures $T_{co,i}^{op}$ and $T_{co,o}^{op}$ at the inlet and outlet due to parasitic heat flows to the heat sink in the real system as well as a different saturation temperature $T_{co,s}^{op}$ and corresponding phase distribution in the condenser. The magnitudes of the heat transfer coefficients rising from k_{sh} over k_{sc} to $k_{2\phi}$ are plausible compared to the local values calculated in SIM.

Symbol	SIM	LHP 1	LHP 2
$\dot{Q}_{cc}^{op}$	$4.653\,\mathrm{W}$	$3.941\,\mathrm{W}$	$2.902\,\mathrm{W}$
$\dot{Q}_{ev}^{op}$	$60\,\mathrm{W}$	$58.93\,\mathrm{W}$	$61.38\,\mathrm{W}$
T_{sk}^{op}	$0\,^{\circ}\mathrm{C}$	$0.45\,^{\circ}\mathrm{C}$	$10.24\,^{\circ}\mathrm{C}$
T_{cc}^{op}	$26.86\,^{\circ}\mathrm{C}$	$27.72\,^{\circ}\mathrm{C}$	$27.07\,^{\circ}\mathrm{C}$
T_{ev}^{op}	$28.58\,^{\circ}\mathrm{C}$	$29.27\,^{\circ}\mathrm{C}$	$28.33\,^{\circ}\mathrm{C}$
$T_{co,i}^{op}$	$27.88\,^{\circ}\mathrm{C}$	$28.81\,^{\circ}\mathrm{C}$	$28.11\,^{\circ}\mathrm{C}$
$T_{co,o}^{op}$	$0\,^{\circ}\mathrm{C}$	$0.45\,^{\circ}\mathrm{C}$	$10.24\,^{\circ}\mathrm{C}$
R_{lk}	$1.226\,\mathrm{K\,W^{-1}}$	$0.7196\,\mathrm{K\,W^{-1}}$	$1.159\,\mathrm{K\,W^{-1}}$
$k_{2\phi}$	$1058\,\mathrm{W\,m^{-2}\,K^{-1}}$	$1049\,\mathrm{W\,m^{-2}\,K^{-1}}$	$1053\,\mathrm{W\,m^{-2}\,K^{-1}}$
k_{sc}	$798.6\,\mathrm{W\,m^{-2}\,K^{-1}}$	$817.9\,\mathrm{W\,m^{-2}\,K^{-1}}$	$804.0\,\mathrm{W\,m^{-2}\,K^{-1}}$
k_{ll}	$2.343\,\mathrm{W\,m^{-2}\,K^{-1}}$	$1.498\,\mathrm{W\,m^{-2}\,K^{-1}}$	$2.218\,\mathrm{W\,m^{-2}\,K^{-1}}$
k_{vl}	$5.647\,\mathrm{W\,m^{-2}\,K^{-1}}$	$2.900\,\mathrm{W\,m^{-2}\,K^{-1}}$	$1.469\,\mathrm{W\,m^{-2}\,K^{-1}}$
k_{sh}	$454.9\,\mathrm{W\,m^{-2}\,K^{-1}}$	$388.4\,\mathrm{W\,m^{-2}\,K^{-1}}$	$455.9\,\mathrm{W\,m^{-2}\,K^{-1}}$
R_{sh}	$0.02566\,\mathrm{K\,W^{-1}}$	$0.02364\,\mathrm{K\,W^{-1}}$	$0.01738\,\mathrm{K\,W^{-1}}$
$L_{2\phi}^{op}$	$0.3268\,\mathrm{m}$	$0.3145\,\mathrm{m}$	$0.5397\,\mathrm{m}$
$\dot{m}^{l,op}$	$50.41\,\mathrm{mg\,s^{-1}}$	$49.02\,\mathrm{mg\,s^{-1}}$	$51.97\,\mathrm{mg\,s^{-1}}$
$T_{cc,i}^{op}$	$1.372\,^{\circ}\mathrm{C}$	$1.344\,^{\circ}\mathrm{C}$	$10.88\,^{\circ}\mathrm{C}$
$T_{co,s}^{op}$	$26.86\,^{\circ}\mathrm{C}$	$27.72\,^{\circ}\mathrm{C}$	$27.07\,^{\circ}\mathrm{C}$
β^{op}	0.45	0.50	0.50
θ_c^{op}	$80°$	$80°$	$80°$
C_{cc}^{op}	$21.85\,\mathrm{J\,K^{-1}}$	$60.90\,\mathrm{J\,K^{-1}}$	$89.57\,\mathrm{J\,K^{-1}}$

Table 7.2: Values of the model parameters and variables of Model C in the OPs of the investigated LHP systems SIM, LHP 1, and LHP 2

A comparison of the measured $1\,\mathrm{W}$ $\dot{Q}_{cc}$ step responses of the investigated LHP systems in their OPs with the respective simulated step response of Model C are presented in Fig. 7.1, 7.2, and 7.3. The four measurable temperatures T_{cc}, T_{ev}, $T_{co,i}$, and $T_{co,o}$ are compared to the results of Model C. In accordance with their respective parameterization, the OPs of all three systems are met by Model C, and the CC dynamics are closely adapted via β^{op}.

Compared to SIM, Model C reaches a different equilibrium point at higher output temperatures after the $1\,\mathrm{W}$ step in Fig. 7.1. Thus, a stationary deviation of approximately $\Delta T_{cc}(2000\,\mathrm{s}) = 0.69\,\mathrm{K}$ between the CC temperatures exists, which also affects the other temperatures. The approximate value of the stationary deviation of the CC temperatures in equilibrium is taken at the end of the figure at $t = 2000\,\mathrm{s}$. This small deviation in T_{cc} is traced back to the different modeling approaches of the internal mass flows resulting in stationary mass flow rates of different sizes, which is discussed in more detail in Sec. 7.2.3. However, the dynamics of the measured temperatures agree well.

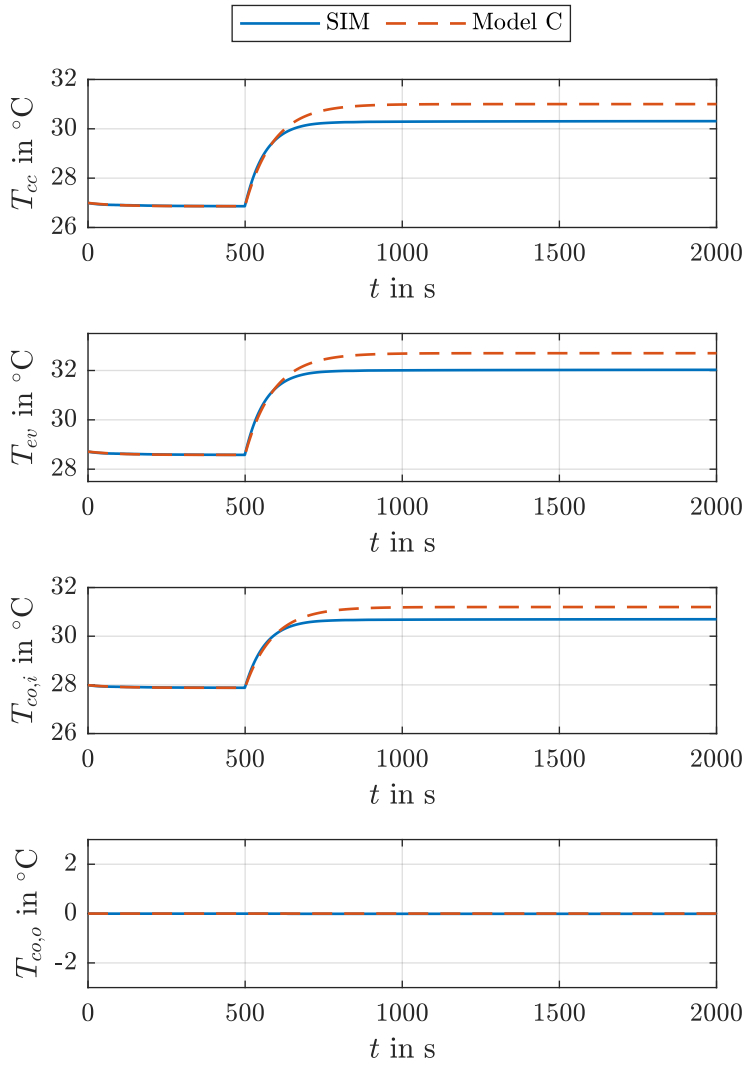

Figure 7.1: Comparison of 1 W $\dot{Q}_{cc}$ step responses of SIM and Model C in the OP

In contrast to the comparison with SIM, more differences are visible between Model C and LHP 1 in Fig. 7.2. Here as well, a stationary deviation between the CC temperature of approximately $\Delta T_{cc}(2800\,\mathrm{s}) = 0.89\,\mathrm{K}$ is present after the 1 W step, but in the opposite direction. The higher CC temperature in the measured data results from the superficial temperature sensor on the CC that is situated near the impact point of the control heater. Hence, a larger temperature difference before and after the step results, which is also passed on to the evaporator temperature. A greater deviation between Model C and LHP 1 presents itself in the third row of Fig. 7.2. Here as well, the difference is caused by the superficial temperature measurement.

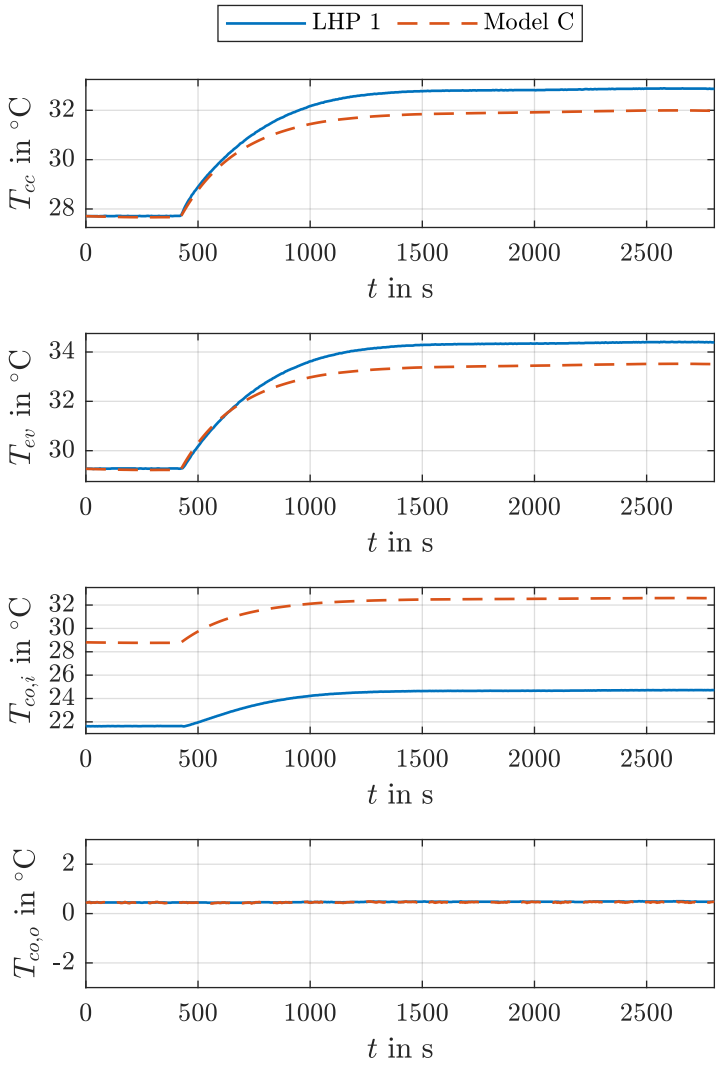

Figure 7.2: Comparison of 1 W $\dot{Q}_{cc}$ step responses of LHP 1 and Model C in the OP

Due to the flow direction during the normal LHP operation, the saturation pressure p_{co} and the corresponding saturation temperature $T_{co,s}$ in the condenser must be slightly higher than in the CC. However, the measured condenser inlet temperature $T_{co,i}$ at the beginning of the superheated condenser region is lower than T_{cc} due to the proximity of the temperature sensor to the cooled condenser area. Thus, parasitic heat flows distort the measurement, and a superficial temperature is measured at the condenser inlet that is too low for the expected fluid temperature $T_{co,i}$. For this reason, the OP value of $T_{co,i}$ for LHP 1 in Table 7.2 is placed between T_{ev}^{op} and $T_{co,s}^{op}$ accordingly. The minor deviations in the dynamics of the four temper-

atures result from Assumption 4.2, because of which the inertia-related delays between the temperatures are neglected in Model C.

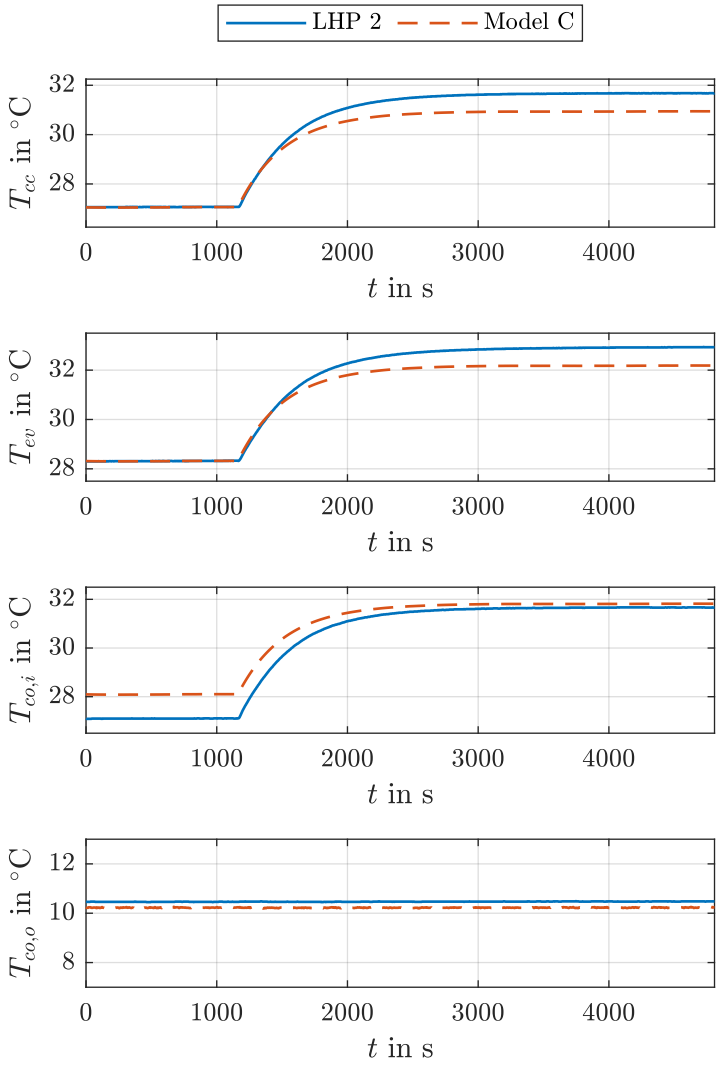

Figure 7.3: Comparison of 1 W $\dot{Q}_{cc}$ step responses of LHP 2 and Model C in the OP

In Fig. 7.3, the measured temperatures of the second LHP design, LHP 2, are compared to Model C. The deviation in the CC temperatures is in a similar range as in the previous figures with a value of approximately $\Delta T_{cc}(4800\,\mathrm{s}) = 0.73\,\mathrm{K}$ at the end of the figure. However, the temperature sensor on the VL measuring $T_{co,i}$ is located further away from the condenser and thus is less distorted by the heat sink. Nevertheless, a lower $T_{co,i}$ than expected is measured here as well. Furthermore, a small, constant deviation between the measured and the simulated

condenser outlet temperature $T_{co,o}$ is shown in the fourth row of Fig. 7.3. The 1 W step has no major impact on $T_{co,o}$ as in the simulations before, since the condenser is not fully used. Hence, the liquid in the subcooling areas of both systems is cooled down to near sink temperature T_{sk}. Due to the local distance of the temperature sensors of LHP 2, the measured $T_{co,o}$ of LHP 2 lays slightly above the measured T_{sk} and $T_{co,o}$ of Model C, respectively. However, the resulting temperature gradient based on a thermal resistance between both sensors is not modeled in Model C. The deviation between both temperatures is $\Delta T_{coo}(4800\,\mathrm{s}) = 0.24\,\mathrm{K}$ and hence small. Overall, the desired agreement between the temperature dynamics of Model C and LHP 2 remains very satisfactory.

Simplified LHP State-Space Model

The six model parameters of the simplified LHP state-space model (5.14), hereinafter called Model S, include the three thermal capacitances C_{cc}^{op}, C_{ev}^{op}, and C_{co}^{op}, the two thermal resistances R_{lk} and R_{co}, and the mass flow rate $\dot{m}$. The latter are determined from the steady-state equations of (5.14). The respective system of equations is solved analytically in dependence on the measured OP values of the states T_{cc}^{op}, T_{ev}^{op}, and T_{co}^{op} and the inputs $\dot{Q}_{cc}^{op}$, $\dot{Q}_{ev}^{op}$, and T_{sk}^{op}:

$$R_{lk} = \frac{\left(T_{cc}^{op} - T_{ev}^{op}\right)\left(\Delta h_{ev}^{v} - \bar{c}_{co,cc}^{l}\left(T_{co}^{op} - T_{cc}^{op}\right) - \bar{c}_{cc,ev}^{l}\left(T_{cc}^{op} - T_{ev}^{op}\right)\right)}{\dot{Q}_{cc}^{op}\left(\Delta h_{ev}^{v} - \bar{c}_{cc,ev}^{l}\left(T_{cc}^{op} - T_{ev}^{op}\right)\right) + \dot{Q}_{ev}^{op}\bar{c}_{co,cc}^{l}\left(T_{co}^{op} - T_{cc}^{op}\right)}, \tag{7.10}$$

$$R_{co} = \frac{\left(T_{co}^{op} + T_{ev}^{op} - 2T_{sk}^{op}\right)\left(\Delta h_{ev}^{v} - \bar{c}_{co,cc}^{l}\left(T_{co}^{op} - T_{cc}^{op}\right) - \bar{c}_{cc,ev}^{l}\left(T_{cc}^{op} - T_{ev}^{op}\right)\right)}{2\left(\dot{Q}_{cc}^{op} + \dot{Q}_{ev}^{op}\right)\left(\Delta h_{ev}^{v} + \bar{c}_{ev,co}^{l}\left(T_{ev}^{op} - T_{co}^{op}\right)\right)}, \tag{7.11}$$

$$\dot{m} = \frac{\dot{Q}_{cc}^{op} + \dot{Q}_{ev}^{op}}{\Delta h_{ev}^{v} - \bar{c}_{co,cc}^{l}\left(T_{co}^{op} - T_{cc}^{op}\right) - \bar{c}_{cc,ev}^{l}\left(T_{cc}^{op} - T_{ev}^{op}\right)}. \tag{7.12}$$

The thermal capacitances C_{cc}^{op}, C_{ev}^{op}, and C_{co}^{op} are approximated by (5.7), (5.10), and (5.13) by means of the outer dimensions of the LHP components and an adequate choice of the volume fraction ratios β^{op} and β_{co}^{op}. Due to the superficial temperature measurements and the chosen boundary between the CC subsystem and the evaporator subsystem (see Fig. 5.1), the capacitances are manually adapted to the system's dynamics in addition. The different values of the variables and parameters of Model S in the respective OPs of SIM, LHP 1, and LHP 2 are given in Table 7.3.

The calculation of R_{lk} and $\dot{m}$ with (7.10) and (7.12) yields OP values very close to the corresponding values of Model C in Table 7.2 due to the similarity of the modeling approaches. The thermal resistance R_{co} describes the effective heat exchanges of the VL, the condenser, and the LL with the surroundings. Thus, its reciprocal approximates the sum of the heat transfer coefficients in Table 7.2 multiplied by their respective effective surface areas. The mentioned differences between the temperature dynamics is reflected in the thermal capacitances C_{cc}^{op}, C_{ev}^{op}, and C_{co}^{op}. The faster dynamics of SIM, which concentrates on the temperatures of the fluid inside the LHP, is approximated by small thermal capacitances, whereas the thermal capacitances for LHP 1 and LHP 2 are larger due to the thermal mass of the walls and the increased volumes of the LHP 2 components, respectively.

Symbol	SIM	LHP 1	LHP 2
$\dot{Q}_{cc}^{op}$	$4.653\,\mathrm{W}$	$3.941\,\mathrm{W}$	$2.902\,\mathrm{W}$
$\dot{Q}_{ev}^{op}$	$60\,\mathrm{W}$	$58.93\,\mathrm{W}$	$61.38\,\mathrm{W}$
T_{sk}^{op}	$0\,^{\circ}\mathrm{C}$	$0.45\,^{\circ}\mathrm{C}$	$10.24\,^{\circ}\mathrm{C}$
T_{cc}^{op}	$26.86\,^{\circ}\mathrm{C}$	$27.72\,^{\circ}\mathrm{C}$	$27.07\,^{\circ}\mathrm{C}$
T_{ev}^{op}	$28.58\,^{\circ}\mathrm{C}$	$29.27\,^{\circ}\mathrm{C}$	$28.33\,^{\circ}\mathrm{C}$
T_{co}^{op}	$0\,^{\circ}\mathrm{C}$	$0.45\,^{\circ}\mathrm{C}$	$10.46\,^{\circ}\mathrm{C}$
R_{lk}	$1.004\,\mathrm{K\,W^{-1}}$	$0.6583\,\mathrm{K\,W^{-1}}$	$1.057\,\mathrm{K\,W^{-1}}$
R_{co}	$0.2210\,\mathrm{K\,W^{-1}}$	$0.2292\,\mathrm{K\,W^{-1}}$	$0.1424\,\mathrm{K\,W^{-1}}$
$\dot{m}$	$50.32\,\mathrm{mg\,s^{-1}}$	$49.00\,\mathrm{mg\,s^{-1}}$	$52.01\,\mathrm{mg\,s^{-1}}$
C_{cc}^{op}	$15\,\mathrm{J\,K^{-1}}$	$35\,\mathrm{J\,K^{-1}}$	$80\,\mathrm{J\,K^{-1}}$
C_{ev}^{op}	$2\,\mathrm{J\,K^{-1}}$	$25\,\mathrm{J\,K^{-1}}$	$15\,\mathrm{J\,K^{-1}}$
C_{co}^{op}	$9\,\mathrm{J\,K^{-1}}$	$9\,\mathrm{J\,K^{-1}}$	$9\,\mathrm{J\,K^{-1}}$

Table 7.3: Values of the model parameters and variables of Model S in the OPs of the investigated LHP systems SIM, LHP 1, and LHP 2

The relation between the different C_{cc}^{op} is similar to Model C in Table 7.2. The variation in their values, however, results from the fixed mass flow rate in Model S.

Fig. 7.4, 7.5, and 7.6 compare the $1\,\mathrm{W}$ $\dot{Q}_{cc}$ step responses of the investigated systems in the OP with the results of Model S. For this purpose, the measured temperatures T_{cc}, T_{ev} and $T_{co,o}$ are compared to the states of Model S. In comparison with Model C, the stationary deviation of T_{cc} in Fig. 7.4 after the $1\,\mathrm{W}$ step increases to approximately $\Delta T_{cc}(2000\,\mathrm{s}) = 1.12\,\mathrm{K}$ due to the neglected influences of the fluid dynamics on the temperatures with a fixed mass flow parameter. This also results in a deviation between the evaporator temperatures in the same range. Another difference is visible in the third row of Fig. 7.4, which also exists in the following two figures with step responses of Model S. The dynamics of the $1\,\mathrm{W}$ step lead to a decrease of T_{co} in order to balance the CC and evaporator temperatures in the measured levels. This is due to the aggregation of the VL, the condenser, and the LL into one temperature node T_{co} that is correlated with the temperature $T_{co,o}$ at the condenser outlet.

The missing influence of the fluid dynamics on the temperatures is also visible when comparing the curves of the temperatures between Model S and the experiments with LHP 1 and LHP 2 in Fig. 7.5 and 7.6. The deviation between the CC temperatures is approximately $\Delta T_{cc}(2800\,\mathrm{s}) = 2.79\,\mathrm{K}$ for LHP 1 and $\Delta T_{cc}(4800\,\mathrm{s}) = 2.50\,\mathrm{K}$ for LHP 2. It becomes clear that Model S with fixed model parameters over the entire operating range is not able to fully describe the steady-state behavior of the temperatures outside the proximity of the OP. For the intended model-based control design, however, the focus is set on a good agreement of the dynamics of the controlled temperatures T_{cc} and T_{ev} in an OP in order to correctly parameterize the controllers to the system's dynamics, which are indeed sufficiently approximated by Model S.

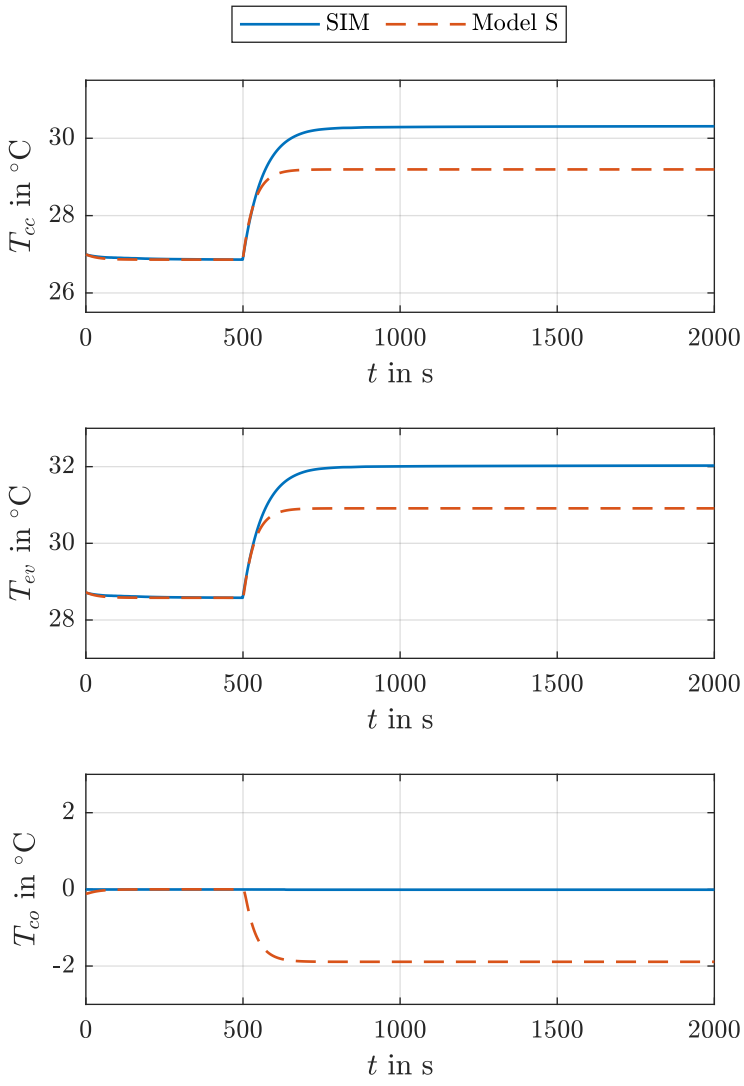

Figure 7.4: Comparison of 1 W $\dot{Q}_{cc}$ step responses of SIM and Model S in the OP

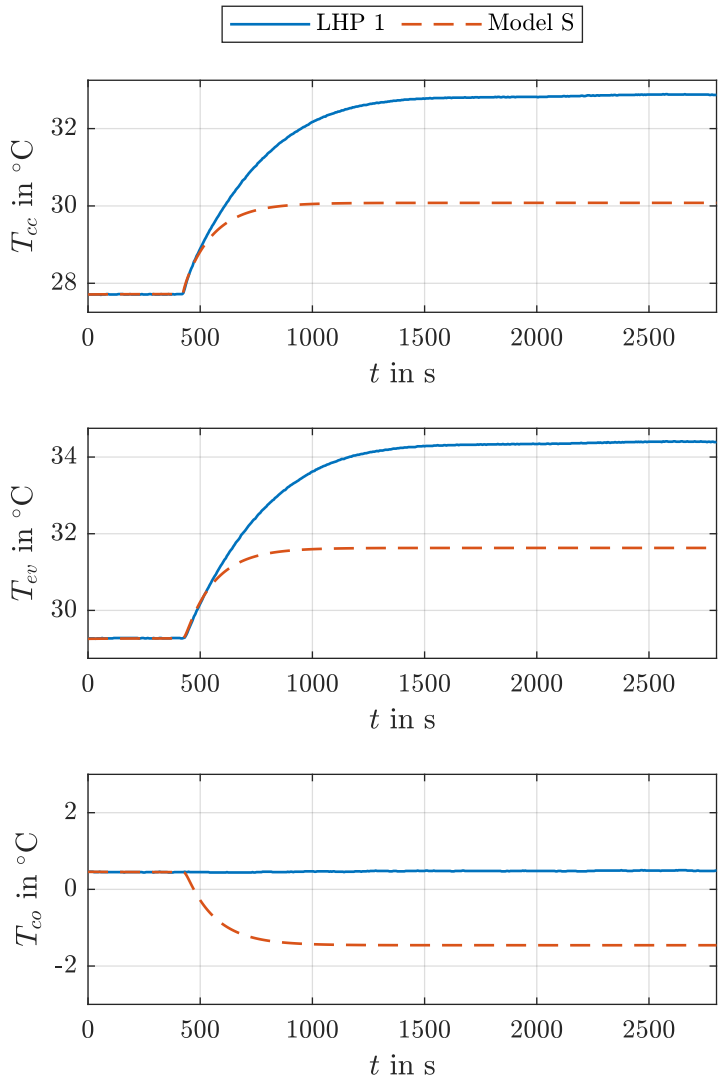

Figure 7.5: Comparison of 1 W $\dot{Q}_{cc}$ step responses of LHP 1 and Model S in the OP

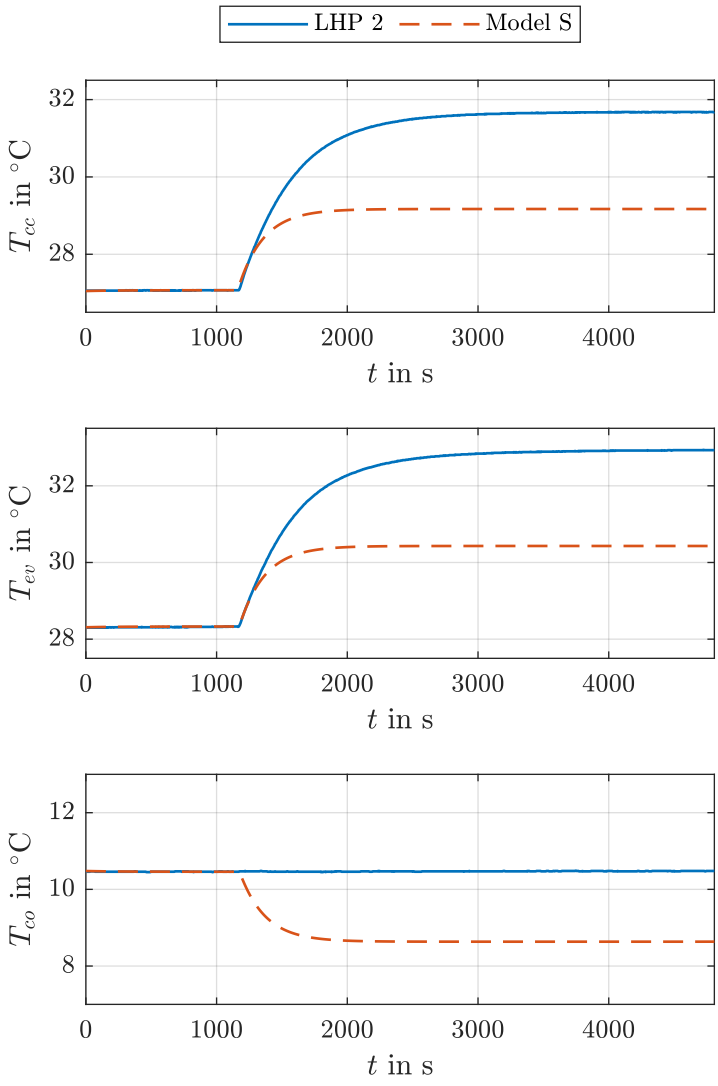

Figure 7.6: Comparison of 1 W $\dot{Q}_{cc}$ step responses of LHP 2 and Model S in the OP

Advanced LHP State-Space Models

For the parameterization of the advanced LHP state-space models in Chapter 6, the same procedure as for Model C is applied. From the masses of the attached structures, the corresponding thermal capacitances in the attached thermal networks are derived according to (3.65) for aluminum with an approximate specific heat capacity $c_p = 900\,\mathrm{J\,kg^{-1}\,K^{-1}}$. The respective thermal resistance R_{sf} between the thermal network of the evaporator and the attached thermal network is chosen to $R_{sf} = 0.0031\,\mathrm{K\,W^{-1}}$.

The following OPs in Table 7.4 are determined for the state-space model (6.27) of the LHP with the attached thermal mass characterized by $C_{ev,sf}$, hereinafter called Model M, with respect to SIM, LHP 1, and LHP 2.

Symbol	SIM	LHP 1	LHP 2
$\dot{Q}_{cc}^{op}$	$4.653\,\mathrm{W}$	$3.941\,\mathrm{W}$	$2.902\,\mathrm{W}$
$\dot{Q}_{sf}^{op}$	$60\,\mathrm{W}$	$58.93\,\mathrm{W}$	$61.38\,\mathrm{W}$
T_{sk}^{op}	$0\,^\circ\mathrm{C}$	$0.45\,^\circ\mathrm{C}$	$10.24\,^\circ\mathrm{C}$
T_{cc}^{op}	$26.86\,^\circ\mathrm{C}$	$27.72\,^\circ\mathrm{C}$	$27.07\,^\circ\mathrm{C}$
$T_{ev,sf}^{op}$	$28.58\,^\circ\mathrm{C}$	$29.27\,^\circ\mathrm{C}$	$28.33\,^\circ\mathrm{C}$
$T_{co,i}^{op}$	$27.88\,^\circ\mathrm{C}$	$28.81\,^\circ\mathrm{C}$	$27.98\,^\circ\mathrm{C}$
$T_{co,o}^{op}$	$0\,^\circ\mathrm{C}$	$0.45\,^\circ\mathrm{C}$	$10.24\,^\circ\mathrm{C}$
R_{lk}	$1.155\,\mathrm{K\,W^{-1}}$	$0.6363\,\mathrm{K\,W^{-1}}$	$0.9586\,\mathrm{K\,W^{-1}}$
$k_{2\phi}$	$1060\,\mathrm{W\,m^{-2}\,K^{-1}}$	$1050\,\mathrm{W\,m^{-2}\,K^{-1}}$	$1053\,\mathrm{W\,m^{-2}\,K^{-1}}$
k_{sc}	$804.8\,\mathrm{W\,m^{-2}\,K^{-1}}$	$845.8\,\mathrm{W\,m^{-2}\,K^{-1}}$	$810.0\,\mathrm{W\,m^{-2}\,K^{-1}}$
k_{ll}	$3.005\,\mathrm{W\,m^{-2}\,K^{-1}}$	$1.566\,\mathrm{W\,m^{-2}\,K^{-1}}$	$1.800\,\mathrm{W\,m^{-2}\,K^{-1}}$
k_{vl}	$4.266\,\mathrm{W\,m^{-2}\,K^{-1}}$	$1.790\,\mathrm{W\,m^{-2}\,K^{-1}}$	$1.097\,\mathrm{W\,m^{-2}\,K^{-1}}$
k_{sh}	$455.8\,\mathrm{W\,m^{-2}\,K^{-1}}$	$388.6\,\mathrm{W\,m^{-2}\,K^{-1}}$	$400.3\,\mathrm{W\,m^{-2}\,K^{-1}}$
R_{sh}	$0.02246\,\mathrm{K\,W^{-1}}$	$0.02042\,\mathrm{K\,W^{-1}}$	$0.01423\,\mathrm{K\,W^{-1}}$
$L_{2\phi}^{op}$	$0.3268\,\mathrm{m}$	$0.3145\,\mathrm{m}$	$0.5397\,\mathrm{m}$
$\dot{m}^{l,op}$	$50.50\,\mathrm{mg\,s^{-1}}$	$49.05\,\mathrm{mg\,s^{-1}}$	$51.98\,\mathrm{mg\,s^{-1}}$
$T_{cc,i}^{op}$	$1.742\,^\circ\mathrm{C}$	$1.383\,^\circ\mathrm{C}$	$10.76\,^\circ\mathrm{C}$
$T_{co,s}^{op}$	$26.86\,^\circ\mathrm{C}$	$27.72\,^\circ\mathrm{C}$	$27.07\,^\circ\mathrm{C}$
β^{op}	0.45	0.50	0.50
θ^{op}	$80°$	$80°$	$80°$
C_{cc}^{op}	$21.85\,\mathrm{J\,K^{-1}}$	$60.90\,\mathrm{J\,K^{-1}}$	$89.57\,\mathrm{J\,K^{-1}}$
$C_{ev,sf}$	$40\,\mathrm{J\,K^{-1}}$	$40\,\mathrm{J\,K^{-1}}$	$40\,\mathrm{J\,K^{-1}}$

Table 7.4: Values of the model parameters and variables of Model M in the OPs of the investigated LHP systems SIM, LHP 1, and LHP 2

The extension of Model C at the evaporator has no significant impact on the model parameters as it can be seen by comparing Tables 7.2 and 7.4. The considered attached mass at the evaporator weighs approximately $m = 44.4\,\mathrm{g}$. With this small mass, the temperature curves of the step responses of Model M in the OP with constant disturbances hardly differ from the ones of Model C. Thus, the explanations of the figures of Model C also apply to the figures of Model M. The respective comparisons between Model M and the considered systems are depicted in Fig. 7.7, 7.8, and 7.9. The stationary deviations of the CC temperatures after the 1 W step are $\Delta T_{cc}(2000\,\mathrm{s}) = 0.68\,\mathrm{K}$, $\Delta T_{cc}(2800\,\mathrm{s}) = 0.90\,\mathrm{K}$, and $\Delta T_{cc}(4800\,\mathrm{s}) = 0.74\,\mathrm{K}$, respectively, and thus slightly smaller than for Model C.

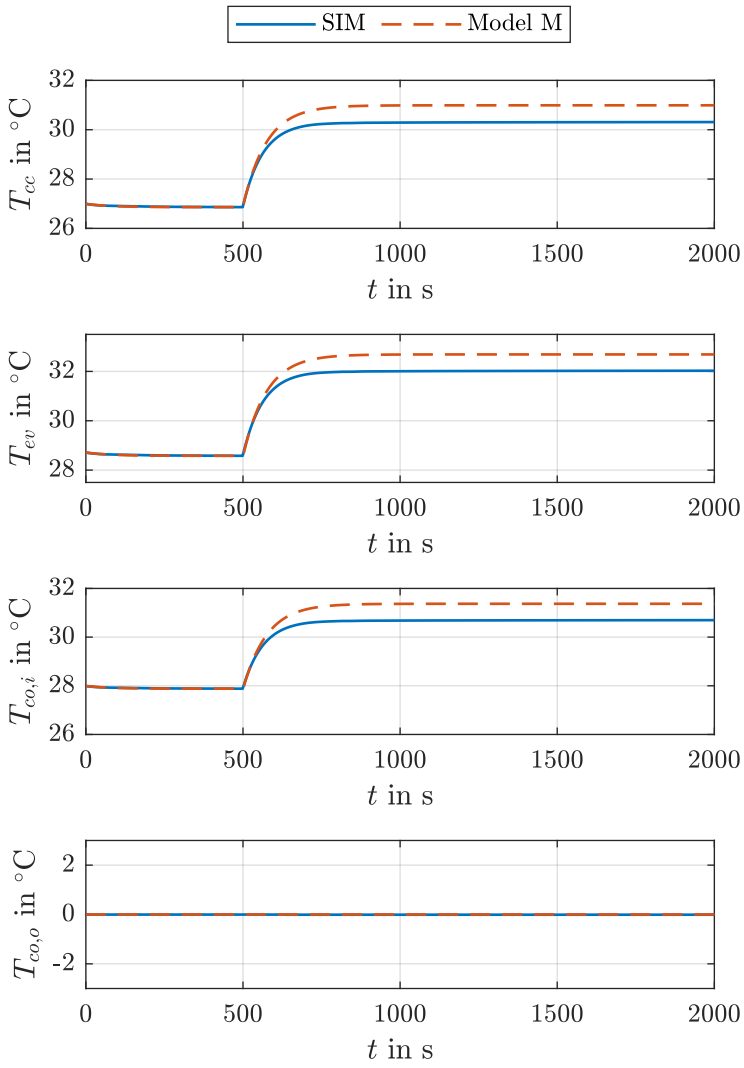

Figure 7.7: Comparison of 1 W $\dot{Q}_{cc}$ step responses of SIM and Model M in the OP

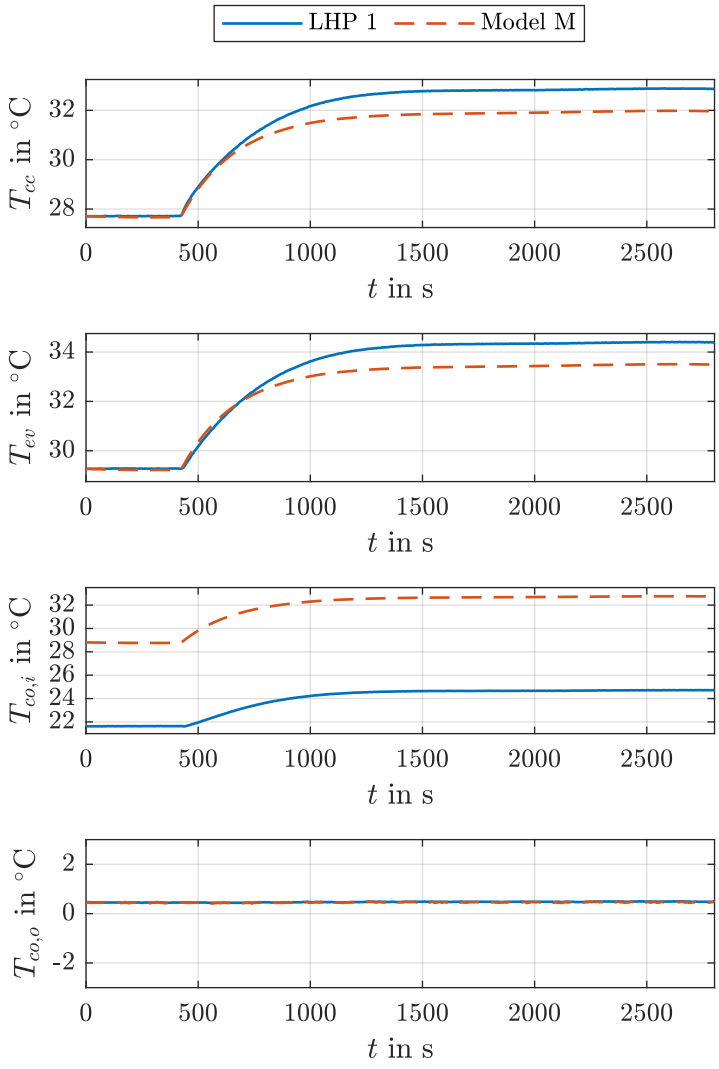

Figure 7.8: Comparison of 1 W $\dot{Q}_{cc}$ step responses of LHP 1 and Model M in the OP

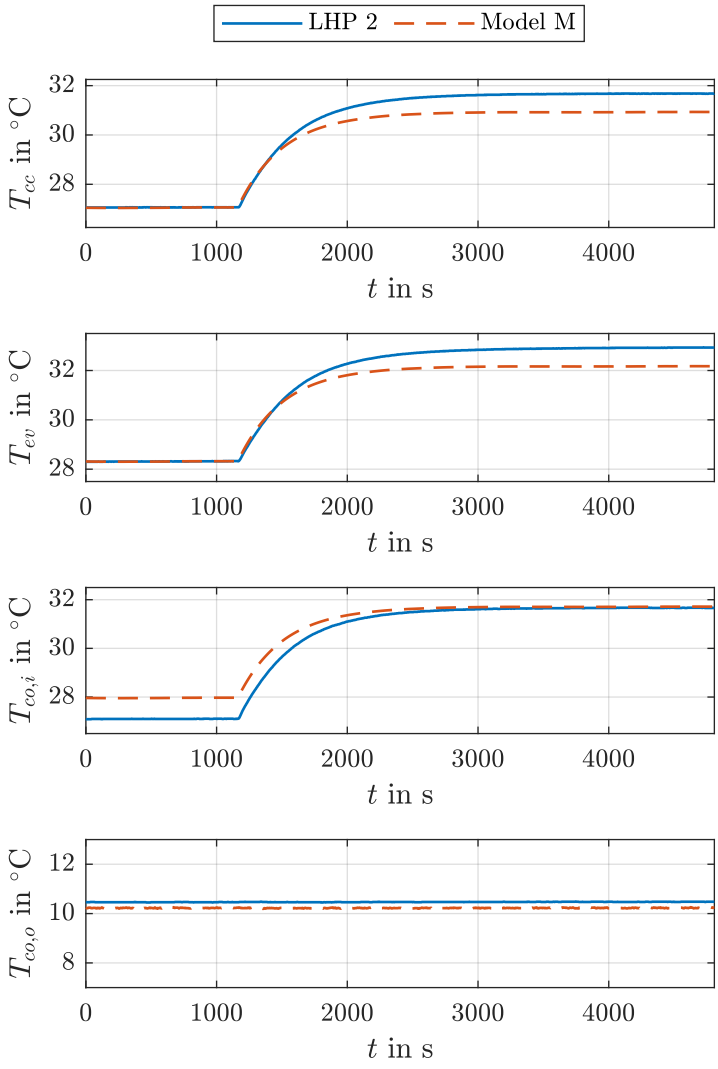

Figure 7.9: Comparison of 1 W $\dot{Q}_{cc}$ step responses of LHP 2 and Model M in the OP

The parameterization of the state-space model (6.38) based on parallel LHPs with ArHPs, indicated by Model P, is done by the same procedure as before. Thus, the optimized model parameter vector is doubled to include the parameters for LHP a and LHP b. Since both condenser pipes run in parallel through the plates of the heat sink, one temperature sensor for the outlet temperature is placed on the condenser system for both LHPs. Hence, the measured condenser outlet temperatures of both LHPs are equal. Furthermore, the temperature measurement point for the condenser outlet coincides with the measurement point of the heat sink. Thus, elevated sink temperatures are determined for the heat transport system, which result in rather high heat transfer coefficients of the condenser subsystem, especially $k_{2\phi}$.

In Table 7.5, the parameters and variables of Model P in the OP are stated with respect to LHP 3.

Symbol	LHP 3	
	LHP a	LHP b
$\dot{Q}_{sf}^{op}$	167.9 W	
T_{sk}^{op}	19.24 °C	
$\dot{Q}_{cc}^{\square,op}$	0 W	0 W
$T_{cc}^{\square,op}$	21.80 °C	21.59 °C
$T_{ev,sf}^{\square,op}$	22.76 °C	22.51 °C
$T_{co,i}^{\square,op}$	22.87 °C	22.64 °C
$T_{co,o}^{\square,op}$	19.24 °C	19.24 °C
$R_{lk}^{\square}$	0.8382 K W^{-1}	0.8735 K W^{-1}
$k_{2\phi}^{\square}$	2188 W m^{-2} K^{-1}	2295 W m^{-2} K^{-1}
$k_{sc}^{\square}$	746.2 W m^{-2} K^{-1}	711.9 W m^{-2} K^{-1}
$k_{ll}^{\square}$	1.054 W m^{-2} K^{-1}	0.4844 W m^{-2} K^{-1}
$k_{vl}^{\square}$	5.832 W m^{-2} K^{-1}	5.201 W m^{-2} K^{-1}
$k_{sh}^{\square}$	633.8 W m^{-2} K^{-1}	639.1 W m^{-2} K^{-1}
$R_{sh}^{\square}$	0.005299 K W^{-1}	0.004973 K W^{-1}
$L_{2\phi}^{\square,op}$	2.4 m	2.4 m
$\dot{m}^{l,\square,op}$	71.71 mg s^{-1}	69.15 mg s^{-1}
$T_{cc,i}^{\square,op}$	19.34 °C	19.28 °C
$T_{co,s}^{\square,op}$	21.80 °C	21.59 °C
$\beta^{\square,op}$	0.85	0.85
$\theta^{\square,op}$	80°	80°
$C_{cc}^{\square,op}$	97.64 J K^{-1}	97.66 J K^{-1}
$C_{hp1}^{\square}$	65 J K^{-1}	65 J K^{-1}
$C_{hp2}^{\square}$	65 J K^{-1}	65 J K^{-1}
$C_{ev,sf}^{\square}$	180 J K^{-1}	180 J K^{-1}
$R_{hp1}^{\square}$	0.1429 K W^{-1}	0.1429 K W^{-1}
$R_{hp2}^{\square}$	0.1429 K W^{-1}	0.1429 K W^{-1}
$R_{hp1,tm}^{\square}$	0.5556 K W^{-1}	0.5882 K W^{-1}
$R_{hp2,tm}^{\square}$	0.5556 K W^{-1}	0.5882 K W^{-1}
$R_{sf,tm}^{\square}$	0.5556 K W^{-1}	0.5882 K W^{-1}

Table 7.5: Values of the model parameters and variables of Model P in the OP of the investigated LHP system LHP 3

The parameters between both LHPs vary slightly due to the different lengths and routing of the pipes. For the thermal capacitance C_{tm} of the LCT dummy, a value of $C_{tm} = 45{,}000\,\mathrm{J\,K^{-1}}$ is assumed considering a total aluminum mass of $m = 50\,\mathrm{kg}$. All other parameters of the thermal network are based on the practical knowledge of the LHP end users and their investigations on the test bench with parallel LHPs.

The corresponding step responses of the parameterized Model P are presented in Fig. 7.10.

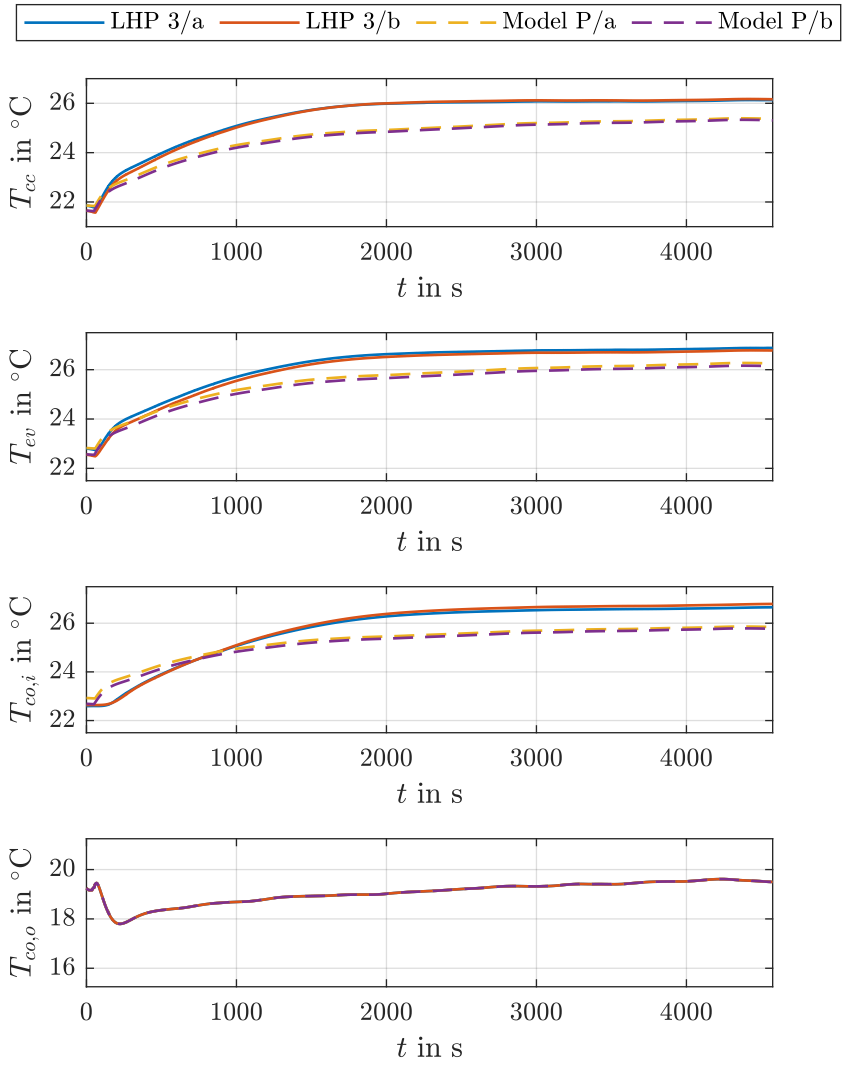

Figure 7.10: Comparison of 1 W $\dot{Q}_{cc}$ step responses of LHP a and LHP b of LHP 3 and Model P in the OP

In the chosen OP with the given heat load $\dot{Q}_{sf}^{op}$, the parallel LHPs are considered to be in the variable conductance mode. Thus, the subcooling regions in the condensers of both LHPs are sufficient to cool the condenser outlet temperatures $T_{co,o}^{a}$ and $T_{co,o}^{b}$ down to near sink temperature T_{sk}. Since the measured sink temperature is taken as the sink temperature of Model P as well, the modeled condenser outlet temperatures follow the measured condenser outlet temperatures in the fourth row of Fig. 7.10. The 1 W step responses of the modeled CC temperatures T_{cc}^{a} and T_{cc}^{b} as well as of the modeled evaporator temperatures T_{ev}^{a} and T_{ev}^{b} are similarly close to their corresponding measured temperatures. The stationary deviations of the modeled and measured CC temperatures after the 1 W $\dot{Q}_{cc}$ step are $\Delta T_{cc}^{a}(4500\,\mathrm{s}) = 0.75\,\mathrm{K}$ and $\Delta T_{cc}^{b}(4500\,\mathrm{s}) = 0.85\,\mathrm{K}$, respectively. Differences between the dynamic behaviors of the condenser inlet temperatures $T_{co,i}^{a}$ and $T_{co,i}^{b}$ are apparent which are caused again by the parasitic heat flows through the walls of the VL to the nearby heat sink as recognizable from the inverted change of the condenser outlet temperatures $T_{co,o}^{a}$ and $T_{co,o}^{b}$ in the lower row.

After the parameterization of the models of the different LHP-based heat transport systems, the control parameters of the proposed controllers are determined based on the corresponding models in the next section.

7.1.2 Control Parameters

In this section, the parameters connected to the different control algorithms in the previous chapters are presented. These parameters are tuned based on the respective state-space models considering the limitation of the change rate of the controlled temperature for a continuous heat transfer of the investigated LHP system (see Sec. 3.2.2). For an extensive comparison of the performances of all controllers, the experimentally evaluated numerical LHP simulation SIM in MATLAB is used, to which the controllers based on Model C and Model S in Chapter 4 and Chapter 5 are adapted. Considering the modeled advanced LHP-based heat transport systems in Chapter 6, their controllers are verified with their respective state-space models in SIMULINK.

The assumed availability of the disturbances for the control design is given in most applications since the heat sink is often temperature-controlled itself, especially in aerospace systems, and the dissipated heat of the heat source can be reconstructed from its operating status. Another possibility could be the estimation of both influences with a disturbance observer which is not in the scope of this thesis.

The combined state and parameter estimation for the state-dependent controllers is implemented based on Sec. 4.2.3. A more elaborate but faster calculation of the discrete LHP states $\boldsymbol{x}(k)$ compared to Euler's forward method is possible with implicit multistep methods [Ada18, p. 54]. Such numerical methods for solving initial value problems improve the numerical stability of the solution. In order to verify their usage for the discretization of the LHP model, MATLAB's `ode15s` solver [Mat20d, p. 11-5] is used in comparison to Euler's forward method. This solver adapts the step size of the discretization automatically. More detailed information about the solver `ode15s` can be found in [SR97].

Some of the proposed controllers in this thesis incorporate a PI controller to eliminate the remaining control error. Besides the classical model-based design methods of PID controllers

based on the analysis of the root locus or the frequency domain to determine a suitable crossover frequency and phase margin for a stable control loop (see [Lun20a, p. 460]), the determination of the controller gains can be facilitated nowadays by PID tuning software as e.g. present in the Control System Toolbox [Mat20b] in MATLAB. With its robust response time algorithm, a stable closed loop of a PID controller with a given linear control system is accomplished, i.e. the poles of the corresponding transfer function of the closed-loop system have negative real parts. The algorithm determines appropriate PID gains based on the desired balance between the speed and the robustness of the PID controller. This balance is specified by an adequate closed-loop response time as reciprocal of the crossover frequency [Mat20a, p. 2-775] and phase margin to achieve either a fast setpoint and disturbance response or a high robustness against modeling errors. Accordingly, the gains of the PI controllers in this thesis are determined to adjust the speed and the robustness of the controller by the mentioned algorithm based on the respective transfer function of the LHP and the desired crossover frequency and phase margin. For all PI controllers, a phase margin of $\varphi = 60°$ is chosen to receive a smooth controlled temperature curve. The crossover frequency is determined in such a way that the change rate of the CC temperature T_{cc} does not exceed the experimentally determined operation limit of $\Delta T_{cc}/\Delta t = 0.07\,\mathrm{K\,s^{-1}}$ during a $1\,\mathrm{K}$ step of the setpoint temperature T_{set} and $T_{set,ev}$, respectively. For the proposed controllers without PI part, the respective control parameters are adjusted manually according to their previous explanations to meet the mentioned specification of the operation limit.

The following two tables contain the determined control parameters for SIM. In Table 7.6, the controllers for the CC temperature based on Model S and Model C are listed. The designation of the controllers consists of the abbreviation of the controller type, the underlying model in the subscript, and the optional extension for the cascade control. The CC controllers include the PI controller with AW structure (piAW/S) in Sec. 5.2.1, the PI controller with disturbance feedforward control (piDF/S) in Sec. 5.2.2, the PI output feedback control (piOF/S) in Sec. 5.2.3, the nonlinear model identification adaptive control (nMIAC/S) in Sec. 5.2.4, and the nonlinear PI state feedback control (nSF/C) in Sec. 4.2.1. Subsequently, the corresponding cascade controllers for the evaporator temperature, i.e. piAWc/S, piDFc/S, piOFc/S, and nMIACc/S in Sec. 5.2.5 and nSFc/C in Sec. 4.2.2, are given in Table 7.7.

Control algorithm	Control parameter				
	K_p in $\mathrm{W\,K^{-1}}$	K_i in $\mathrm{W\,K^{-1}\,s^{-1}}$	$\boldsymbol{K}_x$ in $\mathrm{W\,K^{-1}}$	λ_{ly} in $\mathrm{s^{-1}}$	η_0 in $\mathrm{s^{-1}}$
piAW/S	1.201	0.122	-	-	-
piDF/S	1.201	0.122	-	-	-
piOF/S	0.429	0.548	$[5.000, 0.447, 0.223]$	-	-
nMIAC/S	-	-	-	0.078	-
nSF/C	0.052	0.009	-	-	0.060

Table 7.6: Control parameters of the different CC controllers for SIM

Control algorithm	Control parameter					
	K_{p1} in $\mathrm{W\,K^{-1}}$	K_{p2} in $\mathrm{W\,K^{-1}}$	K_{i2} in $\mathrm{W\,K^{-1}\,s^{-1}}$	$\boldsymbol{K}_x$ in $\mathrm{W\,K^{-1}}$	λ_{ly} in $\mathrm{s^{-1}}$	η_0 in $\mathrm{s^{-1}}$
piAWc/S	2.375	0.236	0.141	-	-	-
piDFc/S	2.375	0.236	0.141	-	-	-
piOFc/S	0.429	0.184	0.958	$[2.857, 0.290, 0.207]$	-	-
nMIACc/S	-	0.760	0.129	-	0.078	-
nSFc/C	0.108	0.032	0.163	-	-	0.050

Table 7.7: Control parameters of the different evaporator controllers for SIM

Using the examples of the CC controllers in SIM, the setpoint responses of the five controllers are compared in Fig. 7.11.

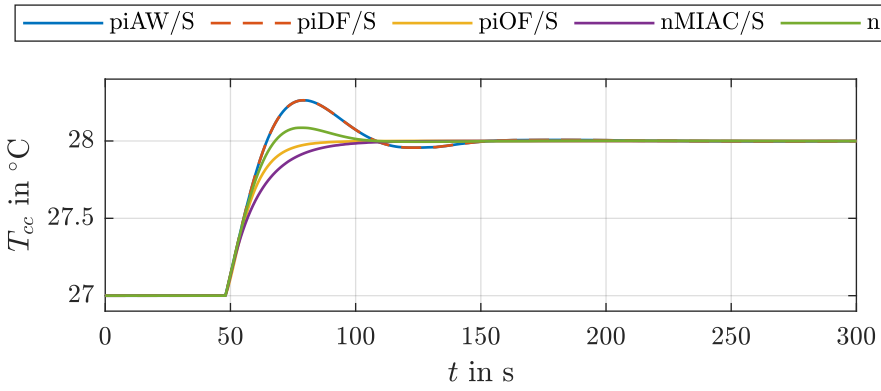

Figure 7.11: Comparison of 1 K T_{set} step responses of the CC control loops in the OP

As expected by the chosen parameterization of the controllers, the operation limit of $\Delta T_{cc}/\Delta t = 0.07\,\mathrm{K\,s^{-1}}$ is met by all control loops. Differences are present at the transient oscillation of the CC temperature T_{cc} when adjusting the new setpoint temperature T_{set}. During this phase, piAW/S and piDF/S show the highest overshoots of $\Delta T_{cc} = 0.26\,\mathrm{K}$ and the longest settling time. In contrast, the other three controllers show a similar settling time while the transient oscillation is damped well by piOF/S and nMIAC/S, and nSF/C produces a small overshoot of $\Delta T_{cc} = 0.09\,\mathrm{K}$. All control loops, however, are stable and follow the setpoint change smoothly.

The performances of the controllers for a single LHP based on Model S and Model M, i.e. piAW/S, piDF/S, piOF/S, nMIAC/S, and nSF/C, are evaluated with respect to an attached thermal mass at the evaporator by adapting the respective controllers to Model M with the temperature change rate limitation in mind. The controllers are parameterized based on two different thermal masses to evaluate the influence of the LHP design on the controller performance. Additionally, the linear controllers piAW/S and piDF/S are designed based on the linearized equations of Model M to achieve the best possible adaption of these controllers to the system. For the identification of the underlying model, these controllers are named piAW/M and piDF/M, accordingly. Furthermore, the nonlinear state feedback controller in Sec. 6.2.1 based on Model M is called nSF/M. The resulting control parameters are given in Table 7.8.

Control algorithm	Thermal mass	Control parameter				
	$C_{ev,sf}$ in $\mathrm{J\,K^{-1}}$	K_p in $\mathrm{W\,K^{-1}}$	K_i in $\mathrm{W\,K^{-1}\,s^{-1}}$	$\boldsymbol{K}_x$ in $\mathrm{W\,K^{-1}}$	λ_{ly} in $\mathrm{s^{-1}}$	η_0 in $\mathrm{s^{-1}}$
piAW/M	40	1.228	0.083	-	-	-
	280	0.870	0.001	-	-	-
piDF/M	40	1.228	0.083	-	-	-
	280	0.870	0.001	-	-	-
piOF/S	40	0.429	0.514	$[4.767, 0.429, 0.215]$	-	-
	280	0.429	0.214	$[2.743, 0.268, 0.153]$	-	-
nMIAC/S	40	-	-	-	0.075	-
	280	-	-	-	0.064	-
nSF/C	40	0.046	0.010	-	-	0.070
	280	0.016	0.005	-	-	0.070
nSF/M	40	0.050	0.010	-	-	0.065
	280	0.045	0.009	-	-	0.065

Table 7.8: Control parameters of the different CC controllers for Model M parameterized in the OP of SIM

For the sake of completeness, the control parameters of nMIACc/S and the nonlinear PI state feedback cascade controller in Sec. 6.2.1, hereinafter named nSFc/M, are adapted to the dynamics of Model M as well. They are used in the verification of the respective controller performances of a single LHP with a critical attached thermal mass of $C_{ev,sf} = 280\,\mathrm{J\,K^{-1}}$. The resulting control parameters are stated in Table 7.9.

Control algorithm	**Control parameter**				
	K_{p1} in $\mathrm{W\,K^{-1}}$	K_{p2} in $\mathrm{W\,K^{-1}\,s^{-1}}$	K_{i2} in $\mathrm{W\,K^{-1}}$	λ_{ly} in $\mathrm{s^{-1}}$	η_0 in $\mathrm{s^{-1}}$
nMIACc/S	-	0.568	0.103	0.075	-
nSFc/M	0.088	0.498	0.118	-	0.065

Table 7.9: Control parameters of the different evaporator controllers for Model M parameterized in the OP of SIM

To compare the performance of the uncoupled state-of-the-art PI controllers with the new nonlinear PI state feedback controller of Model P in Sec. 6.2.2, hereinafter called nSF/P, the PI gains are determined from the linearized Model P with the design procedure described in Sec. 5.2.1. The resulting control parameters of the respective PI controllers, denoted by piAW/P, are given in Table 7.10 besides the control parameters of nSF/P.

Control algorithm	**Control parameter**		
	K_p^a, K_p^b in $\mathrm{W\,K^{-1}}$	K_i^a, K_i^b in $\mathrm{W\,K^{-1}\,s^{-1}}$	η_{10}, η_{20} in $\mathrm{s^{-1}}$
piAW/P	6.700	0.350	-
nSF/P	0.064	0.012	0.065

Table 7.10: Control parameters of the different CC controllers for Model P parameterized in the OP of LHP 3

The corresponding setpoint responses of the different CC controllers for parallel LHPs are shown in Fig. 7.12. Both controllers piAW/P and nSF/P are stable, follow the setpoint change smoothly, and meet the operation limit of $\Delta T_{cc}/\Delta t = 0.07\,\mathrm{K\,s^{-1}}$. Similar to the setpoint responses of the controlled single LHP in Fig. 7.11, the transient oscillations of the CC temperatures T_{cc}^a and T_{cc}^b with piAW/P show higher overshoots of $\Delta T_{cc}^{a/b} = 0.25\,\mathrm{K}$ and longer settling times than with nSF/P ($\Delta T_{cc}^{a/b} = 0.13\,\mathrm{K}$).

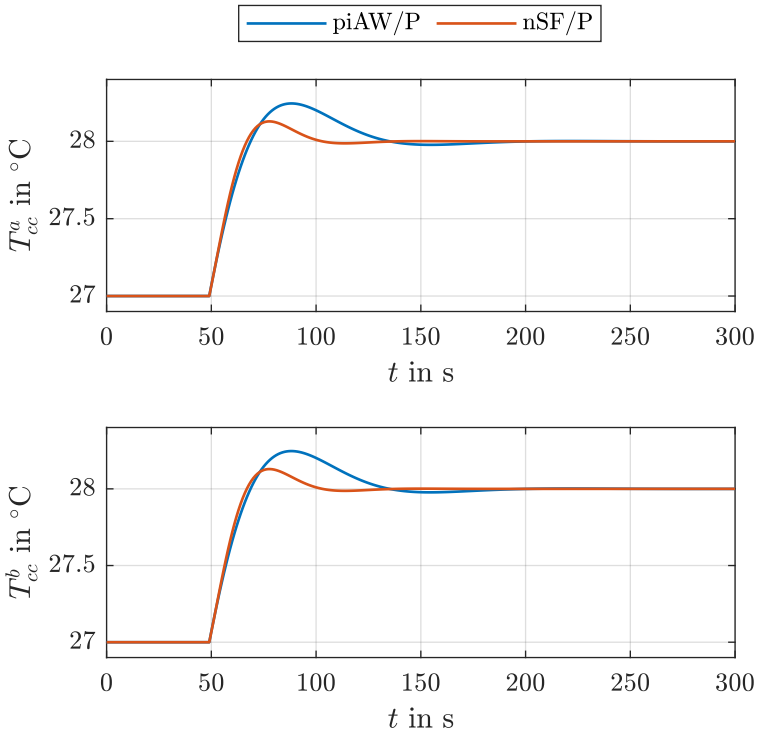

Figure 7.12: Comparison of 1 K T_{set} step responses of the CC control loops of parallel LHPs in the OP

7.2 Validation of the State-Space Models for a Single Loop Heat Pipe

For the validation of the introduced dynamical models of a single LHP in this thesis, their behaviors to changing operating conditions are compared to the available two LHP systems and the numerical LHP simulation. The main focus is set on the models' ability to represent the measured temperatures of the investigated LHP system subject to variations of the system inputs and the disturbances. Furthermore, the impact of the model assumptions on the results are reviewed. In Sec. 7.1.1, the variation of the system input has already been evaluated for each LHP system in the OP with adequate step responses. Here, the focus is set on the variation of the system input outside the OP besides the variation of the disturbances. Subsequently, the numerical LHP simulation is used to dive deeper into the dynamics of internal LHP variables and the applied model order reduction. Finally, the mentioned temperature oscillations during the LHP operation are reproduced and analyzed in dependence on the LHP design.

7.2.1 Response to a Variable System Input

The validation of the introduced modeling approaches comprises the comparison of the measured and simulated variables in consideration of the control engineering application. Thus, a model analysis with variations of the system input follows relating the findings to the expected controller performance. The model accuracy is determined by both the established model equations and the determined model parameters. In order to separate the influence of fixed model parameters from the influence of the model equations on the model accuracy, another set of model parameters is determined for another 1 W $\dot{Q}_{cc}$ step different from the previous OP (see Table 7.2). Using the example of the measured CC temperature T_{cc} of Model C to identify the influence of the fixed model parameters, the new $\dot{Q}_{cc}$ step response of LHP 2 is compared to the results of Model C parameterized in the OP and in the new equilibrium point. The newly determined parameters in the new equilibrium point are given in Table 7.11.

Symbol	LHP 2
$\dot{Q}_{cc}^{op}$	$1.937\,\mathrm{W}$
$\dot{Q}_{ev}^{op}$	$102.2\,\mathrm{W}$
T_{sk}^{op}	$0.62\,^{\circ}\mathrm{C}$
T_{cc}^{op}	$11.74\,^{\circ}\mathrm{C}$
T_{ev}^{op}	$13.77\,^{\circ}\mathrm{C}$
$T_{co,i}^{op}$	$14.21\,^{\circ}\mathrm{C}$
$T_{co,o}^{op}$	$1.61\,^{\circ}\mathrm{C}$
R_{lk}	$1.193\,\mathrm{K\,W^{-1}}$
$k_{2\phi}$	$742.7\,\mathrm{W\,m^{-2}\,K^{-1}}$
k_{sc}	$260.3\,\mathrm{W\,m^{-2}\,K^{-1}}$
k_{ll}	$1.929\,\mathrm{W\,m^{-2}\,K^{-1}}$
k_{vl}	$2.828\,\mathrm{W\,m^{-2}\,K^{-1}}$
k_{sh}	$157.8\,\mathrm{W\,m^{-2}\,K^{-1}}$
R_{sh}	$0.01664\,\mathrm{K\,W^{-1}}$
$L_{2\phi}^{op}$	$1.928\,\mathrm{m}$
$\dot{m}^{l,op}$	$82.10\,\mathrm{mg\,s^{-1}}$
$T_{cc,i}^{op}$	$2.227\,^{\circ}\mathrm{C}$
$T_{co,s}^{op}$	$11.74\,^{\circ}\mathrm{C}$
β^{op}	0.50
θ_{c}^{op}	80°
C_{cc}^{op}	$89.44\,\mathrm{J\,K^{-1}}$

Table 7.11: Values of the model parameters and variables of Model C in the alternative equilibrium point of LHP 2

The alternative equilibrium point includes a higher heat load $\dot{Q}_{ev}^{op}$ and thus a higher mass flow rate $\dot{m}^{l,op}$. The sink temperature T_{sk}^{op}, however, is lower. With a lower $\dot{Q}_{cc}^{op}$, the temperature level of the LHP is also lower. Because of the clearer lower temperature difference between the fluid and the heat sink at the condenser, a larger two-phase region, defined by $L_{2\phi}^{op}$, is necessary to transfer the applied heat load to the heat sink. A major difference between the parameter sets is visible in the heat transfer coefficients. Due to their local dependencies on the mass flow rate, the flow pattern, and the temperature (see Sec. 3.1.2), the different values are still plausible and have the same proportion among each other as in Table 7.2.

The corresponding comparison of Model C with both parameter sets is depicted in Fig. 7.13.

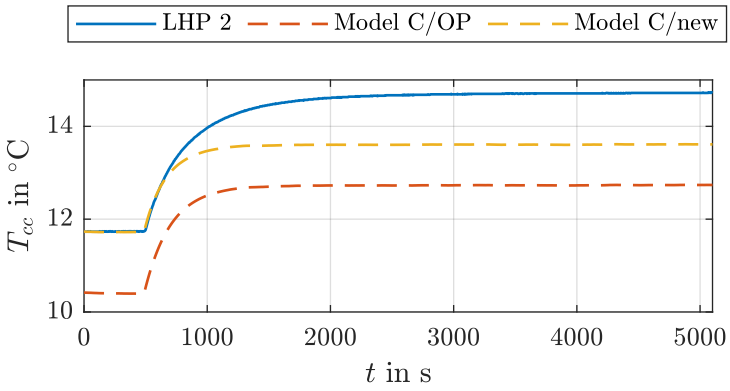

Figure 7.13: Comparison of 1 W $\dot{Q}_{cc}$ step responses of LHP 2, Model C with OP parameters, and Model C with the newly determined parameters in Table 7.11

Due to the determination of the new parameters based on the measured temperatures, the correct initial CC temperature level is met by Model C in Fig. 7.13. In contrast, Model C with the OP parameters shows a permanent offset of $\Delta T_{cc} \approx 2\,\mathrm{K}$. This offset is caused by the fixed OP parameters which are determined in a different equilibrium point. Since it is possible from the nature of the thermodynamic system to arrive at arbitrary temperature levels with an adequate $\dot{Q}_{cc}$, the offsets of the temperatures can be adjusted by adding an offset to the system input $\dot{Q}_{cc}$. Hence, Model C can reach the desired temperature level while its model parameters stay the same by calculating the necessary $\dot{Q}_{cc}$ in the equilibrium point with OP model parameters. This offset adjustment simplifies the comparison of the dynamics of the real system and the models, which have a major impact on the performance of a corresponding model-based designed controller. In the following model comparisons in this chapter, the offset adjustment is performed for all models.

Another reason for focusing on the dynamics is that stationary deviations between a model and the real system can be easily compensated. Based on the determination of the system input $\dot{Q}_{cc}$ by the controller, a stationary deviation due the fixed model parameters or further model discrepancies, such as unknown parasitic heat flows, is automatically compensated. The stationary model deviations are eliminated without great effort by controllers with an

adaptive or integral action, whereas deviations in the dynamics of the model and the real system have a negative impact on the controller performance.

The offset-adjusted comparison of T_{cc} between the $\dot{Q}_{cc}$ step responses of Model C and LHP 2 is depicted in Fig. 7.14.

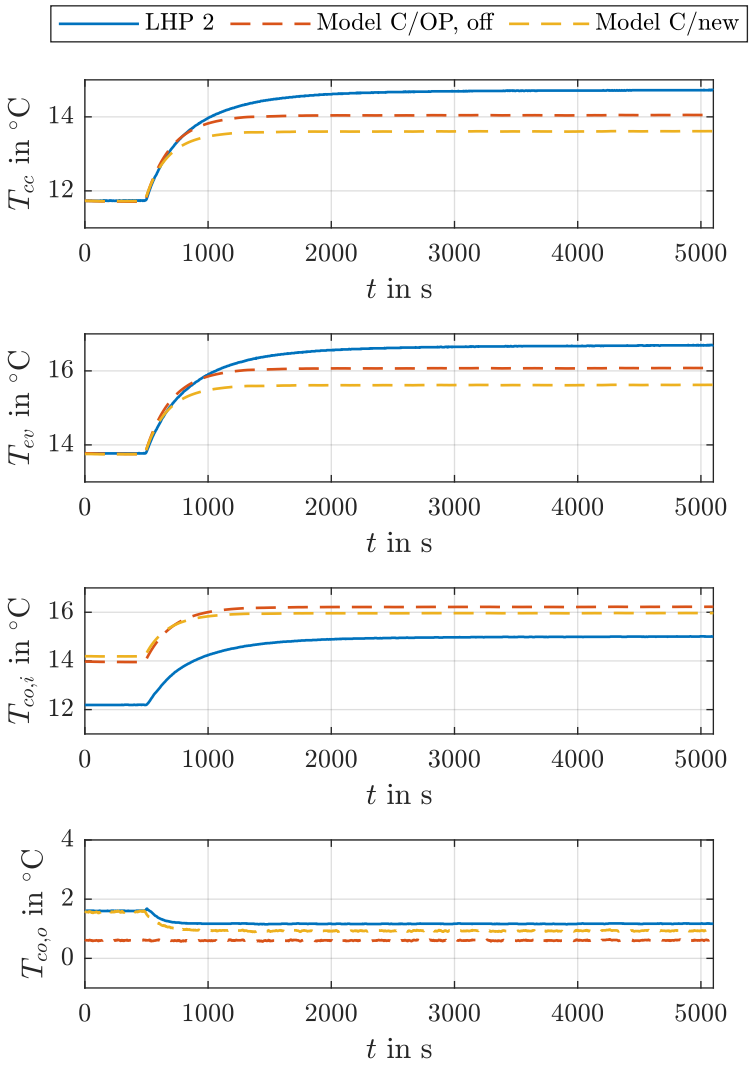

Figure 7.14: Comparison of 1 W $\dot{Q}_{cc}$ step responses of LHP 2, the offset-adjusted Model C with OP parameters, and Model C with the newly determined parameters in Table 7.11

The calculated initial offset is $\Delta\dot{Q}_{cc}(0\,\mathrm{s}) = 0.55\,\mathrm{W}$. Due to the displacement, the model error based on the OP parameters becomes visible. The dynamics in both parameter cases are almost

identical because of the fixed thermal conductance C_{cc} with a fixed volume fraction ratio β. However, the gradients of the CC temperature rise in both cases are similar but slightly higher compared to LHP 2. As before, Model C does not reach the CC temperature level of LHP 2 after the step. Furthermore, the deviation of the heights of the CC step responses are smaller for Model C with OP parameters than with the new parameters, whereupon the absolute deviation at the end of the figure is only $\Delta T_{cc}(5100\,\mathrm{s}) = 0.67\,\mathrm{K}$ and $\Delta T_{cc}(5100\,\mathrm{s}) = 1.11\,\mathrm{K}$, respectively.

A disadvantage of Model C with OP parameters becomes clear in the fourth row of Fig. 7.14 when comparing the condenser outlet temperatures $T_{co,o}$. At the considered OP with a high heat load, the two-phase region in the condenser extends across a major part of the condenser length. That is why the subcooled region is rather small, and the liquid is not fully cooled down to near sink temperature when leaving the condenser. Thus, $T_{co,o}$ of LHP 2 and Model C with the newly determined parameters are elevated and react with a decrease to the $\dot{Q}_{cc}$ step. In contrast, the offset-adjusted response of $T_{co,o}$ of Model C with OP parameters remains constant near the sink temperature since the resulting distribution of the regions in the condenser together with their heat transfer coefficients enables a sufficient cooling of the liquid. Thus, the model is able to reproduce the nonlinear influence of the region lengths on the condenser temperatures. However, this ability depends on the OP of the model parameters. Due to the focus of the model-based designed controllers on controlling the CC or the evaporator temperature, a satisfactory controller performance should still be possible based on a model with fixed model parameters.

The influence of the model discrepancy on the value of the system input $\dot{Q}_{cc}$ in an arbitrary equilibrium point is also obvious from Table 7.2 since the values of $\dot{Q}_{cc}^{op}$ between the first and second column vary although SIM and LHP 1 are based on the same LHP design.

For the general comparison of Model C, Model S, and Model M taking into account variations of the system input, their respective $\dot{Q}_{cc}$ step responses are compared to the results of SIM, LHP 1, and LHP 2. The responses to a $2\,\mathrm{W}$ $\dot{Q}_{cc}$ step starting from $0\,\mathrm{W}$ at a low sink temperature $T_{sk} = -15\,^{\circ}\mathrm{C}$ are depicted in Fig. 7.15. Due to the changed operating conditions with unchanged model parameters, minor deviations in the gradients of the step responses are visible when comparing the temperatures of the models and the simulation. Similar to Fig. 7.4, the stationary deviation of T_{cc} in Fig. 7.15 after the step is greater for Model S ($\Delta T_{cc}(2000\,\mathrm{s}) = 4.28\,\mathrm{K}$) than for Model C ($\Delta T_{cc}(2000\,\mathrm{s}) = 0.84\,\mathrm{K}$) and Model M ($\Delta T_{cc}(2000\,\mathrm{s}) = 0.87\,\mathrm{K}$). The same tendency applies to the evaporator temperature T_{ev}. While the accuracy of Model S in T_{cc} and T_{ev} is sufficient outside the OP, a major error is done when matching the third state T_{co} of Model S with $T_{co,o}$. This error is traced back to the mass flow rate $\dot{m}$ being a fixed parameter of Model S and the strong simplification of the two-phase condenser system with a single temperature node T_{co}. However, it is expected that the desired controllers based on Model S controlling T_{cc} or T_{ev} achieve a sufficient controller performance over the entire operating range due to the good agreement between the measured and modeled T_{cc} and T_{ev}, respectively. Thus, Model S can still represent the first two temperatures T_{cc} and T_{ev} when the sink temperature changes, while a larger model error prevails in the third temperature $T_{co,o}$.

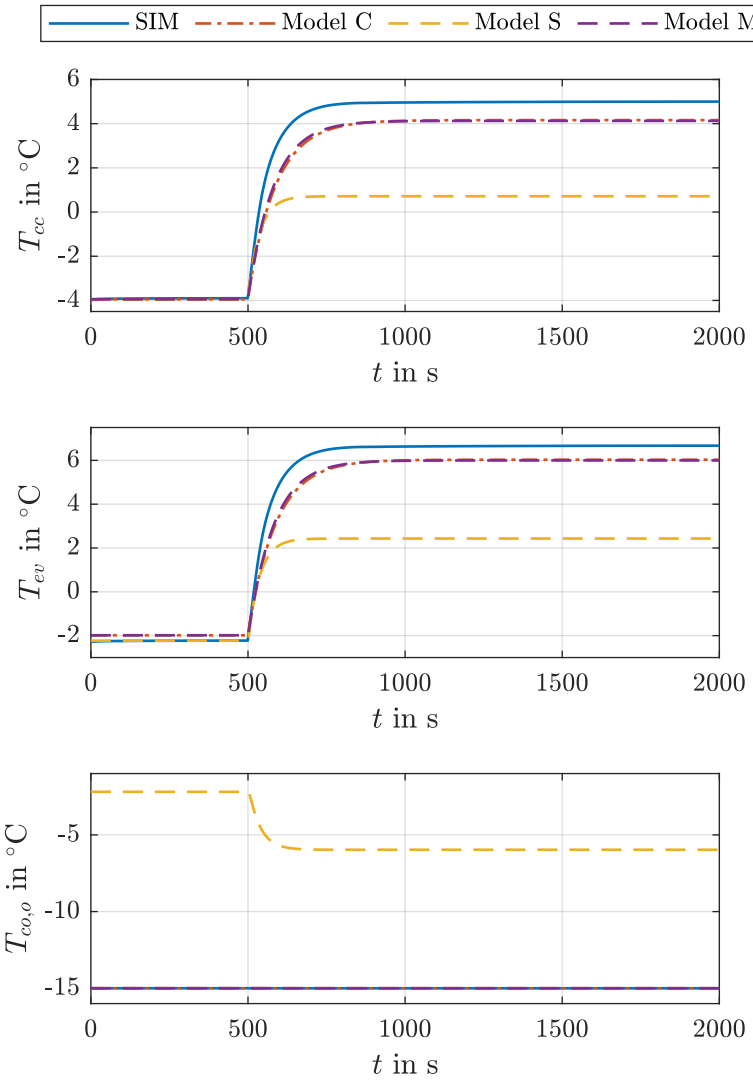

Figure 7.15: Comparison of 2 W $\dot{Q}_{cc}$ step responses of SIM, Model C, Model S, and Model M ($\dot{Q}_{hs} = 60\,\mathrm{W}$, $T_{sk} = -15\,^{\circ}\mathrm{C}$)

In Fig. 7.16, 1 W $\dot{Q}_{cc}$ step responses starting at $\dot{Q}_{cc} = 0\,\mathrm{W}$ are compared to the measured step response of LHP 1. Here as well, T_{cc} and T_{ev} of Model C and Model M have similar curves according to the previous description, while T_{cc} and T_{ev} of Model S show lower step responses due to the fixed parameters and simplified equations. The respective deviations of T_{cc} are $\Delta T_{cc}(7650\,\mathrm{s}) = 1.03\,\mathrm{K}$ for Model C, $\Delta T_{cc}(7650\,\mathrm{s}) = 2.76\,\mathrm{K}$ for Model S, and $\Delta T_{cc}(7650\,\mathrm{s}) = 1.05\,\mathrm{K}$ for Model M.

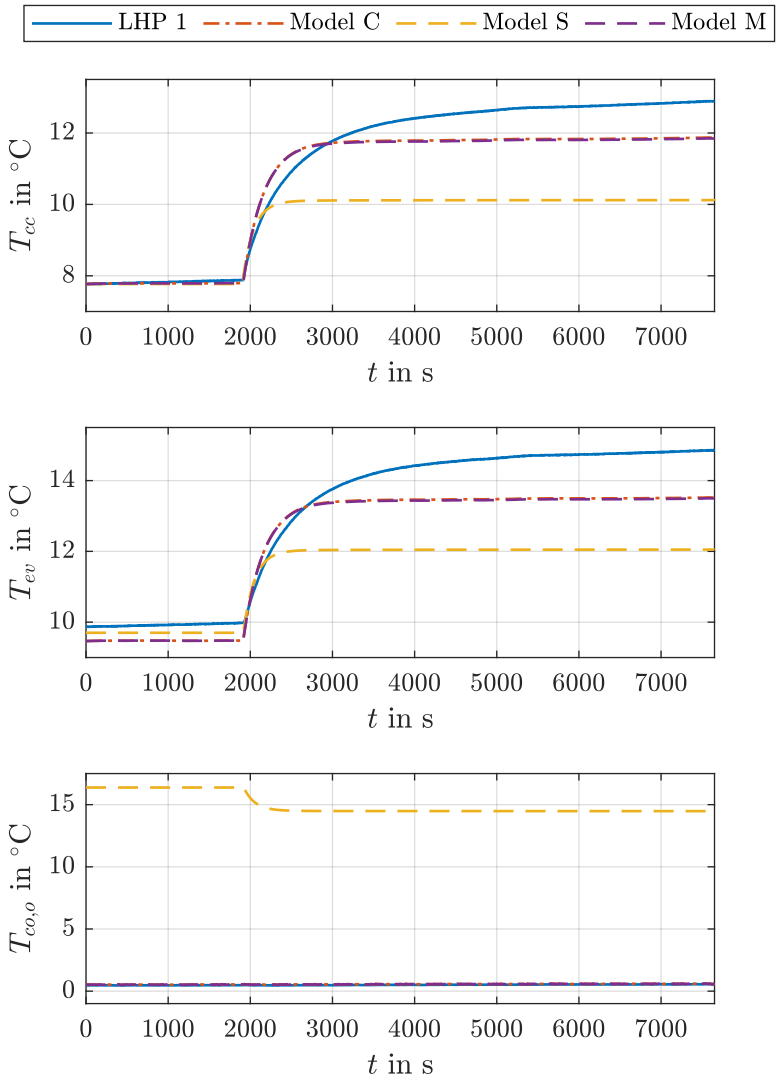

Figure 7.16: Comparison of 1 W $\dot{Q}_{cc}$ step responses of LHP 1, Model C, Model S, and Model M ($\dot{Q}_{hs} = 60\,\mathrm{W}$, $T_{sk} = 0\,^{\circ}\mathrm{C}$)

The dynamics of the step responses of all models still deviate slightly from the measured step response of LHP 1 as in the previous $\dot{Q}_{cc}$ step responses in Fig. 7.15. Again, a major difference between model and reality is present in the third row of Fig. 7.16. The condenser outlet temperature $T_{co,o}$ of Model S is significantly increased compared to the respective temperatures of Model C and Model M as well as LHP 1. In comparison with Fig. 7.2, 7.5, and 7.8, the stationary error after the step has remained about the same for all models. However,

the temperature level adjusted by $\dot{Q}_{cc}$ has a small influence on the dynamic behavior of the temperatures.

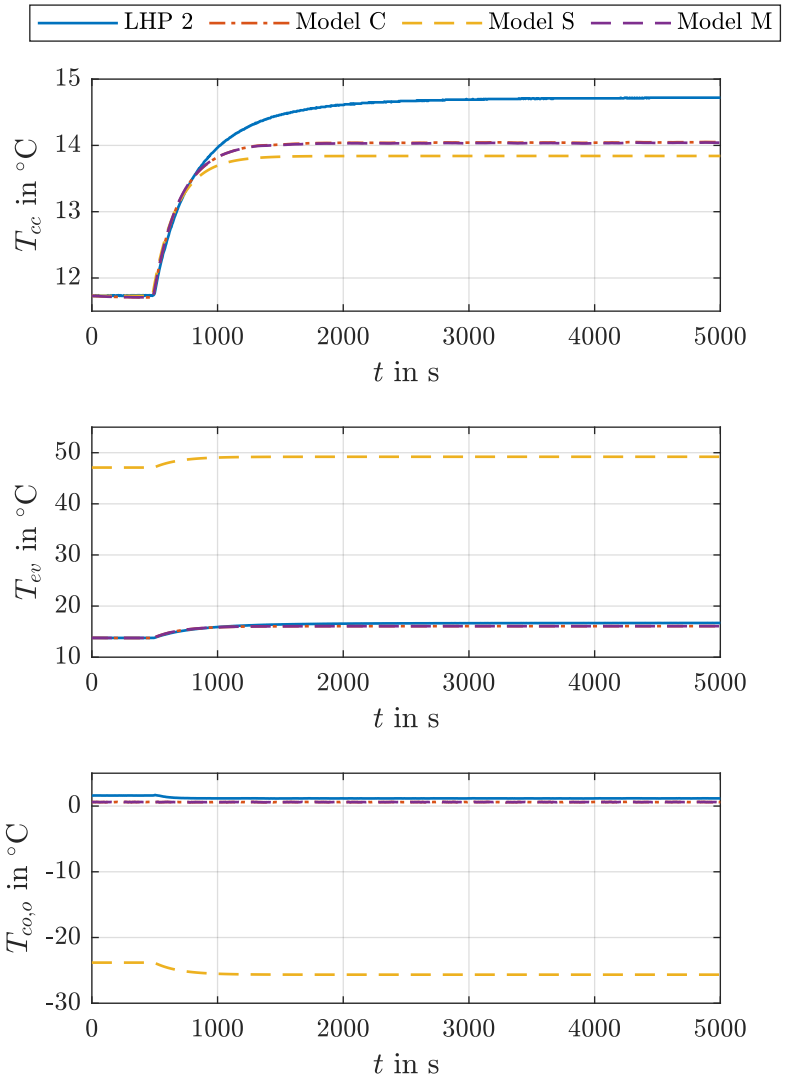

Figure 7.17: Comparison of 1 W $\dot{Q}_{cc}$ step responses of LHP 2, Model C, Model S, and Model M ($\dot{Q}_{hs} = 100\,\mathrm{W}$, $T_{sk} = -15\,^{\circ}\mathrm{C}$)

Fig. 7.17 contains the comparison of 1 W $\dot{Q}_{cc}$ step responses starting from $\dot{Q}_{cc} = 2\,\mathrm{W}$ at a heat load of $\dot{Q}_{hs} = 100\,\mathrm{W}$. All three models are able to match the step response of T_{cc} of LHP 2. The stationary deviation after the step is again higher for Model S ($\Delta T_{cc}(5000\,\mathrm{s}) = 0.88\,\mathrm{K}$) than for Model C ($\Delta T_{cc}(5000\,\mathrm{s}) = 0.67\,\mathrm{K}$) and Model M ($\Delta T_{cc}(5000\,\mathrm{s}) = 0.68\,\mathrm{K}$). However,

a higher heat load produces higher mass flows. This connection is included in the complex models Model C and Model M by the dynamics of the third state $\dot{m}^l$, whose curve of T_{ev} is similar to the one of LHP 2. In contrast, Model S does not adapt its OP parameter $\dot{m}$ and thus, there is not only a stationary deviation in $T_{co,o}$ as in the previous Fig. 7.15 and 7.16, but also in T_{ev}, as the additional heat is used in the model to heat up the evaporator subsystem instead of evaporating the liquid. Furthermore, the higher system input after the step produces a different behavior of the condenser outlet temperatures $T_{co,o}$ of the models. Model S shows a decrease of $T_{co,o}$ based on the increased evaporator temperature T_{ev} which results in an increased heat transfer from the condenser to the heat sink due to an increased temperature difference. The actual curve of $T_{co,o}$ of LHP 2 shows a step-related temperature decrease like Model S as well. In the complex models, the low $T_{co,o}$ is connected to the fixed OP parameters as mentioned above in relation to Fig. 7.14. This discrepancy between the complex models and LHP 2, however, is small and has a negligible effect on the overall LHP behavior of the models, especially on the controlled temperatures T_{cc} and T_{ev}.

7.2.2 Response to Variable Disturbances

For the evaluation of the behavior of the introduced models of the LHP-based heat transport systems with regard to variations of the disturbances, arbitrary test profiles are applied to the heat sink and the heat source. As noted in Sec. 5.1, Model S is restricted to the OP, where the disturbances do not change and thus is not included in this part of the evaluation. In the following, the different results of SIM, LHP 1, and LHP 2 with respect to disturbance variations are compared to those of Model C and Model M.

In Fig. 7.18, a $10\,\mathrm{W}$ $\dot{Q}_{hs}$ step starting from $\dot{Q}_{hs} = 60\,\mathrm{W}$ is applied to SIM and the complex models Model C and Model M. All four measurable temperatures of the simulation and the models are in a good agreement. The stationary error of the CC temperatures T_{cc} after the step is $\Delta T_{cc}(10{,}000\,\mathrm{s}) = 0.14\,\mathrm{K}$ for Model C and $\Delta T_{cc}(10{,}000\,\mathrm{s}) = 0.19\,\mathrm{K}$ for Model M. The dynamics of the step response is also met by both models.

In the real systems LHP 1 and LHP 2, a $-20\,\mathrm{W}$ $\dot{Q}_{hs}$ step is applied starting from $\dot{Q}_{hs} = 80\,\mathrm{W}$ and $\dot{Q}_{hs} = 40\,\mathrm{W}$, respectively, which causes a temperature rise of T_{cc}, T_{ev}, and $T_{co,i}$ in Fig. 7.19 and 7.20. The subcooling regions in the condensers are large enough to cool the liquid down to near sink temperature T_{sk} over the entire time frame in both cases. Here as well, the dynamics of the temperatures are well met by the models. The stationary deviations of T_{cc} after the step in Fig. 7.19 and 7.20 are $\Delta T_{cc}(3000\,\mathrm{s}) = 0.23\,\mathrm{K}$ and $\Delta T_{cc}(7000\,\mathrm{s}) = 0.25\,\mathrm{K}$ for Model C as well as $\Delta T_{cc}(3000\,\mathrm{s}) = 0.19\,\mathrm{K}$ and $\Delta T_{cc}(7000\,\mathrm{s}) = 0.21\,\mathrm{K}$ for Model M. A greater deviation results in the condenser inlet temperature $T_{co,i}$, which is also recognizable in the previous $\dot{Q}_{cc}$ step responses, due to the influence of the heat sink on the temperature sensor. The small difference in the results of Model C and Model M is traced back to the extended thermal network at the evaporator, whereby the measured evaporator temperature is matched with a different model variable, i.e. T_{ev} for Model C and $T_{ev,sf}$ for Model M. The two controlled temperatures T_{cc} and T_{ev}, however, are closely reproduced by the models.

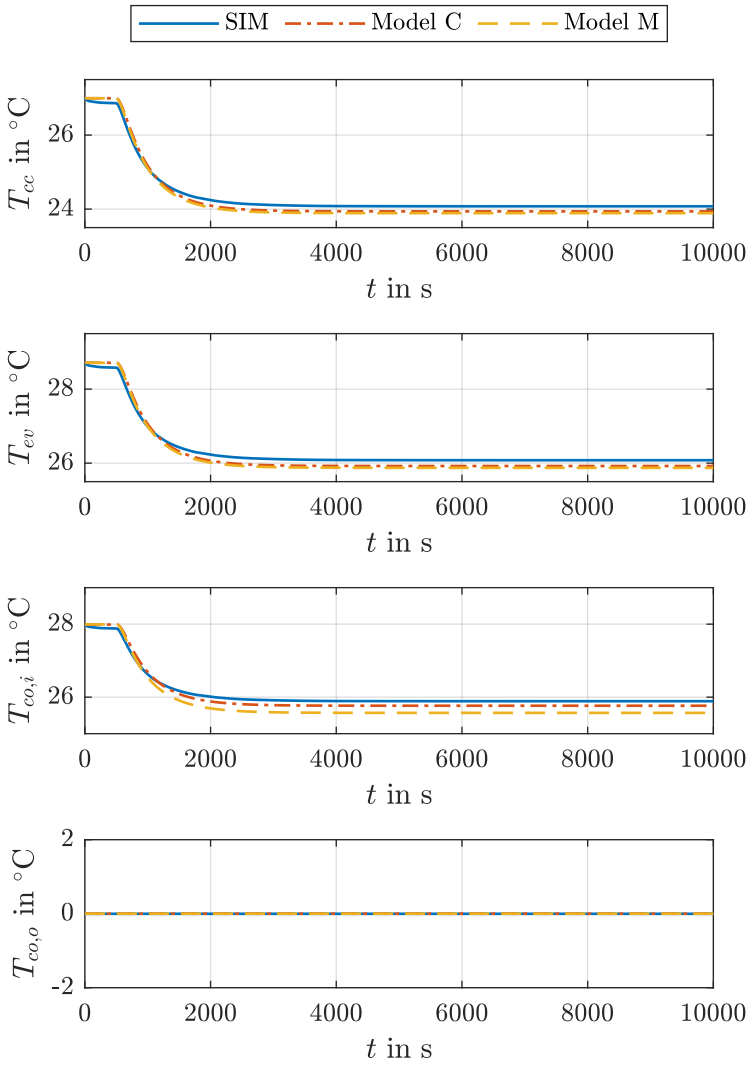

Figure 7.18: Comparison of 10 W $\dot{Q}_{hs}$ step responses of SIM, Model C, and Model M ($T_{sk} = 0\,°\mathrm{C}$)

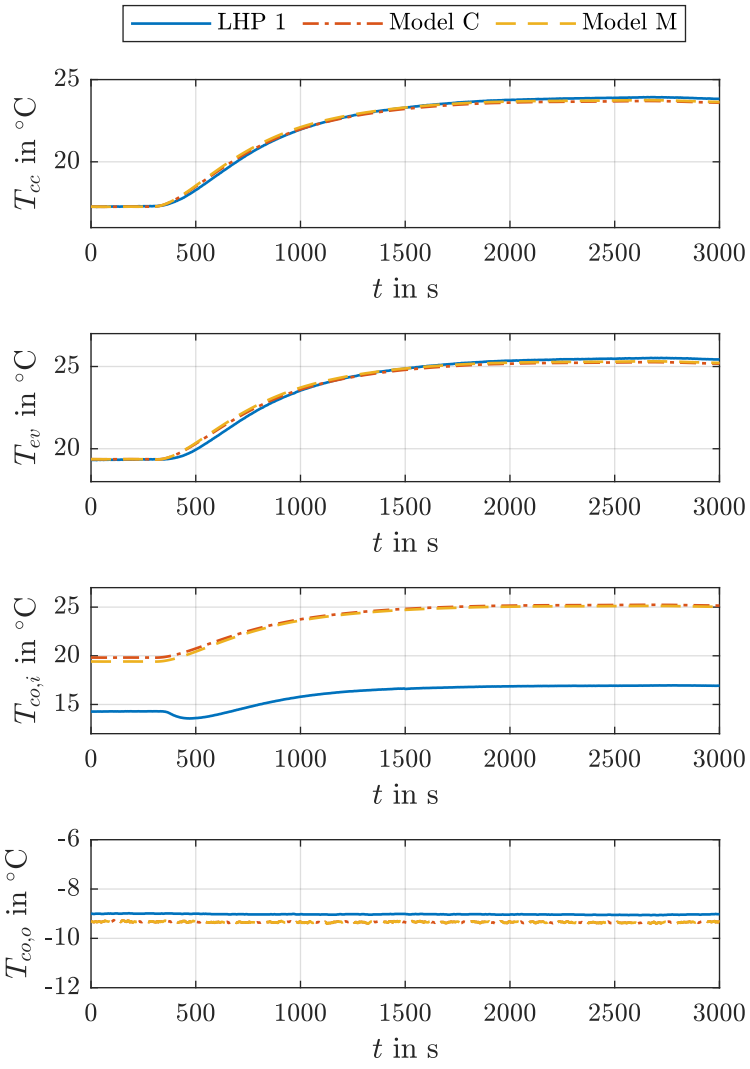

Figure 7.19: Comparison of $-20\,\mathrm{W}$ $\dot{Q}_{hs}$ step responses of LHP 1, Model C, and Model M ($T_{sk} = -10\,^{\circ}\mathrm{C}$)

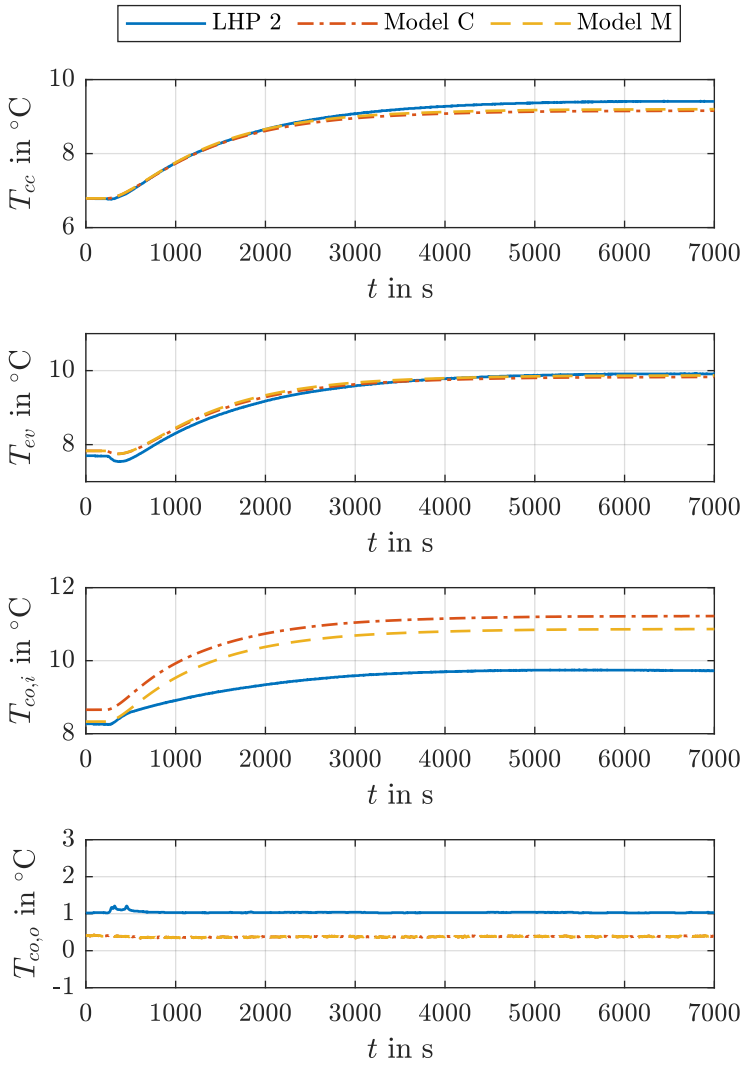

Figure 7.20: Comparison of $-20\,\mathrm{W}$ $\dot{Q}_{hs}$ step responses of LHP 2, Model C, and Model M ($T_{sk} = 0\,^{\circ}\mathrm{C}$)

The variation of the heat sink is realized by ramping up a given temperature difference. The respective comparisons between the system and the models is presented in Fig. 7.21, 7.22, and 7.23.

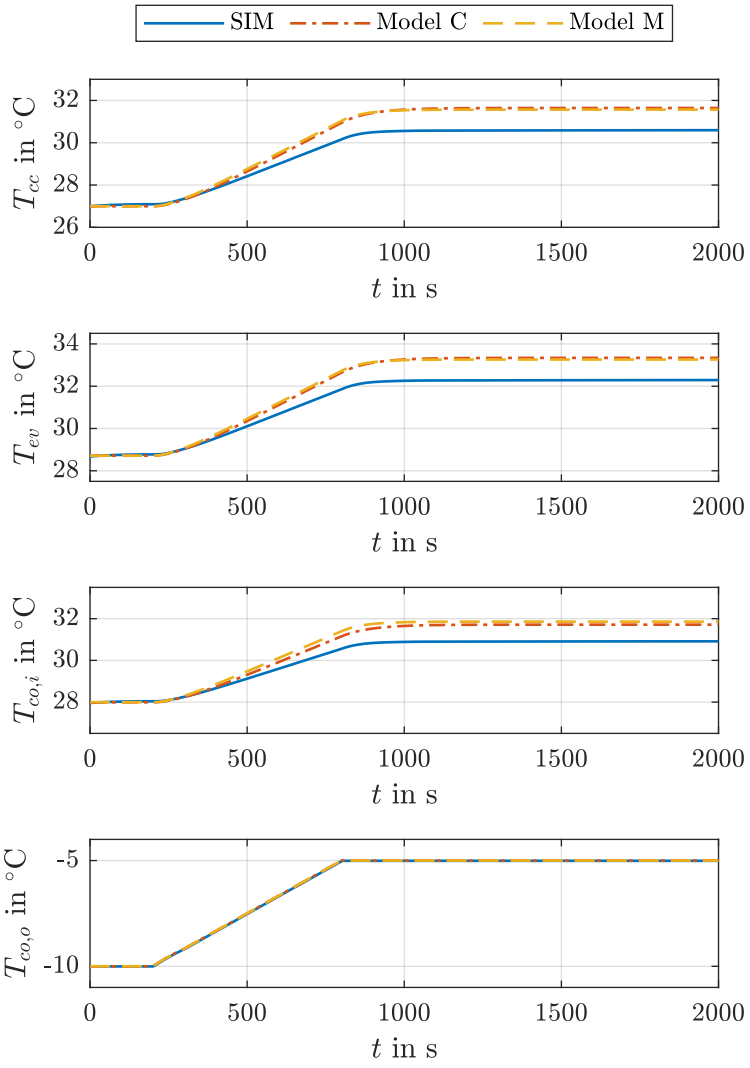

Figure 7.21: Comparison of SIM, Model C, and Model M with a ramp-shaped 5 K T_{sk} variation ($\dot{Q}_{hs} = 60$ W)

In Fig. 7.21, the temperatures of the models reach a higher end level than the simulation when changing the sink temperature from $T_{sk} = -10\,°\mathrm{C}$ to $T_{sk} = -5\,°\mathrm{C}$, although the condenser outlet temperature $T_{co,o}$ are close to each other. A similar exceeding is already present in the other comparisons of Model C and Model M with SIM. As before, the deviation is related to the

mass flow rates, which are adapted to the new conditions to varying degrees. The resulting deviations in T_{cc} are $\Delta T_{cc}(2000\,\mathrm{s}) = 1.05\,\mathrm{K}$ and $\Delta T_{cc}(2000\,\mathrm{s}) = 0.97\,\mathrm{K}$ for Model C and Model M, respectively. In addition, the slope of the temperature increase is slightly higher for the models than for SIM. Nevertheless, the deviations are small enough in order to design an adequate controller.

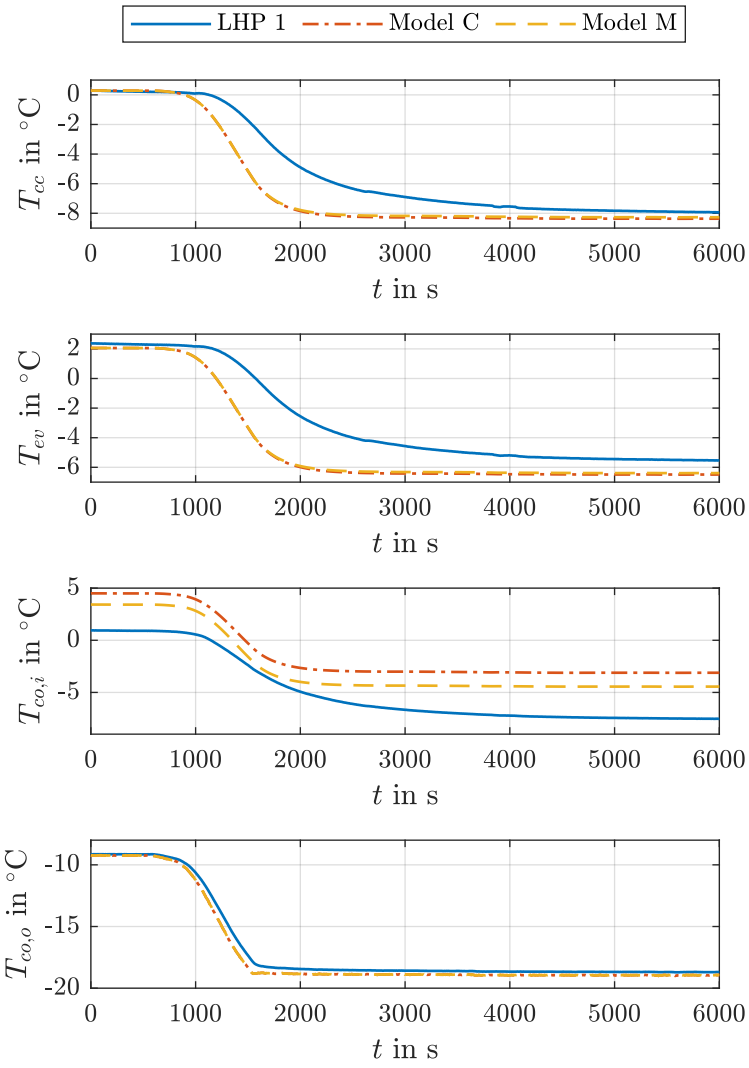

Figure 7.22: Comparison of LHP 1, Model C, and Model M with a ramp-shaped $-10\,\mathrm{K}$ T_{sk} variation ($\dot{Q}_{hs} = 60\,\mathrm{W}$)

A deviation in the delay of the temperatures along the loop is recognizable in Fig. 7.22 and 7.23. While $T_{co,o}$ shows the same curve for all three systems close to the ramp-shaped variation

of the heat sink, the other temperatures follow the variation with a delay. The variable heat transfer between the condenser and the heat sink as well as the transport delay inside the LHP are possible causes for the larger delay on the test benches. A minor stationary error of T_{cc} after the T_{sk} step remains again for both models in both cases. In Fig. 7.22, the deviations in T_{cc} are $\Delta T_{cc}(6000\,\mathrm{s}) = 0.43\,\mathrm{K}$ and $\Delta T_{cc}(6000\,\mathrm{s}) = 0.33\,\mathrm{K}$ for Model C and Model M. Accordingly, the deviations in T_{cc} are $\Delta T_{cc}(8000\,\mathrm{s}) = 0.63\,\mathrm{K}$ and $\Delta T_{cc}(8000\,\mathrm{s}) = 0.65\,\mathrm{K}$ for Model C and Model M in Fig. 7.23.

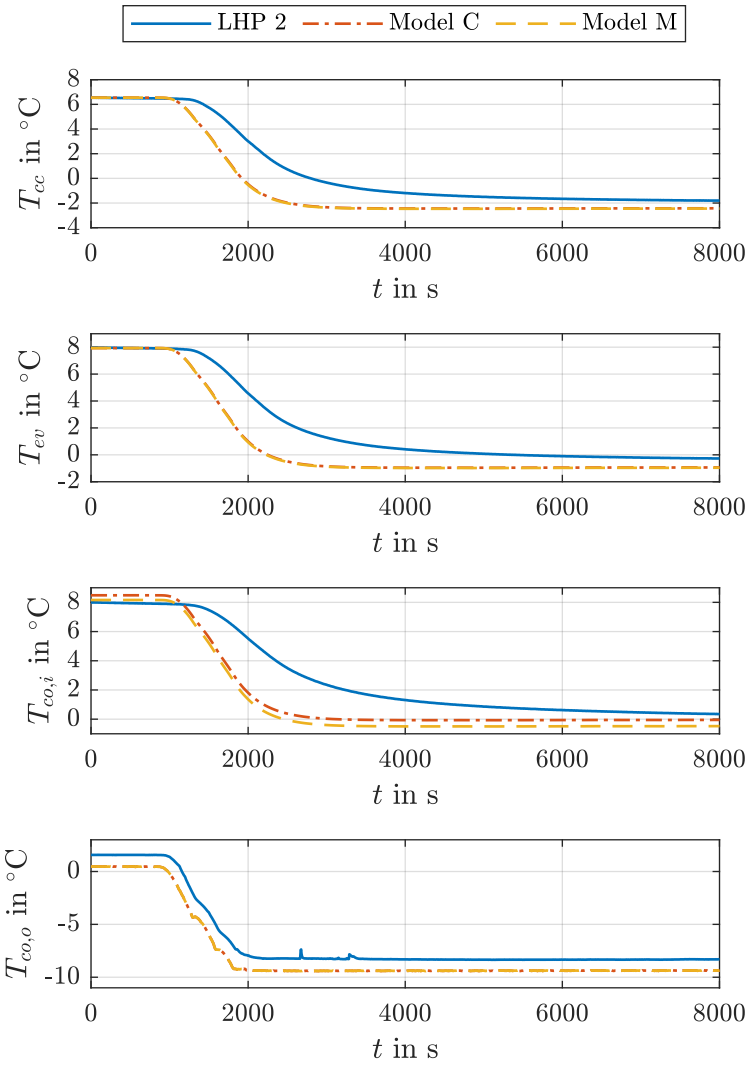

Figure 7.23: Comparison of LHP 2, Model C, and Model M with a ramp-shaped $-10\,\mathrm{K}$ T_{sk} variation ($\dot{Q}_{hs} = 60\,\mathrm{W}$)

7.2.3 Behavior of State Variables

With the availability of the numerical simulation SIM of a single LHP, it is possible to further evaluate the accuracy of the complex models Model C and Model M. Thus, the behavior of the state variables of the complex models are verified, which are not all measured on the test benches. In addition, this section presents the analysis of the LHP fluid dynamics and the tracking of the liquid-vapor interface in the condenser based on the complex models.

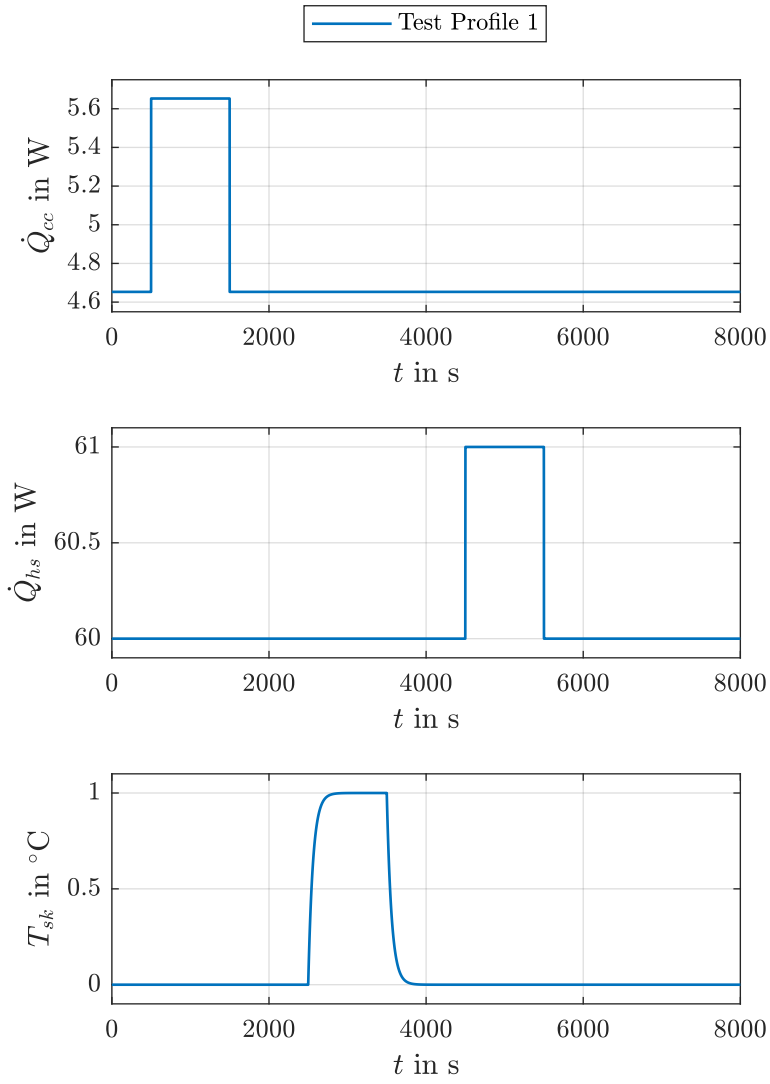

Figure 7.24: Test Profile 1 with variations in the system input and the disturbances including a 1 W $\dot{Q}_{cc}$ step, a 1 W $\dot{Q}_{hs}$ step, and a 1 K T_{sk} step in the OP

The curves of the inputs in Fig. 7.24 are chosen as a test profile in order to compare the unmeasured state variables of both models against the results of SIM. The test profile includes the relevant changes of the operating conditions as separately evaluated in the previous sections. The corresponding step responses of the three systems regarding the three states T_{cc}, $L_{2\phi}$, and $\dot{m}^l$ are given in Fig. 7.25.

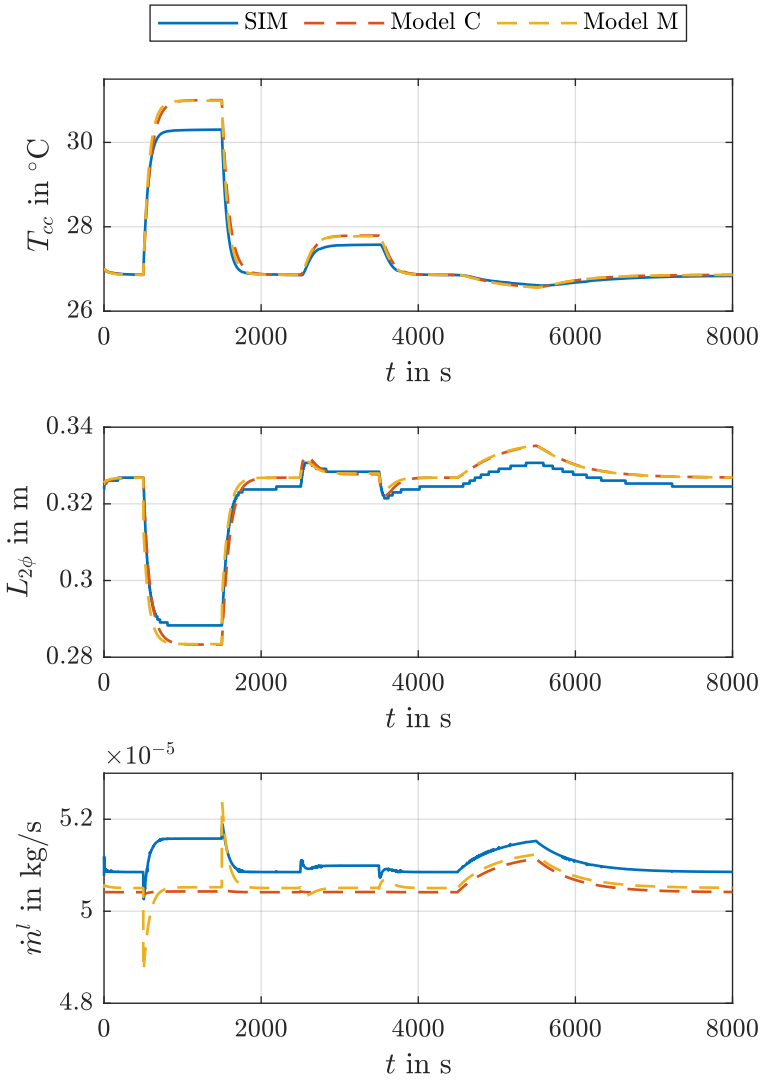

Figure 7.25: Step responses of the state variables T_{cc}, $L_{2\phi}$, and $\dot{m}^l$ of SIM, Model C, and Model M to Test Profile 1 in Fig. 7.24

The curves of the measured state variable T_{cc} of Model C, Model M, and SIM are closely together. The complex models reproduce the dynamics of T_{cc} of SIM precisely, and the reaction to all three steps is consistent. Minor stationary deviations occur due to the varying mass flow rates, as explained in the following. The maximum absolute deviations of T_{cc} between SIM and the models are $\max(\Delta T_{cc}) = 0.80\,\mathrm{K}$ for Model C and $\max(\Delta T_{cc}) = 0.71\,\mathrm{K}$ for Model M in this scenario.

The second state variable $L_{2\phi}$ in the second row of Fig. 7.25 is the two-phase length of the condenser. Here as well, a good accordance with $L_{2\phi}$ of SIM is achieved by both complex models. The dynamic variation of $L_{2\phi}$ to the three inputs is similar between the systems including the over- and undershoots due to the T_{sk} step and the rise due to the $\dot{Q}_{hs}$ step. Although T_{cc} rises during both the $\dot{Q}_{cc}$ step and the T_{sk} step, $L_{2\phi}$ falls and rises instead, accordingly. This is related to the heat transfer kinematic at the condenser. The positive step of $\dot{Q}_{cc}$ causes a rise of T_{cc} and the condenser saturation temperature $T_{co,s}$, respectively. As a result, the temperature difference between $T_{co,s}$ and T_{sk} rises as well causing an increased heat flow to the heat sink and thus a smaller required condensation length $L_{2\phi}$. The maximum absolute deviation of $L_{2\phi}$ are $\max(\Delta L) = 5.6\,\mathrm{mm}$ for Model C and $\max(\Delta L) = 12.6\,\mathrm{mm}$ for Model M. In contrast to the $\dot{Q}_{cc}$ step, a rise of T_{sk} comes along with a lower delayed increase of T_{cc} and $T_{co,s}$. Therefore, the difference between $T_{co,s}$ and T_{sk} forming the heat flow to the heat sink finds a new lower balance, and the condensation length $L_{2\phi}$ increases. The final $\dot{Q}_{hs}$ step results in an increase of the mass flow rates $\dot{m}^v$ as well as $\dot{m}^l$, and $L_{2\phi}$ rises accordingly. However, T_{cc} falls since the heat gain in the LL is smaller due to the increased $\dot{m}^l$, which is depicted in the third row.

Further minor deviations are visible in the third row of Fig. 7.25 when comparing the liquid mass flow rates $\dot{m}^l$ of the systems. The maximum absolute deviations of $\dot{m}^l$ are $\max(\Delta\dot{m}) = 1.4\,\mathrm{mg\,s^{-1}}$ for Model C and $\max(\Delta\dot{m}) = 1.7\,\mathrm{mg\,s^{-1}}$ for Model M. Due to the different condenser models used in SIM and in the complex models Model C and Model M, the over- and undershoots caused by the $\dot{Q}_{cc}$ and the T_{sk} steps are pronounced differently in contrast to the $\dot{Q}_{ev}$ step. As $\dot{m}^l$ results from the balanced accumulated mass change of all LHP components in SIM, $\dot{Q}_{cc}$ and T_{sk} have a greater direct impact on $\dot{m}^l$ of SIM than on $\dot{m}^l$ of the complex models. Their $\dot{m}^l$ is dependent on $\dot{m}^v$ instead (see Sec. 4.1.6), where $\dot{m}^v$ is calculated using the stationary energy balance equation of the evaporator and a fixed mean void fraction in the two-phase region of the condenser. Thus, the difference between the levels of $\dot{m}^l$ before and after the first two steps is greater with SIM than with the complex models. Accordingly, the balanced temperature levels of T_{cc} in the first row after the steps vary between the systems, as mentioned early.

The first peak of $\dot{m}^l$ after the rising flank of the T_{sk} step is lower for both complex models than for SIM. The subsequent undershoot of Model M, however, is similar to the one of SIM since the additional evaporator capacitance $C_{ev,sf}$ incorporates the thermal inertia of the evaporator mass into the model, which is considered for the evaporator fluid in SIM. The resulting manipulation of the net heat load $\dot{Q}_{ev}$ at the evaporator in Model M amplifies the discussed reaction of $\dot{m}^l$ to the T_{sk} step in contrast to Model C. The same applies inverted to the falling flank of the T_{sk} step. An amplification of the behavior of $\dot{m}^l$ is also visible after the $\dot{Q}_{cc}$ step. Similar to SIM, the over- and undershoots of $\dot{m}^l$ are more pronounced with Model M than with Model C.

To analyze the LHP mass flow dynamics, the difference between $\dot{m}^l$ and $\dot{m}^v$ is presented in Fig. 7.26.

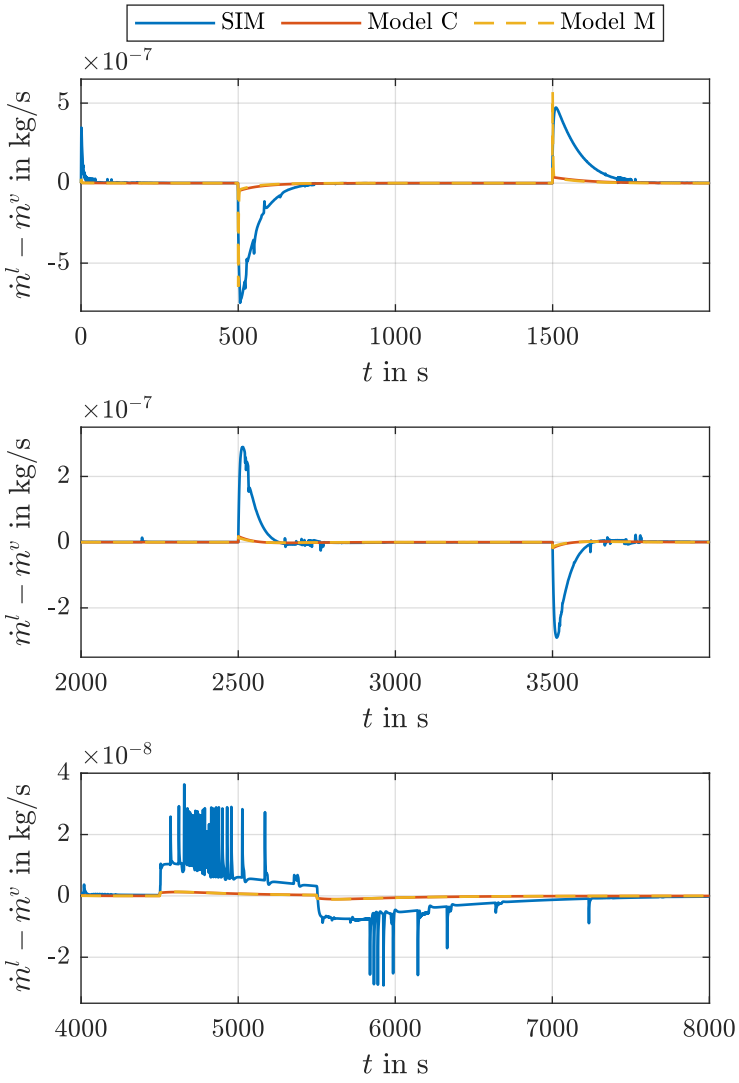

Figure 7.26: Step responses of the difference between the mass flow rates $\dot{m}^l$ and $\dot{m}^v$ of SIM, Model C, and Model M to Test Profile 1 in Fig. 7.24

The three rows correlate with the divided time axis of Fig. 7.25 to take a closer look at the separate step responses. Since the mass flow rates are equal in an equilibrium point, the mass flow difference always converges back to zero after a change of the inputs. The qualitative reaction to the three input changes is similar between the models and SIM. However, a smaller

displacement of the mass flow difference of the complex models from zero is visible compared to SIM due to the mentioned modeling mismatch. Only for the $\dot{Q}_{cc}$ step, Model M shows initial spikes due to the integrated evaporator mass, which quickly return to the curve of Model C.

For tracking the liquid-vapor interface in the condenser, the lengths of the condenser regions are calculated based on the condenser inlet in the complex models. Thus, the position of the liquid-vapor interface results from the sum of the lengths L_{sh} and $L_{2\phi}$. For the test profile in Fig. 7.24, the variations of the position of the liquid-vapor interface and the condenser outlet temperature $T_{co,o}$ are depicted in Fig. 7.27.

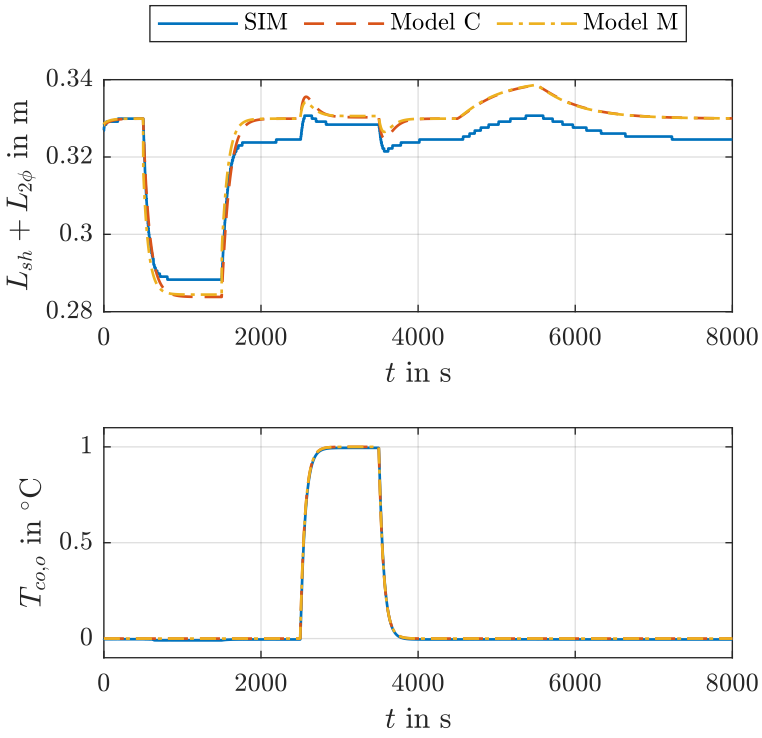

Figure 7.27: Step responses of the liquid-vapor interface in the condenser of SIM, Model C, and Model M to Test Profile 1 in Fig. 7.24

The maximum absolute deviations of the sums toward SIM are $\max(\Delta L) = 8.2\,\mathrm{mm}$ for Model C and $\max(\Delta L) = 12.7\,\mathrm{mm}$ for Model M. Since L_{sh} is small compared to $L_{2\phi}$, the differences between the curves in the first row of Fig. 7.27 and in the second row of Fig. 7.25 are small as well. With a considered total length $L_{co} = 1.85\,\mathrm{m}$, the remaining length L_{sc} of the subcooled region is large enough to cool the liquid down to near sink temperature at the condenser outlet as can be seen by comparing $T_{co,o}$ in the second row of Fig. 7.27 to T_{sk} in the third row of Fig. 7.24. The only deviation between the complex models and SIM is present during the $\dot{Q}_{cc}$ step when $T_{co,o}$ of SIM with its numerical solution method falls below T_{sk}

which contradicts the second law of thermodynamics (cf. Sec. 3.1.2). Such a contradiction is not possible with the heat exchanger approach of the complex models (see Sec. 4.1.4).

All curves of the mass flows and the region lengths in the previous figures are plausible from the models' point of view. To determine the proximity to the real LHP systems on the test benches, appropriate measurements of the interior of the LHP are necessary, which is not in the scope of this thesis.

7.2.4 Validation of the Order Reduction of the Complex Dynamical Model

A reduction of the order of the four-dimensional state-space model (4.66), hereinafter denoted as Model 4D, to the final three-dimensional state-space model (4.84), i.e. Model C, has been performed and qualitatively analyzed in Sec. 4.1.7. By assuming a constant volume fraction ratio β^{op} and thus a constant thermal capacitance C_{ce}^{op}, the model equations have been simplified, and the order of Model 4D has been reduced. Now, the simplification is quantitatively investigated by comparing the results of SIM and both models. For the comparison, the same parameter set is used as defined in Table 7.2 to set the focus on the differences of the model equations.

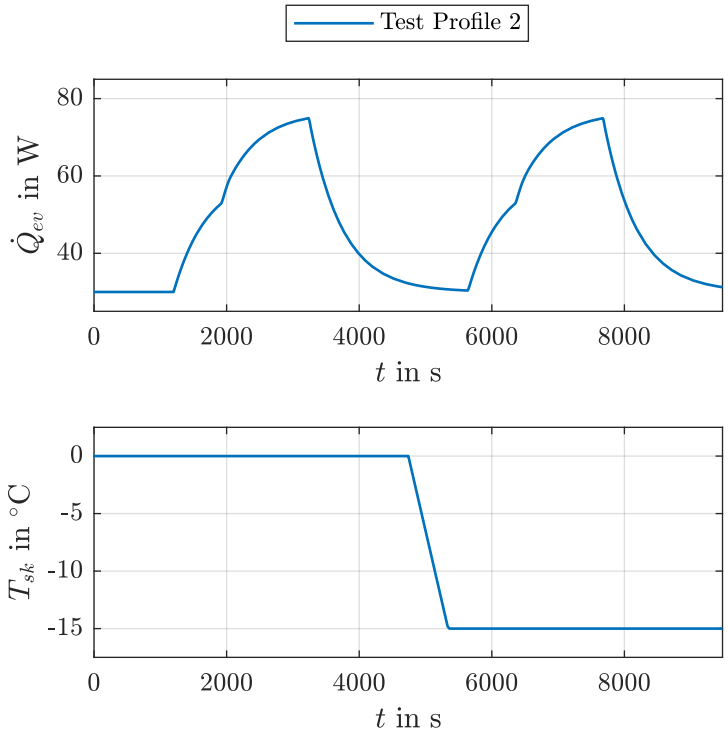

Figure 7.28: Test Profile 2 with variations in the disturbances across the LHP operating range

A test profile is chosen that includes the variation of the disturbances, i.e. the heat load $\dot{Q}_{ev}$ and the sink temperature T_{sk}, at a constant system input $\dot{Q}_{cc}$, which is commonly used in qualification tests of LHPs. Their respective curves are depicted in Fig. 7.28.

The presented test profile expands over a great part of the operating range of the LHP to evaluate the performance of the models outside the OP as well. The corresponding state variables of both models in comparison to the state variables of SIM are presented in Fig. 7.29.

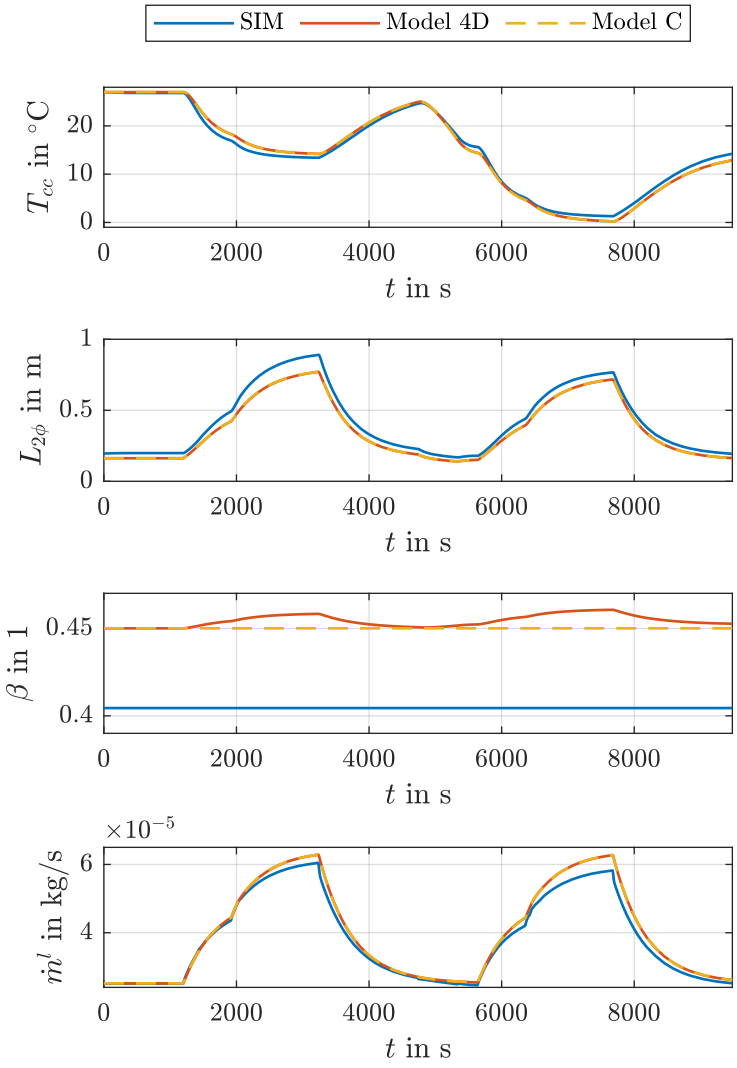

Figure 7.29: Results of SIM, Model 4D, and Model C to Test Profile 2 in Fig. 7.28

A similar curve of the three state variables T_{cc}, $L_{2\phi}$, and $\dot{m}^l$ results from the chosen test profile despite the differences in the state variable β. For the comparison of the models with SIM, β of SIM is calculated by solving (4.83) with the fixed thermal capacity of the two-phase CC given in [MKHW19], since no separate determination is included. Due to the different modeling approaches, a negligible stationary deviation between the β curves of SIM and Model C exists. Although β of Model 4D slightly adapts to the variations of the disturbances, the effect of a varying β on the overall LHP behavior is low. Hence, the state variables T_{cc}, $L_{2\phi}$, and $\dot{m}^l$ of Model 4D and Model C in Fig. 7.29 are similar, and the model simplification is valid. Furthermore, $L_{2\phi}$ and $\dot{m}^l$ are proportional to $\dot{Q}_{ev}$ of Fig. 7.28, while T_{cc} decreases with increasing $\dot{Q}_{ev}$. A decreasing T_{sk} reduces the rise and fall of the three state variables during the variation of $\dot{Q}_{ev}$, respectively.

The results in Fig. 7.29 underline once again the very good agreement between the complex dynamical models and the experimentally validated numerical LHP simulation SIM over the entire operating range of the LHP.

7.2.5 Occurrence of Temperature Oscillations

The investigated conventional LHP systems SIM, LHP 1, and LHP 2 include minor attached masses at the evaporators. Thus, Model C without considering a thermal mass at the evaporator and Model M with an appropriate thermal capacitance for the mass show related results in the previous model validation when comparing the measured and simulated temperatures. As discussed in Sec. 2.4, temperature oscillations in the normal operation of the LHP within its operating range are traced back to a significant thermal evaporator mass, as theoretically shown in the literature. With the introduced Model M, it is now possible to analyze the stability of conventional LHPs with attached thermal mass and to simulate corresponding temperature oscillations. In addition, an adequate controller compensating these oscillations can be designed based on the introduced model in a subsequent step.

The curves of the measured temperatures of Model M parameterized in the OP of SIM (see Table 7.4) for three different thermal masses

$$C^1_{ev,sf} = 40\,\mathrm{J\,K^{-1}}, \tag{7.13}$$

$$C^2_{ev,sf} = 260\,\mathrm{J\,K^{-1}}, \tag{7.14}$$

$$C^3_{ev,sf} = 280\,\mathrm{J\,K^{-1}} \tag{7.15}$$

are depicted in Fig. 7.30. For the investigation of the stability of the nonlinear system Model M, the stability of the chosen OP of the system is regarded. Based on a displacement from the equilibrium point, the stability of the OP is analyzed in dependence on $C_{ev,sf}$. Due to the bidirectional connection between the LHP fluid cycle and the evaporator mass, which is situated between the LHP and the heat source, the net heat load $\dot{Q}_{ev}$ at the evaporator is manipulated both by the fluid temperature of the evaporator, i.e. T_{ev}, and by the temperature $T_{ev,sf}$ of the evaporator mass near the heat source. The interaction between both subsystems can cause temperature oscillations when the difference between the dynamics of the related temperatures are sufficiently large depending on the value of $C_{ev,sf}$.

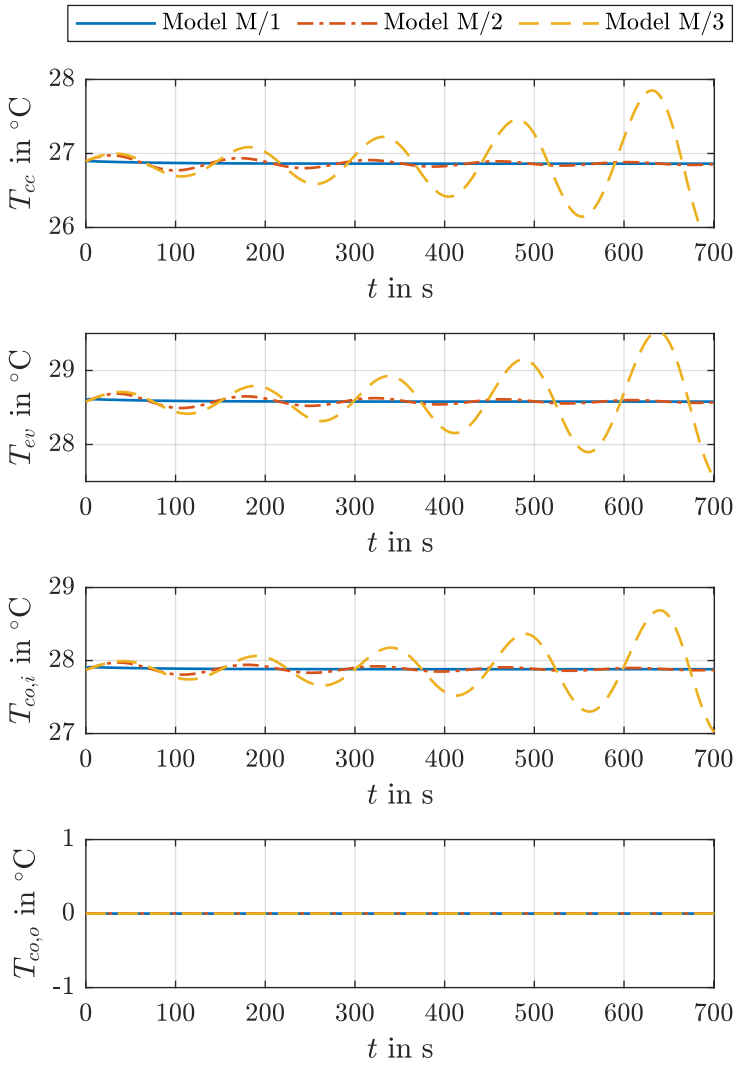

Figure 7.30: Comparison of Model M in the OP of SIM with different thermal masses $C^1_{ev,sf} = 40\,\mathrm{J\,K^{-1}}$, $C^2_{ev,sf} = 260\,\mathrm{J\,K^{-1}}$, and $C^3_{ev,sf} = 280\,\mathrm{J\,K^{-1}}$

In the chosen OP, the applied initial offset of the CC temperature is $T^{off}_{cc} = 0.03\,\mathrm{K}$. As expected, the temperatures of Model M with the smallest thermal mass (7.13) are stable and run into the balanced OP, as presented in Fig. 7.30. By increasing the thermal mass to the value of (7.14), decreasing temperature oscillations become visible, but the trajectories of the temperatures are still stable. The stability limit of the OP is crossed when the thermal mass is

further increased to the value of (7.15). Then, increasing oscillations are present, and the OP is unstable.

The stability limit can be calculated by means of Theorems 4.1 and A.1. For this purpose, the characteristic polynomial of the Jacobian of (6.27a) is established and the necessary and sufficient conditions of Theorem A.1 are solved for the thermal mass $C_{ev,sf}$. The most restrictive condition for a stable OP finally results from the second and third leading principal minors:

$$0 < C_{ev,sf} < 269.1\,\mathrm{J\,K^{-1}}. \tag{7.16}$$

Thus, the upper limit in (7.16) lays between (7.14) and (7.15) which confirms the results of the simulative comparison in Fig. 7.30.

The presented system stability analysis can be performed with any other LHP parameterization. For the other two investigated LHP systems LHP 1 and LHP 2, the respective upper limits in (7.16) are $C_{ev,sf} = 864.3\,\mathrm{J\,K^{-1}}$ and $C_{ev,sf} = 1844.7\,\mathrm{J\,K^{-1}}$, respectively. The different sizes of the $C_{ev,sf}$ limits match the rising order of the sizes of the thermal masses of the respective CC (cf. Table 7.4). The dependence of the operating stability of an LHP on the relation between the thermal masses of the CC and the evaporator thus coincide with the theoretical considerations in [HB12]. Thanks to the introduced Model M in this thesis, these findings can now be reproduced in simulations for the first time.

7.3 Analysis of the State-Space Model for Parallel Loop Heat Pipes

The combination of two LHPs across a thermal mass, as given by the heat transport system of an LCT, poses additional challenges to the modeling and control process. Besides the exact modeling of the heat flows in the attached LCT structure and between the LHPs, the manipulation of two controllers on one system must be coordinated to ensure overall stability. In this section, the focus is therefore set again on the dynamics of parallel LHPs under variation of the system inputs.

In Fig. 7.31, another $1\,\mathrm{W}$ $\dot{Q}_{cc}$ step at a different equilibrium point of LHP 3 is measured and compared to the results of Model P. The offset adjustment of the system inputs, as explained in Sec. 7.2.1, is applied to evaluate the validity of the fixed OP values over the operating range of LHP 3. In comparison to the $1\,\mathrm{W}$ $\dot{Q}_{cc}$ step in Fig. 7.10, both the heat load $\dot{Q}_{hs}$ and the sink temperature T_{sk} are reduced. Here as well, the dynamics of the CC temperature T_{cc} in the first row of Fig. 7.31 are closely reproduced by Model P despite the fixed model parameters. Only a small stationary deviation between the modeled and the measured T_{cc} remains after the step ($\Delta T^a_{cc}(2200\,\mathrm{s}) = 0.35\,\mathrm{K}$, $\Delta T^b_{cc}(2200\,\mathrm{s}) = 0.17\,\mathrm{K}$).

For the evaporator temperature T_{ev} in the second row, a similarly precise behavior of Model P is shown where the simulated temperatures follow the measured temperatures closely. The largest deviation is present in the third row with the condenser inlet temperatures $T_{co,i}$. The reasons are connected to the unmodeled influences of the close condenser system on the pipes causing parasitic heat flows between the condenser and the VL. Due to the sensor

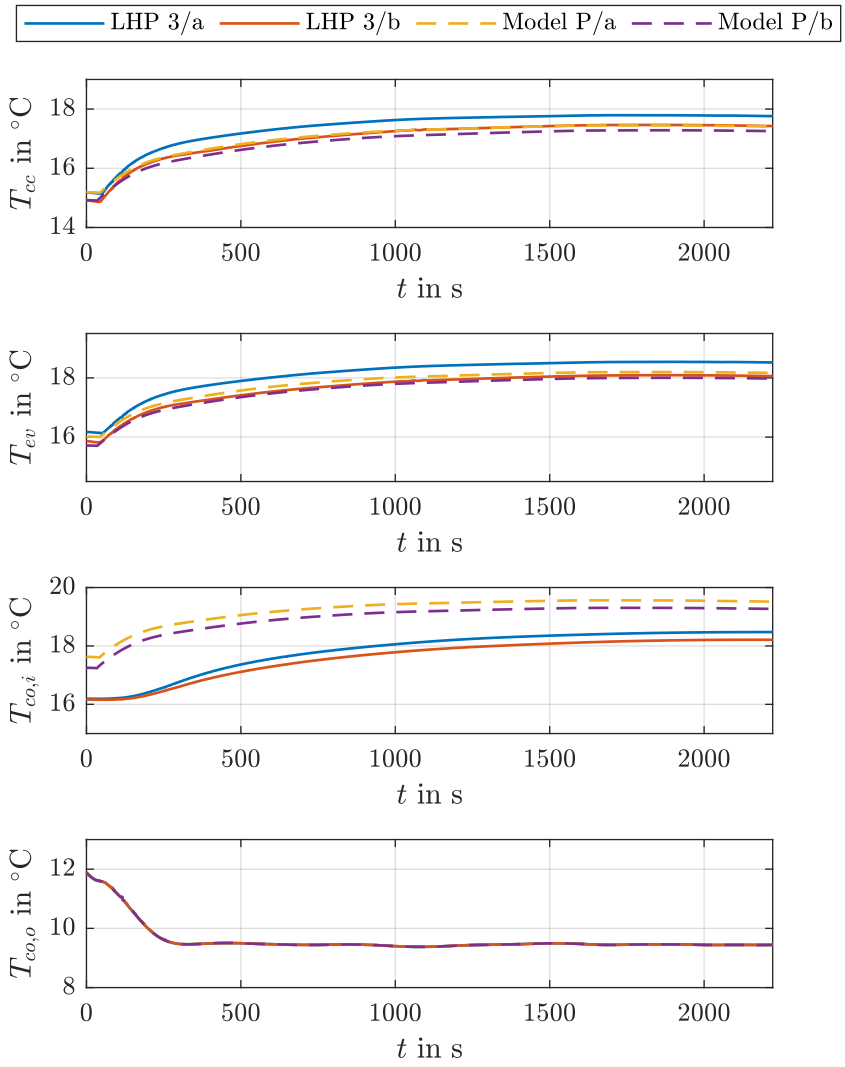

Figure 7.31: Comparison of 1 W $\dot{Q}_{cc}$ step responses of LHP a and LHP b of LHP 3 and Model P ($\dot{Q}_{hs} = 126$ W, $T_{sk} = 10\,°\mathrm{C}$)

placement on the condenser mentioned in Sec. 7.1.1, the measured and simulated condenser outlet temperatures $T_{co,o}$ are very close to the sink temperature T_{sk} and coincide with each other. Overall, Model P with fixed parameters keeps a satisfactory behavior toward variations of the system inputs under a balanced heat distribution between both LHPs.

The analysis of the oscillation behavior of Model P with regard to the thermal masses of the evaporators yields a different result compared to Model M with a single LHP. According to the procedure in Sec. 7.2.5, the upper limits of $C^a_{ev,sf}$ and $C^b_{ev,sf}$ for LHP 3 are

$C_{ev,sf} = 149{,}835\,\mathrm{J\,K^{-1}}$. This would be equivalent to an aluminum mass of approximately $m = 166\,\mathrm{kg}$. Since such a value is hardly ever reached or desired in any application, a connection between the operating stability and the thermal masses of the evaporator can not be confirmed for Model P. Instead, instability is reached in simulations due to an unbalanced heat distribution between both LHPs and thus an unequal operation of the coupled LHPs. The heat distribution in a heat transport system depends on the individual heat source structure. Based on an exact investigation of the heat flow paths of each distributed heat source instead of the total heat load, a more detailed thermal network of the heat source structure can be constructed to evaluate the stability limit of each heat transport system separately.

7.4 Simulative Validation of the Controller Performances

The objective of this section is the evaluation of the proposed controllers concerning various aspects of an effective LHP-based heat transport system, i.e. its stability, accuracy, and disturbance rejection. The operating conditions are varied to test the controller performance over the entire operating range of the respective applications at a constant setpoint temperature. Two quantitative validation metrics are chosen to evaluate both the static and the dynamic performance of the controllers:

1. The maximal absolute deviation (MAD) specifies the largest stationary difference between the points of two temperature curves at the same instant of time t to assess the accuracy of the controllers with regard to the characterization of the thermal interface of the heat transport system.

2. The root mean square error (RMSE), i.e. the square root of the mean squared difference between all points of two temperature curves, considers the temporal change to evaluate the smoothness of the controlled temperatures with regard to the thermal load of the system.

In the following analysis of the controller performances, the model-based designed PI controller piAW/S is comparable with the heuristic state-of-the-art PI controller in the literature. The setpoint temperatures T_{set} for the CC temperature T_{cc} and $T_{set,ev}$ for the evaporator temperature T_{ev} of the controllers are fixed on the following values, which are within the specifications of the considered applications:

$$T_{set} = 27\,^{\circ}\mathrm{C}, \tag{7.17}$$

$$T_{set,ev} = 29\,^{\circ}\mathrm{C}. \tag{7.18}$$

First, the temperature control of single LHPs is evaluated taking into account the complexity, computational effort, and implementation requirements of the respective controllers. Subsequently, the temperature control of advanced LHP-based heat transport systems including the single LHP with attached thermal mass and the parallel LHPs are investigated and analyzed.

7.4.1 Temperature Control of a Single Loop Heat Pipe

A typical benchmark for the performance of an LHP-based heat transport system is the variation of the disturbances along its operating range. In the application, these variations correspond to the changing dissipated heat of the cooled object in accordance with its operating status and the variability of the heat sink. In Fig. 7.32, such a benchmark profile is presented which is used for the subsequent validation of the controller performances.

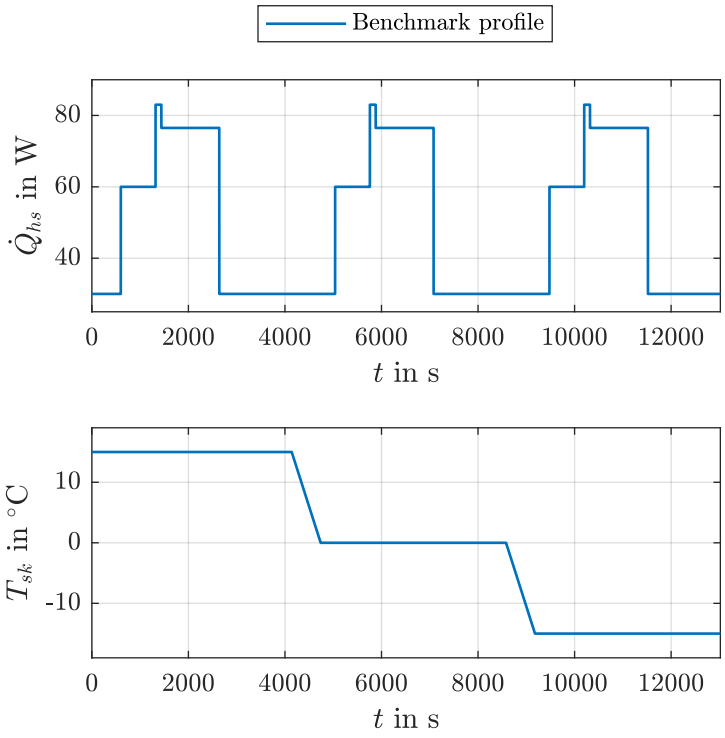

Figure 7.32: Benchmark profile of a single LHP

Both the CC controllers in Table 7.6 and the evaporator controllers in Table 7.7 are tested in SIM with the benchmark profile in Fig. 7.32.

Compensation Chamber Control

The comparison of the controlled CC temperatures T_{cc} of the different control loops is presented in Fig. 7.33.

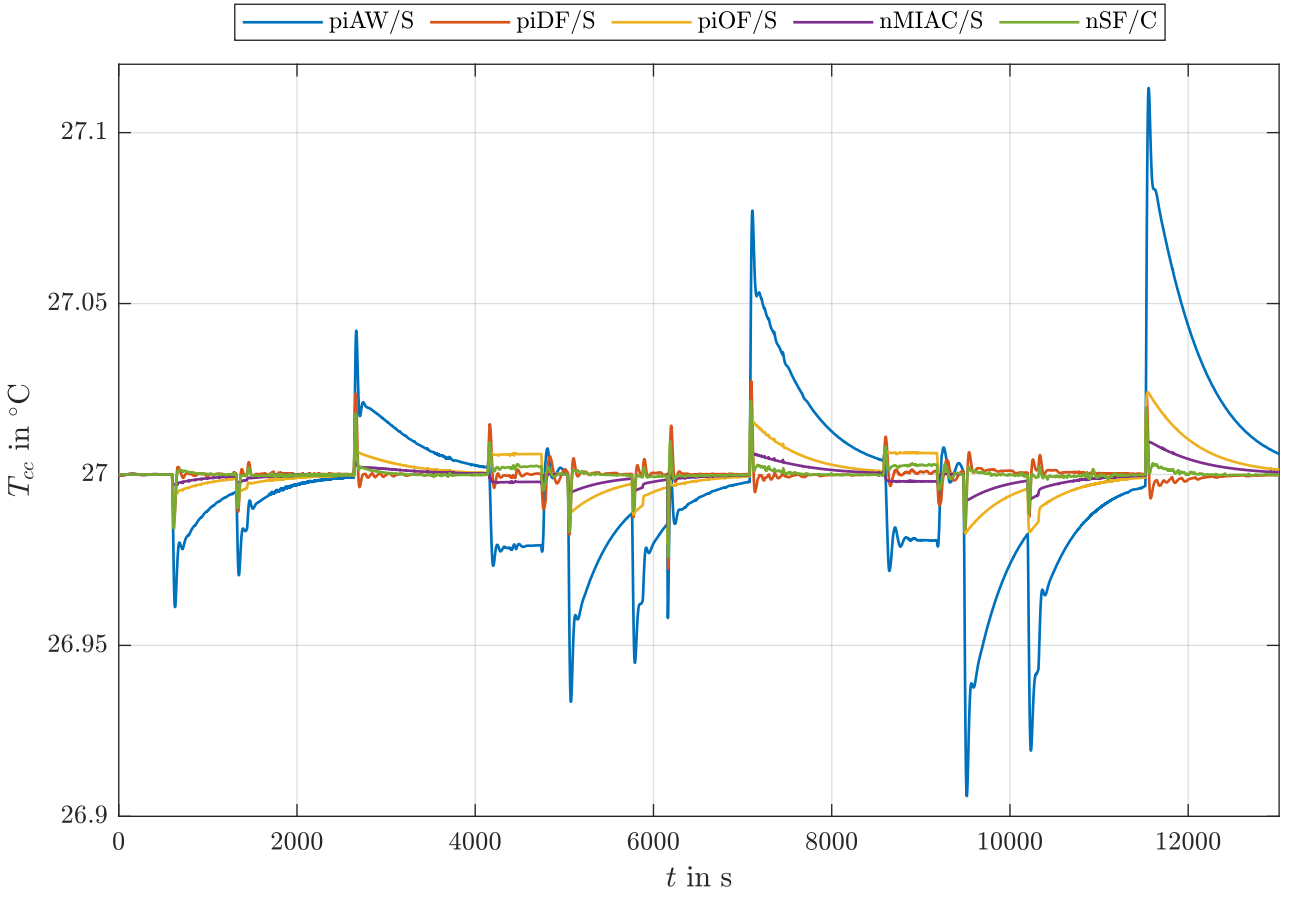

Figure 7.33: Disturbance behavior of the proposed CC controllers with respect to the benchmark profile in Fig. 7.32

The largest deviation from the setpoint temperature T_{set} is reached by piAW/S and thus by the state-of-the-art controller. All other controllers proposed in this thesis achieve a better performance result. While a heat load change yields an over- or undershoot dependent on the movement on the U-shaped curve of the SSOT (see Fig. 3.9) with a subsequent convergence to the setpoint, a change of the sink temperature results in an offset of T_{cc}. The qualitative results are underlined by the quantitative metrics in Table 7.12.

Controller	**MAD** in K	**RMSE** in K	**Required temperature sensors**	**Required disturbances**
piAW/S	0.113	0.0252	T_{cc}	-
piDF/S	0.0276	0.00278	T_{cc}	$\dot{Q}_{ev}, T_{sk}$
piOF/S	0.0241	0.00615	$T_{cc}, T_{ev}, T_{co,o}$	-
nMIAC/S	0.0155	0.00260	T_{cc}, T_{ev}	$\dot{Q}_{ev}, T_{sk}$
nSF/C	0.0241	0.00223	T_{cc}, T_{ev}	$\dot{Q}_{ev}, T_{sk}$

Table 7.12: Evaluation of the proposed CC controllers based on Model S and Model C

The lowest over- and undershoots are visible in T_{cc} controlled by nMIAC/S. Accordingly, its MAD is the smallest. However, the convergence to T_{set} is slower for nMIAC/S and is exceeded by piDF/S and nSF/C. Measured by the RMSE, the deviation error for nMIAC/S is smaller than for piDF/S, but nSF/C achieves the smallest RMSE and thus the best disturbance rejection. Although piOF/S has a similar MAD like nSF/C, its overall performance measured by the RMSE is the second worst.

The good performance of piDF/S is traced back to the good agreement between the stationary and the transient LHP simulation of SIM. Thus, the controller performance of piDF/S is also significantly dependent on the agreement between the stationary model and the real system in contrast to the dependence of the performances of the other controllers on their dynamic models. The improved performances of the proposed controllers are bought by the additionally required knowledge of the system's operating state. Therefore, additional sensors are necessary which come along with elevated costs. As presented in the third and fourth column of Table 7.12, piDF/S, nMIAC/S, and nSF/C with the lowest RMSE require the availability of the disturbances to include the directly connected dynamics of the mass flow rates. In contrast, piOF/S achieves an improved performance compared to piAW/S by two additional temperature sensors. Due to the proximity of the sensors to the impact points of the disturbances, a faster reaction to disturbance changes is possible.

Computational Time

In order to evaluate the different controllers with respect to the necessary computing power of the target processor hardware, the computational time of each controller step is averaged over the total time frame of the benchmark profile. The CPU used for the simulations is an Intel Core i7-7700 at 3.60 GHz and with 16 GB of RAM. The results of the different controllers are given in Table 7.13.

Controller	Mean computational time in ms
piAW/S	0.0114
piDF/S	0.06
piOF/S	0.0153
nMIAC/S	1.36
nSF/C	17.2

Table 7.13: Evaluation of the computational time of the proposed CC controllers based on Model S and Model C

As expected, piAW/S being based on the state-of-the-art PI controller has the lowest mean computational time and thus the lowest processor requirements. Similarly small is the mean computational time of piOF/S due to both their simple controller structures. The disturbance feedforward control implemented as lookup table requires additional computational time in order to interpolate the output value of the table. A significantly larger distance exists to the next fastest controller, piDF/S. In contrast, the mean computational time of nMIAC/S is already above $1\,\mathrm{ms}$ which is traced back to the optimization method to determine the identified model parameters for the subsequent state estimation. The largest mean computational time, however, is necessary for nSF/C based on Model C. Since the state feedback controller is based on the state estimation via an SRUKF, additional computational time is needed for the discrete transformation of the sigma points through the stiff system equations (see Sec. 4.2.3). The computational time of nSF/C in Table 7.13 is based on the proposed implementation of MATLAB's `ode15s` solver. However, a mean computational time of $595\,\mathrm{ms}$ is measured when the multi-rate framework and Euler's forward method is implemented. Such a high computational time is already close to the sampling time $T_{st} = 1\,\mathrm{s}$ commonly used for the control cycles of LHPs considering the additional computational time required for processing the data of sensors and actors. Hence, the choice of the controller also depends on the available processor hardware of the developed LHP-based heat transport system. However, the real-time capability of all introduced controllers has been verified by assuring that the respective maximal computational time over all simulation steps is smaller than T_{st}.

Anti-Windup Strategy

For the verification of the proposed AW strategy, the controlled CC temperatures T_{cc} and the manipulated variables $\dot{Q}_{cc}$ of all controllers are depicted in Fig. 7.34.

Due to a reduction of the heat load $\dot{Q}_{ev}$ during the saturation of the control heater, T_{cc} rises again, and a lower $\dot{Q}_{cc}$ is sufficient to keep T_{cc} at T_{set}. The controller piAW/S leaves the saturation the latest since the output x_{aw} of the AW structure is the largest, and the overshoot is most distinct. Both the controllers with integral action and AW strategy, namely piAW/S, piDF/S, piOF/S, and nSF/C, as well as nMIAC/S leave the saturation of the control heater smoothly without major overshoots.

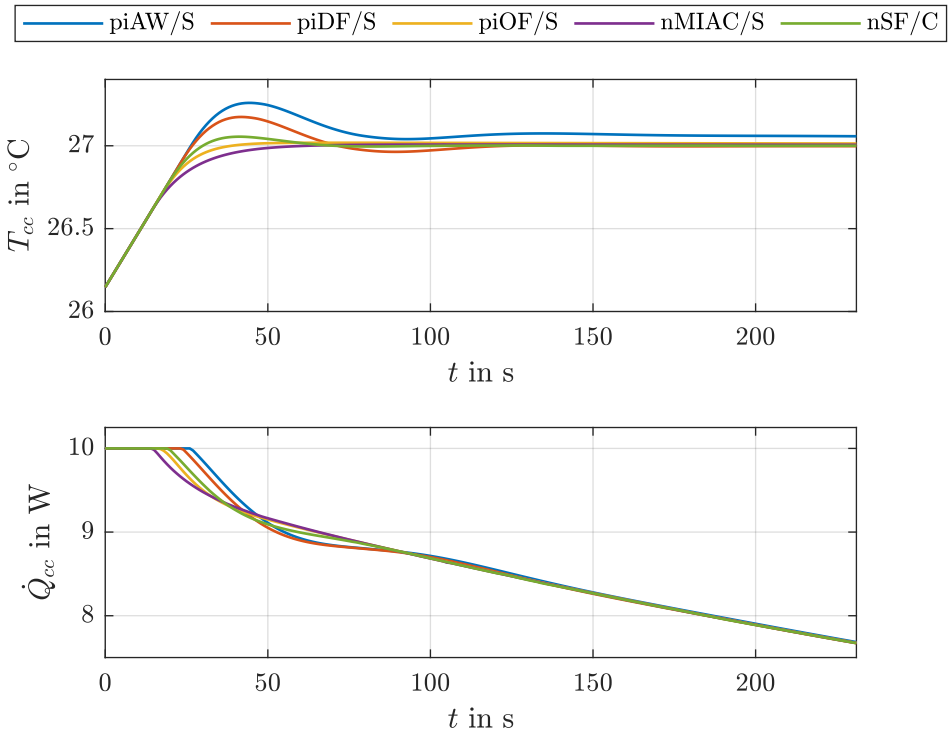

Figure 7.34: Performance comparison of the proposed CC controllers when leaving the saturation of the control heater ($T_{sk} = -25\,°\mathrm{C}$)

Integrated State Estimation Methods

In order to analyze the satisfactory performance of nMIAC/S and nSF/C in Fig. 7.33 closer, their integrated state estimation methods are evaluated in this section separately.

In Fig. 7.35, the results of the state prediction for the nonlinear Lyapunov-based controller of nMIAC/S are presented in comparison with the corresponding temperatures of SIM. The two state variables in the first two rows are closely reproduced by the state prediction based on Model S since the two model parameters $\dot{m}$ and U_{lk} are optimized by the parameter identification with respect to both measured state variables. As it can already be seen in the validation of Model S in Sec. 7.2.1, a major deviation is visible when comparing the third state variable of Model S, the condenser temperature T_{co}, with the condenser outlet temperature $T_{co,o}$ of SIM. As expected, this mapping is indeed imperfect from the model's point of view, but the measured temperature $T_{co,o}$ comes closest to the effective model temperature T_{co}, which is the overall temperature of the three subsystems VL, condenser, and LL. Since the other model parameters of Model S are fixed in the OP based on the mapping of T_{co} and $T_{co,o}$ in Sec. 7.1.2, a close agreement between all three curves of Fig. 7.35 is achieved in the proximity of the OP at approximately $t = 5900\,\mathrm{s}$.

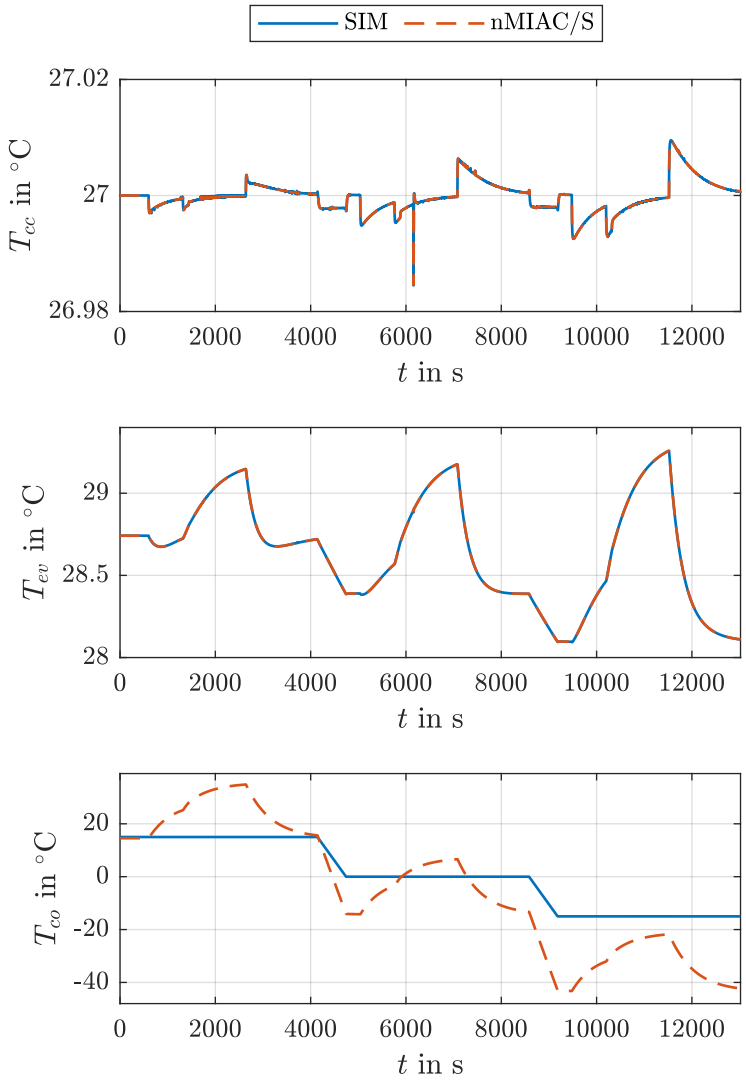

Figure 7.35: Comparison of the predicted states of nMIAC/S with the corresponding temperatures of SIM

The integrated parameter identification based on the measured temperatures T_{cc} and T_{ev} is responsible for the high agreement between T_{cc} and T_{ev} of Model S and SIM. The optimized model parameters $\dot{m}$ and U_{lk} enable the adaption of Model S to the varying operating conditions. A comparison of the identified parameters of nMIAC/S with the corresponding variables of SIM is presented in Fig. 7.36.

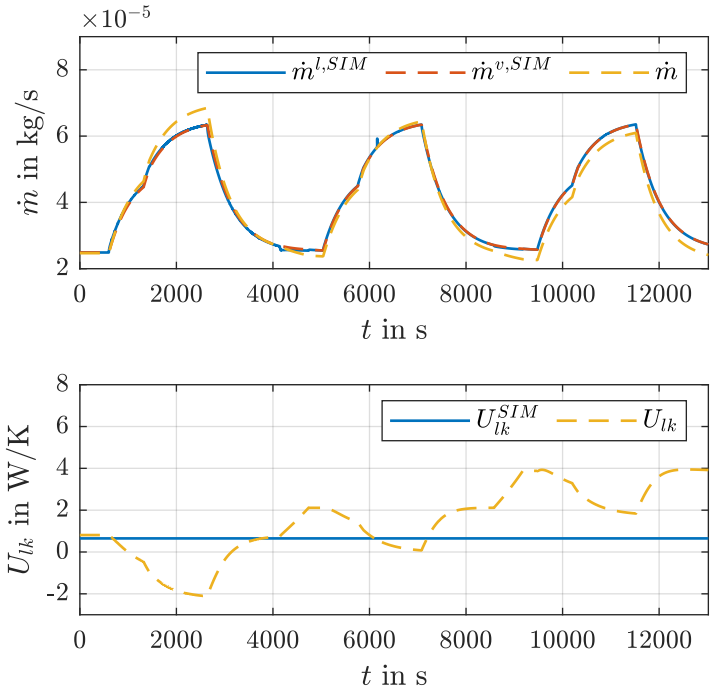

Figure 7.36: Comparison of the identified model parameters of nMIAC/S with the corresponding parameters of SIM

The simulated mass flow rates $\dot{m}^{l,SIM}$ and $\dot{m}^{v,SIM}$ show a similar behavior confirming the remarks in Assumption 5.1. Thus, a single mass flow rate $\dot{m}$ is sufficient to approximate the LHP fluid dynamics in Model S closely. Due to the online identification of $\dot{m}$ in dependence on the heat load $\dot{Q}_{ev}$, the variation of the mass flow rate can be considered in the state prediction based on Model S. Besides the mass flow rate, the CC dynamics are influenced by the heat leak between the CC and the evaporator as part of the heat load. Furthermore, the temperature of the liquid entering the CC is governed by the other disturbance, the sink temperature T_{sk}. By identifying the thermal conductance U_{lk} in nMIAC/S, the adaption of the temperature difference between T_{cc} and T_{ev} to the changing operating conditions including the variation of both disturbances is considered. The energy balance in the CC is set by adapting the heat leak from the evaporator through U_{lk} to the incoming liquid flow from the condenser subsystem at T_{co}. In comparison to the fixed U_{lk}^{SIM} of SIM, where the heat leak is fitted to experimental data in dependence on the disturbances, the identified U_{lk} changes over time but within a reasonable order of magnitude close to the constant U_{lk}^{SIM}. Thus, the deviation between both U_{lk} is caused by the adaption of the CC energy balance to the measured temperatures besides the adaption to the varying disturbances. In summary, the performance of nMIAC/S is very satisfactory due to the adaption of the controlled CC dynamics based on the parameter identification.

The reason for the spikes of T_{cc} in Fig. 7.33 and 7.35 at approximately $t = 6100\,\mathrm{s}$ can be explained using Fig. 7.36. A spike is also visible in $\dot{m}^{l,SIM}$ at the same time which is traced

back to numerical inaccuracies in the balancing solution method of the numerical LHP simulation SIM for the mass flow rates $\dot{m}^{l,SIM}$ and $\dot{m}^{v,SIM}$. This numerical inaccuracy of the mass flow rates reproduces in the simulated temperature T_{cc} and thus is not related to the action of the controller.

The combined state and parameter estimation of nSF/C is based on an SRUKF for the states T_{cc}, $L_{2\phi}$, and $\dot{m}^l$ as well as an SRUKF for the parameter R_{sh}, which include the influences of the disturbances on the LHP dynamics through the complex equations of Model C. Due to the considered phase transition in the condenser, an adaption of the CC energy balance is not necessary compared to the nMIAC algorithm. The results of the combined state and parameter estimation of the nSF/C in the closed control loop are depicted in Fig. 7.37.

In the third row, the estimated liquid mass flow rate $\dot{m}^l$ follows the simulated $\dot{m}^l$ of SIM closely. Despite the different modeling approaches of the mass flow in Model C and SIM, a high agreement is achieved. Another good result is obtained for the length $L_{2\phi}$ of the two-phase condenser region. While a high agreement is present at the lower sink temperatures, the already mentioned deviation at high sink temperatures due to the fixed OP parameters is also the reason for a slightly higher deviation in $L_{2\phi}$. The biggest deviation, however, is visible in the controlled CC temperature T_{cc}. Compared to the estimated T_{cc}, a small deviation of less than $0.55\,\mathrm{K}$ remains because of the discrepancy between the reached temperature equilibria for the same value of the input variable $\dot{Q}_{cc}$ (see Sec. 7.2.1). The integrated parameter estimation with another SRUKF contributes to the decrease of this discrepancy besides an improved general estimation of the states. As depicted in the fourth row of Fig. 7.37, the agreement between the estimated R_{sh} and the equivalent resistance of SIM is high. Thus, the influence of the flow dynamics in the evaporator on the states under varying operating conditions are correctly reproduced.

With regard to the CC temperature control in Fig. 7.12, the PI controller of nSF/C takes over the adjustment of the controller output subject to the state deviations in comparison with the adaptive function of nMIAC/S. By using the measured T_{cc} instead of the estimated T_{cc} inside the nSF/C, its disturbance rejection is further improved due to the relief of the PI controller.

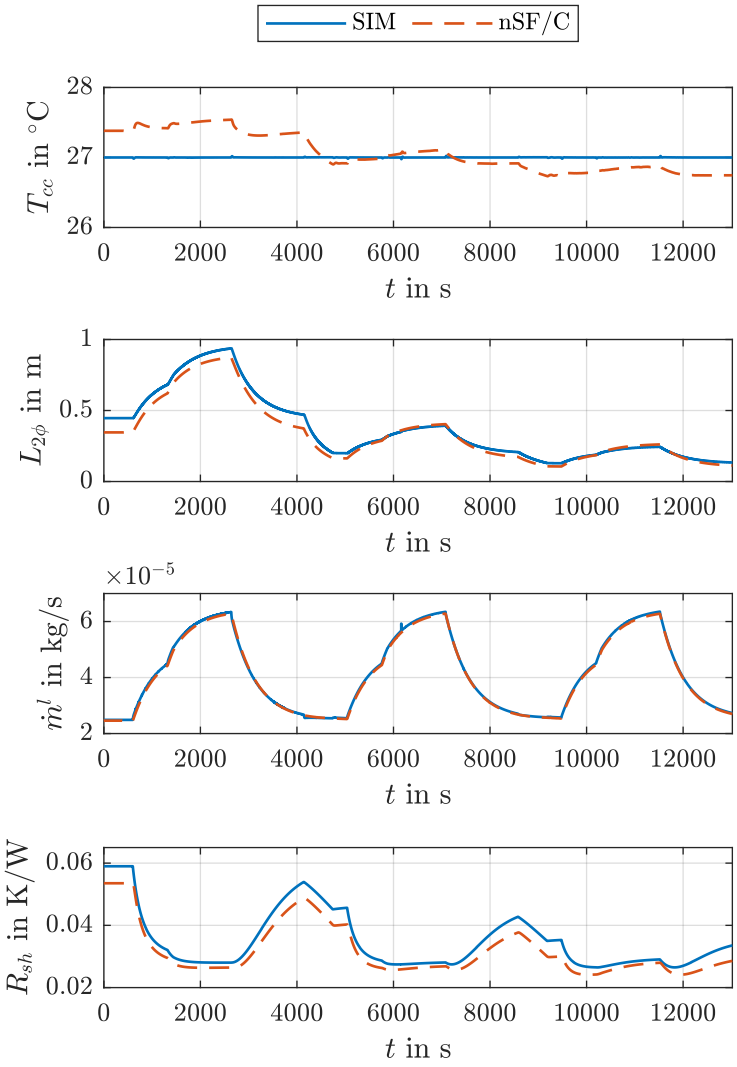

Figure 7.37: Comparison of the estimated variables of nSF/C with the corresponding variables of SIM

Evaporator Control

With the benchmark profile in Fig. 7.32, the evaporator controllers based on a cascade control are evaluated next. The results of the controllers in SIM are presented in Fig. 7.38.

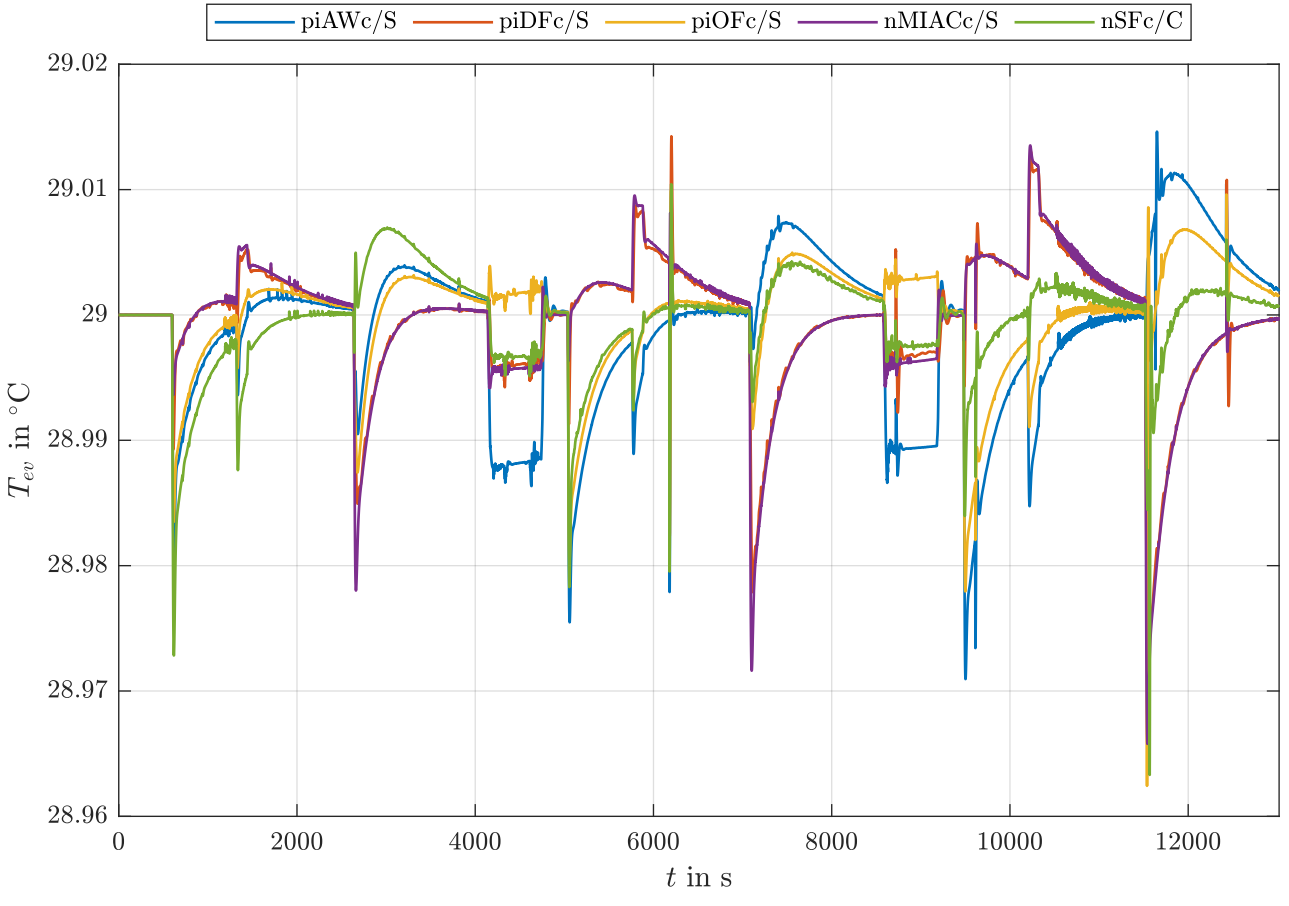

Figure 7.38: Disturbance behavior of the proposed evaporator controllers with respect to the benchmark profile in Fig. 7.32

All introduced evaporator controllers show a good disturbance rejection considering the small y-axis range of $0.06\,\mathrm{K}$. Although the controlled T_{ev} of nSFc/C shows the largest deviation from the setpoint temperature $T_{set,ev}$ at the highest sink temperature T_{sk}, the performance of nSFc/C improves with falling T_{sk} resulting in a decreasing control error. The larger control error of nSFc/C at higher T_{sk} is related to the fact that Model C with fixed model parameters yields the largest model error compared to SIM at these operating conditions due to unconsidered changing heat transfer processes and fluid kinematics. In contrast to nSFc/C, the other cascade controllers based on Model S show increasing over- and undershoots with decreasing T_{sk}. It is noticeable that piDFc/S and nMIACc/S show a similar curve of the controlled evaporator temperature T_{ev} because of their good CC control characteristics in the inner control loop. Thus, the setpoint temperature T_{set} dictated by the outer control loop is closely realized by both controllers. In contrast, piAWc/S and piOFc/S have the worst performance under disturbance variation since they do not consider the disturbances explicitly in their control law.

The quantitative analysis of the performance of the evaporator controllers is performed with the metrics in Table 7.14.

Controller	**MAD** in K	**RMSE** in K	**Required temperature sensors**	**Required disturbances**
piAWc/S	0.0291	0.00640	T_{cc}, T_{ev}	-
piDFc/S	0.0291	0.00498	T_{cc}, T_{ev}	$\dot{Q}_{ev}, T_{sk}$
piOFc/S	0.0376	0.00415	$T_{cc}, T_{ev}, T_{co,o}$	-
nMIACc/S	0.0342	0.00537	T_{cc}, T_{ev}	$\dot{Q}_{ev}, T_{sk}$
nSFc/C	0.0367	0.00392	T_{cc}, T_{ev}	$\dot{Q}_{ev}, T_{sk}$

Table 7.14: Evaluation of the proposed evaporator controllers based on Model S and Model C

Once again, the cascade control piAWc/S with the state-of-the-art PI controllers achieves the worst overall performance based on the RMSE. For changes of both the heat sink and the heat source, the control error of piAWc/S is the largest. However, its MAD is slightly smaller than the MAD of the other controllers due to a better reaction to the dropping dissipated heat of the heat source after every operating cycle (see Fig. 7.32). The best overall result based on the RMSE is achieved by nSFc/C due to the exact state and parameter estimation based on Model C.

7.4.2 Compensation of Temperature Oscillations

In this section, the behavior of the introduced controllers for a single LHP with a relevant thermal mass at the evaporator is investigated. Furthermore, the controller performances for a stable and for an unstable thermal mass setting are compared and evaluated.

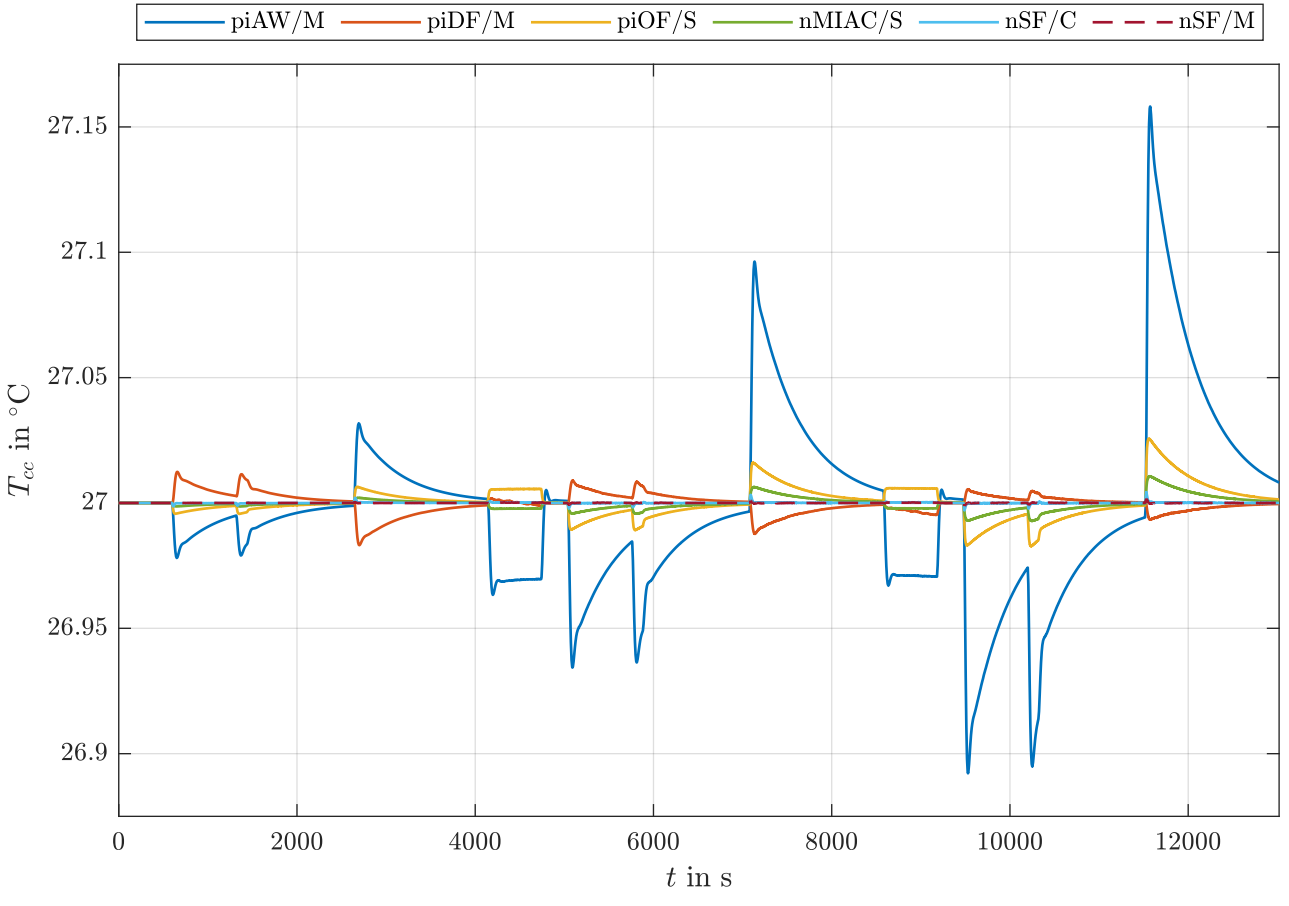

Figure 7.39: Disturbance behavior of the proposed controllers for a single LHP with $C_{ev,sf} = 40\,\mathrm{J\,K^{-1}}$ with respect to the benchmark profile in Fig. 7.32

As elucidated in Sec. 7.2.5, the oscillatory behavior of a single LHP depends on the size of the attached thermal mass at the evaporator. At a thermal mass of $C_{ev,sf} = 40\,\mathrm{J\,K^{-1}}$, the behavior of Model C and Model M is similar and stable. Thus, all introduced controllers, namely piAW/M, piDF/M, piOF/S, nMIAC/S, nSF/C, and nSF/M, are able to stabilize the CC temperature T_{cc} and keep the desired setpoint temperature T_{set} as depicted in Fig. 7.39.

The largest deviations from T_{set} occur for piAW/M while the smallest control errors are achieved by the nonlinear PI state feedback controllers nSF/C and nSF/M. Both controllers benefit from the good agreement between Model C and Model M for the exact input-output linearization.

With increasing thermal mass, the LHP temperatures start to oscillate until the stability limit is reached according to (7.16). As simulations of the proposed control approaches show, not all of the controllers are able to stabilize T_{cc} and compensate for the temperature oscillations despite their adaption to the increasing thermal mass. With decreasing sink temperature T_{sk}, the amplitudes of the oscillations increase until the control loops become unstable. Furthermore, the stability limit is reached with piAW/M, piDF/M, and nSF/C for lower $C_{ev,sf}$ than with piOF/S. Only nMIAC/S and nSF/M enable a stable temperature control due to their accurate adaption to the disturbance impacts. The successful performances of both controllers at $C_{ev,sf} = 280\,\mathrm{J\,K^{-1}}$ above the calculated stability limit of Model M is presented in Fig. 7.40.

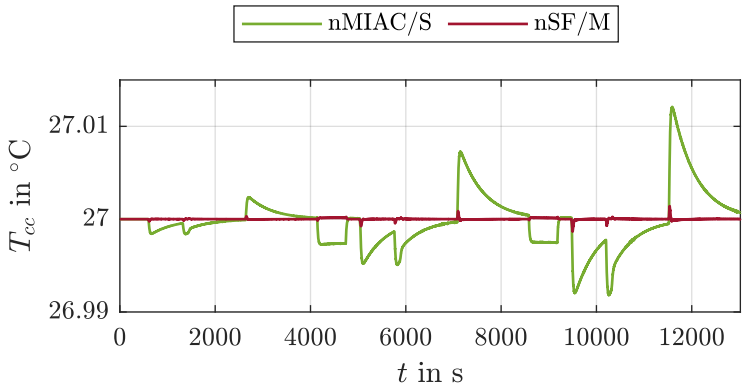

Figure 7.40: Disturbance behavior of the oscillation-compensating CC controllers for a single LHP with $C_{ev,sf} = 280\,\mathrm{J\,K^{-1}}$ with respect to the benchmark profile in Fig. 7.32

For a stable state estimation of nSF/M with an SRUKF based on Model M, the sampling time must be reduced to $T_{st} = 0.1\,\mathrm{s}$ in the simulations compared to the SRUKF based on Model C with $T_{st} = 1\,\mathrm{s}$. This leads to a slightly increased computational time but is still within the requirements of the LHP control cycle. However, without considering the thermal mass in the nonlinear PI state feedback control, as it is the case with nSF/C based on Model C, a stable temperature control without oscillations cannot be achieved. While nMIAC/S achieves the desired compensating performance due to its parameter identification, although it is based on Model S, nSF/M rebuilds the modulation of the net heat load physically with the attached

thermal network of the evaporator. Thus, the disturbance rejection of nSF/M yields clearly smaller over- and undershoots compared to nMIAC/S in Fig. 7.40.

The same stability results as before with the CC controllers apply to the evaporator controllers of a single LHP with attached thermal mass. Thus, only the respective cascade controllers based on nMIAC/S and nSF/M are able to compensate the temperature oscillations. The performance of nSFc/M is verified as well in simulations and compared to nMIACc/S. Both controllers are parameterized based on Model M as given in Table 7.9. The results of the simulations are presented in Fig. 7.41.

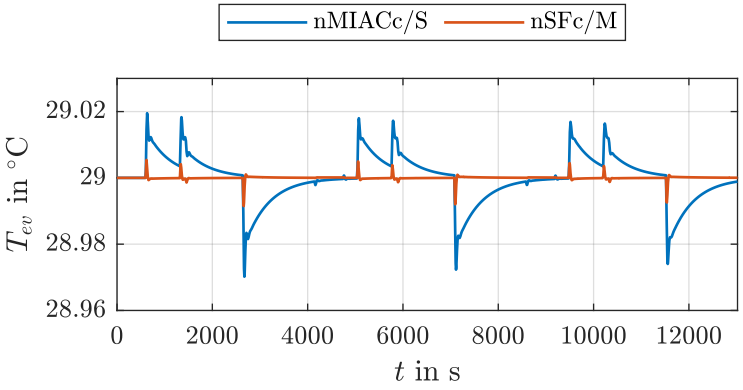

Figure 7.41: Disturbance behavior of the oscillation-compensating evaporator controllers for a single LHP with $C_{ev,sf} = 280\,\mathrm{J\,K^{-1}}$ with respect to the benchmark profile in Fig. 7.32

Over the operating range of the LHP, both controllers nMIACc/S and nSFc/M keep the controlled evaporator temperature T_{ev} in a narrow corridor around the setpoint temperature $T_{set,ev}$. Although both controllers are based on different evaporator models within Model S and Model M, a stable control loop is achieved in both cases due to the parameter adaption and the physical foundation, respectively.

7.4.3 Temperature Control of Parallel Loop Heat Pipes

For the verification of the performances of piAW/P and nSF/P, the test profile in Fig. 7.42 is used. The test profile considers the increased heat transport capability of the parallel LHPs by means of an increased dissipated heat of the heat source compared to Fig. 7.32.

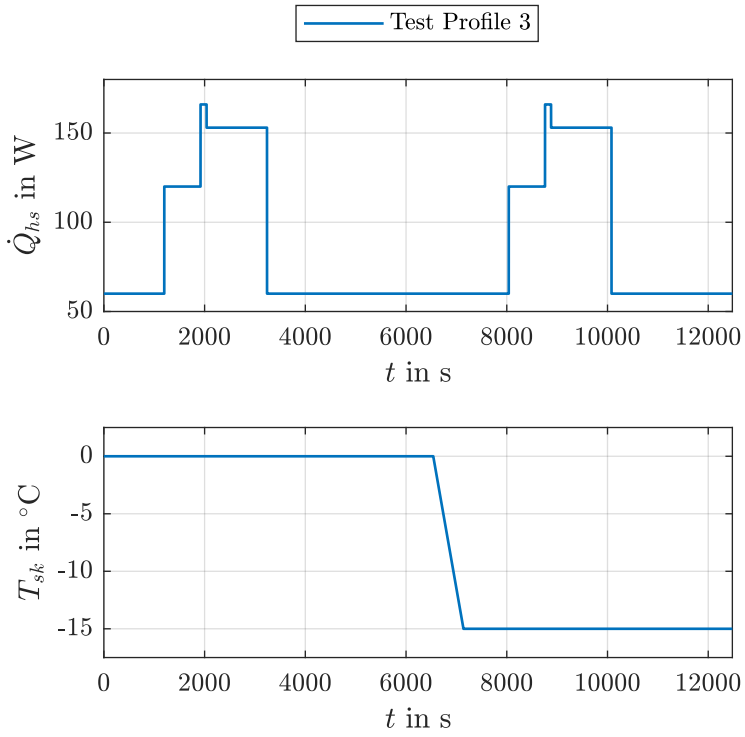

Figure 7.42: Test Profile 3 with variations in the disturbances across the operating range of LHP 3

The corresponding comparison of the performances of both controllers is depicted in Fig. 7.43. To set the focus on the controllers, the state input of nSF/P is connected with the state feedback of the system. For the realization of nSF/P, the state estimation based on the SRUKF in Sec. 4.2.3 for a single LHP can be extended accordingly.

The controlled CC temperatures T_{cc}^{a} and T_{cc}^{b} of both LHPs are given in the first and the second row of Fig. 7.43, respectively. Both controllers stabilize the system and keep T_{cc}^{a} and T_{cc}^{b} near the setpoint temperature T_{set}. A smaller deviation from T_{set} is achieved by the introduced nSF/P compared to the state-of-the-art PI controllers of piAW/P. During the sink temperature change, a larger deviation between T_{set} and T_{cc} results for piAW/P than for nSF/P. The deviations caused by heat load changes turn out to be smaller than in the case of a single LHP due to the low disturbance dynamics based on the increased delay of the thermal mass of the LCT dummy (cf. Table 7.1). As a consequence of the same parameterization of the controllers for LHP a and LHP b, the heat transport performance of both LHPs is comparable and thus leads to similar T_{cc} curves during the modeled balanced heat distribution.

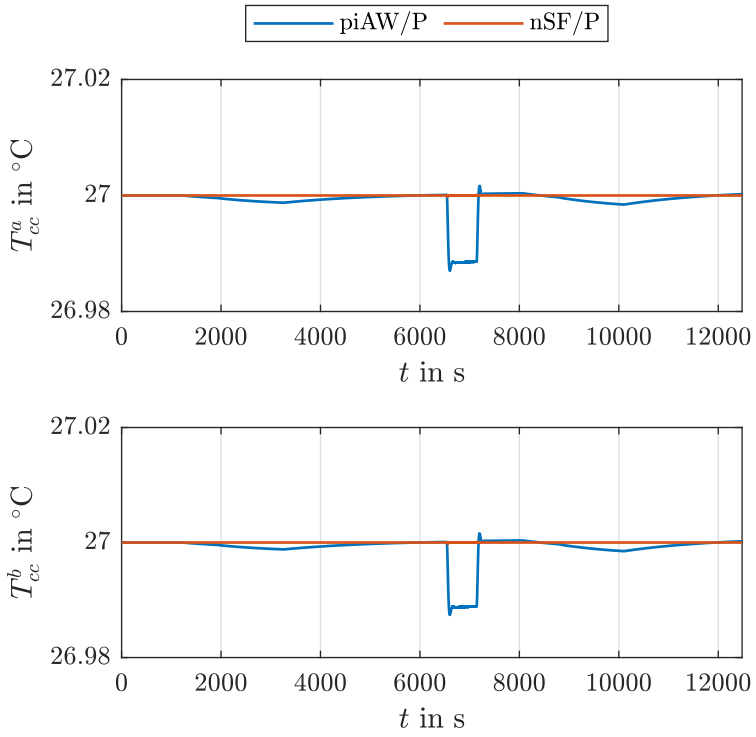

Figure 7.43: Disturbance behavior of the proposed CC controllers for parallel LHPs based on Test Profile 3 in Fig. 7.42

7.4.4 Numerical Stability Analysis of the Control Loops Based on the Complex Model

In this section, the numerical results of the stability analysis of the control loops with the controllers based on the complex models, i.e. nSF/C, nSF/M, and nSF/P, are presented. While the other proposed controllers based on Model S are stable due to their individual control designs and parameterizations, the stability of the internal dynamics of Model C, Model M, and Model P must be evaluated specifically according to Sec. 4.2.1, 6.2.1 and 6.2.2, respectively.

Model C

For the stability of the zero dynamics of Model C in dependence on the OP, its Jacobian (4.114) is evaluated according to Theorem 4.1. In order to consider the multiple equilibrium points of the LHP, (4.114) is analyzed for a number of sample OPs which are determined at equilibrium over the entire operating range. Furthermore, the external state variable x_{ex}^{op} is fixed in the setpoint temperature T_{set} according to (7.17) in order to calculate the different internal state vectors $\boldsymbol{x}_{in}^{op}$ in the balanced OP in dependence on the varying disturbance vector $\boldsymbol{d}^{op}$. The numerical solution of the stationary state equations (7.2) to (7.4) with the model parameters of

SIM in Table 7.2 is obtained by minimizing the squared sum of the equations for $\boldsymbol{x}_{in}^{op}$ and the input variable u^{op} with the direct search method applied in Sec. 5.2.4. For the analysis of the eigenvalues of the resulting Jacobians, the Hurwitz criterion in Appendix A.2 is applied which refers to the characteristic polynomial of a Jacobian. Since the first condition in Theorem A.1 is a necessary and sufficient condition for the second-order characteristic polynomial (4.115), the corresponding coefficients γ_0 and γ_1 must be positive for stable eigenvalues and thus stable OPs of the zero dynamics. The calculated coefficients in dependence on the determined OPs are depicted in Fig. 7.44 as surface plots above $\boldsymbol{d}^{op}$.

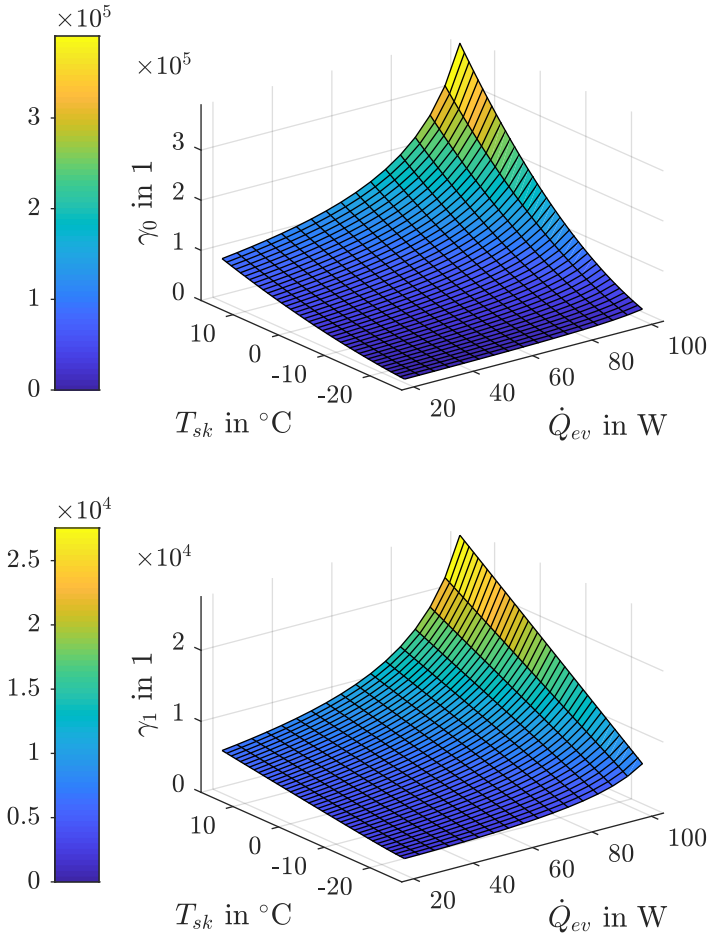

Figure 7.44: Surface plots of the coefficients γ_0 and γ_1 of the characteristic polynomial (4.115) of the zero dynamics of Model C in different OPs within the LHP operating range at $x_{ex}^{op} = T_{set}$

The slopes of the surfaces in Fig. 7.44 deliver insight into the dynamics of a controlled LHP. The highest values of the coefficients are reached for the highest heat load $\dot{Q}_{ev}$ and the highest sink

temperature T_{sk}. With falling $\dot{Q}_{ev}$ as well as falling T_{sk}, the values of the coefficients decrease. As coefficients of the characteristic polynomial of the zero dynamics, the absolute values of the eigenvalues become smaller as the coefficients decrease. Hence, the zero dynamics become slower. Transferred to the overall dynamics of the LHP, the lower both disturbances the slower the system reacts to input changes. This explains the decreasing performance of the controllers with falling T_{sk} resulting in increasing over- and undershoots, e.g. from the left to the right of Fig. 7.33.

Considering the exponents of the z-axes in Fig. 7.44, both surfaces are situated above zero and do not cross the xy-plane. Therefore, the coefficients γ_0 and γ_1 in (4.115) are positive over the LHP operating range. This means that the eigenvalues of the Jacobian (4.114) are negative, and thus, the OPs of the zero dynamics of Model C are locally exponentially stable according to Theorems 4.1 and A.1, i.e. nSF/C stabilizes Model C over the entire operating range.

Model M

Due to the extension of the state vector $\boldsymbol{x}$ of Model M in (6.27) by $T_{ev,sf}$ compared to Model C, the Jacobian of the zero dynamics of Model M in Theorem 4.1 is four-dimensional. Hence, the corresponding characteristic polynomial is three-dimensional, and both the coefficients γ_0 to γ_2, since $\gamma_3 = 1$, and the minors M_1 to M_3 has to be evaluated according to the previously described procedure. The resulting surface plots of the calculated coefficients and minors are presented for $C_{ev,sf} = 280\,\mathrm{J\,K^{-1}}$ in Fig. 7.45 and 7.46.

As depicted in both figures, the slopes of the surfaces are similar to the ones in Fig. 7.44, since the fundamental behavior of Model C and Model M is similar as well. They also explain the varying controller performances in Fig. 7.39 as mentioned before. All surfaces are fully situated again above zero, and the coefficients and minors are positive. Hence, the OPs of the zero dynamics of Model M are locally exponentially stable according to Theorems 4.1 and A.1, i.e. nSF/M stabilizes Model M over the entire operating range of the running LHP.

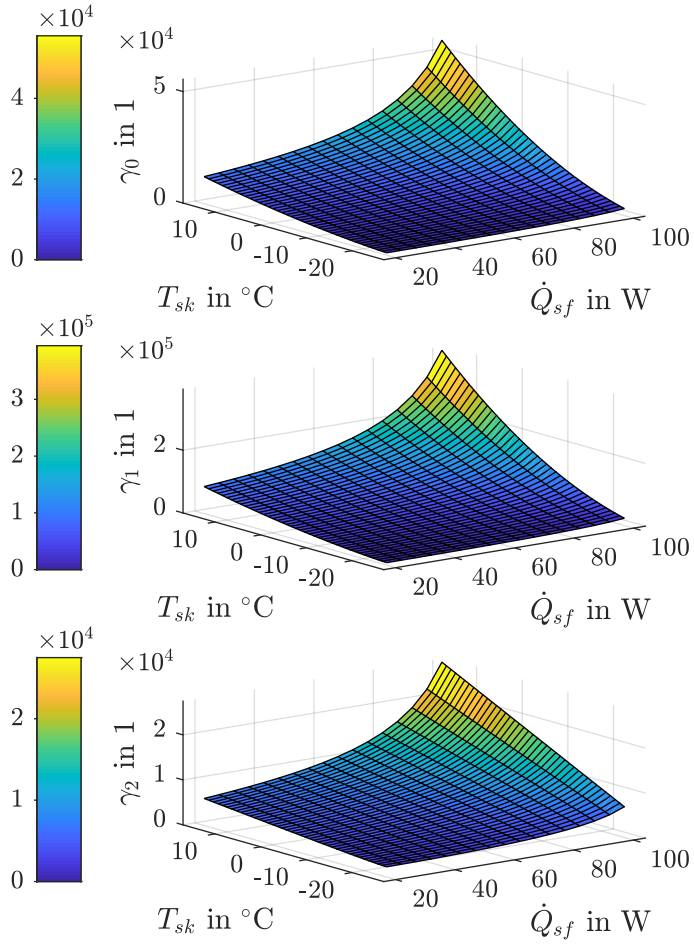

Figure 7.45: Surface plots of the coefficients γ_0, γ_1, γ_2 of the characteristic polynomial of the zero dynamics of Model M in different OPs within the LHP operating range at $x_{ex}^{op} = T_{set}$

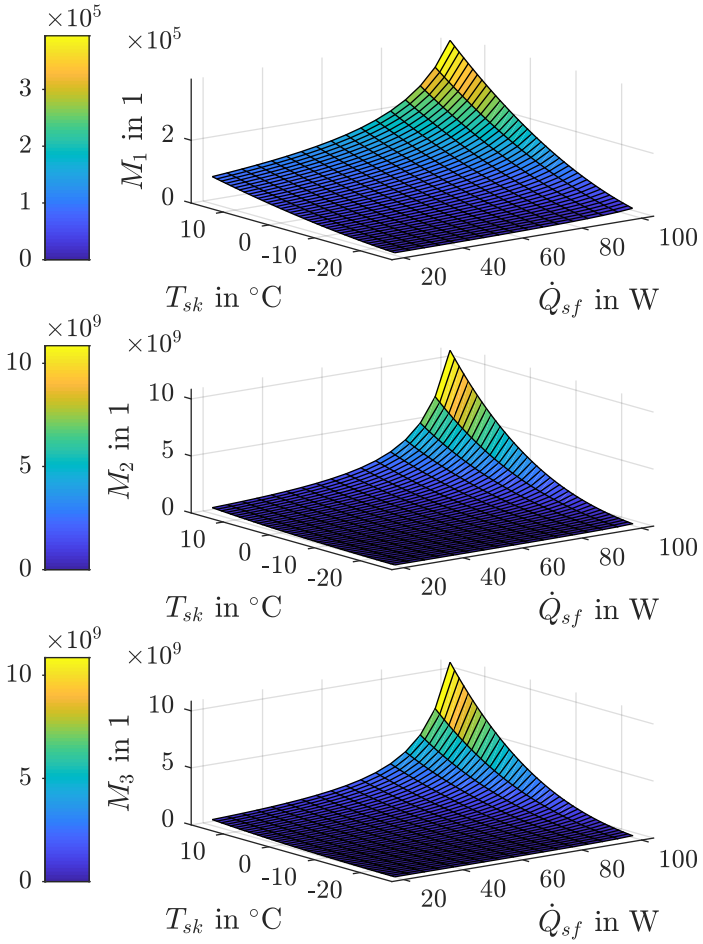

Figure 7.46: Surface plots of the minors M_1, M_2, and M_3 of the characteristic polynomial of the zero dynamics of Model M in different OPs within the LHP operating range at $x_{ex}^{op} = T_{set}$

Model P

The stability of the OP of the zero dynamics of Model P in dependence on the disturbances further increases the complexity of the calculation according to the previous procedure due to the increased dimension of thirteen of the state vector (6.39). While the operating range with the respect to the heat sink stays the same, the range of the dissipated heat of the heat source increases due to the double heat transfer by the parallel LHPs. Thus, $\dot{Q}_{hs}$ ranges from $40\,\mathrm{W}$ to $200\,\mathrm{W}$. Because of the resulting high number of coefficients and minors and the connected high values, the illustration of all corresponding surface plots is omitted here. Instead, the minima of both are listed in the following, whereby the inequalities of Theorem A.1 can be verified:

$$
\begin{aligned}
\min(\gamma_0) &= 2.1, & \min(M_1) &= 1.1 \cdot 10^{4},\\
\min(\gamma_1) &= 1.1 \cdot 10^{4}, & \min(M_2) &= 3.9 \cdot 10^{9},\\
\min(\gamma_2) &= 3.6 \cdot 10^{5}, & \min(M_3) &= 1.5 \cdot 10^{16},\\
\min(\gamma_3) &= 4.9 \cdot 10^{6}, & \min(M_4) &= 3.4 \cdot 10^{23},\\
\min(\gamma_4) &= 3.2 \cdot 10^{7}, & \min(M_5) &= 2.6 \cdot 10^{31},\\
\min(\gamma_5) &= 1.1 \cdot 10^{8}, & \min(M_6) &= 3.1 \cdot 10^{39},\\
\min(\gamma_6) &= 1.6 \cdot 10^{8}, & \min(M_7) &= 2.7 \cdot 10^{47},\\
\min(\gamma_7) &= 1.0 \cdot 10^{8}, & \min(M_8) &= 4.5 \cdot 10^{54},\\
\min(\gamma_8) &= 1.9 \cdot 10^{7}, & \min(M_9) &= 4.8 \cdot 10^{60},\\
\min(\gamma_9) &= 1.1 \cdot 10^{6}, & \min(M_{10}) &= 9.7 \cdot 10^{63},\\
\min(\gamma_{10}) &= 2.0 \cdot 10^{3}, & \min(M_{11}) &= 9.7 \cdot 10^{63},\\
\min(\gamma_{11}) &= 1.0.
\end{aligned}
$$

Since the listed minima of the coefficients and minors are positive, all their values are positive. Thus, the OPs of the zero dynamics of Model P are locally exponentially stable according to Theorems 4.1 and A.1, i.e. nSF/P stabilizes Model P over the entire operating range of the running LHP.

7.5 Discussion

In order to discuss the performance of the models and corresponding controllers in the previous validation, the differences as well as their advantages and disadvantages are highlighted in this section. Finally, answers to the initial research questions in Sec. 2.5 are found based on the discussion.

The benefit of a complex model with and without additional thermal mass and its impact on the corresponding controller performance has been clearly shown in the previous sections.

Combining the mass flow dynamics with the thermodynamics of an LHP enables the complex state-space modeling of a correct disturbance behavior of the measured temperatures on a physical basis. The corresponding nonlinear PI state feedback control law is thus able to consider these influences during the control of the CC or evaporator temperature. By simplifying the state-space model around an OP, the linear and nonlinear controllers based on this model are restricted to that OP and their performances vary in other equilibrium points over the entire operating range. Nevertheless, the adaption of the relevant model parameters in the nonlinear state feedback controller of nMIAC related to the mass flows and the heat leak let it reach almost the same performance as being based on the complex model. Thus, both the nMIAC and the nonlinear PI SF are able to compensate oscillations and achieve the best disturbance rejection as verified in Sec. 7.4.2.

For the review of the proposed controllers for a single LHP, the different controller types are assessed qualitatively with respect to five categories. These categories include the implementation effort concerning the complexity of the respective algorithms, the general performance of the controllers based on the relevant disturbance rejection, the computational effort for the target processor dependent on the computational time of the implemented controllers in Table 7.13, the ability to compensate temperature oscillations due to an attached thermal mass (see Sec. 7.4.2), and the number of required sensors of each controller regarding the effort and costs of the application. The grading distinguishes between four grades: ++, +, -, --. These symbols correspond to the rating of each category between low and high or bad and good, respectively. The results of the assessment are recorded in Table 7.15.

Controller type	**Implementation effort**	**Disturbance rejection**	**Computational effort**	**Oscillation compensation**	**Sensor requirement**
PI controller with AW strategy	++	--	++	--	++
PI controller with DF	-	+	+	--	-
PI OF	+	+	++	--	+
nMIAC	--	++	-	++	--
nonlinear PI SF	--	++	--	++	-

Table 7.15: Evaluation table of the introduced controller types for a single LHP

The grades in this evaluation table are the results of the analysis in the previous sections in this chapter. The table facilitates the choice of the correct controller for the specific application by an LHP end user being a tradeoff between the desired performance and hardware requirements. While the PI controller, as commonly used in the literature, has an advantage over the more complex controllers regarding their implementation and computational efforts as well as their sensor requirements, an improved disturbance rejection and oscillation compensation comes along with a higher degree of complexity. A better disturbance rejection of the PI controller with DF is outweighed by a worsening in all other categories. In contrast, the PI OF achieves

this advantage at a similar computational effort with a better sensor requirement since it does not need knowledge about the disturbances. The good performance of the PI controller with DF, however, is based on the good agreement between the stationary and the transient model of SIM. On the test bench, a higher mismatch between model and reality may be expected, as a lower benefit compared to the PI controller appears in the test bench results presented in [GMK+18]. The best performances are achieved by the nMIAC and the nonlinear PI SF. For such a performance, the nMIAC needs one more temperature sensor than the nonlinear PI SF for the CC temperature control. However, the computational effort is higher for the nonlinear PI SF due to the more elaborate state estimation. In contrast to the other controllers, their implementation efforts are clearly increased due to the integrated optimization method and unscented Kalman filter, respectively.

The parallel LHPs are modeled by connecting their evaporators via the thermal network of the supporting structure with a single heat source. The investigated $\dot{Q}_{cc}$ step responses are closely reproduced by the introduced model. However, the sensibility of such a system with respect to its stability can already be experienced when determining the equilibrium states for the parameterization and numerical stability analysis as well as in the subsequent simulation. Minor changes to the model parameters may already result in infinite solutions. Furthermore, an imbalance between LHP a and LHP b due to the supposed heat distribution promote unstable temperature curves. The impact of the evaporator masses on the stability of the system cannot be verified. Instead, a reconstruction of the heat flow paths with a more detailed thermal network could clarify the situation of the imbalance, which is an application-specific challenge to the LHP end user. For now, the proposed MIMO controller shows the potential of model-based designed advanced controllers for the improved performance of heat transport systems with multiple LHPs.

Following the initial research questions in Sec. 2.5, an answer to each question can now be found:

1. According to the comprehensive validation of each proposed controller, the best performance for a single LHP is achieved by a nonlinear state feedback controller extended by a PI controller based on a complex LHP model.

2. An essential insight into the overall dynamic behavior of an LHP is gained through the combined detailed modeling of the heat transfer and the fluid flow. Only this combination enables the modeling of variations of the disturbances whereby a correct reproduction of the states over the entire operating range becomes possible. A model-based control design of linear controllers is already successful by concentrating on the temperature dynamics of an LHP alone. However, the corresponding optimization-based adaption of relevant model parameters improves the performance of a temperature-based adaptive controller significantly.

3. The extension of a single LHP with an arbitrary thermal network in state-space form for the modeling of advanced LHP-based heat transport systems provides the LHP end user with further possibilities to model individual future LHP-based heat transport systems. Especially the explicit consideration of a variable thermal mass at the evaporator makes it possible to simulate and investigate the temperature oscillations during the continuous LHP operation. The simulation of such temperature oscillation makes it possible to

test the compensation ability of LHP controllers besides their disturbance rejection. As it has been shown in this chapter, the model extension can be transferred to the subsequent model-based control design smoothly.

4. In the end, two proposed controllers have been identified which are able to compensate the temperature oscillations in contrast to the state-of-the-art PI controller. Besides the aforementioned nonlinear state feedback controller based on the extended accurate Model M, the unstable LHP system can be controlled by the adaptive controller based on the simplified Model S, which both enable the smooth control of the CC and evaporator temperature.

7.6 Conclusion

This chapter has delivered the evaluation of the introduced state-space models and the proposed linear and nonlinear controllers. The dynamical models have been thoroughly validated with measurements from two different single LHPs on a test bench and a numerical LHP simulation confirming the validity and the transferability of the introduced models. The controllers have proven their stable performance and improved disturbance rejection compared to the state-of-the-art controller, and their advantages and disadvantages have been listed. The choice of the correct controller for the specific application is finally a tradeoff between performance and hardware requirement.

The investigation of the $\dot{Q}_{cc}$ step responses has shown the weaknesses of Model S compared to Model C and Model M. However, Model S has achieved a good model accuracy in certain operating areas sufficiently representing the dynamics of relevant temperatures of an LHP for a subsequent model-based design of simple controllers with low processor requirements as preferred in aerospace systems.

The strongest disturbance rejection of a Model S-based controller is achieved by the proposed nMIAC that adapts the disturbance-related model parameters to the mass and fluid dynamics through the model identification adaptive structure. In contrast, the physical modeling of the disturbance behavior with Model C and Model M, mainly based on incorporating the relevant mass flow dynamics and phase transitions, has enabled a precise reproduction of the LHP temperatures subject to disturbance changes. The corresponding model-based designed controllers have gained even further performance advantages compared to the state-of-the-art controllers.

The correct agreement between Model P and the parallel LHPs of the heat transport system of an LCT has been validated with measured data of another test bench. For a balanced heat distribution, Model P with its simplified thermal network representation of an LCT models the advanced LHP-based heat transport system precisely as it has been shown by the comparison of the control heater steps. Accordingly, the corresponding MIMO controller has shown an improved performance compared to the separate PI controllers of the state of the art.

In the case of parallel LHPs, these temperature oscillations, however, have not been reproducible with Model P. Instead, temperature oscillations during the normal LHP operation of

parallel LHPs are more likely to be caused by the individual heat distribution of the connecting thermal mass of the heat source and not by the specific LHP designs.

Besides the desired model-based control designs, the simulation of the LHP behavior with an attached thermal mass and its impact on the LHP dynamics is now possible with Model M. Thus, the theoretical arguments in [HB12] have been reproduced in simulations for the first time. Furthermore, the simulations have confirmed the cause for temperature oscillations during the normal operation of an LHP when a significant evaporator mass is present. Thus, a quantitative answer to the question when a running LHP starts to oscillate is possible. As previously shown, these temperature oscillations are compensable by two of the proposed controllers in contrast to the common state-of-the-art PI controller.

8 Conclusions

The increasing number of temperature-sensitive electronic components in aerospace and terrestrial systems comes along with a need for more effective thermal control systems. LHPs as passive, two-phase heat transport systems are in the focus of the industry for the construction of successful thermal management systems. In addition to ensuring the multiphase heat transfer from the heat source to the heat sink, adequate control methods and algorithms are necessary to keep the cooled objects at optimal operating conditions. Control heaters provide a potent solution with a low risk of failure for the operating temperature (OT) control of LHPs. So far, simple controllers with a heuristic parameterization are commonly used in the literature to control the heater output showing moderate performances with a high design effort at the same time. For a structural approach to the design of control algorithms with improved performance for the control heaters of current and future LHP-based systems, a model-based control design is pursued in this thesis for the first time.

The first complex dynamical model of a conventional LHP is based on a system of differential equations in the desired state-space form. The decomposition of the multiphase system is chosen according to its components. It simplifies the derivation of the required energy balance equations from the respective conservation laws to form the final three-dimensional state-space model with lumped parameters. A major emphasis is set on integrating the mass flow dynamics into the model. The mass flows are connected to the phase transition in the two-phase regions of the LHP and govern the disturbance behavior of the LHP. The resulting nonlinear model is able to reproduce the measured temperatures of an LHP subject to changes in the operating conditions. For the corresponding nonlinear model-based control design, a PI state feedback controller is designed based on the exact input-output linearization that fits to the present model structure. The classical approach to govern the OT is the control of the compensation chamber (CC) temperature. Owing to the complex model, a corresponding cascade control design is now possible to achieve smoother temperature curves of the cooled object. This is achieved by keeping the evaporator temperature, i.e. the temperature closest to the object, near its constant setpoint temperature. The required feedback of the unmeasured states in both controllers is provided by a nonlinear state estimation with a square-root unscented Kalman filter (SRUKF).

Based on the detailed investigation of a single LHP with the complex state-space model, the model-based control design approach is extended to advanced LHP systems including LHPs with attached thermal mass and parallel LHPs. For these complex thermodynamic systems, the introduced model of a single LHP is adapted based on the thermal analogy of electrical networks. Analogously, the state feedback controllers are adjusted to the new models. Besides the consideration of extended state vectors in both cases, the MIMO form of the controller is designed to include the coupled dynamics of parallel LHPs. The modular model-based control

design approach in this thesis provides access to further investigations and improvements of advanced heat transport systems with multiple components or LHPs.

Taking into account the complexity of the previous LHP state-space model and the increased hardware requirements of the corresponding controllers, a simplified second state-space model of a conventional LHP is derived. This model includes less model parameters and fully measurable states. It enables the model-based design of various controllers that consider different LHP-specific extensions to improve the disturbance rejection. The proposed linear controllers include an additional disturbance feedforward control based on a stationary LHP model, which is commonly established for the characterization and design of LHPs. Furthermore, an output feedback control based on the fully measurable states of the linearized model is designed, accordingly. In addition to the linear controllers, a nonlinear model identification adaptive control is proposed based on the simplified model. This approach directly includes the influence of the disturbances in the controller by optimizing the related model parameters with regard to the measured temperatures. For the alternative control of the evaporator temperature, all introduced controller types are extended to cascade controllers. Thus, a range of controllers with different hardware requirements is made available for single LHPs to address the various constraints of power demand and mass in aerospace and terrestrial applications.

The practical relevance and transferability of the proposed models is verified with measurement data from different LHP designs on various test benches. The improved performance of the controllers compared to the state of the art is verified in simulations showing the tradeoff between complexity and performance. The stability of the multiple operating points (OPs) of the controlled nonlinear systems is proven numerically based on Lyapunov's indirect method. A critical stability factor of single LHPs is the attached thermal mass at the evaporator that can have a negative impact on the controller performance. The simulated temperature oscillations of single LHPs are consistent with the theoretical findings in the literature. In contrast to the state-of-the-art PI controller, two of the proposed controllers are able to compensate these oscillations and stabilize the LHP in the desired OP. The same type of oscillation cannot be reproduced in parallel LHPs. However, the heat distribution between both LHPs is more likely to cause instabilities which can only be considered by adequate measurements of the heat flows and a corresponding detailing of the thermal network of the laser communication terminal (LCT) structure.

In summary, this thesis contributes to the model-based control design for LHP-based heat transport systems. Besides the detailed consideration of single LHPs, the procedure is also adapted to the control design of parallel LHPs in advanced LHP systems. The introduced models are able to simulate the significant dynamics of an LHP. Furthermore, the proposed controllers are successfully applied in simulations showing an improved performance and accuracy. This thesis can be seen as a foundation for the dynamical modeling and model-based control design for future LHP-based heat transport systems. Its results may be a guideline to update current control parameters, improve control designs, and efficiently adapt controllers to new applications.

A Appendix

In this appendix, the physical properties of the considered working fluid inside the LHP and their mathematical approximations are stated, which are used throughout this thesis. Furthermore, the algorithms of the state and the parameter estimation based on unscented Kalman filtering are described in detail, before the implemented startup strategy of a controlled LHP is shortly presented.

A.1 Physical Properties of the Working Fluid

The working fluid of the considered LHP is ammonia. The corresponding values of the physical properties are taken from the tables in [WKSK10] with respect to the reference temperature $T_{ref} = 0\,^{\circ}\mathrm{C}$. In the following, all temperatures are expressed in $^{\circ}\mathrm{C}$.

The density ρ^l of the saturated liquid is approximated with the polynomial

$$\rho^l(T) = -4 \cdot 10^{-5} \cdot T^3 - 0.0027 \cdot T^2 - 1.3522 \cdot T + 638.57. \tag{A.1}$$

The density ρ^v of the saturated vapor is approximated with the polynomial

$$\rho^v(T) = 1 \cdot 10^{-5} \cdot T^3 - 0.0017 \cdot T^2 + 0.1229 \cdot T + 3.4553. \tag{A.2}$$

The specific heat capacities are

$$c_p^l(T) = 5 \cdot 10^{-4} \cdot T^3 + 3 \cdot T^2 + 5.6 \cdot T + 4616.5 \tag{A.3}$$

for the saturated liquid and

$$c_p^v(T) = 0.1 \cdot T^2 + 15.1 \cdot T + 2680.8 \tag{A.4}$$

for the saturated vapor.

The heat of evaporation Δh^v is given by

$$\Delta h^v(T) = -3 \cdot 10^{-2} \cdot T^3 - 11.5 \cdot T^2 - 3572.3 \cdot T + 1262300. \tag{A.5}$$

The dynamic viscosity μ^l of the liquid is approximated by the polynomial

$$\begin{aligned} \mu^l(T) = \big(&-2 \cdot 10^{-8} \cdot T^5 + 10^{-6} \cdot T^4 - 10^{-4} \cdot T^3 \\ &+ 0.0151 \cdot T^2 - 1.8665 \cdot T + 170.1\big) \cdot 10^{-6}. \end{aligned} \tag{A.6}$$

The Antoine parameters are

$$A_{wf} = 21.633, \tag{A.7}$$

$$B_{wf} = 2026.1, \tag{A.8}$$

$$C_{wf} = 235.00. \tag{A.9}$$

The surface tension σ of the saturated liquid is

$$\sigma(T) = 0.10175 \cdot \left(1 - \frac{T + 273.15}{405.50}\right)^{1.21703} \tag{A.10}$$

according to [KJS10].

A.2 Hurwitz Criterion

Theorem A.1 (Hurwitz criterion [Lun20a, p. 434])
Consider the polynomial

$$p(\lambda) = \gamma_n \cdot \lambda^n + \gamma_{n-1} \cdot \lambda^{n-1} + ... + \gamma_1 \cdot \lambda + \gamma_0. \tag{A.11}$$

All zeros of (A.11) *have a negative real part if both following conditions hold:*

1. *All coefficients γ_i are positive:*

$$\gamma_i > 0, \quad i = 0, 1, 2, ..., n. \tag{A.12}$$

2. *The n leading principal minors $\boldsymbol{M}_i$ of the $(n \times n)$-matrix*

$$\boldsymbol{H} = \begin{bmatrix} \gamma_1 & \gamma_3 & \gamma_5 & \gamma_7 & \cdots & \\ \gamma_0 & \gamma_2 & \gamma_4 & \gamma_6 & \cdots & \\ 0 & \gamma_1 & \gamma_3 & \gamma_5 & \cdots & \\ 0 & \gamma_0 & \gamma_2 & \gamma_4 & \cdots & \\ \vdots & \vdots & \vdots & \vdots & \ddots & \\ & & & & & \gamma_n \end{bmatrix} \tag{A.13}$$

are positive:

$$M_i > 0, \quad i = 1, 2, ..., n. \tag{A.14}$$

A.3 Discrete Implementation

The implementation of the continuous controllers on electronic hardware requires a discrete representation of the corresponding equations. By choosing sufficiently high sampling rates compared to the maximal frequency of the signal, both a quasi-continuous reconstruction of the controlled temperature signal and a quasi-continuous control signal are realized. According to the *Nyquist-Shannon sampling theorem*, the sampling rate must be greater than twice the maximum frequency of the signal (see [Lun20b, p. 430]). Due to the slow temperature processes of the LHP, such a realization is possible without increased hardware requirements. Thus, a simple discretization method is sufficient for the proposed control law. For the discrete representation in this thesis, Euler's backward method is used to perform the transformation between the continuous and the discrete time domain. In the case of the state feedback controllers, the structure of the differential equations of the resulting state variables can lead to increased hardware requirements based on the required state estimation, which makes it necessary to use different discretization methods (see Sec. 4.2.3).

A.4 Numerical Analysis of the Rank of the Observability Matrix

The rank of the observability matrix $\boldsymbol{Q}_{obs}$ in (4.150) is analyzed for a number of sample values for the states $T_{cc}(t)$, $L_{2\phi}(t)$, and $\dot{m}^l(t)$ as well as the inputs $\dot{Q}_{cc}(t)$, $\dot{Q}_{ev}(t)$, and $T_{sk}(t)$ distributed over the entire LHP operating range. Since $\boldsymbol{Q}_{obs}$ is a quadratic matrix, its determinant must be nonzero for $\boldsymbol{Q}_{obs}$ to be regular and thus full rank. Due to the dependence on six parameters, some example values of the calculation are given in Table A.1:

$\det(\boldsymbol{Q}_{obs})$	T_{cc} in °C	$L_{2\phi}$ in m	$\dot{m}^l$ in mg s^{-1}	$\dot{Q}_{cc}$ in W	$\dot{Q}_{ev}$ in W	T_{sk} in °C
$6.92 \cdot 10^6$	20	0.8	50	3	60	5
$1.55 \cdot 10^7$	25	1.2	50	3	60	5
$1.47 \cdot 10^7$	25	0.8	60	3	60	5
$1.51 \cdot 10^7$	25	0.8	50	4	60	5
$1.34 \cdot 10^7$	25	0.8	50	3	50	5
$2.53 \cdot 10^7$	25	0.8	50	3	60	0

Table A.1: Example values of the determinant of the observability matrix $\boldsymbol{Q}_{obs}$ in (4.150)

A.5 Square-Root Unscented Kalman Filtering

The algorithm of the square-root unscented Kalman filter (SRUKF) used in this thesis is based on [vdMW01]. The advantage of a direct time update of the matrix square root of the state covariance matrix results from the application of the *Cholesky factorization*. At the same time, this factorization guarantees the calculation of positive semidefinite state covariances in each time step for unique matrix square roots [vdMW01]. For more information about the algorithm and the underlying linear algebra techniques, the reader is referred to [vdMW01] and [vdM04].

A.5.1 State Estimation

For the discrete state estimation, a nonlinear system extended with additive process and measurement noise is considered:

$$\boldsymbol{x}(k) = \boldsymbol{F}(\boldsymbol{x}(k-1), \boldsymbol{u}(k-1)) + \boldsymbol{\nu}_{pn}(k-1), \tag{A.15a}$$

$$\boldsymbol{y}(k-1) = \boldsymbol{G}(\boldsymbol{x}(k-1), \boldsymbol{u}(k-1)) + \boldsymbol{\nu}_{mn}(k-1), \tag{A.15b}$$

with the vector functions $\boldsymbol{F}$ and $\boldsymbol{G}$ as well as the process noise $\boldsymbol{\nu}_{pn}(k)$ and the measurement noise $\boldsymbol{\nu}_{mn}(k)$ being Gaussian. The estimated state vector $\hat{\boldsymbol{x}}(k)$ is initialized by the expectation $\mathbb{E}\{\cdot\}$ of the initial state vector $\boldsymbol{x}_0$:

$$\hat{\boldsymbol{x}}_0 = \mathbb{E}\left\{\boldsymbol{x}_0\right\}. \tag{A.16}$$

Accordingly, the initialization of the Cholesky factor $\boldsymbol{S}(k)$ is done via the Cholesky factorization of the initial state covariance matrix denoted by the function chol() (see also [Mat20c, p. 1-1489]):

$$\boldsymbol{S}_0 = \text{chol}\left(\mathbb{E}\left\{(\boldsymbol{x}_0 - \hat{\boldsymbol{x}}_0) \cdot (\boldsymbol{x}_0 - \hat{\boldsymbol{x}}_0)^\top\right\}\right). \tag{A.17}$$

For the calculation of the sigma points $\mathsf{x}(k)$, the previous state estimates $\hat{\boldsymbol{x}}(k-1)$ are weighted with $\boldsymbol{S}(k-1)$:

$$\mathsf{x}(k-1) = \left[\hat{\boldsymbol{x}}(k-1) \quad \hat{\boldsymbol{x}}(k-1) + \eta_{ukf} \cdot \boldsymbol{S}(k-1) \quad \hat{\boldsymbol{x}}(k-1) - \eta_{ukf} \cdot \boldsymbol{S}(k-1)\right], \tag{A.18}$$

with the scaling parameters η_{ukf} and λ_{ukf}:

$$\eta_{ukf} = \sqrt{n + \lambda_{ukf}}, \tag{A.19}$$

$$\lambda_{ukf} = n \cdot \left(\alpha_{ukf}^2 - 1\right). \tag{A.20}$$

The spread of the sigma points (A.18) is set by the SRUKF parameter α_{ukf}, for which usually holds [vdMW01]:

$$10^{-4} \leq \alpha_{ukf} \leq 1. \tag{A.21}$$

The next step is the transformation of the sigma points $\mathsf{x}(k)$ with the nonlinear function $\boldsymbol{F}$ in (A.15a):

$$\mathsf{x}(k) = \boldsymbol{F}\left(\mathsf{x}(k-1), \boldsymbol{u}(k-1)\right). \tag{A.22}$$

By weighting the transformed $\mathsf{x}(k)$, the updated state vector $\hat{\boldsymbol{x}}^{-}(k)$ is determined:

$$\hat{\boldsymbol{x}}^{-}(k) = \sum_{i=0}^{2n} Z_i^a \cdot \mathsf{x}_i(k), \tag{A.23}$$

with Z^a being the weight of a sigma point. The first weight Z_0^a in (A.23) is given by

$$Z_0^a = \frac{\lambda_{ukf}}{n + \lambda_{ukf}}, \tag{A.24}$$

while the rest of the weights are calculated by

$$Z_i^a = \frac{1}{2\left(n + \lambda_{ukf}\right)}, \quad i = 1, ..., 2n. \tag{A.25}$$

To propagate $\boldsymbol{S}(k)$ in time, the *QR decomposition* (see also [Mat20c, p. 1-10168]) is first used to calculate the updated Cholesky factor $\boldsymbol{S}^{-}(k)$:

$$\boldsymbol{S}^{-}(k) = \mathrm{qr}\left(\left[\sqrt{Z_1^b} \cdot \left(\mathbf{x}_{1:2n}(k) - \hat{\boldsymbol{x}}^{-}(k)\right) \quad \sqrt{\boldsymbol{R}_{pn}}\right]\right), \tag{A.26}$$

with the process noise covariance matrix $\boldsymbol{R}_{pn}$ and the weights Z^b, where

$$Z_1^b = Z_1^a. \tag{A.27}$$

The compound matrix in (A.26) consists of the weighted state error of the sigma points and the matrix square root of $\boldsymbol{R}_{pn}$ [vdMW01]. Second, consecutive updates with the transition error denoted by the function cholupdate() are applied to the upper triangular part of $\boldsymbol{S}^{-}(k)$ that has the necessary square matrix form (see also [Mat20c, p. 1-1499]):

$$\boldsymbol{S}^{-}(k) = \mathrm{cholupdate}\left(\boldsymbol{S}^{-}(k), \mathsf{x}_0(k) - \hat{\boldsymbol{x}}^{-}(k), \sqrt{Z_0^b}\right), \tag{A.28}$$

with

$$Z_0^b = \frac{\lambda_{ukf}}{n + \lambda_{ukf}} + \left(1 - \alpha_{ukf}^2 + \beta_{ukf}\right). \tag{A.29}$$

The positive SRUKF parameter β_{ukf} is chosen to $\beta_{ukf} = 2$ assuming Gaussian distribution of the states $\boldsymbol{x}(k)$ [vdM04, p. 56]. Depending on the sign of Z_0^b, either an update or a downdate is performed in (A.28) with the absolute value of Z_0^b (see [QSWL18]).

For the prediction of the system's outputs, the sigma points $\mathbf{x}(k)$ are also transformed with the nonlinear function $\boldsymbol{G}$ of (A.15b) to form the sigma points $\mathbf{y}(k)$ of the output:

$$\mathbf{y}(k) = \boldsymbol{G}\left(\mathbf{x}(k-1), \boldsymbol{u}(k-1)\right). \tag{A.30}$$

Accordingly, the updated output vector $\hat{\boldsymbol{y}}^{-}(k)$ is given by

$$\hat{\boldsymbol{y}}^{-}(k) = \sum_{i=0}^{2n} Z_i^a \cdot \mathsf{y}_i(k). \tag{A.31}$$

Thus, the correction of the state estimates with the measurements follows in the filter process. Similar to (A.26) and (A.28), the Cholesky factor $\boldsymbol{S}_y(k)$ is calculated and updated subsequently:

$$\boldsymbol{S}_y^-(k) = \text{qr}\left(\left[\sqrt{Z_1^b}\cdot\left(\mathbf{y}_{1:2n}(k) - \hat{\boldsymbol{y}}^-(k)\right) \quad \sqrt{\boldsymbol{R}_{mn}}\right]\right), \tag{A.32}$$

$$\boldsymbol{S}_y^-(k) = \text{cholupdate}\left(\boldsymbol{S}_y^-(k), \mathsf{y}_0(k) - \hat{\boldsymbol{y}}^-(k), \sqrt{Z_0^b}\right), \tag{A.33}$$

with $\boldsymbol{R}_{mn}$ being the measurement noise covariance matrix. The cross-covariance matrix $\boldsymbol{P}_{xy}(k)$ is then calculated by

$$\boldsymbol{P}_{xy}(k) = \sum_{i=0}^{2n} Z_i^b \cdot \left(\mathsf{x}_i(k) - \hat{\boldsymbol{x}}^-(k)\right)\cdot\left(\mathsf{y}_i(k) - \hat{\boldsymbol{y}}^-(k)\right)^\top. \tag{A.34}$$

With (A.34), the Kalman gain matrix $\boldsymbol{K}_{ukf}(k)$ is derived:

$$\boldsymbol{K}_{ukf}(k) = \left(\boldsymbol{P}_{x,y}(k)/\boldsymbol{S}_y^-(k)^\top\right)/\boldsymbol{S}_y^-(k), \tag{A.35}$$

where the nested divisions are efficiently solved by a QR decomposition with pivoting [vdMW01]. Thus, the state estimates $\hat{\boldsymbol{x}}(k)$ result from the correction of $\hat{\boldsymbol{x}}^-(k)$:

$$\hat{\boldsymbol{x}}(k) = \hat{\boldsymbol{x}}^-(k) + \boldsymbol{K}_{ukf}(k)\cdot\left(\boldsymbol{y}(k) - \hat{\boldsymbol{y}}^-(k)\right). \tag{A.36}$$

Finally, another time update is required for the correction of the Cholesky factor $\boldsymbol{S}(k)$:

$$\boldsymbol{S}(k) = \text{cholupdate}\left(\boldsymbol{S}^-(k), \boldsymbol{K}_{ukf}(k)\cdot\boldsymbol{S}_y^-(k), -1\right). \tag{A.37}$$

A.5.2 Parameter Estimation

The discrete parameter estimation with an SRUKF is directly derived from Sec. A.5.1 by describing the nonlinear output equation (A.15b) in dependence on the parameter vector $\boldsymbol{p}$ to be estimated:

$$\boldsymbol{y}(k) = \boldsymbol{H}(\boldsymbol{x}(k), \boldsymbol{p}), \tag{A.38}$$

with the nonlinear function $\boldsymbol{H}$. Thus, a new state-space model can be established for the stationary process of $\boldsymbol{p}(k)$ [vdMW01]:

$$\boldsymbol{p}(k) = \boldsymbol{p}(k-1) + \boldsymbol{\nu}_{ppn}(k-1), \tag{A.39a}$$

$$\boldsymbol{y}_d(k-1) = \boldsymbol{H}(\boldsymbol{x}(k-1), \boldsymbol{p}(k-1)) + \boldsymbol{e}_{ukf}(k-1), \tag{A.39b}$$

with the parameter process noise $\boldsymbol{\nu}_{ppn}(k)$ and the residual output error $\boldsymbol{e}_{ukf}(k)$ between the desired output vector $\boldsymbol{y}_d(k)$ and the output of $\boldsymbol{H}$. The convergence and tracking performance of the parameter estimation is determined by the chosen variances in $\boldsymbol{\nu}_{ppn}(k)$ [vdMW01].

Due to the stationary state equation (A.39a), the time update of the state covariance is much simpler. As a result, the prediction part of the SRUKF algorithm for the parameter estimation is shorter than in the previous section. After the initialization of the estimated parameter

vector $\hat{\boldsymbol{p}}(k)$ and its corresponding Cholesky factor $\boldsymbol{S}_p(k)$ in accordance with the approaches in (A.16) and (A.17), the updated parameter vector $\hat{\boldsymbol{p}}^-(k)$ is directly given by the previous estimated parameter vector $\hat{\boldsymbol{p}}(k-1)$:

$$\hat{\boldsymbol{p}}^-(k) = \hat{\boldsymbol{p}}(k-1). \tag{A.40}$$

The updated Cholesky factor $\boldsymbol{S}_p^-(k)$ is calculated by weighting past data exponentially [vdMW01]:

$$\boldsymbol{S}_p^-(k) = \gamma_{ukf}^{-\frac{1}{2}} \cdot \boldsymbol{S}_p(k-1), \tag{A.41}$$

with the weighting factor $\gamma_{ukf} < 1$. Thus, the sigma points $\mathbf{p}(k)$ are determined by

$$\mathbf{p}(k) = \begin{bmatrix} \hat{\boldsymbol{p}}^-(k) & \hat{\boldsymbol{p}}^-(k) + \eta_{ukf} \cdot \boldsymbol{S}_p^-(k) & \hat{\boldsymbol{p}}^-(k) - \eta_{ukf} \cdot \boldsymbol{S}_p^-(k) \end{bmatrix}. \tag{A.42}$$

Subsequently, the sigma points $\mathbf{p}(k)$ are transformed by $\boldsymbol{H}$ similar to (A.30):

$$\mathbf{y}_d(k) = \boldsymbol{H}\left(\boldsymbol{x}(k), \mathbf{p}(k)\right). \tag{A.43}$$

With (A.43), the updated desired output vector $\hat{\boldsymbol{y}}_d^-(k)$ is given by

$$\hat{\boldsymbol{y}}_d^-(k) = \sum_{i=0}^{2n} Z_i^a \cdot \mathsf{y}_{d,i}(k). \tag{A.44}$$

For the correction step with measurements, the parameter estimation follows the same procedure as for the state estimation starting from (A.32). In the procedure, the variables of (A.15) are replaced by their corresponding variables of (A.39), which finally yields the estimated parameter vector $\hat{\boldsymbol{p}}(k)$ and the Cholesky factor $\boldsymbol{S}_p(k)$.

A.6 Startup Strategy for Actively Controlled Loop Heat Pipes

When the controller of the control heater of an actively controlled LHP is turned on, a high deviation between the controlled temperature and the desired setpoint temperature may exist dependent on the operating status of the LHP. Based on a high control error, a high control heater output would be dictated by a control algorithm to quickly raise the OT toward its setpoint temperature. As a result, the LHP would shutdown and stop the heat transfer from the heat source to the heat sink (see Sec. 3.2.2). In order to achieve a gentle setpoint approach, an adequate startup process for the controller of the control heater is required.

For the discrete OT control of an LHP, the actual setpoint temperature $T_{set,act}$ for the controller is initialized at the controlled temperature T and increases continuously with a fixed value, until it reaches the desired setpoint temperature T_{set}. The fixed value is calculated by the maximum setpoint rate K_r and the sampling time T_{st}. The variable K_r is chosen in accordance with the permitted maximum temperature gradient of the LHP, e.g. the experimentally determined operation limit of $\Delta T_{cc}/\Delta t = 0.07\,\mathrm{K\,s^{-1}}$ in this thesis. The setpoint ramp allows the LHP to reach its desired OP smoothly without interrupting its operation. The relevant controller startup is tracked by the boolean variable $reset$. The overall startup strategy is implemented as follows:

Algorithm 1 Controller startup

1: **if** $T_{set} - T_{set,act} > T_{st} \cdot K_r$ **and** $reset$ is true **then**
2: $\quad T_{set,act} \leftarrow T_{st} \cdot K_r + T_{set,act}$
3: **else**
4: $\quad reset \leftarrow$ false
5: $\quad T_{set,act} \leftarrow T_{set}$
6: **end if**

References

Public References

[AAV+12] A. Ambirajan, A. Adoni, J. Vaidya, A. Rajendran, D. Kumar, and P. Dutta. Loop heat pipes: a review of fundamentals, operation, and design. *Heat Transfer Engineering*, 33(4-5):387–405, 2012.

[Ada18] J. Adamy. *Nichtlineare Systeme und Regelungen. (German) [Nonlinear systems and controls].* Springer Berlin Heidelberg, 3rd edition, 2018.

[AFN19] T. Adachi, K. Fujita, and H. Nagai. Numerical study of temperature oscillation in loop heat pipe. *Applied Thermal Engineering*, 163, 2019.

[AG93] F. Allgöwer and E. Gilles. Nichtlinearer Reglerentwurf auf der Grundlage exakter Linearisierungstechniken. (German) [Nonlinear controller design by exact linearization techniques]. VDI Berichte Nr. 1026, 1993.

[Ant88] L. Antoine. Tensions des vapeurs: nouvelle relation entre les tensions et les températures. *Comptes Rendus des Séances de l'Académie des Sciences*, 107:681–684, 1888.

[AT03] M. Araki and H. Taguchi. Two-degree-of-freedom PID controllers. *International Journal of Control, Automation, and Systems*, 1(4):401–411, 2003.

[BA95] C. Bohn and D. Atherton. An analysis package comparing PID anti-windup strategies. *IEEE Control Systems Magazine*, 15(2):34–40, 1995.

[BBD98] C. Baker, W. Bienert, and A. Ducao. Loop heat pipe flight experiment. In *28th International Conference on Environmental Systems (ICES)*, SAE Technical Paper Series, No. 981813. SAE International, 1998.

[BCG+18] M. Bernagozzi, S. Charmer, A. Georgoulas, I. Malavasi, N. Michè, and M. Marengo. Lumped parameter network simulation of a loop heat pipe for energy management systems in full electric vehicles. *Applied Thermal Engineering*, 141:617–629, 2018.

[BK16] H. Baehr and S. Kabelac. *Thermodynamik. (German) [Thermodynamics].* Springer Berlin Heidelberg, 16th edition, 2016.

[BLW10] L. Bai, G. Lin, and D. Wen. Modeling and analysis of startup of a loop heat pipe. *Applied Thermal Engineering*, 30(17-18):2778–2787, 2010.

[BS19] H. Baehr and K. Stephan. *Wärme- und Stoffübertragung. (German) [Heat and mass transfer].* Springer Berlin Heidelberg, 10th edition, 2019.

[BSR+05] F. Bodendieck, R. Schlitt, O. Romberg, K. Goncharov, V. Buz, and U. Hildebrand. Precision temperature control with a loop leat pipe. In *35th International Conference on Environmental Systems (ICES)*, SAE Technical Paper Series, No. 2005-01-2938. SAE International, 2005.

[BWN+97] W. Bienert, D. Wolf, M. Nikitkin, Y. Maidanik, Y. Fershtater, S. Vershinin, and J. Gottschlich. Proof-of-feasibility of multiple evaporator loop heat pipes. In *Sixth European Symposium on Space Environmental Control Systems*, volume 400 of *ESA Special Publication*, pages 393–398, 1997.

[Cha14] M. Chaudhry. *Applied hydraulic transients*. Springer New York, 3rd edition, 2014.

[CHKK98] K. Cheung, T. Hoang, J. Ku, and T. Kaya. Thermal performance and operational characteristics of loop heat pipe (NRL LHP). In *28th International Conference on Environmental Systems (ICES)*, SAE Technical Paper Series, No. 981580. SAE International, 1998.

[Chu03] P. Chuang. *An improved steady-state model of loop heat pipe based on experimental and theoretical analyses*. PhD thesis, Pennsylvania State University, Department of Mechanical and Nuclear Engineering, 2003.

[CM05] M. Chernysheva and Y. Maydanik. Operating temperature of loop heat pipe. In *6th Minsk International Seminar "Heat Pipes, Heat Pumps, Refrigerators"*, pages 122–128, Minsk, Belarus, 2005.

[CVM07] M. Chernysheva, S. Vershinin, and Y. Maydanik. Operating temperature and distribution of a working fluid in LHP. *International Journal of Heat and Mass Transfer*, 50(13):2704–2713, 2007.

[DLWW12] S. Dong, Y. Li, J. Wang, and J. Wang. Fuzzy incremental control algorithm of loop heat pipe cooling system for spacecraft applications. *Computers & Mathematics with Applications*, 64(5):877–886, 2012. Advanced Technologies in Computer, Consumer and Control.

[Eur14] European Space Agency (ESA). European Data Relay System (EDRS). Retrieved from `http://www.esa.int/ESA_Multimedia/Images/2014/06/European_Data_Relay_System_EDRS`, 2014. Accessed: 11-25-2021.

[Eur15a] European Space Agency (ESA). *EDRS: the European Data Relay System*. ESA Communications Production, Noordwijk, 2015.

[Eur15b] European Space Agency (ESA). Laser communication terminal. Retrieved from `http://www.esa.int/ESA_Multimedia/Images/2015/06/Laser_communication_terminal`, 2015. Accessed: 11-25-2021.

[Föl16] O. Föllinger. *Regelungstechnik. (German) [Control technology]*. VDE Verlag, Berlin, 12th edition, 2016.

[Fur06] M. Furukawa. Model-based method of theoretical design analysis of a loop heat pipe. *Journal of Thermophysics and Heat Transfer*, 20(1):111–121, 2006.

[GGK00] K. Goncharov, O. Golovin, and V. Kolesnikov. Loop heat pipe with several evaporators. In *30th International Conference on Environmental Systems (ICES)*, SAE Technical Paper Series, No. 2000-01-2407. SAE International, 2000.

[GGK+13] K. Goncharov, O. Golovin, A. Kochetkov, M. Balykin, K. Korzhov, Y. Panin, and V. Antonov. On methods for loop heat pipe control by external heat action. *Solar System Research*, 47(7):554–560, 2013.

[GKB06] K. Gongharov, A. Kochetkov, and V. Buz. Development of loop heat pipe with pressure regulator. In *36th International Conference on Environmental Systems (ICES)*, SAE Technical Paper Series, No. 2006-01-2171. SAE International, 2006.

[GKU+03] S. Gyoubu, M. Kosaka, H. Uda, K. Tanikake, K. Kitanaka, and Y. Sugiyama. Anti-windup feedforward controller design for reference input. In *SICE 2003 Annual Conference*, volume 2, pages 1856–1859, 2003. IEEE Cat. No. 03TH8734.

[GTPK05] C. Gregori, A. Torres, R. Pérez, and T. Kaya. LHP modeling with EcosimPro and experimental validation. In *35th International Conference on Environmental Systems (ICES)*, SAE Technical Paper Series, No. 2005-01-2934. SAE International, 2005.

[HB12] T. Hoang and R. Baldauff. A theory for temperature oscillations in loop heat pipes. In *42nd International Conference on Environmental Systems (ICES)*. American Institute of Aeronautics and Astronautics (AIAA), 2012.

[HB16] T. Hoang and R. Baldauff. Nonlinear dynamics in loop heat pipe operation. In *46th AIAA Thermophysics Conference*. American Institute of Aeronautics and Astronautics (AIAA), 2016.

[HBM15] T. Hoang, R. Baldauff, and J. Maxwell. Stability theory for loop heat pipe design, analysis and operation. In *45th International Conference on Environmental Systems (ICES)*, 2015.

[HHL09] B. Huang, H. Huang, and T. Liang. System dynamics model and startup behavior of loop heat pipe. *Applied Thermal Engineering*, 29(14):2999–3005, 2009.

[HK03] T. Hoang and J. Ku. Transient modeling of loop heat pipes. In *1st International Energy Conversion Engineering Conference (IECEC)*. American Institute of Aeronautics and Astronautics (AIAA), 2003.

[HK04] T. Hoang and J. Ku. Mathematical modeling of loop heat pipes with mutiple capillary pumps and multiple condensers, part I steady state simulations. In *2nd International Energy Conversion Engineering Conference*. American Institute of Aeronautics and Astronautics (AIAA), 2004.

[HMS16] E. Hering, R. Martin, and M. Stohrer. *Physik für Ingenieure. (German) [Physics for engineers]*. Springer Berlin Heidelberg, 12th edition, 2016.

[Hoa19] T. Hoang. Linear stability analysis for loop heat pipe operations. In *49th International Conference on Environmental Systems (ICES)*, 2019.

[Isi95] A. Isidori. *Nonlinear control systems*. Springer London, 1995.

[JGKY15] W. Joung, K. Gam, Y. Kim, and I. Yang. Hydraulic operating temperature control of a loop heat pipe. *International Journal of Heat and Mass Transfer*, 86:796–808, 2015.

[JU97] S. Julier and J. Uhlmann. New extension of the Kalman filter to nonlinear systems. In *Signal Processing, Sensor Fusion, and Target Recognition VI*. SPIE, 1997.

[Kal60] R. Kalman. A new approach to linear filtering and prediction problems. *Journal of Basic Engineering*, 82(1):35–45, 1960.

[KAS18] M. Khalili, A. Abolmaali, and M. Shafii. Experimental and analytical study of thermohydraulic performance of a novel loop heat pipe with an innovative active temperature control method. *Applied Thermal Engineering*, 143:964–976, 2018.

[KB01] J. Ku and G. Birur. Active control of the operating temperature in a loop heat pipe with two evaporators and two condensers. In *31st International Conference on Environmental Systems (ICES)*, SAE Technical Paper Series, No. 2001-01-2188. SAE International, 2001.

[KG06] T. Kaya and J. Goldak. Numerical analysis of heat and mass transfer in the capillary structure of a loop heat pipe. *International Journal of Heat and Mass Transfer*, 49(17-18):3211–3220, 2006.

[Kha15] H. Khalil. *Nonlinear control*. Pearson, Boston, 2015.

[KJS10] M. Kleiber, R. Joh, and R. Span. D3 properties of pure fluid substances. In *VDI Heat Atlas*, pages 301–418. Springer Berlin Heidelberg, 2010.

[Klu13] M. Kluwe. Regelung linearer Mehrgrößensysteme. (German) [Control of linear multivariable systems]. Lecture notes, Institute of Control Systems (IRS), Karlsruhe Institute of Technology (KIT), 2013.

[KN07] J. Ku and H. Nagano. Loop heat pipe operation with thermoelectric converters and coupling blocks. NASA Technical Reports Server No. 20070030119, 5th International Energy Conversion Engineering Conference and Exhibit (IECEC), 2007.

[KOB04] J. Ku, L. Ottenstein, and G. Birur. Thermal performance of a multi-evaporator loop heat pipe with thermal masses and thermal electrical coolers. In *13th International Heat Pipe Conference*, Shanghai, China, 2004.

[KOK+01] J. Ku, L. Ottenstein, M. Kobel, P. Rogers, and T. Kaya. Temperature oscillations in loop heat pipe operation. In *AIP Conference Proceedings*, volume 552, pages 255–262. American Institute of Physics (AIP), 2001.

[KPGT08] T. Kaya, R. Pérez, C. Gregori, and A. Torres. Numerical simulation of transient operation of loop heat pipes. *Applied Thermal Engineering*, 28(8):967–974, 2008.

[KPM11a] J. Ku, K. Paiva, and M. Mantelli. Loop heat pipe operation using heat source temperature for set point control. NASA Technical Reports Server No. 20110015274, 41st International Conference on Environmental Systems, 2011.

[KPM11b] J. Ku, K. Paiva, and M. Mantelli. Loop heat pipe transient behavior using heat source temperature for set point control with thermoelectric converter on reservoir. NASA Technical Reports Server No. 20110015224, 9th Annual International Energy Conversion Engineering Conference, 2011.

[KR03] J. Ku and J. Rodriguez. Low frequency high amplitude temperature oscillations in loop heat pipe operation. In *33rd International Conference on Environmental Systems (ICES)*, SAE Technical Paper Series, No. 2003-01-2386. SAE International, 2003.

[KR10] D. Khrustalev and G. Robertson. Advances in transient modeling of loop heat pipe systems with multiple components. In *AIP Conference Proceedings*, volume 1208, pages 55–67. American Institute of Physics (AIP), 2010.

[KRJD90] P. Krishnaswamy, G. Rangaiah, R. Jha, and P. Deshpande. When to use cascade control. *Industrial & Engineering Chemistry Research*, 29(10):2163–2166, 1990.

[KSK+14] D. Khrustalev, C. Stouffer, J. Ku, J. Hamilton, and M. Anderson. Temperature control with two parallel small loop heat pipes for GLM program. *Frontiers in Heat Pipes*, 5(9), 2014.

[Ku99] J. Ku. Operating characteristics of loop heat pipes. In *29th International Conference on Environmental Systems (ICES)*, SAE Technical Paper Series, No. 1999-01-2007. SAE International, 1999.

[Ku03] J. Ku. High frequency low amplitude temperature oscillations in loop heat pipe operation. In *33rd International Conference on Environmental Systems (ICES)*, SAE Technical Paper Series, No. 2003-01-2387. SAE International, 2003.

[Ku08] J. Ku. Methods of controlling the loop heat pipe operating temperature. In *38th International Conference on Environmental Systems (ICES)*, SAE Technical Paper Series, No. 2008-01-1998. SAE International, 2008.

[Ku16] J. Ku. Loop heat pipe startup behaviors. In *46th International Conference on Environmental Systems (ICES)*, 2016.

[KW15] C. Kolbe-Weber. The coldest place in the universe. Retrieved from `https://www.helmholtz.de/en/aeronautics-space-and-transport/the-coldest-place-in-the-universe/`, 2015. Accessed: 11-25-2021.

[LKLT17] K. Langeheinecke, A. Kaufmann, K. Langeheinecke, and G. Thieleke. *Thermodynamik für Ingenieure. (German) [Thermodynamics for engineers].* Springer Fachmedien Wiesbaden, 10th edition, 2017.

[LPDJ07] S. Launay, V. Platel, S. Dutour, and J. Joly. Transient modeling of loop heat pipes for the oscillating behavior study. *Journal of Thermophysics and Heat Transfer*, 21(3):487–495, 2007.

[LRWW98] J. Lagarias, J. Reeds, M. Wright, and P. Wright. Convergence properties of the Nelder–Mead simplex method in low dimensions. *SIAM Journal on Optimization*, 9(1):112–147, 1998.

[Lun20a] J. Lunze. *Regelungstechnik 1. (German) [Control technology 1].* Springer Berlin Heidelberg, 12th edition, 2020.

[Lun20b] J. Lunze. *Regelungstechnik 2. (German) [Control technology 2].* Springer Berlin Heidelberg, 10th edition, 2020.

[LWL10] Y. Li, Y. Wang, and K. Lee. Dynamic modeling and transient performance analysis of a LHP-MEMS thermal management system for spacecraft electronics. *IEEE Transactions on Components and Packaging Technologies*, 33(3):597–606, 2010.

[Mat20a] MathWorks. *Control system toolbox reference.* The MathWorks, Inc., Natick, Massachusetts, USA, 2020.

[Mat20b] MathWorks. *Control system toolbox user's guide.* The MathWorks, Inc., Natick, Massachusetts, USA, 2020.

[Mat20c] MathWorks. *MATLAB function reference.* The MathWorks, Inc., Natick, Massachusetts, USA, 2020.

[Mat20d] MathWorks. *MATLAB mathematics documentation.* The MathWorks, Inc., Natick, Massachusetts, USA, 2020.

[May05] Y. Maydanik. Loop heat pipes. *Applied Thermal Engineering*, 25(5-6):635–657, 2005.

[MKHW19] S. Meinicke, P. Knipper, C. Helfenritter, and T. Wetzel. A lean approach of modeling the transient thermal characteristics of loop heat pipes based on experimental investigations. *Applied Thermal Engineering*, 147:895–907, 2019.

[MVPF10] Y. Maydanik, S. Vershinin, V. Pastukhov, and S. Fried. Loop heat pipes for cooling systems of servers. *IEEE Transactions on Components and Packaging Technologies*, 33(2):416–423, 2010.

[Nat18] G. Naterer. *Advanced heat transfer.* CRC Press, 2nd edition, 2018.

[NKS99] M. Nikitkin, E. Kotlyarov, and G. Serov. Basics of loop heat pipe temperature control. In *29th International Conference on Environmental Systems (ICES)*, SAE Technical Paper Series, No. 1999-01-2012. SAE International, 1999.

[NM65] J. Nelder and R. Mead. A simplex method for function minimization. *The Computer Journal*, 7(4):308–313, 1965.

[NNK13] M. Nishikawara, H. Nagano, and T. Kaya. Transient thermo-fluid modeling of loop heat pipes and experimental validation. *Journal of Thermophysics and Heat Transfer*, 27(4):641–647, 2013.

[NW07] M. Nikitkin and D. Wolf. Development of LHP with low control power. In *37th International Conference on Environmental Systems (ICES)*, SAE Technical Paper Series, No. 2007-01-3237. SAE International, 2007.

[Ort13] A. Ortseifen. *Entwurf von modellbasierten Anti-Windup-Methoden für Systeme mit Stellbegrenzungen. (German) [Design of model-based anti-windup methods for systems with actuator limitations].* PhD thesis, Department of Electrical Engineering and Information Technology, Technical University (TU) of Darmstadt, 2013.

[PAP16] N. Putra, B. Ariantara, and R. Pamungkas. Experimental investigation on performance of lithium-ion battery thermal management system using flat plate loop heat pipe for electric vehicle application. *Applied Thermal Engineering*, 99:784–789, 2016.

[QSWL18] J. Qi, K. Sun, J. Wang, and H. Liu. Dynamic state estimation for multi-machine power system by unscented kalman filter with enhanced numerical stability. *IEEE Transactions on Smart Grid*, 9(2):1184–1196, 2018.

[RMT16] F. Romera, D. Mishkinis, and A. Torres. Qualification of a thermal control system for laser communication terminals. In *2016 Spacecraft Thermal Control Workshop (STCW)*, The Aerospace Corporation, El Segundo, California, USA, 2016.

[RWH07] C. Ren, Q. Wu, and M. Hu. Heat transfer with flow and evaporation in loop heat pipe's wick at low or moderate heat fluxes. *International Journal of Heat and Mass Transfer*, 50(11-12):2296–2308, 2007.

[Shu08] K. Shukla. Thermo-fluid dynamics of loop heat pipe operation. *International Communications in Heat and Mass Transfer*, 35(8):916–920, 2008.

[Shu15] K. Shukla. Heat pipe for aerospace applications—an overview. *Journal of Electronics Cooling and Thermal Control*, 5(1):1–14, 2015.

[Sid15] G. Sidebotham. *Heat transfer modeling.* Springer International Publishing, 2015.

[Sim06] D. Simon. *Optimal state estimation.* John Wiley & Sons, 2006.

[SN17] K. Sato and H. Nagano. Transient mathematical modeling of a reservoir controlled loop heat pipe. In *47th International Conference on Environmental Systems (ICES)*, 2017.

[SR97] L. Shampine and M. Reichelt. The MATLAB ODE suite. *SIAM Journal on Scientific Computing*, 18(1):1–22, 1997.

[SSSM13] P. Stephan, K. Schaber, K. Stephan, and F. Mayinger. *Thermodynamik. (German) [Thermodynamics]*, volume 1. Springer Berlin Heidelberg, 19th edition, 2013.

[Sto07] K. Stowe. *An introduction to thermodynamics and statistical mechanics.* Cambridge University Press, Cambridge, UK New York, 2nd edition, 2007.

[Str14] H. Struchtrup. *Thermodynamics and energy conversion.* Springer Berlin Heidelberg, 2014.

[TMK14] A. Torres, D. Mishkinis, and T. Kaya. Mathematical modeling of a new satellite thermal architecture system connecting the east and west radiator panels and flight performance prediction. *Applied Thermal Engineering*, 65(1-2):623–632, 2014.

[TT13] G. Teschl and S. Teschl. *Mathematik für Informatiker. (German) [Mathematics for computer scientists]*, volume 1. Springer Berlin Heidelberg, 4th edition, 2013.

[UK17] E. Ungar and J. Ku. Actively controlled loop heat pipes as a human spacecraft external active thermal control system. In *47th International Conference on Environmental Systems (ICES)*, 2017.

[Unb08] H. Unbehauen. *Regelungstechnik I. (German) [Control technology I]*. Vieweg+Teubner, 15th edition, 2008.

[vBS15] P. von Böckh and M. Stripf. *Technische Thermodynamik. (German) [Technical thermodynamics]*. Springer Berlin Heidelberg, 2nd edition, 2015.

[vBW17] P. von Böckh and T. Wetzel. *Wärmeübertragung. (German) [Heat transfer]*. Springer Berlin Heidelberg, 7th edition, 2017.

[vdM04] R. van der Merwe. *Sigma-point Kalman filters for probabilistic inference in dynamic state-space models*. PhD thesis, Oregon Health and Science University, OGI School of Science and Engineering, 2004.

[vdMW01] R. van der Merwe and E. Wan. The square-root unscented Kalman filter for state and parameter-estimation. In *IEEE International Conference on Acoustics, Speech, and Signal Processing. Proceedings*. IEEE, 2001.

[vdPvdM27] B. van der Pol and J. van der Mark. Frequency demultiplication. *Nature*, 120(3019):363–364, 1927.

[vEvG13] J. van Es and H. van Gerner. Benefits and drawbacks of using two-phase cooling technologies in military platforms. *Electronics Cooling*, 2013.

[Vis06] A. Visioli. *Practical PID control*. Springer London, 2006.

[VR08] V. Vlassov and R. Riehl. Mathematical model of a loop heat pipe with cylindrical evaporator and integrated reservoir. *Applied Thermal Engineering*, 28(8):942–954, 2008.

[WBB78] G. Wedekind, B. Bhatt, and B. Beck. A system mean void fraction model for predicting various transient phenomena associated with two-phase evaporating and condensing flows. *International Journal of Multiphase Flow*, 4(1):97–114, 1978.

[WGWS10] W. Kast (Revised by H. Nirschl), E. Gaddis, K. Wirth, and J. Stichlmair. L1 pressure drop in single phase flow. In *VDI Heat Atlas*, pages 1053–1116. Springer Berlin Heidelberg, 2010.

[WKSK10] W. Wagner, H. Kretzschmar, R. Span, and R. Krauss. D2 properties of selected important pure substances. In *VDI Heat Atlas*, pages 153–300. Springer Berlin Heidelberg, 2010.

[Zoh16] B. Zohuri. *Heat pipe design and technology*. Springer International Publishing, 2016.

[ZSC+08] W. Zimbeck, G. Slavik, J. Cennamo, S. Kang, J. Yun, and E. Kroliczek. Loop heat pipe technology for cooling computer servers. In *11th Intersociety Conference on Thermal and Thermomechanical Phenomena in Electronic Systems*. IEEE, 2008.

Own Publications and Conference Contributions

[GH20] T. Gellrich and S. Hohmann. Model-based design of a cascade control for loop heat pipes. *9th FDIBA Conference*, Vol. 4, 2020.

[GMK+18] T. Gellrich, S. Meinicke, P. Knipper, S. Hohmann, and T. Wetzel. Two-degree-of-freedom heater control of a loop heat pipe based on stationary modeling. In *48th International Conference on Environmental Systems (ICES)*, 2018.

[GMSH20a] T. Gellrich, Y. Min, S. Schwab, and S. Hohmann. Model-free control design for loop heat pipes using deep deterministic policy gradient. *IFAC-PapersOnLine*, 53(2):1575–1580, 2020.

[GMSH20b] T. Gellrich, J. Moeller, S. Schwab, and S. Hohmann. Extended nonlinear dynamical modeling and state estimation for the temperature control of loop heat pipes. In *2020 IEEE Conference on Control Technology and Applications (CCTA)*. IEEE, 2020.

[GSHH18] T. Gellrich, T. Schuermann, F. Hobus, and S. Hohmann. Model-based heater control design for loop heat pipes. In *2018 IEEE Conference on Control Technology and Applications (CCTA)*. IEEE, 2018.

[GSO+20] T. Gellrich, C. Sester, M. Okraschevski, S. Schwab, H. Bauer, and S. Hohmann. Dynamic state-space modeling and model-based control design for loop heat pipes. *preprint, arXiv:2001.05793*, 2020.

[GZSH19] T. Gellrich, X. Zhang, S. Schwab, and S. Hohmann. Nonlinear model identification adaptive heater control design for loop heat pipes. In *2019 IEEE Conference on Control Technology and Applications (CCTA)*. IEEE, 2019.

[KGH17] S. Krebs, T. Gellrich, and S. Hohmann. Interval observers for LPV systems and application to the guaranteed state estimation of an induction machine. *IFAC-PapersOnLine*, 50(1):2794–2799, 2017.

Supervised Theses

[Ge21] F. Ge. Model predictive control of loop heat pipes in satellites. Master's thesis, Department of Electrical Engineering and Information Technology, Karlsruhe Institute of Technology (KIT), 2021.

[Kov18] C. Kovacs. Entwurf eines Gain-Scheduling-Reglers für Loop Heat Pipes. (German) [Design of a gain-scheduling control for loop heat pipes]. Bachelor's thesis, Department of Electrical Engineering and Information Technology, Karlsruhe Institute of Technology (KIT), 2018.

[Lia18] L. Liang. Modellierung eines Wärmetransportsystems im Satelliten. (German) [Modeling of a heat transfer system in a satellite]. Master's thesis, Department of Electrical Engineering and Information Technology, Karlsruhe Institute of Technology (KIT), 2018.

[Min19] Y. Min. Control design for loop heat pipes using reinforcement learning. Master's thesis, Department of Electrical Engineering and Information Technology, Karlsruhe Institute of Technology (KIT), 2019.

[Nag18] T. Nagel. Modellierung und Regelung einer Loop Heat Pipe mittels Neuronalem Netz. (German) [Modeling and control of a loop heat pipe using neural networks]. Master's thesis, Department of Electrical Engineering and Information Technology, Karlsruhe Institute of Technology (KIT), 2018.

[Ses19] C. Sester. Dynamische Modellierung eines Wärmetransportsystems im Satelliten. (German) [Dynamical modeling of a heat transport system in a satellite]. Master's thesis, Department of Mechanical Engineering, Karlsruhe Institute of Technology (KIT), 2019.

[Tei17] T. Teichmann. Thermalregelung eines Satelliten am Prüfstand. (German) [Thermal control of a satellite on a test bench]. Bachelor's thesis, Department of Electrical Engineering and Information Technology, Karlsruhe Institute of Technology (KIT), 2017.

[Tos20] A. Tos. Fuzzy-Regelung für Loop Heat Pipes. (German) [Fuzzy control for loop heat pipes]. Bachelor's thesis, Department of Electrical Engineering and Information Technology, Karlsruhe Institute of Technology (KIT), 2020.

[Zha18] X. Zhang. Entwurf einer adaptiven Regelung für Loop Heat Pipes. (German) [Design of an adaptive control for loop heat pipes]. Master's thesis, Department of Mechanical Engineering, Karlsruhe Institute of Technology (KIT), 2018.